Design and Analysis of an Interplanetary SmallSat

Multispectral Asteroid Photography Low-thrust Explorer Student Iris Reduced volUme Probe (MAPLE SIRUP)

A Major Qualifying Project Report
Submitted to the Faculty of the WORCESTER POLYTECHNIC INSTITUTE
in Partial Fulfillment of the Requirements
for the Degree of Bachelor of Science
in Aerospace Engineering

by

Smith Edwards

Matthew Kirejczyk

Bradley LaGrasse

Elijah Levi

Gracie Lodge-McIntire

Ian Mayer

Peter Zollinger

May 6, 2021

Approved by: _____

Professor Zachary R. Taillefer, Advisor

Aerospace Engineering Department

WPI

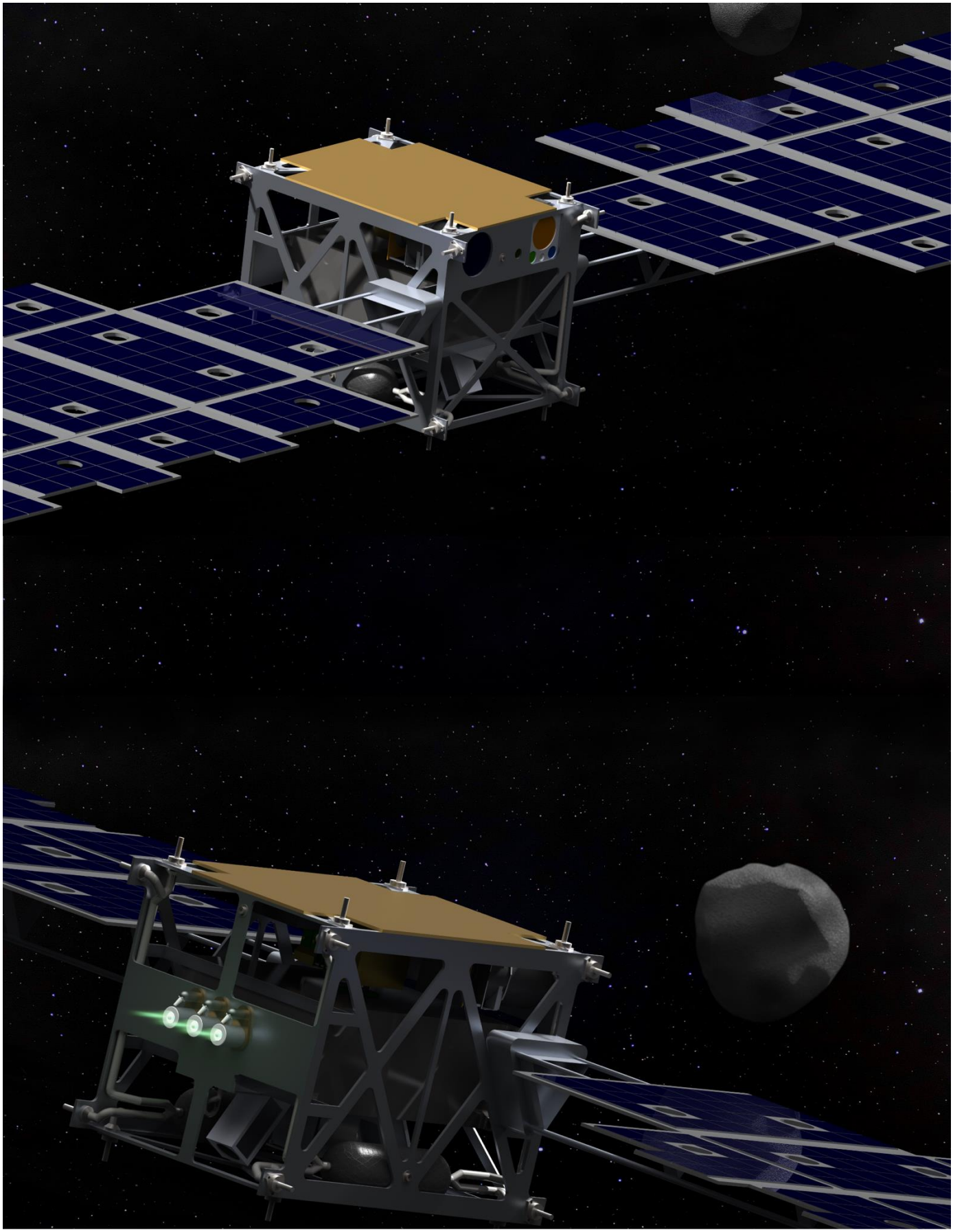

Abstract

This project presents the design and analysis of a 150kg small interplanetary spacecraft. This spacecraft is inserted into a near-GEO orbit and transfers to an elliptical orbit around asteroid 7 Iris. At Iris, this spacecraft will gather color photographs, spectral data, and topographic data using onboard sensors. Also, the spacecraft will record plasma activity along its trajectory using a plasma spectrometer. A novel iodine-fueled electric propulsion system is presented and a low-thrust trajectory to an observation orbit at Iris is determined. Fuel volume reduction of 40% is achieved compared to traditional xenon systems with minimal impact on performance, allowing the spacecraft to remain within the rideshare constraints. Power needs were satisfied using a combination of batteries, a solar array, and an EPS board. Simulations using sun-tracking were performed in STK allowing for accurate models of the generated, stored, and consumed power throughout the mission. Using these models, a solar array with an end-of-life power generation capability of 375W was achieved. A radio, antenna, and on-board computer were chosen to allow the spacecraft to communicate via the Deep Space Network ground stations. The data transfer rate was modeled by the Shannon-Hartley capacity theorem, and access windows were determined using Systems Toolkit. The attitude determination and control system uses star trackers and sun sensors to determine the orientation of the spacecraft throughout the mission. Multiple numerical simulations were performed in MATLAB to prove that the chosen Sputnix reaction wheel system can perform all analyzed maneuvers and be routinely desaturated using 16 Marotta microthrusters. Environmental factors including thermal, radiation, vibration, and debris were considered, and constraints were provided to each subsystem. Environmental simulations demonstrated the need for thermal control and radiation shielding in the form of MLI blankets. The spacecraft's thermal properties during different phases of flight were analyzed using a

simplified CAD model important into COMSOL Multiphysics software. Thermal control systems were sized through iterative simulation testing to rely on minimal heating power by thermally isolating components, retaining waste heat. The design and construction of a thermal vacuum chamber test cell to simulate the thermal environment of space is also presented. A preliminary test was performed to measure temperatures experienced by a sample inside the chamber at rough vacuum under the heating of four 250-Watt heat bulbs. Temperature data for heat-up and cool-down cycles were collected and compared to thermal simulations done in COMSOL Multiphysics. Experimental temperatures were found to be approximately 20°C higher than simulated. The difference between the measured and thermal simulation temperatures could be due to several factors, including imperfect vacuum conditions during testing, a lack of active cooling of the shroud, and additional heat sources such as reflected radiation from the tank wall.

Acknowledgments

The MQP team would like to thank Dynavac for their generous donation of the liquid nitrogen shroud for our TVAC assembly. Additionally, we would like to thank Dr. Adriana Hera for her assistance with thermal and structural simulations of the spacecraft and TVAC assembly, and Christian Cooper for assistance with manufacturing additional TVAC components. We would also like to thank our advisor, Professor Zachary Taillefer for his knowledge and guidance throughout this entire project.

Table of Authorship

Introduction	All
Payload Subsystem	Kirejczyk
Structural Subsystem	Lodge-McIntire
Propulsion Subsystem	Zollinger
Power Subsystem	Mayer
Command and Data Handling Subsystem	Edwards
Attitude Determination and Control Subsystem	LaGrasse
Environment Subsystem	Kirejczyk
Thermal Control Subsystem	Levi
Thermal Vacuum Chamber	Kirejczyk, LaGrasse, Levi, Zollinger
Conclusion and Future Work	All
Social Impacts	Levi, Mayer

Table of Contents

Table of Figures

Table of Tables

1 Introduction

NASA classifies SmallSats as spacecraft with a mass of less than 180 kg and typically similar in size to a refrigerator. CubeSats are a standardized type of SmallSats based on units consisting of 10 x 10 x 10 cm sides and a mass of 1 kg [1]. Started in 1999 by California Polytechnic State University and Stanford University, the CubeSat program allows private organizations, governments, and especially students the opportunity to put payloads in space at a relatively low cost. The standardized size and design allow components to be mass-produced and purchased off-the-shelf rather than custom-designed for each mission. Since the start of this program, hundreds of SmallSats have been used in orbits near Earth [2]. Recently, however, there has been growing interest in using SmallSats for interplanetary missions. In 2018, MarCO A and B became the first CubeSats in interplanetary space when they flew alongside the Mars InSight Lander and transmitted the successful landing back to Earth [3]. The planned test mission Artemis 1 will carry thirteen CubeSats beyond low-Earth orbit (LEO), where some will maneuver into orbit around the Moon.

This Major Qualifying Project (MQP) team designed a SmallSat for an interplanetary mission. This project provides a design and orbital analysis for an interplanetary SmallSat to travel to and conduct scientific operations at the asteroid 7 Iris. It also describes the design and construction of a thermal vacuum test chamber in Section 10.

There have been several past MQPs at Worcester Polytechnic Institute (WPI) focusing on the design of CubeSats and other small spacecraft. One is the “Design and Analysis of the Sphinx-NG CubeSat,” MQP, which performed design and multiple subsystem analysis for a spacecraft carrying the SphinX-NG space weather observation instrument [4]. The MQP “Design and Analysis of a 6U CubeSat and Mission” similarly aimed to design a mission to carry a mass

spectrometer, inserting from the ISS into an elliptical orbit and collecting data on Earth's atmospheric weather patterns [5]. Both projects, alongside others undertaken by WPI students, focus on LEO, MEO, and GEO space environments. These missions also do not require a large ΔV, as they are generally deployed near or directly into their target orbits by a launch vehicle or the ISS. Therefore, while some work from previous MQPs will be relevant to the analysis of the interplanetary mission, techniques, and focuses of the mission will differ due to the drastically different mission parameters and requirements.

1.1 Project Goals

The goal of this project is to conceptualize and design an interplanetary CubeSat and its mission. The destination is 7 Iris, an asteroid in the Main Asteroid Belt between Mars and Jupiter. In achieving this goal, the propulsion system must have the requisite power. With a determined trajectory and requisite ΔV, this CubeSat will leave Earth orbit and traverse to 7 Iris. The power system must be sufficient to supply all thrusters, in both the propulsion and attitude determination and control subsystems. To track and maintain the correct attitude, sensors must collect and transmit critical information. Additionally, the mission has a scientific purpose – determining the feasibility of mining 7 Iris. As mentioned before, this asteroid may contain precious metals. Instruments capable of performing such a task must be powered and controlled, and the information must be collected and transmitted back to Earth. Lastly, a primary structure must be selected to which all the mentioned subsystems are mounted, and which can be attached to a launch vehicle as a secondary payload until orbit insertion.

1.2 Subsystems

Spacecraft are complex systems, requiring many dedicated subsystems that must work together to achieve the desired mission objectives. The following introduces these various subsystems and their design goals.

1.2.1 Payload

The mission is to travel 2.4 AU, or 359,990,000 km, to 7 Iris, an asteroid orbiting the sun in the main belt between Mars and Jupiter. 7 Iris is classified as an S-type asteroid meaning it has a stony composition and could contain numerous metal compositions [6]. Also, Iris is the fourth brightest object in the asteroid belt and the lack of documented data makes it a target of interest. To collect new data on 7 Iris, MAPLE SIRUP will be equipped with payloads that can analyze its composition and features.

The payload is one of the most important components of the spacecraft because it drives the mission requirements. The type of payload aboard a satellite is dependent on the mission objectives and type of information sought. Many satellites in LEO are carrying communication and navigation equipment that allow our cell phones and GPS to function. In addition, LEO satellites can be used for military reconnaissance and remote sensing such as crop monitoring, land use mapping, and disaster monitoring.

Satellites in GEO are unique since their orbits are at the same speed as Earth’s rotation. Due to this, the satellite remains fixed over a single location on Earth. These satellites typically function as weather satellites, navigation satellites, television broadcasting, and are important for defense and intelligence applications. As satellites begin to enter Interplanetary space their missions become focused on research and less on utility. Satellites are sent to find out more about our universe, what it contains, and possibilities for the future of human life. With the help

of imaging satellites, scientists have estimated there are 100 billion galaxies full of stars, asteroids, and planets. All of which contain precious minerals, new materials, different magnetic spheres, and mysteries for humans to solve [7].

The satellite in this report will contain payloads that are key to further exploring the surface characteristics of 7 Iris and its adjacent space atmosphere [8].

Objectives:

1. Identify payloads that will provide needed data about 7 Iris
2. Identify a secondary mission objective to perform when traveling to 7 Iris
3. Create a mass and power budget
4. Identify the operating temperatures of these components

1.2.2 Structures

The objective of the structural system of the CubeSat is to contain and mobilize the satellite components. Each subsystem is attached to and built into or upon the primary structure. For the satellite to function as a complete system, it requires a chassis on which power is generated, propulsion is based, and the enacting of the various functions of the mission through instrumental utilization. The primary structure must be structurally sound, lightweight, and durable, and the design and configuration of this structure must maximize internal volume for components.

1.2.3 Propulsion

The role of the primary propulsion system is to provide ΔV to change orbits, such as during Earth escape, heliocentric transfers, and Iris rendezvous. The objective of the propulsion subsystem is to perform all required maneuvers while delivering the spacecraft to the mission

target and conforming to size, power, and other requirements. To properly assess the primary propulsion system, however, a trajectory and associated ΔVs must first be obtained. Various methods such as analytical calculations, previous mission estimates, and numerical simulation can be used to determine maneuver requirements.

There are two main types of propulsion systems often considered for spacecraft. The first and more common propulsion system to consider is chemical propulsion. This system is characterized by chemically reacting propellent to create hot gases and produce thrust. Most spacecraft utilize chemical propulsion for either their main or auxiliary propulsion systems because of its relative simplicity and high thrust. However, chemical propulsion systems offer lower values for specific impulses (I_{sp}), in the range of 200 – 300 s in exchange for increased thrust when compared to other systems.

The second propulsion system to consider is electric propulsion (EP), which uses electricity to accelerate particles and create thrust in various ways, such as by heating, arcing, or ionizing propellent. Doing so can require significant amounts of power, typically more than chemical propulsion. Although EP systems, especially for large spacecraft with significant ΔV, require more power than a chemical system they offer much higher $I_{sp,}$ with values from 600 – 4000 s depending on the type of thruster.

Objectives:

1. Determine required ΔV to rendezvous with Iris
2. Select appropriate propulsion system type to complete mission
3. Select appropriate thruster to perform required maneuvers near Earth, during heliocentric transfer, and in Iris orbit

4. Integrate thruster, fuel system, and other associated hardware into overall spacecraft structure

1.2.4 Power

The overall objective of the electrical power subsystem (EPS) is to manage the supply, storage, and distribution of electrical power to the spacecraft subsystems. To accomplish this, there are four main functions of the power subsystem: power generation, distribution, conditioning, storage. The second objective of the power subsystem is to consider the power requirements of the components on the spacecraft to guarantee that these functions are accomplished effectively. Additionally, a power budget concerning all the components of the spacecraft will be created to properly allocate power. The last objective of the power subsystem is to evaluate and select the hardware that will be most effective in providing, distributing, conditioning, and storing power for the spacecraft.

Objectives:

1. Create power budget for all the components on the spacecraft
2. Select appropriate solar cells and array to power the spacecraft
3. Select appropriate batteries for storing power
4. Select appropriate EPS board to condition and distribute power
5. Properly integrate the hardware into the spacecraft

1.2.5 Command and Data Handling

The commands and data handling subsystem (CDH) is what controls the spacecraft's communication with the ground. It consists of antennas, transmitters, receivers, an onboard computer, and data storage. CDH is connected to most of the spacecraft because it receives,

processes, and passes on commands from the ground to the spacecraft using the flight software installed to its onboard computer. It is unique in that it must interface with ground stations, the sole link between Earth and the spacecraft.

For this mission, the spacecraft will need to transmit and receive data over long distances. This limits the choice of the ground station because few ground stations are capable of reliably receiving signals from beyond Earth orbit. It also limits the data budgets, as transmitting and receiving increases power use.

Objectives:

1. Investigate the use of ground stations capable of deep space communication for the mission
2. Create data budgets for uplink and downlink data transfers
3. Select components to meet functionality with minimal mass and power consumption

1.2.6 Attitude Determination and Control

An attitude determination and control (ADC) system is used to determine the spacecraft's attitude and adjust it to the desired orientation whenever necessary. These could be small adjustments to help maintain a certain orientation, or larger rotations to prepare the spacecraft for a maneuver. For this mission, the main purposes of the ADC system will be to keep the solar panels pointed towards the sun to receive maximum solar power, to ensure the spacecraft has the correct attitude before performing orbital maneuvers, and to keep the payload pointed at Iris during the science collection period. The tasks of the ADC system are normally organized into three main phases: Detumble, Initial Attitude Determination, and Attitude Maintenance [4].

The first phase, detumble, is performed once the satellite is released into orbit from the launch vehicle. The ADC system uses sensors, such as gyroscopes, to measure the spacecraft's rotation, and actuators to counter that spin and bring the satellite to a steady-state. The next stage, initial attitude determination, uses other sensors, such as sun sensors, star sensors, or even GPS, to determine the satellite position. The rest of the mission falls into the third phase, known as attitude maintenance. This segment uses sensors, actuators, and control algorithms to maintain the desired orientation [9]. Once the first maneuver is made, the satellite will need to point towards the sun for most of the mission to maximize the power generation by the solar panels. Then, when it arrives at the next orbital maneuver, it will rotate to the desired orientation to perform the maneuver. Here is a list of the main objectives to be accomplished in this subsystem.

Objectives:

1. Select optimal sensors and control algorithms for attitude determination.
2. Analyze disturbance torques acting on the spacecraft and major pointing requirements for the mission.
3. Calculate total external torques needed and select actuators to execute these required torques.
4. Design a control system to estimate the spacecraft's attitude and determine the torque required to reach the desired orientation at any time.

1.2.7 Environment

As a satellite travels through various regions of space, it will encounter space plasmas and weather, a wide range of thermal loading, and electromagnetic phenomena. To survive for extended periods in these harsh environments, it is important to equip the satellite with defense

mechanisms in the form of thermal and radiation control systems, including passive schemes such as material selection and coatings, and active schemes such as heat exchangers.

LEO contains additional hazards such as drag, magnetic fields, plasma, and space debris which may not be found in deep space, and several sources of thermal radiation. The extra drag forces, although small, make it crucial that the payload is sheltered from substantial amounts of thermal or electromagnetic charges from small collisions [10]. As the spacecraft travels further into GEO and eventually interplanetary orbits, the atmospheric density decreases. This lowers the drag force on the spacecraft and decreases the amount of UV irradiance from the Sun because there are fewer particles to be ionized by the UV waves. In LEO there is an excess of high-density plasma radiation relative to the magnetosphere and solar wind. As the spacecraft travels through the plasma, it can cause degradation of the spacecraft's solar arrays and increase surface contamination [11]. Once again, the plasma flux decreases in interplanetary space, but photons, solar wind, and plasma can become an issue as the spacecraft comes closer to other planets and asteroids.

Objectives:

1. Identify hazardous space conditions and their effect on the spacecraft
2. Create a model of radiation absorption across the lifespan of the spacecraft
3. Provide recommendations to Thermal, Communications, and ADC subsystems

1.2.8 Thermal Control

The goal of the spacecraft's thermal control is to keep all spacecraft components within their survival temperatures while not operating, and within their operational temperatures when operating [12]. Electronics and batteries are generally sensitive to temperature change due to

their narrow survival and operational temperature ranges, and so their requirements govern the thermal control system [13]. In CubeSats and other small spacecraft, little mass is budgeted to thermal control, due to the high mass requirements of other mission-critical subsystems and ability for simple thermal control by regulating the amount of power provided to onboard electronics to act as an inefficient heater system.

To create a viable thermal control system for this mission, two thermal models of the spacecraft will be created as sub-objectives: a model of heating of the spacecraft from solar radiation flux, and a model of heating of the spacecraft from internal electronics. Using this analysis, a comprehensive thermal control system will be designed. This design is constrained by the minimal mass allowance and will mostly utilize the pre-existing components of other subsystems, primarily the structure, to act as thermal conductors and radiators to minimize mass. Ideally, the thermal control system will be mostly or entirely passive, generating heat through routine use of onboard electronics and dissipating heat through radiation. By balancing the rate at which heat is generated and heat is dissipated, thermal equilibrium at operational temperature can be achieved.

Objectives:

1. Identify the thermal environments that the spacecraft will encounter.
2. Create models of the spacecraft in the identified thermal environments.
3. Iteratively simulate and modify the models to identify the thermal control systems necessary for mission completion.
4. Determine whether an entirely passive thermal control system is possible, to minimize subsystem mass.

1.3 Mission Operations

As mentioned in Section 1.1, the target of this mission is the main-belt asteroid 7 Iris. The mission is broken down into three broad phases based on the central body at that time. Table 1, below, breaks down the mission phases further into specific segments of the mission.

Mission Phase	Segment Name	Description
Near-Earth Operations	Rideshare Launch/Deployment	MAPLE SIRUP launched onboard host spacecraft and deployed near GEO
	On-Orbit Checkout	Initial attitude determination and other system initializations while positioning for departure burn
	Earth Departure Burn	Spiral out from Earth orbit onto interplanetary trajectory
	Earth Departure Coast	Coast between Earth and Mars to align for inclination change
Deep-Space Operations	Inclination Burn	Adjusts inclination to align planes with 7 Iris and raise apogee past Mars
	Mars-Crossing Coast	Coast past orbit of Mars to align for apogee raise
	Apogee Raise Burn	Raises orbit to intersect near 7 Iris' perihelion
	Belt Coast	Coast in Asteroid Belt to meet 7 Iris
	Iris Catch-Up Burn	Burn to rendezvous with 7 Iris
Near-Iris Operations	Positioning Coast	Coast near 7 Iris to reach position for proper capture maneuvers
	Relative Velocity Burn	Negates relative velocity as stage one of capturing
	Close Approach Coast	Coast to near periridian for final capture
	Iris Circularization Burn	Final main thruster maneuver to complete capture around 7 Iris
	Primary Mission	MAPLE SIRUP collects data about 7 Iris using primary payload

Table 1. Mission Phases and Segments

1.4 Project Management

The project was primarily organized using a Gantt chart, as seen in Figure 1. These charts are useful for keeping track of the timeframes allocated to various tasks and allow for easy modification as the project evolves and tasks end up taking more or less time than initially anticipated. Every three weeks a new team member was designated as the project manager. They were responsible for setting meeting times, modifying the Gantt chart, and setting the agenda for weekly meetings with our advisor.

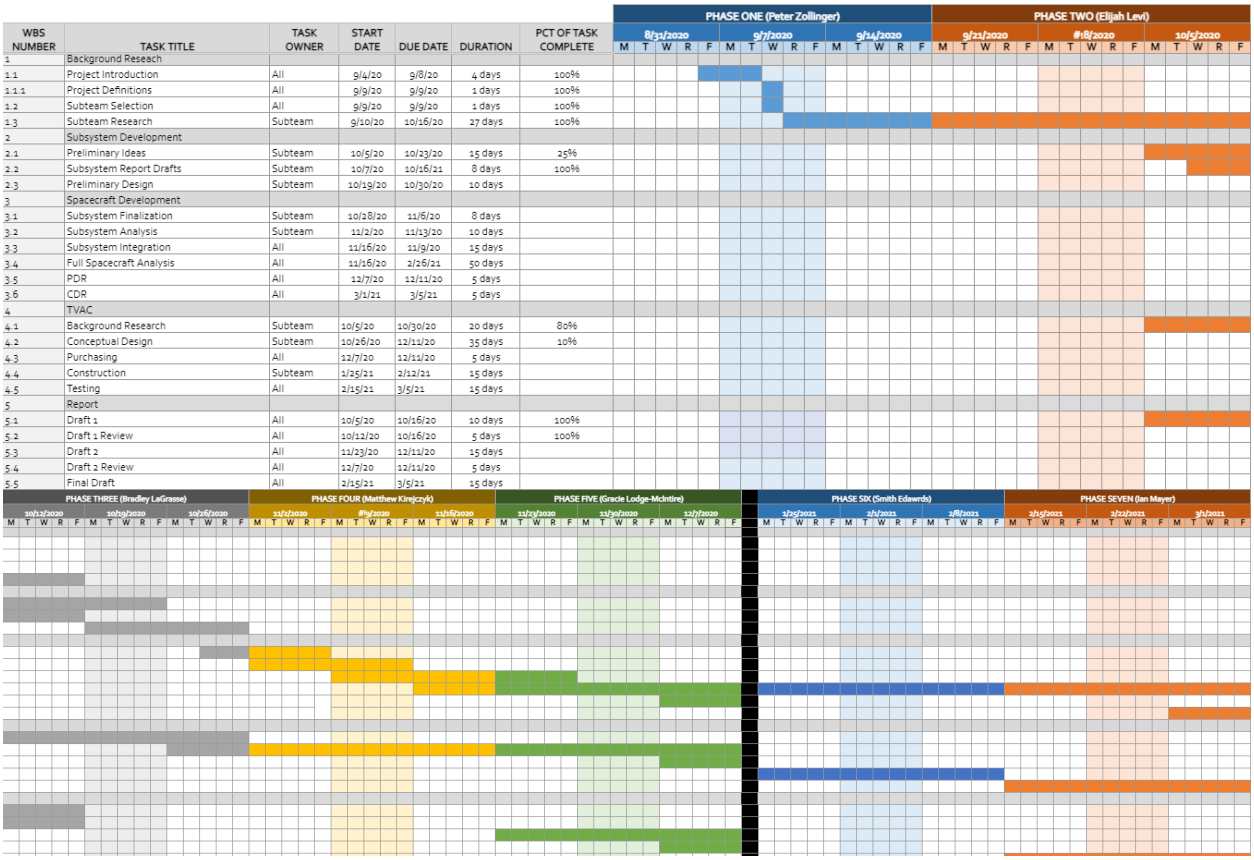

WBS NUMBER	TASK TITLE	TASK OWNER	START DATE	DUE DATE	DURATION	PCT OF TASK COMPLETE
1	Background Reseach					
1.1	Project Introduction	All	9/4/20	9/8/20	4 days	100%
1.1.1	Project Definitions	All	9/9/20	9/9/20	1 days	100%
1.2	Subteam Selection	All	9/9/20	9/9/20	1 days	100%
1.3	Subteam Research	Subteam	9/10/20	10/16/20	27 days	100%
2	Subsystem Development					
2.1	Preliminary Ideas	Subteam	10/5/20	10/23/20	15 days	25%
2.2	Subsystem Report Drafts	Subteam	10/7/20	10/16/21	8 days	100%
2.3	Preliminary Design	Subteam	10/19/20	10/30/20	10 days	
3	Spacecraft Development					
3.1	Subsystem Finalization	Subteam	10/28/20	11/6/20	8 days	
3.2	Subsystem Analysis	Subteam	11/2/20	11/13/20	10 days	
3.3	Subsystem Integration	All	11/16/20	11/9/20	15 days	
3.4	Full Spacecraft Analysis	All	11/16/20	2/16/21	50 days	
3.5	PDR	All	12/7/20	12/11/20	5 days	
3.6	CDR	All	3/1/21	3/5/21	5 days	
4	TVAC					
4.1	Background Research	Subteam	10/5/20	10/30/20	20 days	80%
4.2	Conceptual Design	Subteam	10/26/20	12/11/20	35 days	10%
4.3	Purchasing	All	12/7/20	12/11/20	5 days	
4.4	Construction	Subteam	1/25/21	2/12/21	15 days	
4.5	Testing	All	2/15/21	3/5/21	15 days	
5	Report					
5.1	Draft 1	All	10/5/20	10/16/20	10 days	100%
5.2	Draft 1 Review	All	10/12/20	10/16/20	5 days	100%
5.3	Draft 2	All	11/23/20	12/11/20	15 days	
5.4	Draft 2 Review	All	12/7/20	12/11/20	5 days	
5.5	Final Draft	All	2/15/21	3/5/21	15 days	

Figure 1. MQP Scheduling Gantt Chart

1.5 Thermal Vacuum Chamber

Because of the extreme environment experienced by spacecraft, it is necessary to validate the behavior of components and systems using special equipment before launch. The primary

method of testing this behavior is dedicated vacuum chambers, called thermal vacuum chambers (TVAC), designed to not only simulate a lack of atmosphere but also the wide range of temperatures expected during a mission. Generally, TVACs are designed to incorporate both the vacuum, heating, and cooling elements into the same structure [14], however, this project focuses on creating a device to be used in an existing vacuum chamber due to the resources available to WPI.

Objectives:

1. Research existing small TVAC designs
2. Design thermal component for existing vacuum chamber that produces required temperature variations
3. Construct prototype thermal environment device
4. Test device in vacuum chamber to validate performance so it can be used in the analysis of future aerospace and related projects

1.5.1 Facilities

The facility used for this project is room HL016 in the basement of Higgins Laboratory on WPI's campus. It includes a 50" x 72" stainless steel vacuum chamber (T2, seen on the right in Figure 2) and supporting instrumentation. The pumping system consists of a rotary mechanical pump, positive displacement blower combination with a pumping speed of over 560 liters/s (10^{-2} - 10^{-3} Torr). In addition, a 20" CVI TM500 cryopump provides up to 10,000 liters/s on nitrogen, 8500 liters/s on argon, and 4600 liters/sec on xenon at pressures in the range of 10^{-4} to 10^{-7}Torr. The base pressure for this facility is in the mid-10^{-7} Torr range. Ancillary instrumentation includes a set of Pirani and hot cathode vacuum gauges and a mass flow meter. A dedicated workspace for this MQP was set aside on the far side of the room, equipped with

various hand tools and a soldering station for the construction of physical and electrical components. Additional tools and machines were available through WPI's Washburn Shops.

Figure 2. Higgins Lab 016

2 Payload

When choosing the payload for a mission, numerous considerations are made regarding operating temperature, cost, technology readiness level, flight heritage, structural fit, and scope of the mission. When we arrive at 7 Iris the mission objective will be to image the asteroid using several different types of cameras to learn more about its surface topography, material, atmosphere composition, temperature, and numerous other characteristics. Also, the chosen sensors need to be compatible with the communication system and have proper shielding to withstand deep space environments.

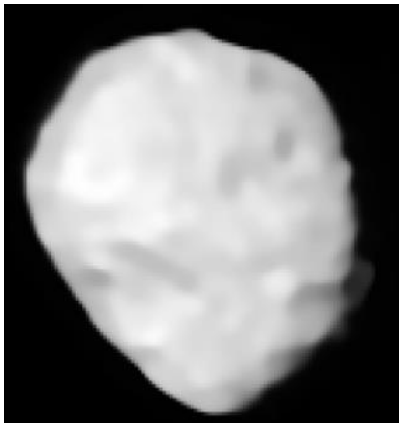

Figure 3. Very Large Telescope Image of 7 Iris [56]

The scope of a spacecraft mission can vary drastically and determines the payload of the spacecraft. For example, satellite Libertad 2 was a 3U construction, weighed 4 kgs, and was positioned in LEO to capture satellite images of Colombia. Since the satellite was very small, the scope of the mission only included images. The proper payload that corresponds with the mission is a camera that can be positioned and pointed using the CubeSats attitude Control Modes [15]. Libertad 2 shows that a simple and flight-proven option is sometimes all that is needed to complete a mission.

OTB-1 spacecraft is a similar-sized CubeSat that was intended for deep space. This spacecraft's main payload was a Deep Space Atomic Clock that NASA sponsored from its Space Technology Mission Directorate (STMD). In addition to the main payload, OTB-1 contained an atmospheric experiment called USAF AFA iMESA-R (Integrated Miniaturized Electrostatic Analyzer-Reflight), a debris experiment called NRL LARADO, and a solar panel experiment called AFRL MSA (Modular Solar Array). Getting a spacecraft into orbit is extremely expensive so carrying multiple sensors is a way to minimize the cost per experiment. These experiments help grow technology readiness and gather data on the deep space environment [16].

2.1 Payload Selection

For the scope of MAPLE SIRUP's mission, four main payloads were chosen including a color visual imager, an infrared spectrometer, a Lidar camera, and a plasma spectrometer. The combinations of these four payloads will enable the investigation and characterization of 7 Iris' surface features and material composition.

2.1.1 Color Visual Imager

A color visual imager allows the satellite to take ordinary pictures of the asteroid like a picture one would take on Earth. This mission is creating a profile of an asteroid that has never been properly imaged, so the color imager provides detail as to what the asteroid looks like to humans. Also, these color images can be overlapped with other sensor information to accurately map and pinpoint areas of interest on the asteroid. These pictures will provide a general understanding of the asteroid's color, shape, size, and composition. Most pictures taken in deep space are color corrected so it is difficult to identify the true characteristics of the asteroid. Since the satellite is nearly 150 kg it is important to limit our SWaP within the chassis while not

sacrificing performance benefits. The TriScape100 Imager, as seen in Figure 4, combines lightweight with efficiency.

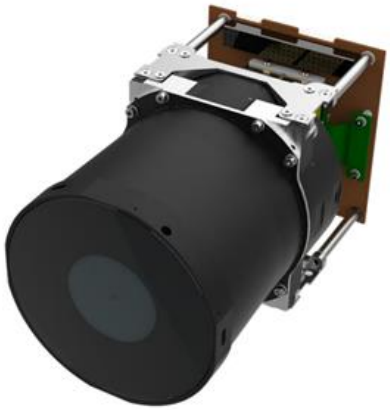

Figure 4. TriScape100 Color Imager [116]

The camera has a spatial resolution of 4.75 m GSD at a 500 km orbit. The orbit MAPLE SIRUP will follow at Iris will be 82km by 332.1 km meaning that the camera will be able to take high-quality images without any issues. Most images will try to be captured towards the apoapsis to minimize the number of images needed to capture the entire asteroid. Other imagers such as the Gecko Imager weighed 480g, 97 x 96 x 60 mm, and had an operating temperature of 10 to 30 degrees Celsius. This imager was not chosen because its image quality was only 39 m GSD at a 500km orbit and its operating temperature was not as wide as the TriScape imager [17]. The TriScape camera has a 128 Gb non-volatile storage that allows it to carry up to 8700 image frames. This onboard storage is crucial since the images will have to be communicated at a much slower rate than they are taken as discussed in section Data Rate. The imager has a mass of 1.1 kg, power consumption of fewer than 6 watts, and a dimensional volume of 98 x 98 x 176 mm. Further details can be found in Figure 5 below.

Optics	
Focal Length	580 mm ±1 mm
Aperture	95 mm
Full Field of View	2.22° (across-track)
Imaging	
Configuration	Snapshot
Sensor Technology	CMOS
Effective Pixels	4096 x 3072
Pixel Size	5.5 µm
Pixel Depth	10-bit
Spectral Filter	RGB Bayer Filter
NIR Blocking Filter	670 nm cut-off
Maximum Frame Rate	180 fps
Transmittance	61% (at 550 nm) (1)
On-Board Electronics	
Storage Capacity	128 Gigabyte NAND Flash
Maximum Image Frames	8700
Image Processing	Binning, Thumbnails, Video Modes (optional)
Image Compression	Lossy/Lossless (optional)
Control Interface	I^2C or SPI CAN, RS-422 (optional) Customer specific interface (optional)
Data Interface	LVDS (or customer specific interface, optional)
Power Supply	5 V DC
Power Consumption	< 6 W (during imaging mode)
Mechanical	
Mass	1.1 kg
Dimensions	98 x 98 x 176 mm
Environmental	
Operating Temperature	-10 to +50 °C
Radiation (TID)	> 15 krad

Figure 5: TriScape 100 Imager Specifications

2.1.2 Infrared Spectrometer

The Argus 2000, as seen in Figure 6, is an affordable miniature infrared spectrometer with integrated optics that are great for pollution monitoring, radiation monitoring, greenhouse gas monitoring, and molecular analysis. Infrared Spectrometers record the relative amount of energy as a function of the wavelength/frequency of the infrared radiation when it passes through a sample. In the case of 7 Iris, if the wavelengths of photon energies emitted match some materials on the surface of the asteroid then those wavelengths will be absorbed and will not return to the sensor. These absences in energy can be correlated to the types of material the IR encountered.

Carbon is often an element of interest since it could indicate past life. Figure 7 below shows what possible data may look like for four different types of carbonate.

Figure 6. Argus 2000 Infrared Spectrometer [115]

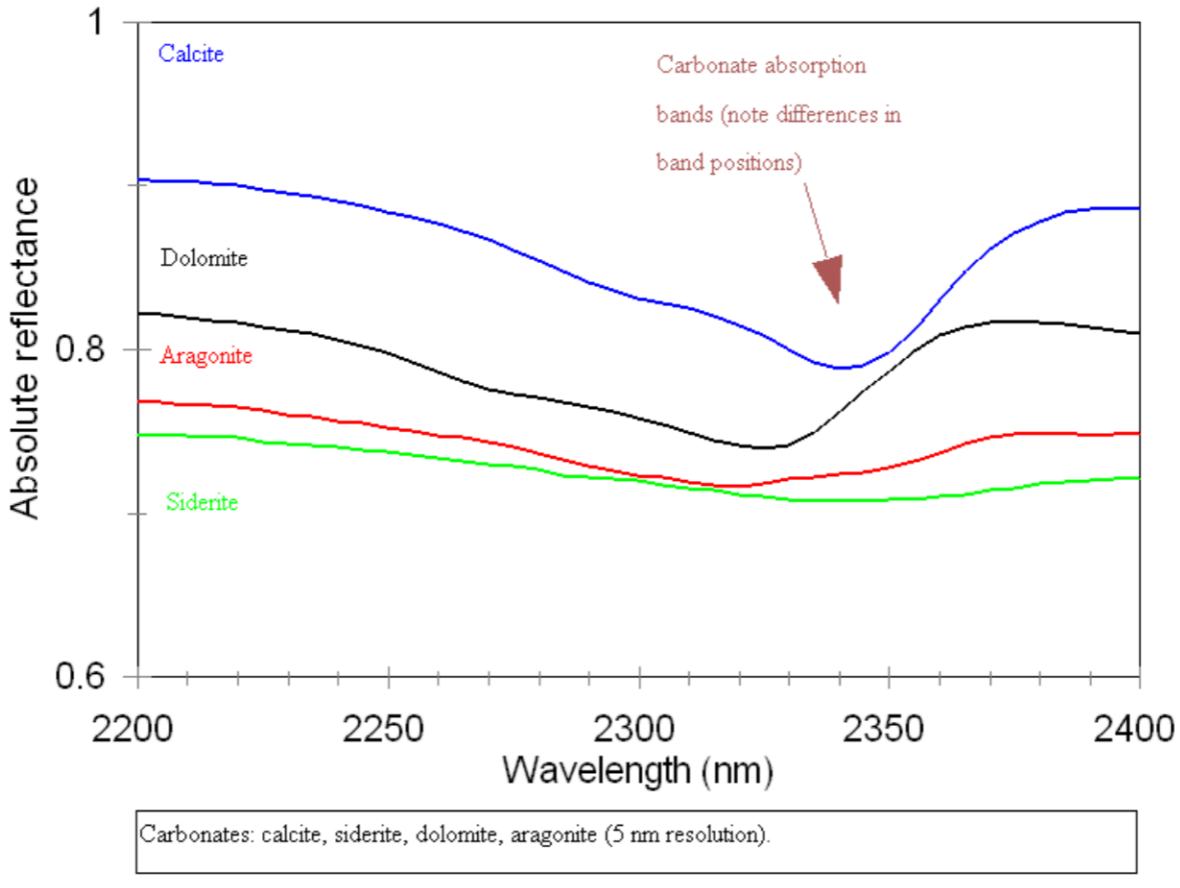

Figure 7. Reflectance Spectra of Four Types of Carbonates [115]

A similar infrared spectrometer is BIRCHES. This spectrometer is 1.5U, 2 kg, and uses 12-25 W of power. This spectrometer provides much more detailed recordings than the argus 2000 but the large size and power as well as the scope of the mission make it overkill for the mission's needs [18]. The team chose to remain with the Argus 2000 Infrared Spectrometer which operates within 700 nm up to 2200 nm infrared band in varying operating modes making it a versatile device. The spectrometer is actively cooled and only weighs 280 g while consuming 1.47 W at max power. The spectrometer has an envelope of 46 x 80 x 80 mm, an operating temperature of -20 ℃ to 40 ℃, and a survival temperature of -25 ℃ to 50C. The Argus 2000 is composed of InGaAs and has a compact form factor allowing it to withstand any space conditions. The integration time is between 500 microseconds to 4.096 seconds which is the amount of time it takes the IR spectrometer to send and receive its wavelengths. When comparing the Argus 2000 to The satellite's ADCS system including reaction wheels and thrusters allows for dead band pointing which will provide clear imaging [19].

2.1.3 Lidar

Lidar has become a topic of interest especially due to its integration into smartphone imaging technology. Lidar is a method for measuring distance by illuminating the target with laser light and measuring the reflection with a sensor. Differences in laser return times and wavelengths can then be used to make digital 3-D representations of the target. With a small form factor of 2U (100 x 100 x 200 mm), the Fibertek CubeSat Lidar Concept Design, seen in Figure 8, provided unmatchable imaging ability compared to its size and weight. This compact system only weighs 2 kg, and max power usage of 14.3 W. Lidar can be used for center of mass determination, obstacle, and surface texture identification, and measuring column content of CO2, methane, water vapor, and ice detection [20]. The concept Lidar is capable of imaging topography at over

100 km and the addition of special optics can allow it to reach up to 1000 km. Since the orbit around 7 Iris will be between 82 km and 332 km it is ideal that the Lidar image the surface of Iris when close to the periapsis. The ranging function has a 10-degree viewing angle when in its long-distance configuration meaning that if the average distance to Iris is 207.05 km then the swath would be 20.705 km. 7 Iris rotates about once every seven hours in addition to MAPLE SIRUP's orbit would allow the entire surface to be imaged within several days. Since this sensor is a concept, it is not known exactly how much data it will produce. To estimate the data production, the sensor will be compared to the laser altimeter on the Change'E-1 spacecraft. The Change'E-1 spacecraft had a similar orbit around the moon at 200 km and the laser altimeter weighed 15.7 kg and consumed 25 W of power. This laser produced 384 bit/s with a spot size of 120 m [21]. If all Lidar measurements were taken at around 100 km, then the swath would be 10 km. If the data rate is similar between the two then it can be assumed that the Fibertek Concept Lidar would produce a continuous 4 kB/s of data. This data rate can be reduced by increasing the shot spacing instead of shooting continuously. Also, the improvement of data collection since Change'E-1's mission in 2007 makes it safe to assume that data can be collected at 4 kilobytes/sec from all portions of MAPLE SIRUP's orbit [22]. Lastly, radiation testing of this Lidar sensor has not been completed but other Lidar systems have been tested at dose rates between 5 Krad and 50 Krad which indicates that this Lidar sensor would perform similarly [23].

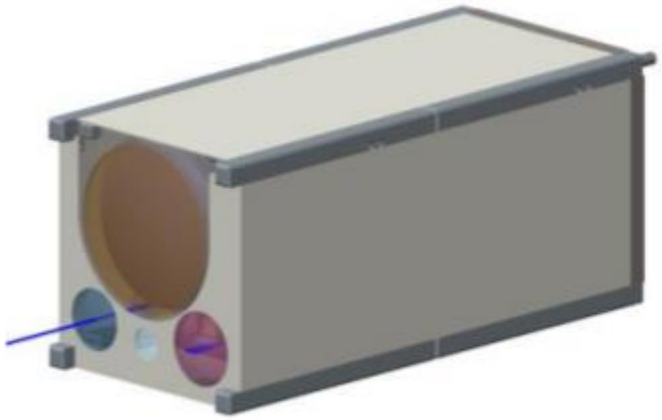

Figure 8. Fibertek 2U CubeSat Lidar Concept Design [20]

2.1.4 Plasma Spectrometer

The analysis of the space environment, particularly plasma and solar wind, are a topic of interest since they interfere with human communication networks. By gathering information along the trajectory, it will allow scientists to better understand the flow of energy from solar wind throughout the magnetosphere as well as the coupling between different spatial regions. This area of space exploration requires much more research so a successful flight of MAPLE SIRUP would be a large step in the right direction.

A plasma spectrometer is an instrument that detects and analyzes plasma (ions and electrons) in the vicinity of the spacecraft. Since MAPLE SIRUP will utilize ion thruster as propulsion, the plasma spectrometer will only collect data during parts of the trajectory when the thrusters are off to ensure that the spectrometer does not plasma from the propulsion system. The plasma spectrometer is different from an infrared spectrometer since the plasma spectrometer targets particles near the spacecraft while the infrared targets materials further away. Also, the plasma spectrometer measures the composition of ions whereas the infrared measures absorption, emission, and reflection of infrared.

Previous plasma spectrometers that flew on Cluster II and THEMIS are too large for the mission, weighing nearly 6 kg [24]. Innovations in chip manufacturing, deep etching, and double-sided lithography have made it possible to create a spectrometer that fits within a 15 x 15 x 17.5 mm form factor, weighs 0.5 kg, and only draws 0.75 W of power. As seen in Figure 9, the yellow portion is a collimator stack showing an interposer layer with conductors to provide vertical interconnection to each energy analyzer layer's large electrodes. The collimator also serves as a structure to narrow the field of view for desired particles colliding with the spectrometer in a parallel path. The blue/green portion is a stack of 25 lithographically fabricated energy analyzer layers. The ions are intended to enter from the slits in the left of the analyzer and exit from the right. The contact points between each layer of the analyzer provide electrical contact for individual biasing of the curved plate bands shown in Figure 10. These plates filter out background light while allowing the target particles to enter. This spectrometer has been lab-tested, can measure particles in the 3-20 keV, has a directional field of view, and a 100% duty cycle. By creating an array of these sensors, we can create a geometric factor that exceeds a conventional plasma spectrometer while maintaining a low form factor [25]. The particles that are collected create a colored array as seen in Figure 11.

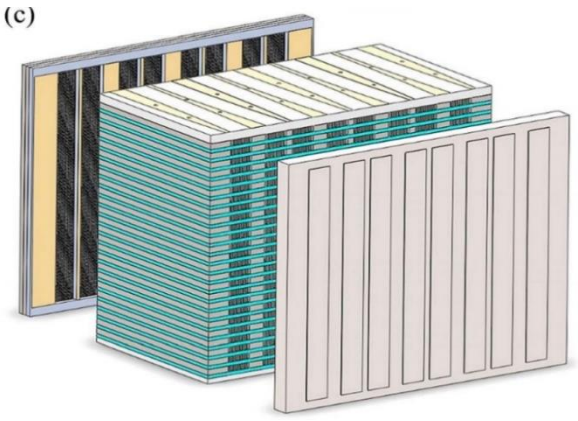

Figure 9. Plasma Spectrometer [25]

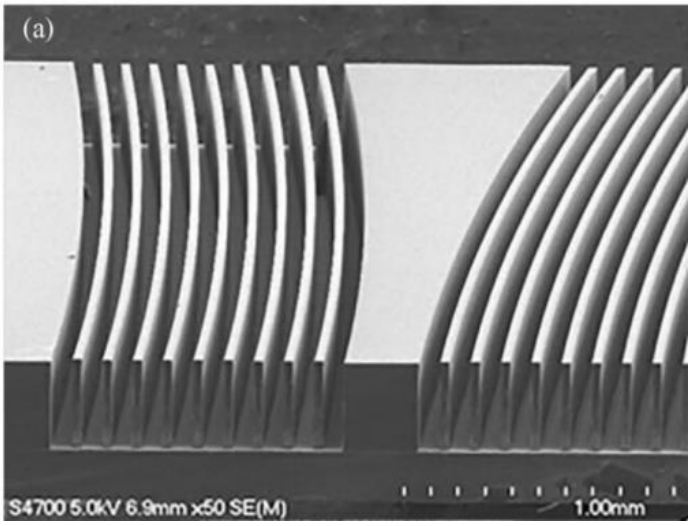

Figure 10. Side View from Entrance Side of Two Bands of Energy Analyzer [24]

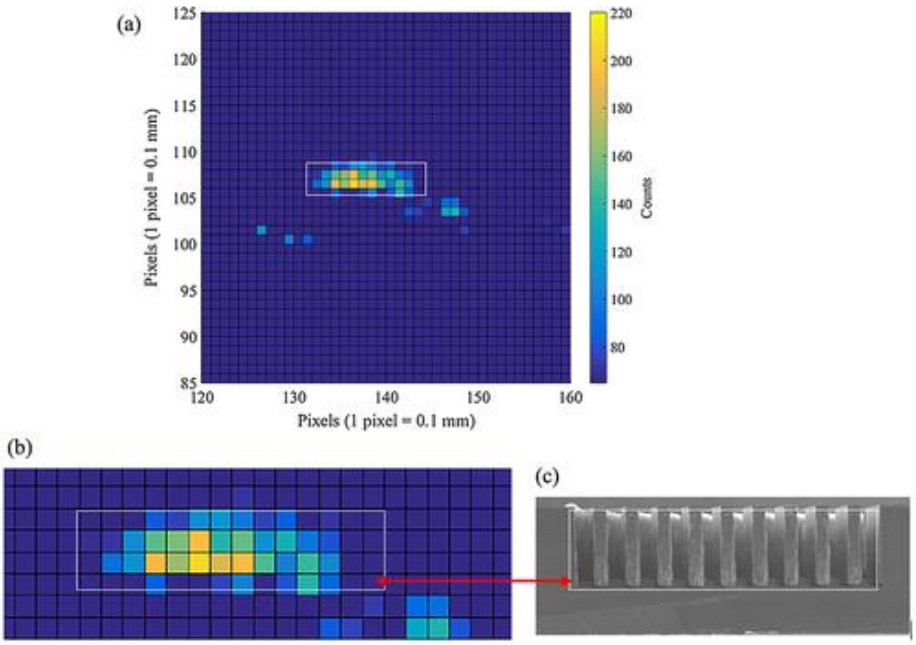

Figure 11. Transmitted 5 keV Electron Flux Through a Single Band of a Single Energy Analyzer Layer [24]

2.2 Payload Requirements and Constraints

MAPLE SIRUP's payload allows the spacecraft to collect vast amounts of information about 7 Iris and interplanetary space, but some constraints must be considered when choosing and using payloads.

As the spacecraft is taken into GEO and released from the rideshare it will undergo vibrations and G-forces that could damage the satellite. The mounting of all components in the structure must undergo random vibration, or "vibe", testing to ensure that it will survive these conditions and reach interplanetary space. Also, as the spacecraft operates, some items will induce vibration such as the reaction wheels. The payloads need to be able to handle this vibration. One way of doing so is mounting the payloads with washers to dampen any transfer of energy. The color imager is one of the most sensitive payloads and has a vibration rating of 14.1 Grms and radiation tolerance exceeding 15 Krad. These tolerances will serve as constraints when analyzing the payload's survivability. Table 2 contains a complete list of general measurements and constraints for all payloads.

Category	TriScape100 Color Imager	Argus 2000 IR Spectrometer	Fibertek 2U Concept Lidar	Concept Plasma Spectrometer
Weight	1.1 kg	280 g	2 kg	0.5 kg
Size	9.8 x 9.8 x 17.6 cm	4.6 x 8.0 x 8.0 cm	10 x 10 x 20 cm	1.5 x 1.5 x 1.75 cm
Power Consumption	< 6 W	1.4625 W	14.3 W	0.75 W
Operating Temp.	-10 to 50 ℃	-20 to 40 ℃	15 ℃ *	-20 to 40 ℃ *
Survival Temp.	-25 to 65 ℃	-25 to 50 ℃	-25 to 55 ℃ *	-25 to 55 ℃ *
Vibration Tolerance	14.1 Grms	> 12 Grms	>10 Grms	> 12 Grms *
Radiation Tolerance	>25 Krad	Unlisted	Similar tested at 5 to 50 Krad	Unknown
Data Production	14.71 MB / Image	513 Bytes / Image	4 Kilobytes / Sec	8.2 kilobyte / Data Packet

Table 2. Payload Specifications

*= Estimation

2.2.1 Time of Use

The payloads will have certain operating windows to make sure the sensors are powered properly and protected when not in use. The color imager, infrared spectrometer, and Lidar will only be used when MAPLE SIRUP reaches 7 Iris. The plasma spectrometer will periodically record along the satellite's trajectory to 7 Iris in addition to measuring plasma activates around 7 Iris. To eliminate skewed data, the plasma spectrometer will be turned on during the downtime of the satellite's main propulsion system. This will ensure that no iodine particles will enter the plasma spectrometer and alter any findings. Also, the plasma spectrometer collimator is designed

with a field of view that reduces the detection of non-target particles. It would be unlikely for particles of iodine to travel around the spacecraft and enter the collimator perfectly parallel to its direction of travel.

3 Structures

CubeSats are constructed by multiples of the standard dimension “U,” meaning 10 cm x 10 cm x 10 cm. Several companies provide these structures designed with mounting locations for other components. For example, Pumpkin, Inc. constructs CubeSats using the monocoque approach. This style has loads carried by an external skin to maximize internal volume. Pumpkin, for these models, creates crafts from 1U to 6U in size. This approach allows more space for instruments while also minimizing structural mass, leaving more mass allowance for other components. Similarly, Clyde Space utilizes the monocoque structure, but only for 1U to 3U. For reference, the 3U chassis has a mass of 0.155 kg and dimensions of 0.1 x 0.1 x 0.1135 m.

Another popular design is a modular frame. EnduroSat utilizes this approach for satellites from 1U to 6U. Like is common, EnduroSat uses Aluminum 6061-T651 for construction. Their 3U satellite primary structure has a mass of 0.29 kg. This design is more massive than the Clyde Space CubeSat, which should be considered during the design process. Nanoavionics also produces modular frames for their primary CubeSat structures. This company builds satellites from 1U-12U. Similar to the EnduroSat design, their 3U design weighs significantly more than the monocoque design, 0.254 kg. Radius CubeSat Structures utilized a highly modular frame for their CubeSat design. These satellites range from 1U to 12U in size and appear simplistic in design when compared to the complex “external skin” of the monocoque approach. While still heavier than the monocoque structures, the 3U design weighs the least of the modular frames, at 0.24 kg [26].

The structural design will be based on the structural needs for the project and structural complexity. By maximizing internal volume and minimizing primary structure mass, propulsion

will require less thrust, and there will be more space for internal components for the other subsystems.

3.1 Material Selection

Regarding past examples, the common options are 6061-T6 Al, 7075 Al, or Al 5052-H32 [26]. The CubeSat is favored to be lightweight and durable. To preserve structural stability, it is favorable to have parts welded together, or as few fasteners as possible. Thus, the material must be capable of being welded with consideration to the required expertise.

Due to its commonness in CubeSat design, Aluminum 6061-T6 is the initial selection for the design process. The material has an ultimate tensile strength of around 310 MPa and a yield strength of around 276 MPa. Not only strong, 6061-T6 has a low thermal conductivity of 0.896 J/g-°C [27]. Allite Super Magnesium appeared as another option during the design process. Lightweight, strong, shock-absorbent, and having low thermal conductivity, these properties are comparable to those of 6061-T6 aluminum. The ultimate tensile strength is 298-352 MPa, and the yield strength is about 212-303 MPa. Additionally, the thermal conductivity is 69-78 W/m-K [60]. Both are designed to withstand and accommodate welding applications.

The final selection of Aluminum 6061-T6 is due to the practicality of usage. This material, properties broadly tested and utilized in many aerospace applications, is reliable. The properties are also detailed in the SolidWorks software, allowing for reliable design and structural analysis. Due to its relatively “cutting edge” nature, Super Magnesium is not available on SolidWorks. The material properties would require manual input. With comparable characteristics, the preference of Aluminum 6061-T6 reduces the possibility of human error and unpredicted results in utilization.

3.2 Main Structure Design

From initial research, the difficulty in assembly preferred the modular design for the primary chassis. It prioritized available space for internal components and mounting locations. As the design process continued, the necessity for minimized mass proved more significant. The modular design is not as stable as the skeleton design as seen in Figure 12.

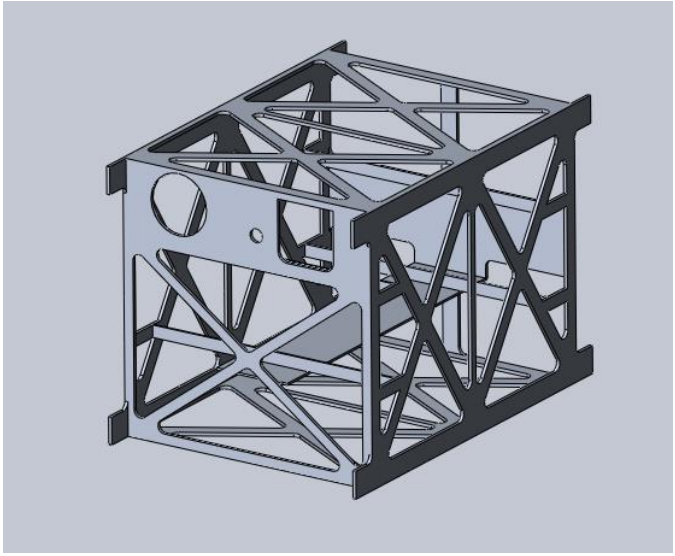

Figure 12. Skeleton Frame Design

The “webbed” structure provides cross-bracing and support for the chassis while maintaining a lightweight assembly. The outer dimensions of the body are 0.4 x 0.4 x 0.5 m. The aluminum is 5 mm thick, and the entire structure has a mass of approximately 6.15 kg. The wide platform extending along the long axis supports the iodine propellant tank and provides a surface for mounting the reaction wheel and two star trackers. The horizontal bars through the body provide iodine tank and ACS propellant tank support.

The front face of the spacecraft, seen in Figure 13, has cut-outs for the TriScape100 Color Imager, Infrared Spectrometer, and LiDAR sensor. These are depicted by the larger yellow circle, smaller yellow circle, and yellow square, respectively, in Figure 13. The coarse sun sensor, denoted as the red circle, also rests on this face. Seen through the cross-braces, the red oblongs represent the propellant tanks for the attitude thrusters, seen in red on all eight corners.

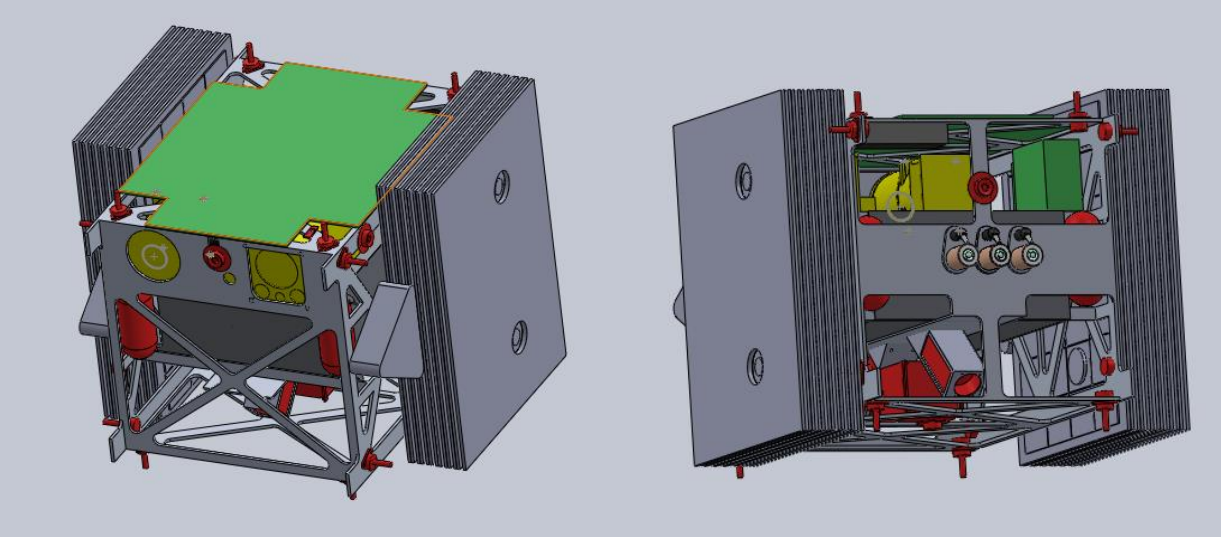

Figure 13. Full Assembly Design (Stowed Arrays)

The ACS thrusters are placed in the corners of the primary structure to maximize the moment arm. Additionally, to not impinge on the stowed solar arrays, the thrusters are placed on tabs extending from the main body. The large green surface on the top face of the craft is the Patch Antenna, and the small red rectangular prism in the front top-right is a fine sun sensor.

On the back face of the craft, the three BHT-200-I thrusters and cathode bases sit along the middle, horizontal brace. The red cube seen below the iodine fuel tank is the Sputnix reaction wheel and the rectangular prism sitting at an angle is one of the two star trackers.

3.3 Release from Launch Vehicle

Due to the size of the satellite, the mission will utilize the PODS (Payload Orbital Delivery System). This method works in that a primary mission will “host” another, carrying the secondary mission to near-GEO. Created by Maxar Space Infrastructure (MSI), the POD system is designed for an SSL-1300 series satellite. As seen in Figure 14, the primary mission will host the other within the central cylinder.

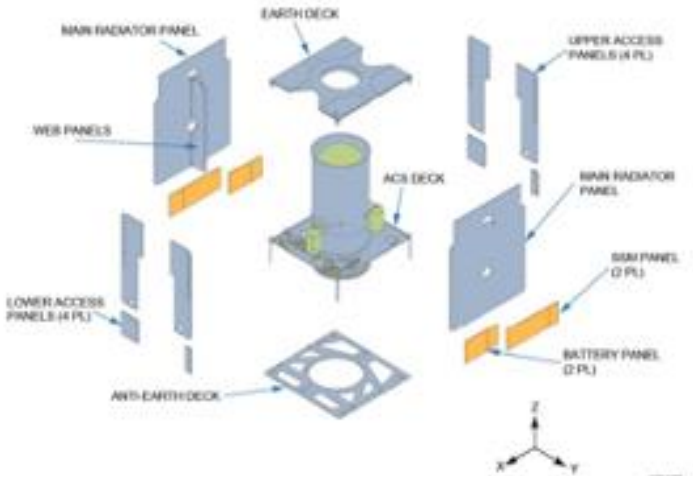

Figure 14. Primary Mission Satellite Composition

This central cylinder supports the RPA (Rideshare Payload Assembly). The RPA consists of the ejectable payload, the satellite described in this paper, and the PEM (Payload Ejection Mechanism). The PEM is standard, created by MSI. The company advertises its ability to deploy a typical payload with a tumble rate <0.5 degrees/second/axis [28]. The ejection mechanism is typically attached to a chassis, which is subsequently attached to the CubeSat. This system includes four Separation Nuts and one Frangibolt, the pyrotechnic separation acting as the final ejection mechanism. Due to its cumbersome size (1.0m x 1.0m) and geometry, the chassis is forgone for a direct attachment to the satellite. The SepNuts and Frangibolt are still utilized, connecting the PEM to the primary structure. The chassis and PEM can be seen in Figure 16.

Figure 16. PODS Chassis (left) and PEM (right)

With the ACS thrusters and solar arrays mounted on the outside of the primary structure, the final dimensions for the satellite are 0.71 x 0.96 x 0.50 m. The standard size for the RPA is 1.0 x 0.5 x 0.4 m. Therefore, the structure requires the extended RPA with dimensions of 1.0 x 1.0 x 0.6 m. The standard location for the RPA is denoted by the number 2, and the extended RPA is denoted by the number 1 in Figure 15.

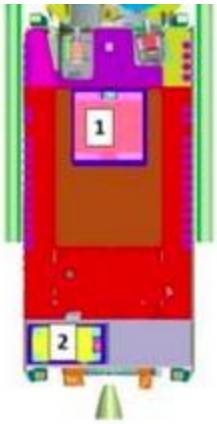

Figure 15. RPA Locations

3.4 Modal Analysis

Modal analysis reveals the natural frequencies of the structure. If the spacecraft during launch or in transit experiences vibrations at one of such frequencies the structure is likely to deform and catastrophically fail. This analysis, performed using ANSYS, is detailed below.

3.4.1 Natural Frequencies

The force of launch on the spacecraft creates a risk of mechanical failure. The acceleration of the launch vehicle inhibits vibrational motion. Before direct experiment of the structure and individual components, steps are taken to analyze their natural frequencies. If met, the structure reaches resonance, causing mechanical failure.

All structures have a natural frequency, a frequency at which a system oscillates without an input or damping force. This value is a function of mechanical properties: material stiffness and mass. The PODS rideshare states that the RPA should have a minimum natural frequency of 10Hz in lateral and axial directions and it is suggested that the spacecraft have a minimum frequency of 100 Hz.

Independent of incurred loads, the natural frequencies are modified only through structural design (e.g. body material). Thus, the natural frequencies of the design must be determined through modal analysis. Modal analysis finds any number of natural frequencies of the system. These values are then compared to the frequencies the body will experience. For the craft, the launch environment is examined. If any natural frequencies appear, the main body would reach resonance and would thus have to be redesigned. The launch vehicle for this mission is the Falcon 9.

According to the Falcon User's Guide [29], spacecraft that comply with guidelines such as the General Environmental Verification Standard (GEVS) are unlikely to fail as the payload of a Falcon 9 or Falcon Heavy. However, it is still vital to examine the vibrations of the flight environment. This will be further discussed in Section 3.5.

3.4.2 Simplified Model

The entire assembly for MAPLE SIRUP is composed of numerous components with specific material properties. For simplified analysis, reducing simulation time, smaller components are removed, and complex components are simplified. Connections between the propellant tanks, sensors, and main frame are modeled as *Bonded*. This is due to the complexity and small size of mounting apparatus, and thus creates a “glued”-like connection. For example, the iodine propellant tank has two *Bonded* connections to cross-braces instead of the more specific connection with bolts. As shown below, the resultant model is simplified without compromising specific structural properties. Mass is significant in these calculations and removing too many components results in an inaccurate analysis of natural frequencies.

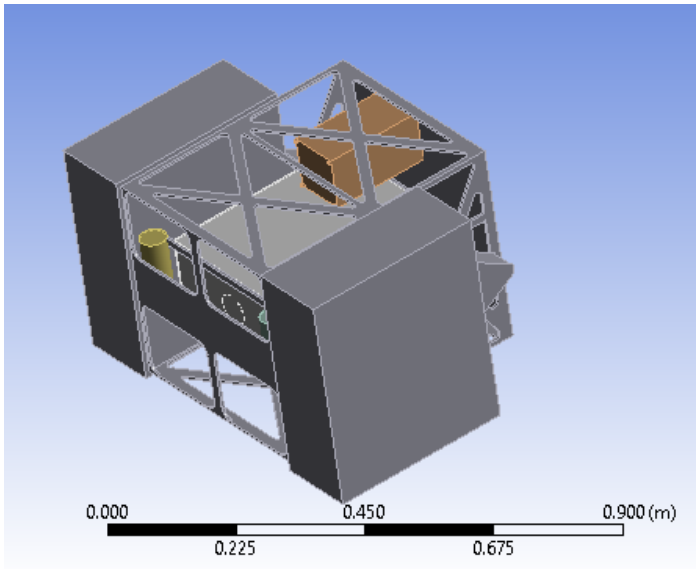

Figure 17: Simplified Model of MAPLE SIRUP

The simulation is accomplished in ANSYS. Once the geometry is uploaded to the software, the materials are applied to their corresponding components from the ANSYS material database. Though unnecessary for modal analysis, a fixed support to the bottom face is established, simulating the connection to the PODS system. As suggested by Dr. Adriana Hera, I selected to examine the first ten modes of vibration under the analysis settings.

3.4.3 Results

The natural frequencies at which these modes occur are detailed in Table 3 below.

Mode	Frequency (Hz)
1	134.65
2	141.73
3	167.57
4	174.69
5	216.38
6	231.75
7	268.41
8	329.83
9	374.16
10	389.52

Table 3. First Ten Natural Frequencies

The modes described are the shape of deformation and oscillation the structure would experience under the corresponding natural frequency. The first mode of vibration, at 134.66 Hz, is the vertical motion of the LiDAR sensor, impacting the top of the frame, displayed below. This mode would damage the LiDAR sensor, frame, and patch antenna.

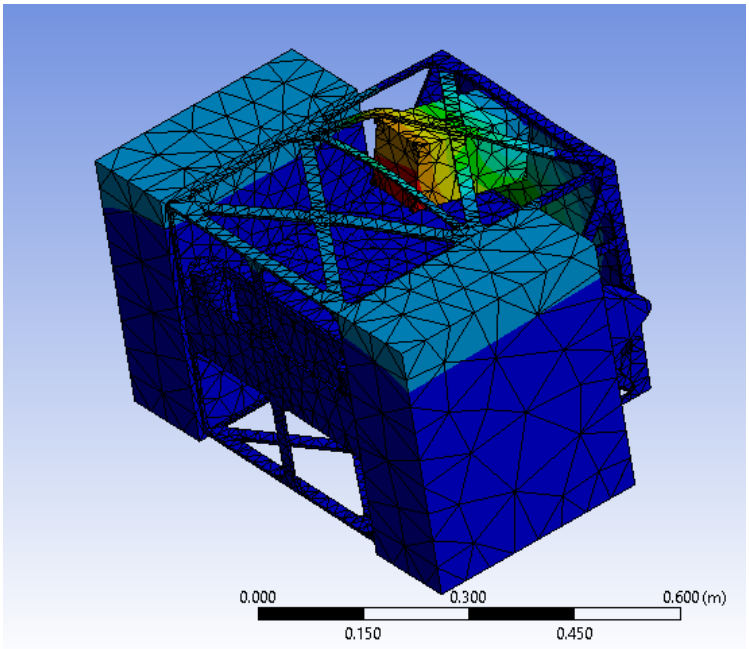

Figure 19: First Frequency Mode Shape

The second mode, occurring at 141.73 Hz, is the vertical oscillation of the LiDAR combined with the side-to-side motion of the main frame and convex and concave deformation of the front panel. The impact between the LiDAR and the frame occurs, as seen below. This mode would damage the frame, LiDAR, solar arrays, patch antenna, and the sun sensors on the top and front face of the craft.

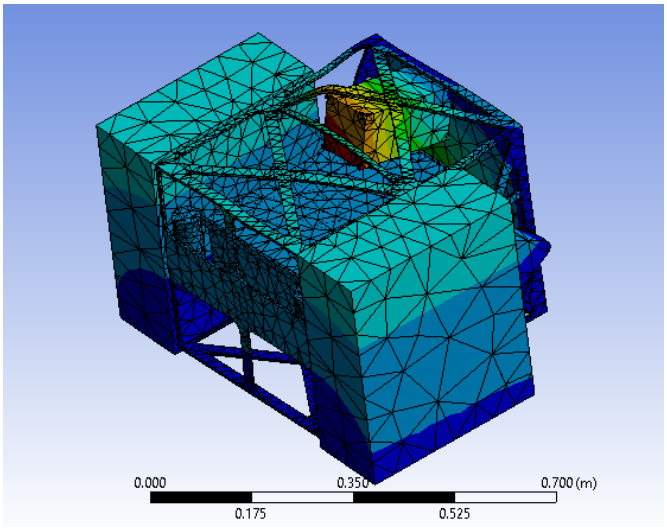

Figure 18: Second Frequency Mode Shape

The third mode shape, occurring at 167.57 Hz, takes the form of the oscillation of cross-braces on the top of the frame. This potential deformation would impact the patch antenna and main body of the craft, as seen in Figure 20.

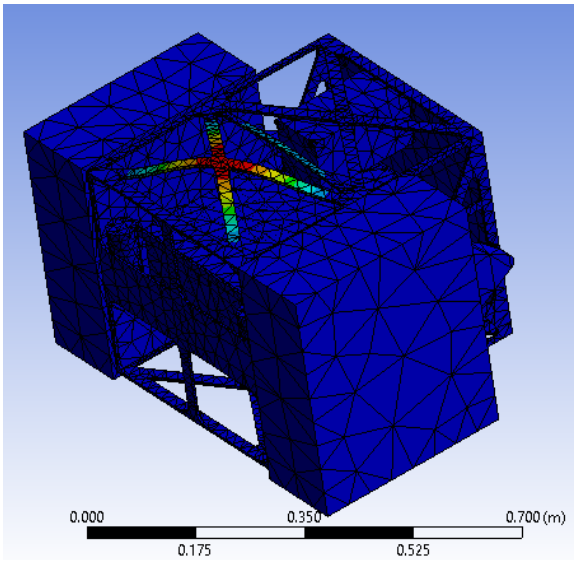

Figure 20: Third Frequency Mode Shape

The fourth mode shape, at 174.69 Hz, occurs within the craft, expanding and contracting the iodine tank surfaces. Though throughout the tank, the bottom face of the tank has the more significant amplitude, pictured below in Figure 21.

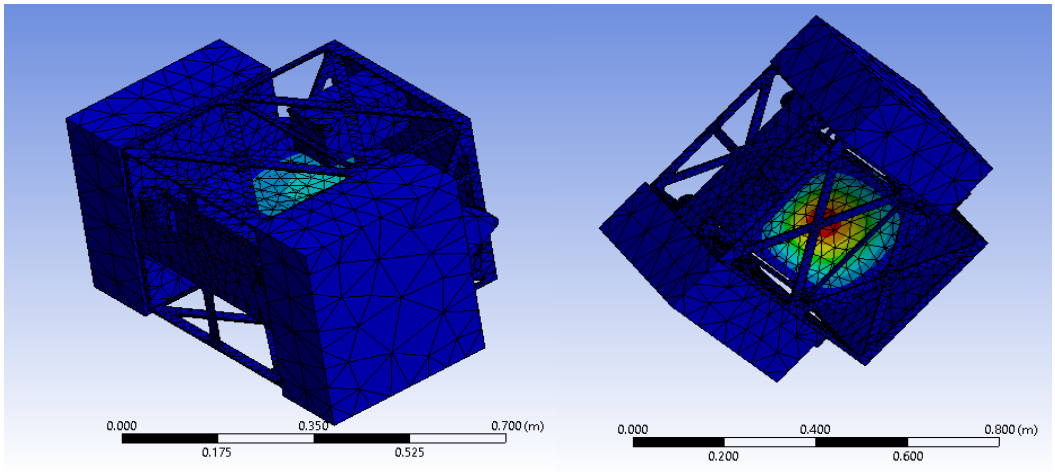

Figure 21: Fourth Frequency Mode Shape

At 216.38 Hz, the fifth mode takes a similar shape to the fourth. The iodine tank's top and bottom faces oscillate vertically. However, the amplitude of the top face has a greater amplitude than the bottom, as pictured below in Figure 23. These movements would directly cause catastrophic failure to the iodine tank and supporting structures.

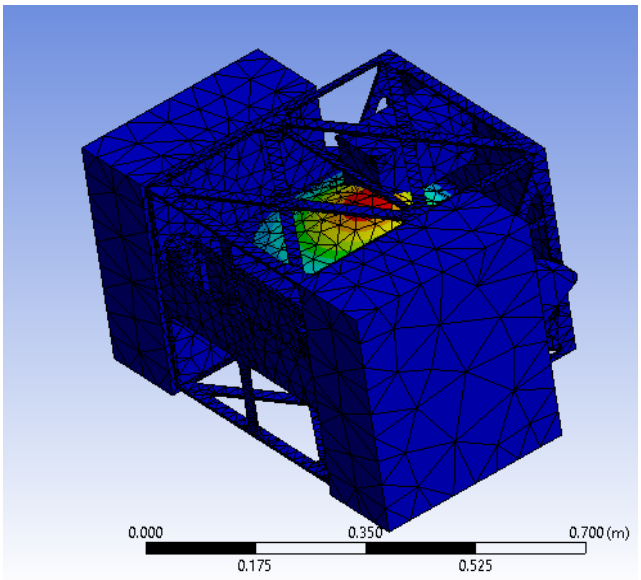

Figure 23: Fifth Frequency Mode Shape

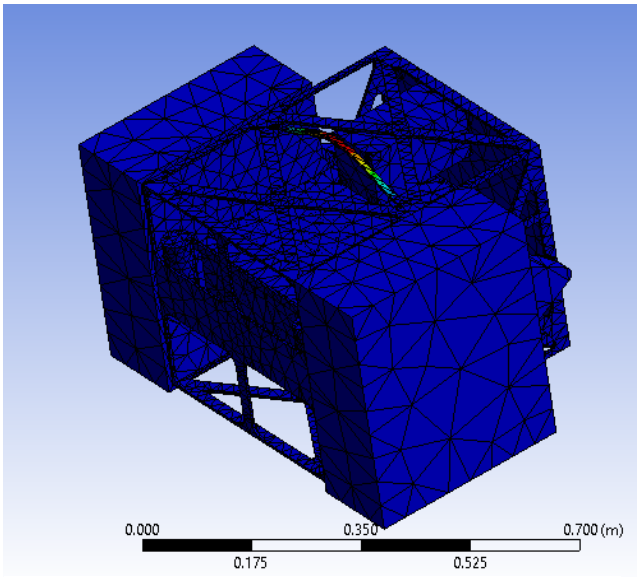

Figure 22: Sixth Frequency Mode Shape

Next, at 231.75 Hz, the sixth mode shape takes place in the middle brace of the top face of the main body. It oscillates vertically, impinging on the patch antenna. This shape is pictured in Figure 22.

The seventh mode of vibration occurs in the back face of the craft, where the main thrusters would be affected. This is displayed below in Figure 24.

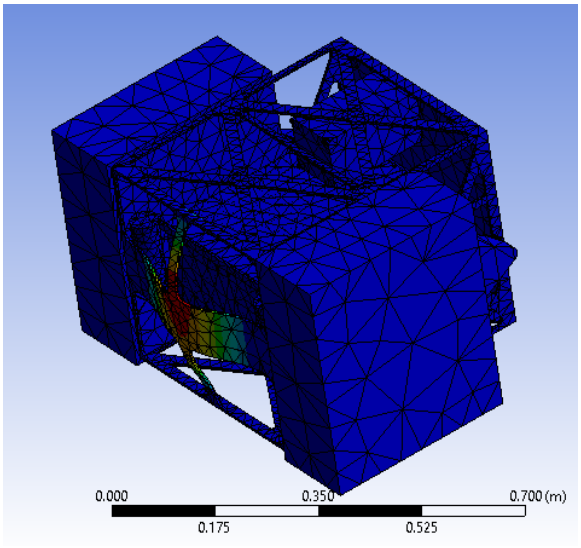

Figure 24: Seventh Frequency Mode Shape

The eighth mode, similar to the fourth, occurs primarily in the bottom face of the iodine tank. This oscillation, however, takes the shape of a sine curve, as seen in Figure 25.

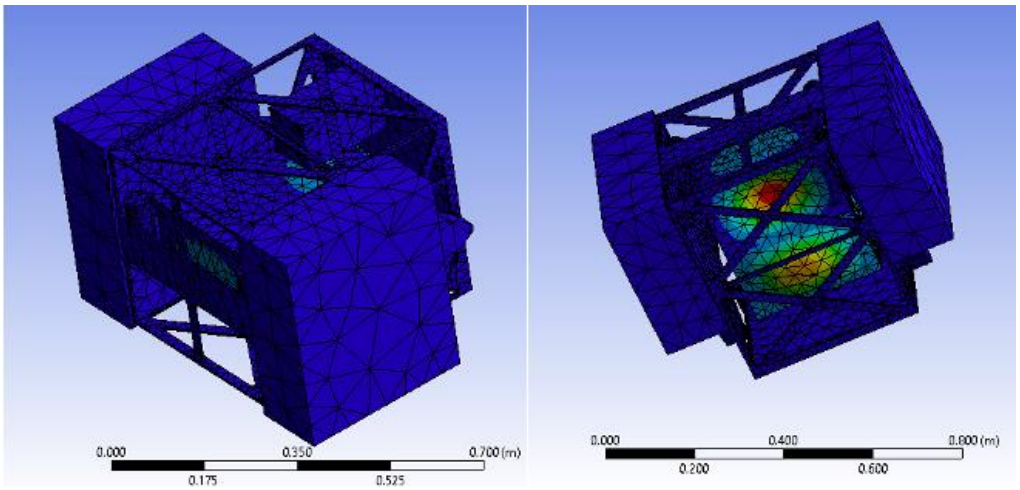

Figure 25: Eighth Frequency Mode Shape

The ninth frequency mode takes the shape of the lateral expansion and contraction of the craft. Inverse contraction and expansion occur along the axis normal to that motion. This is pictured in Figure 26 below. This mode shape would cause mechanical failure throughout the craft and internal components.

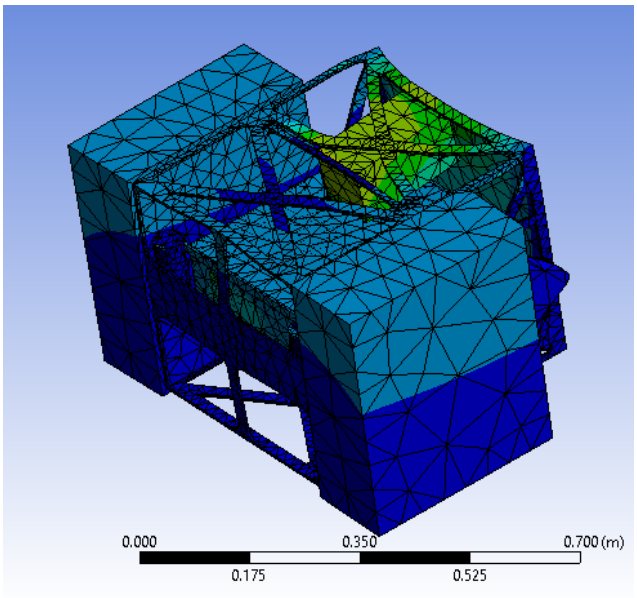

Figure 26: Ninth Frequency Mode Shape

The tenth frequency mode shape occurs primarily in the bottom face of the iodine tank. It takes the form of a sine curve, similar to the eighth mode, but occurs along the axis normal to the deformation of the eighth mode. This shape is pictured in Figure 27.

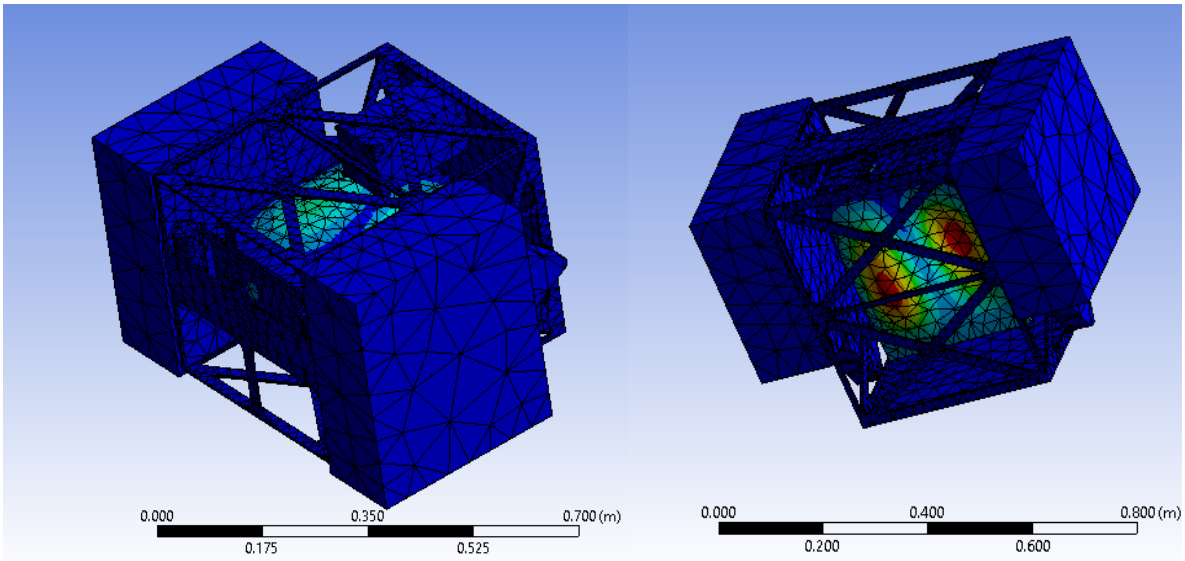

Figure 27: Tenth Frequency Mode Shape

All frequency modes detailed above are to be avoided. Reaching resonance would cause irreparable damage to the structure and functionality of the craft. Therefore, an examination of the excitation during the launch is required.

3.5 Random Vibration Analysis

Random vibration analysis is the examination of undetermined vibrations over a range of frequencies. Modal analysis looks at a single, sinusoidal input, finding the natural frequencies of a structure. However, in reality, inputs are rarely simple sinusoids. Rather than looking at one frequency, random vibration analysis excites many frequencies, all frequencies within a defined spectrum. This analysis then allows the examination of how a system reacts to excitation conditions of a specific environment [30].

3.5.1 Power Spectral Density

The power spectral density (PSD) quantifiably describes the distribution of power of the input signal with respect to its frequency. These values allow for a complete random vibration

analysis of the structure. The signals are completely random, and it is thus impossible to determine the specific contribution of a particular frequency.

For each specific launch vehicle, a PSD chart is generated to detail the excitation environment of the vehicle. The PSD chart for the Falcon 9 and Falcon Heavy is shown below in Figure 28. Excitation and resultant stresses on a spacecraft within the launch vehicle can be simulated.

Additionally, it is necessary to evaluate the spacecraft using GEVs. This "contains a baseline for demonstrating by test or analysis the satisfactory performance of hardware in the expected mission environments, and that minimum workmanship standards have been met" [31]. NASA payloads, subsystems, and components must meet these guidelines. The PSD requirements are detailed below.

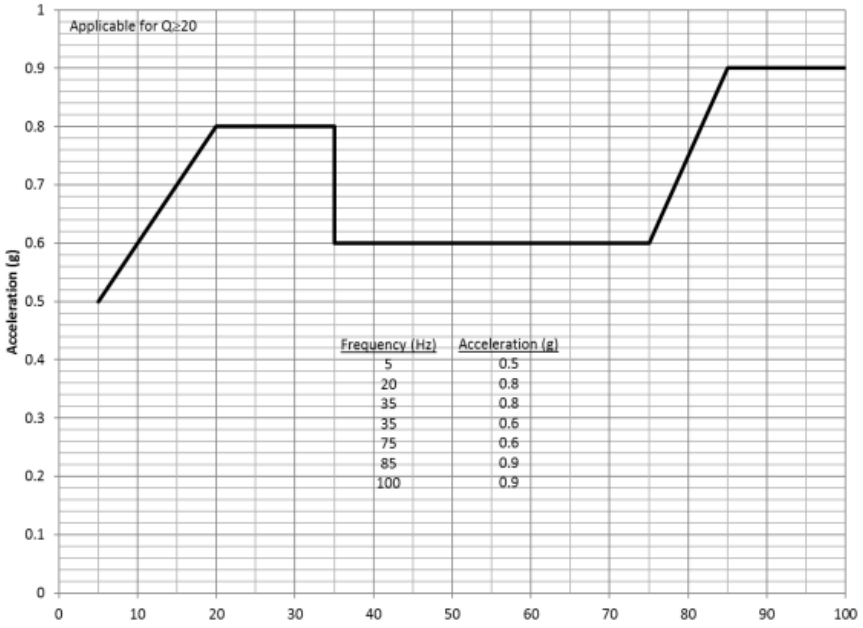

Figure 28. Maximum Equivalent Sine Environment for the Falcon 9 and Falcon Heavy [31]

The internal components, all less than 50lbs, follow the guidelines in the top portion of the graph. The overall assembly fits the category for components under 400 lbs. The PSD chart for

both is shown below in Figure 29. Input into ANSYS, the PSD G acceleration allows for complete random vibration analysis.

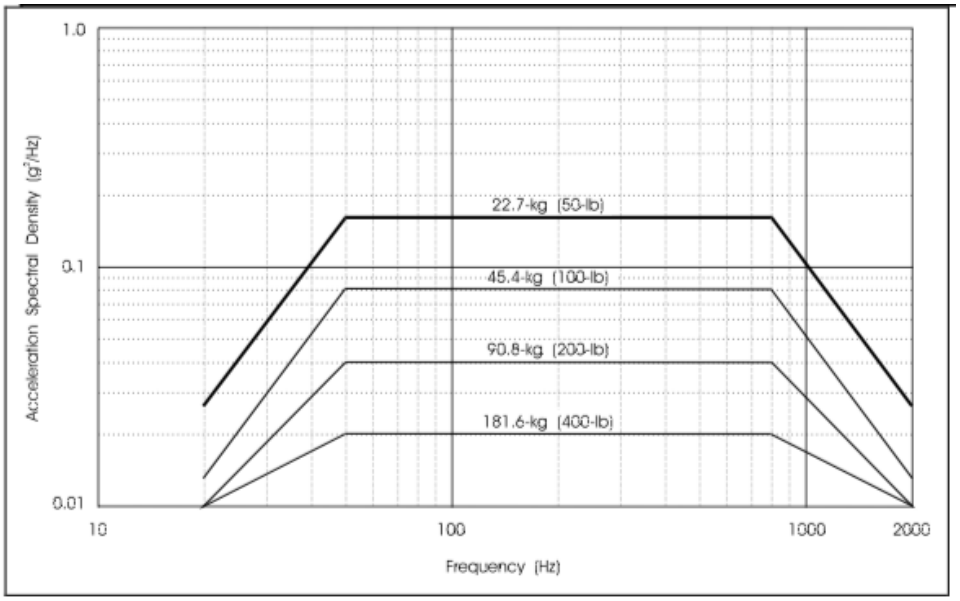

Figure 29. GEVS Power Spectral Density Chart

3.5.2 Von-Mises Stress

Used to determine places, if any, the material of the structure has begun to yield, the Von-Mises stress is derived from strain energy density. This energy density, the total strain energy stored in each differential volume of the body, contains two parts: volumetric energy and deviatoric energy. Volumetric energy results in the change of the body's volume. Deviatoric energy is used to distort the shape of the material. Von-Mises stress is derived from the total stress component resulting in deviatoric energy [32].

3.5.3 Results

After inputting the prerequisite modal analysis from the previous section, the PSD charts and values are entered into ANSYS. Establishing the fixed support on the bottom face, the simulation is then run, the output being the Von-Mises stress on the spacecraft.

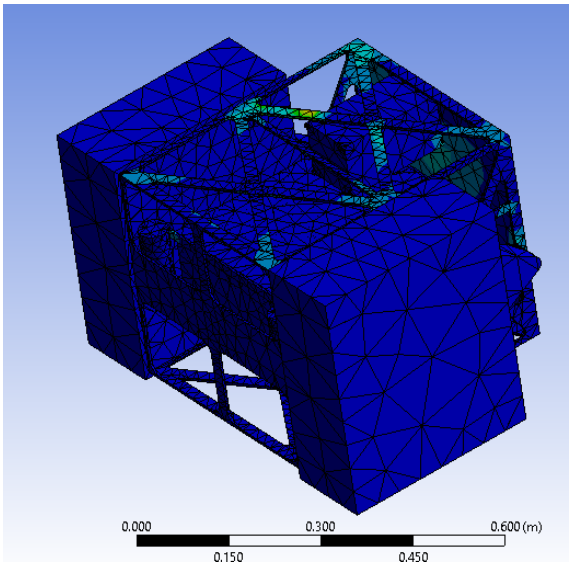

Figure 30. Equivalent stresses under Falcon 9/Heavy conditions

First, the resultant stresses are examined from the incurred excitation from the Falcon Heavy. The stress contour goes from 3.684e-6 Pa in dark blue to 1.7873e7 Pa in red. Figure 31 shows that significant stresses occur on the top and back faces.

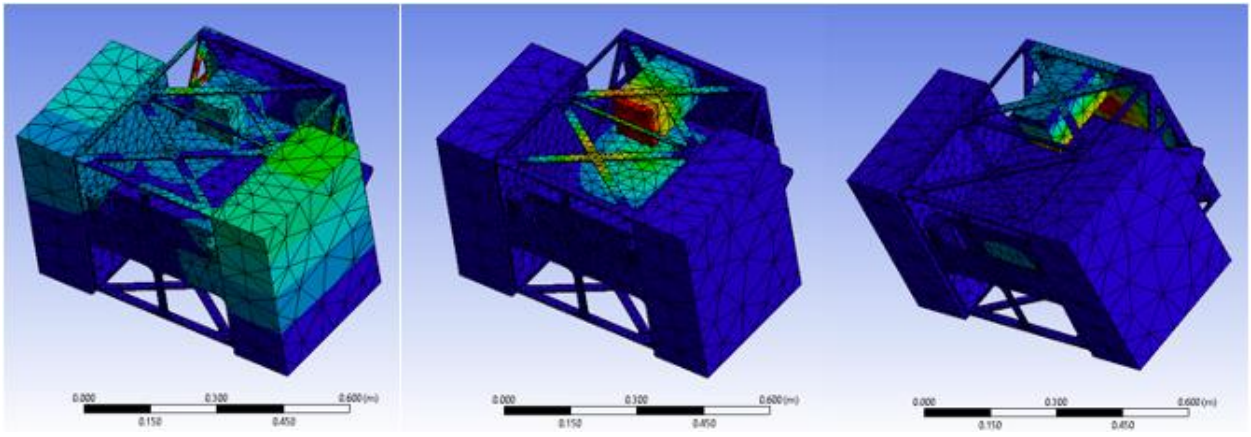

Figure 31. Falcon Heavy X, Y, and Z-Axis Deformation (left to right)

The yield strength of 6061-T6 Al is approximately 241 MPa (2.41e8 Pa). The maximum incurred equivalent stress is within the threshold and is thus unlikely to yield with these particular loading conditions. Evaluating the directional deformation shows the possible resultant deformations (likelihood 68.269%), seen in Figure 31. The maximum x-axis deformation is 0.012515 mm; the maximum y-axis deformation is 0.17332 mm; the maximum z-axis deformation is 0.094008 mm.

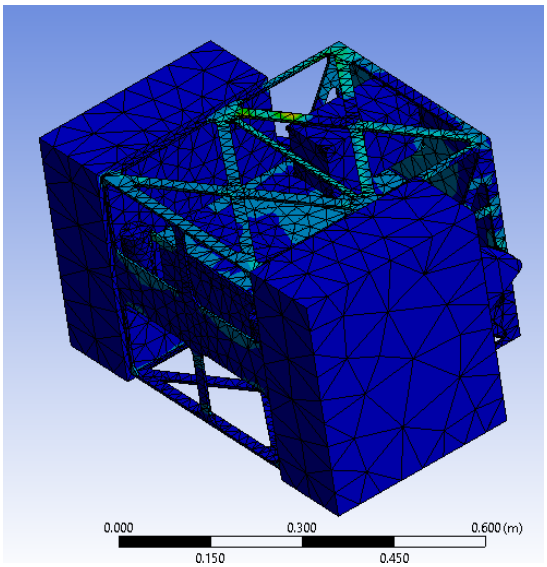

Figure 32. Equivalent Stresses Under GEVs 50lb. Analysis

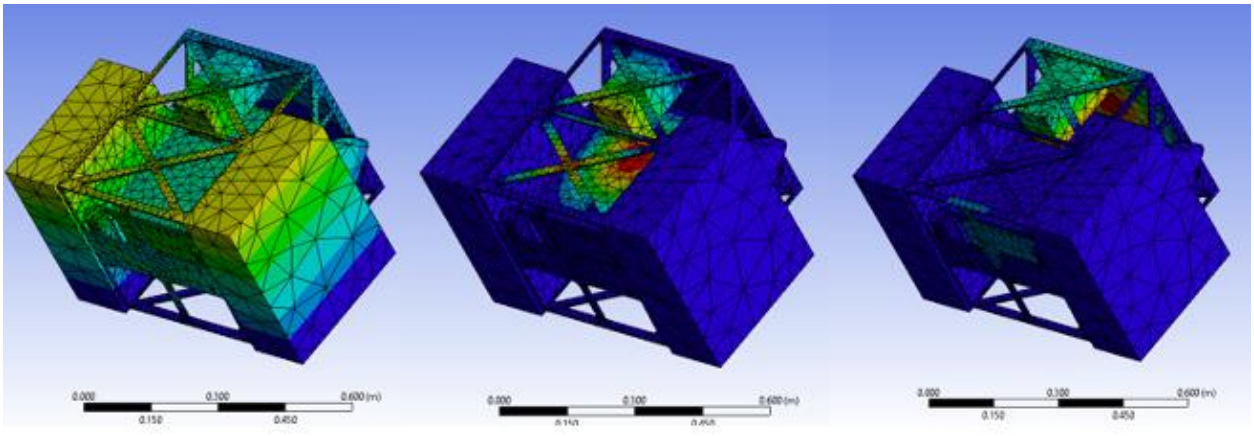

Figure 33. GEVS 50lb Component X, Y, and Z-Axis Deformation (left to right)

Next, the resultant stresses are examined from the GEVS 50 lb. analysis. The stress contour goes from 1.9212e-5 Pa in dark blue to 4.4434e7 Pa in red. Figure 32 shows that the significant stresses occur throughout the frame, outer and internal braces. They occur over the fuel tank and LiDAR sensor.

The maximum incurred equivalent stress is within the threshold and is thus unlikely to yield with these particular loading conditions. Evaluating the directional deformation shows the possible resultant deformations (likelihood 68.269%) seen in Figure 33. The maximum x-axis deformation is 0.08468 mm; the maximum y-axis deformation is 0.46327 mm; the maximum z-axis deformation is 0.21942 mm.

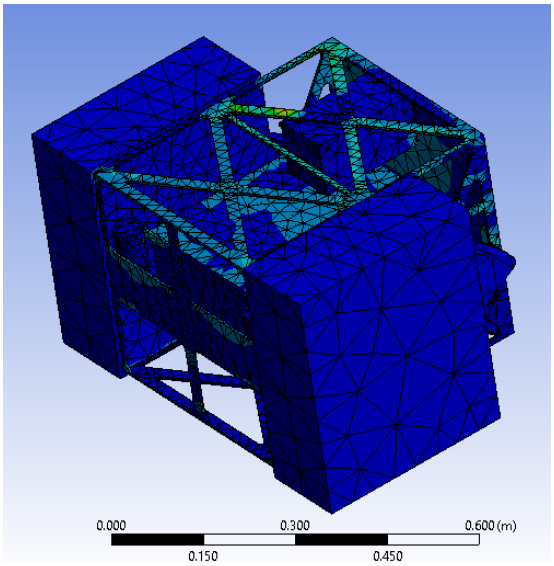

Figure 34. Equivalent Stresses Under GEVs 400lb. Analysis

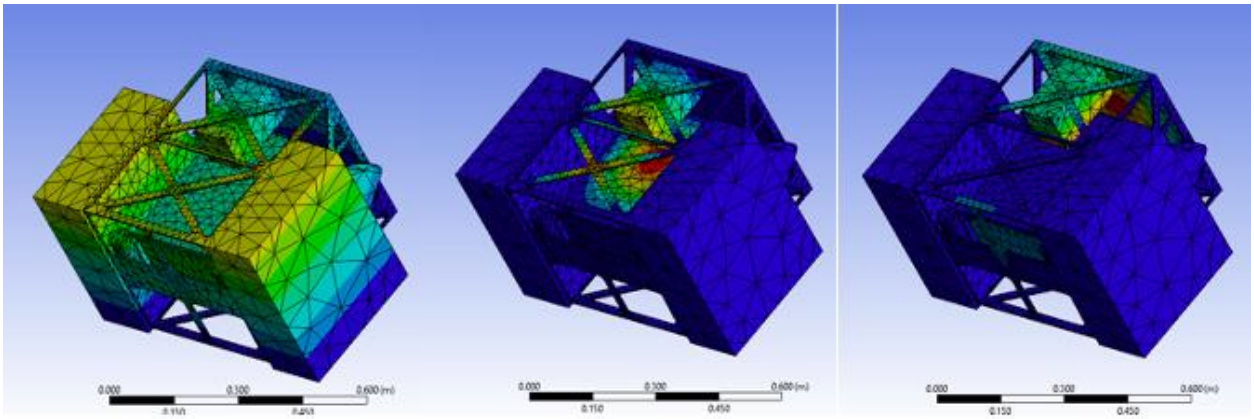

Figure 35. GEVS 400lb Component X, Y, and Z-Axis Deformation (left to right)

Lastly, the resultant stresses are examined from the GEVS 400 lb. analysis. The stress contour goes from 7.9422e-7 Pa in dark blue to 1.8375e6 Pa in red. Figure 34 shows that the significant stresses occur throughout the frame, outer and internal braces. They occur over the fuel tank and LiDAR sensor.

The maximum incurred equivalent stress is within the threshold. Evaluating the directional deformation shows the resultant deformations, seen in Figure 35. The maximum x-axis deformation is 0.0035069 mm; the maximum y-axis deformation is 0.019148 mm; the maximum z-axis deformation is 0.0090739 mm.

3.6 Flight Environment

The reactions of the spacecraft are shown through the ANSYS analysis given material properties, boundary conditions, and flight environment. Modal analysis reveals the frequencies at which the craft is likely to fail. Random vibration analysis examines the resultant stresses, deformations, and potential damages caused by the excitation environment of the launch.

Spacecraft that comply with the GEVs are “generally covered” for this flight environment [29]. The environment is detailed in the graph below.

The random vibration environment of the aircraft fits within the envelope of the minimum random vibration spectrum.

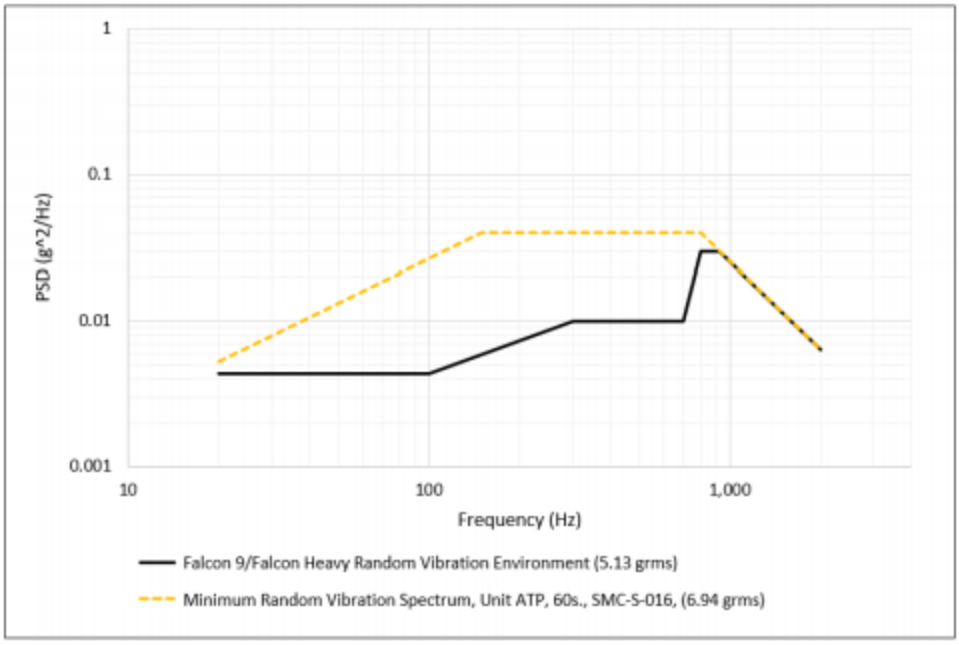

Figure 36. Falcon 9/Heavy Random Vibration Maximum Predicted Environment

4 Propulsion

The role of the primary propulsion system is to carry out orbit changes required by the designated mission. Since this mission is interplanetary, it will require significant ΔV and flight times necessitating careful consideration when designing trajectories and selecting system components. This section discusses the design and analysis of the main propulsion system for MAPLE SIRUP, including hardware selection and orbital analysis.

4.1 Thruster Selection

Electric thrusters are categorized by their acceleration method: electrostatic, electromagnetic, and electrothermal. Two types of electrostatic thruster are Hall Effect Thrusters (HET) and ion thrusters.

HETs use a predominantly axial electric field, generated by a metal anode at the base of an annular channel, and a radial magnetic field to generate a plasma discharge and accelerate ions. Electrons to initiate and sustain the plasma discharge are supplied by a hollow cathode external to the annular channel. The radial magnetic field inhibits the electron motion to the anode, and the crossed electric and magnetic fields result in electrons drifting in the azimuthal direction in the channel (Hall current). This increases the efficiency of the plasma generation, so-called ultimately propellant utilization. The hollow cathode also supplies electrons to neutralize the accelerated ions that form the thrust beam, to maintain a charge balance and prevent spacecraft charging. HETs typically operate with higher thrust but lower I_{sp} when compared to Ion thrusters for a given power consumption because of an increased mass flow capability. HETs have significant flight heritage on geostationary spacecraft, however, their application on smaller spacecraft is more limited [33].

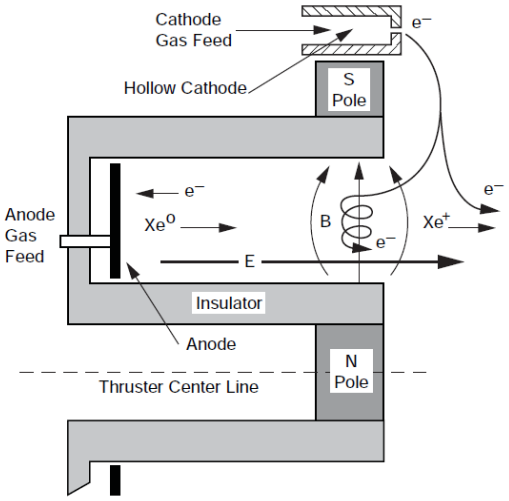

Figure 37. Hall Effect Thruster Cross-Section Schematic [114]

Ion thrusters also electrostatically accelerate ions; however, the methods of plasma generation and ion acceleration are different from HETs. In ion engines, the propellant is ionized inside a discharge chamber using either electrostatic or RF fields to accelerate electrons supplied by a cathode. The ions are then extracted from the discharge and accelerated using a series of voltage-biased grids to generate the thrust beam. The thrust beam is neutralized to prevent a charge imbalance using a second cathode outside the discharge chamber. Ion thrusters typically have a lower thrust-to-power ratio than HETs but a much higher specific impulse.

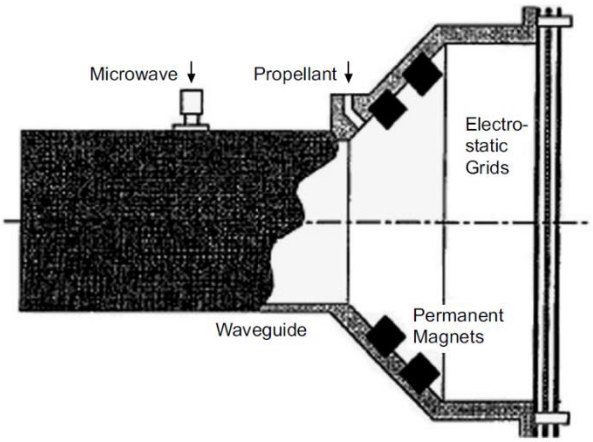

Figure 38. Microwave Ion Thruster Cross-Section Schematic [114]

4.1.1 System Type

As discussed in Section 1.2.3 and expanded on in Section 4.1, there are two main types of propulsion systems: chemical and electric. Each system is best suited to a particular application based on its characteristics as well as the goals and constraints of the specific mission. For this mission, the choice was focused on the I_{sp} of each type given the high ΔVs required. The equations for ΔV and I_{sp} are shown Equation 4.1 and Equation 4.2 and respectively,

$$\Delta V = g I_{sp} \ln\left(\frac{m_0}{m_f}\right) \tag{4.1}$$

$$I_{sp} = \frac{T}{\dot{m} g} \tag{4.2}$$

In these equations, m_0 and m_f are the initial and final masses respectively, T is the thrust and $\dot{m}$ is the mass flow rate. An I_{sp} below 1200 s does not deliver a reasonable payload mass (> 1/3 initial mass) assuming an approximate ΔV of 11 km/s taken from NASA's DAWN mission to the asteroids Vesta and Ceres in the early 2010s [34]. This estimated ΔV is supported by a calculation using the Edelbaum Equation [35], Equation 4.3.

$$\Delta V = \sqrt{V_i^{\,2} + V_f^{\,2} - V_i V_f \cos\left(\frac{\pi}{2}\Delta i\right)} \tag{4.3}$$

This equation estimates a low thrust transfer between a circular orbit at Earth's semimajor axis and a circular orbit at 7 Iris' semimajor axis yielding 10.5 km/s, where the orbital velocity is given by Equation 4.4 with μ as the gravitational parameter of the parent body and r as the orbital radius. Both ΔVs are only rough approximations but provide insight into high-level propulsion system requirements. Such ΔVs rule out any form of chemical propulsion, narrowing the trade space to only electric thrusters.

$$V_c = \sqrt{\frac{\mu}{r}} \tag{4.4}$$

4.1.2 Hardware Comparison

The selected thruster must follow certain thrust, efficiency, power, and size constraints given the small size of our spacecraft. A list of available electric thrusters was created to evaluate each on desired metrics and can be seen in Figure 39.

Name	Isp (s)	Power (W)	Thrust (mN)	Score
RIT 10 EVO	3000	435	15	0.944
RIT uX	3000	50	0.5	0.875
BHT-200 I max	1818	300	17.4	0.860
BHT-200 I	1482	200	12.9	0.856
BHT-200	1516	200	12.6	0.853
BHT-200 max	1791	300	16.8	0.837
BHT-600	1585	600	42	0.794
CAM200 HP	1600	300	17	0.790
RIT 5 EVO	1900	145	5	0.744
IHET300	1300	300	15	0.655
Halo HP	1350	450	21	0.592

Figure 39. Thruster Decision Matrix [109, 36, 106, 110, 111, 112, 113]

Thrusters with nominal power requirements over 600 W were not included in this matrix based on solar flux being ~240 W/m^2 at 7 Iris. Thrusters having an I_{sp} less than 1200 s were also not included in the matrix for the reasons stated in Section 4.1.1. The remaining candidate thrusters were then ranked according to their normalized I_{sp}, thrust, and power as follows with weights α=.5, β=.4, and γ=.1.

$$score = \alpha \frac{I_{sp}}{\overline{I_{sp}}} + \beta \frac{T}{\overline{T}} - \gamma \frac{P}{\overline{P}} \tag{4.5}$$

These weights were selected to bias high I_{sp} without ignoring thrust or power. Since I_{sp} is the most important characteristic for this mission it receives the highest weight. Because minute thrust makes mission planning difficult, it must also be accounted for in the score. Power was already limited during the selection process based on initial assumptions, so its weight is lower as there is less variability to filter out.

As seen in Figure 39, the top thrusters are the Ariane RIT 10 X and RIT μX, followed by various iterations of the Busek BHT-200. The "I" following BHT-200 denotes the performance values using iodine propellant as opposed to the more traditional xenon, which will be discussed in Section 4.2. Ultimately, the BHT-200, pictured in Figure 40, was selected because the nominal power requirement for the RIT 10 X was slightly too high and the thrust of even several RIT μX was too low. Additionally, the BHT-200 offers flexibility in propellants, also discussed in Section 4.2.

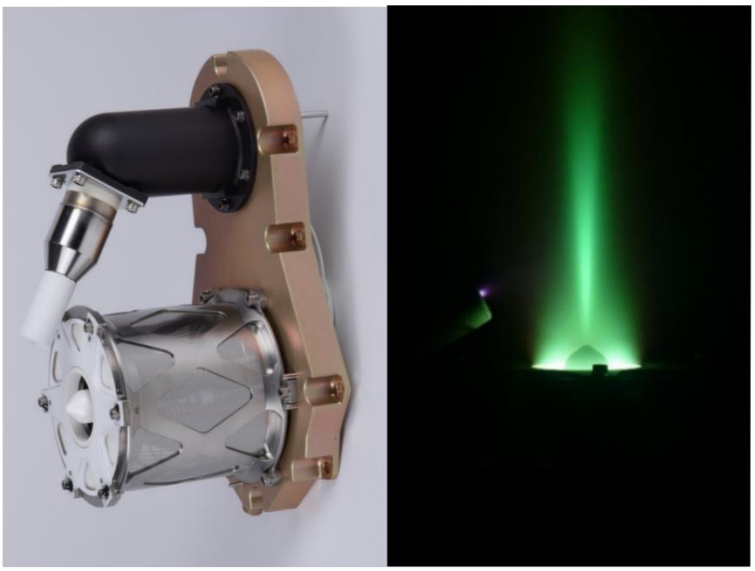

Figure 40. Busek BHT-200 Hall Effect Thruster [106, 40]

4.2 Propellant

Typically, electric propulsion systems use high pressure densified xenon gas as a propellant because of its high atomic weight and large ionization cross-section [36]. Additionally, xenon has a favorable density of approximately 2.4 kg/L at 40 MPa [37] when to other noble gasses like krypton with a density of 1.6 kg/L at 40 MPa [38] or traditional chemical propellants such as monomethyl hydrazine (MMH) at .874 kg/L [39]. Gaseous propellants however have the disadvantage that they must be stored in bulky high-pressure tanks, such as the one pictured in

Figure 41. Figure 42 and Figure 43 detail the density and impulse density of various propellants at several pressures respectively.

Figure 41. Example of High-Pressure Xenon COPV [105]

Recent research has investigated the use of solid-storable propellants such as iodine for HETs [40]. Solid iodine has a density of 4.93 kg/L [41], at least twice that of xenon, without the need for a pressure vessel meaning reduced weight and increased safety and flexibility. Additionally, the relevant properties of iodine (atomic weight, ionization energy, ionization cross-section) are similar to that of xenon [36], meaning minimal change in thruster performance. Iodine does have to be vaporized before being fed into the thruster but has a very low vapor pressure so only needs to be modestly heated before sublimating [42].

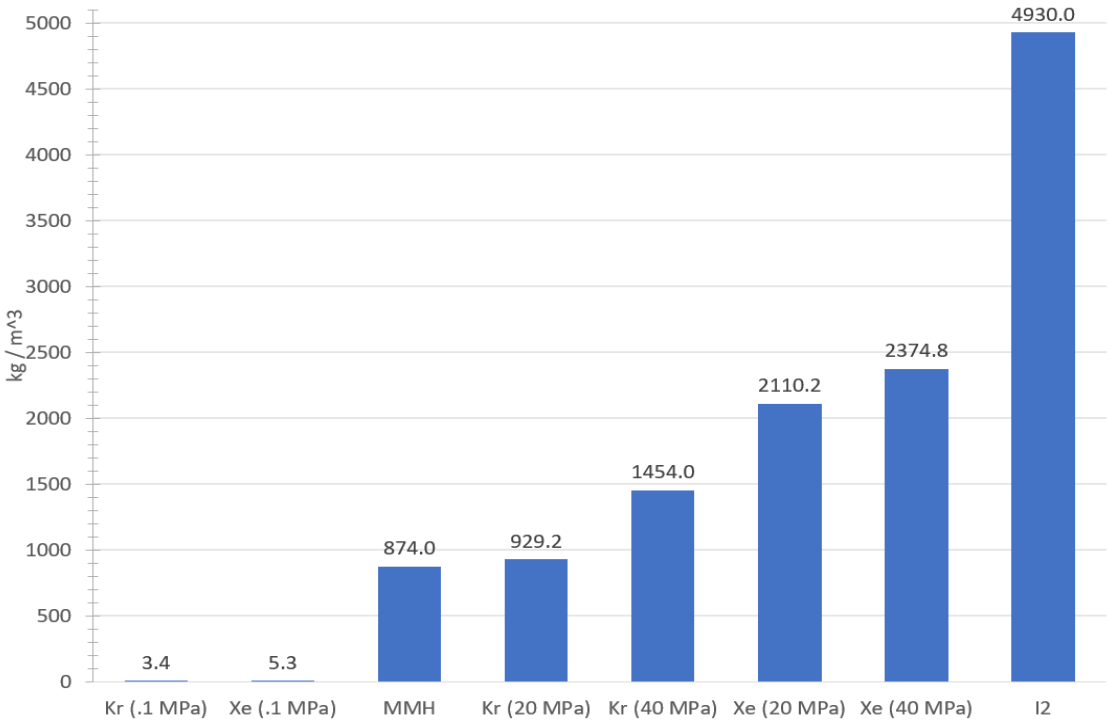

Figure 42. Densities of Various Propellants (25 °C) [38, 37, 39, 41]

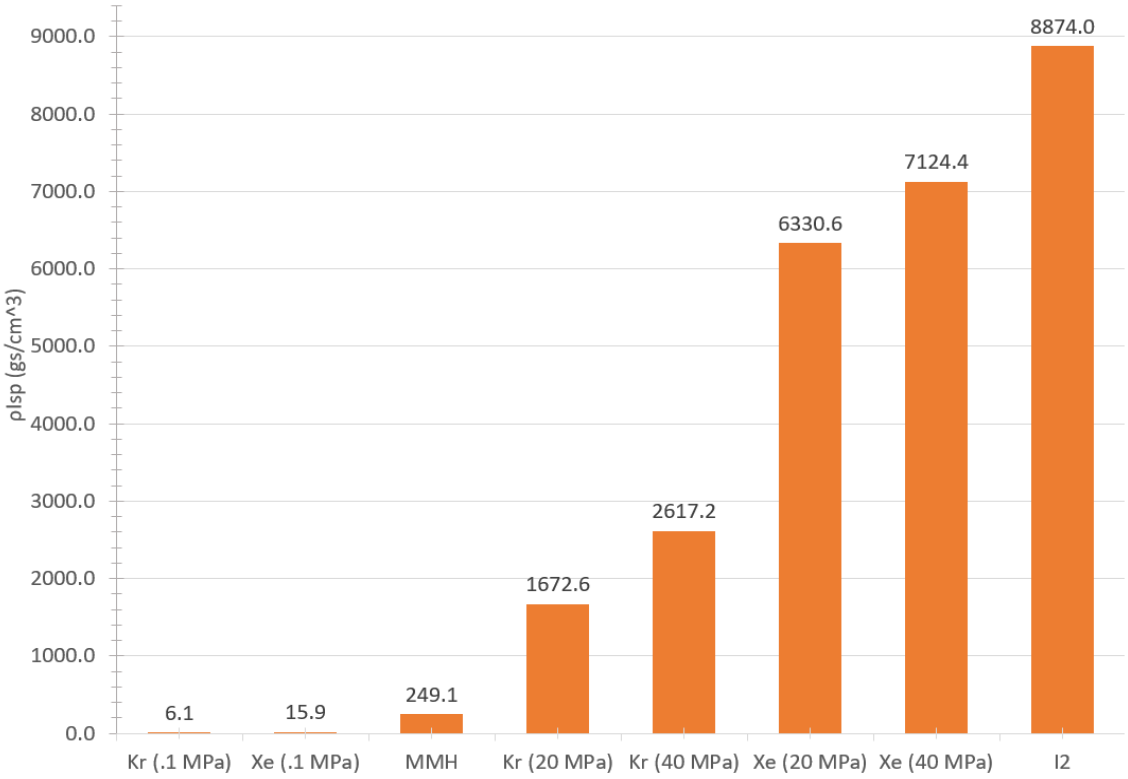

Figure 43. Isp Densities of Various Propellants [38, 37, 39, 41, 106, 109]

4.2.1 Propellant Performance

Because of the favorable performance of the BHT-200 in Section 4.1.2, the possibility of using iodine as a propellant became available as Busek Co. Inc. has tested this thruster with iodine and other alternative propellants. The thrust from iodine is slightly higher than that of xenon at a given input power with the gap widening above around 350 W as seen in Figure 44. The I_{sp} of iodine falls slightly below xenon until around 275 W after which it gains a slight edge, as seen in Figure 45. Iodine propellant was selected for its superior performance and system-level advantages.

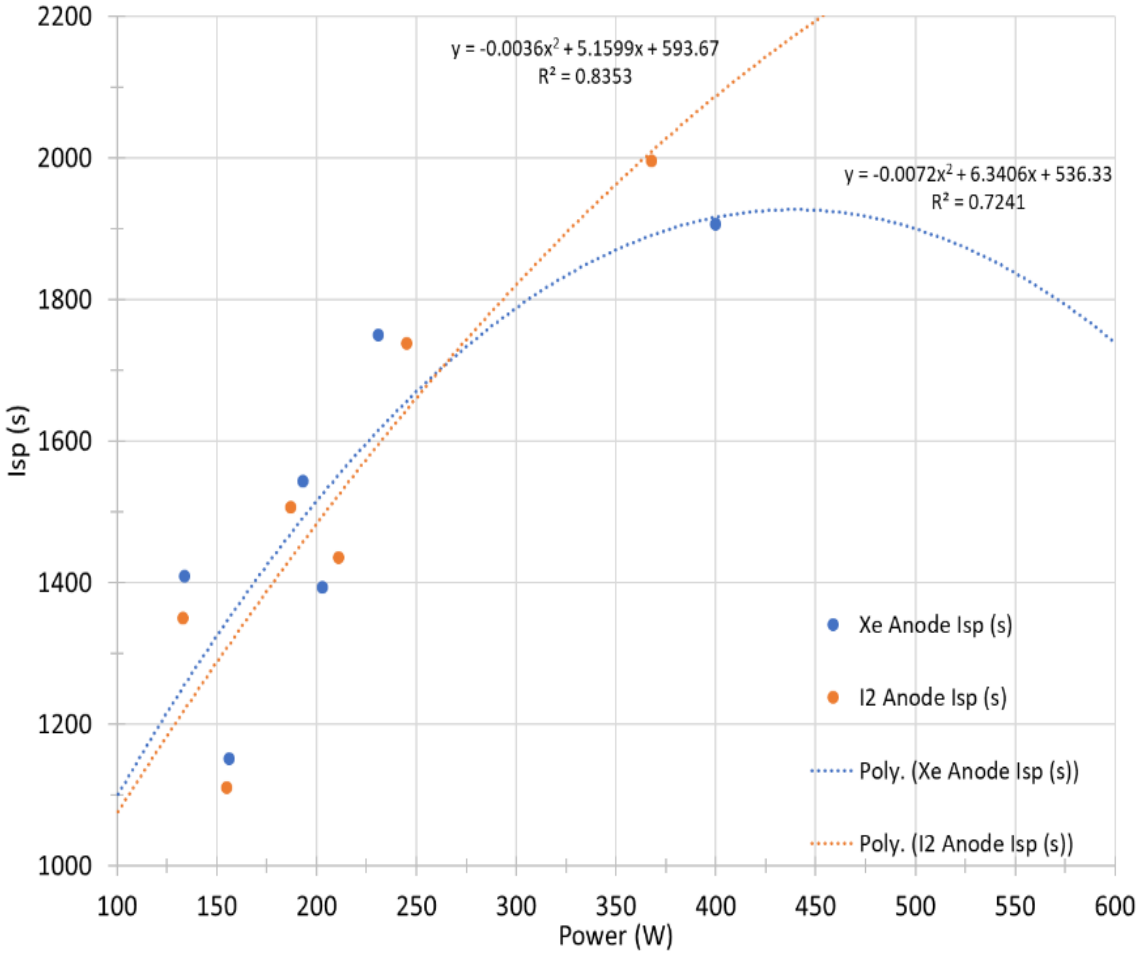

Figure 44. Isp vs Power of Xe and I2 Propellant with BHT-200-I [36]

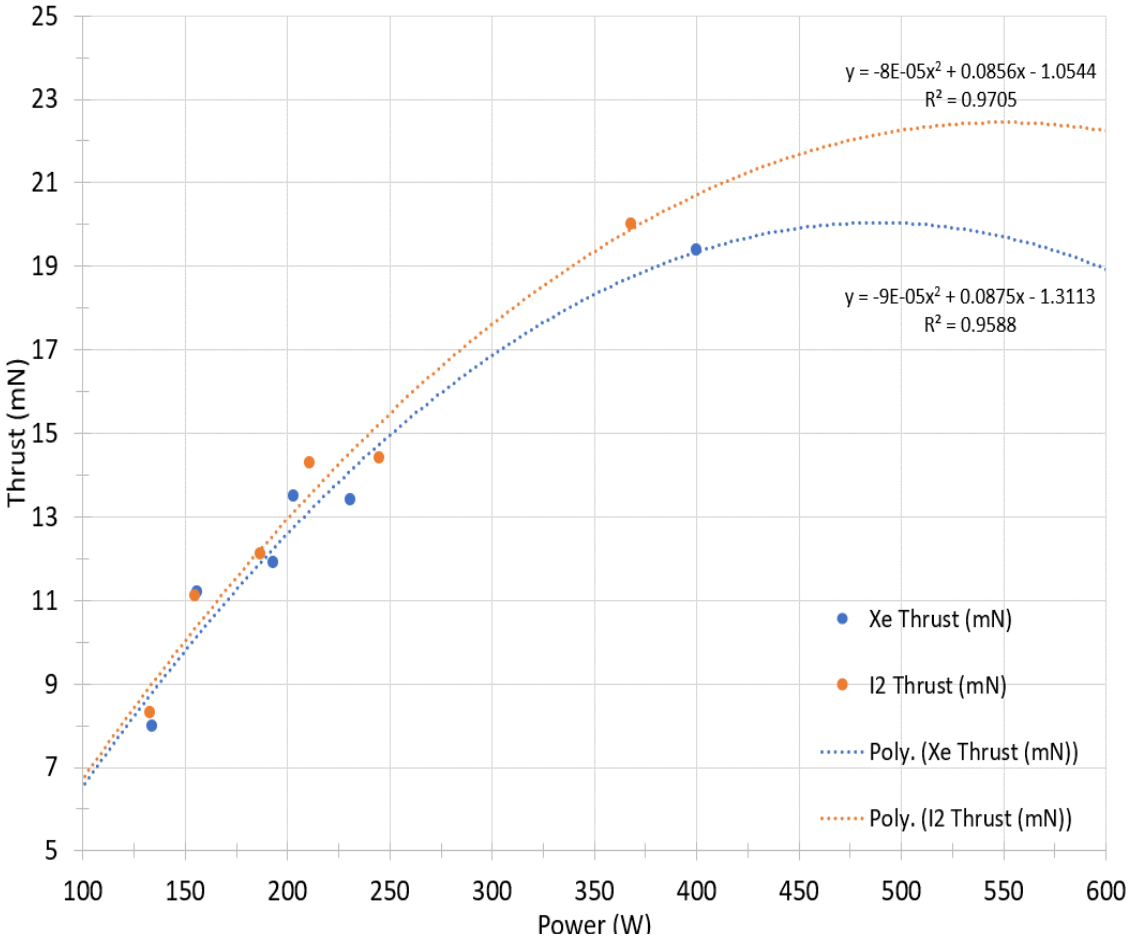

Figure 45. Thrust vs Power of Xe and I2 Propellant with BHT-200-I [36]

4.2.2 Propellant Tank

Since iodine is stored as a solid, it is easier to contain than more traditional gaseous propellants. This makes containing the propellant less challenging; however, it is also less conventional. A simple structure is sufficient to contain the iodine since it is not under pressure. Iodine's reactivity, however, does need to be accounted for when selecting the material for the tank. The material selected for the propellant tank is Allite AE81 Super Magnesium alloy for its low density, high strength, moderate thermal conductivity, workability, and low reactivity with iodine [43].

4.2.3 Feed System

The propellant does not simply flow directly from the tank to the thrusters, it must go through piping designed to regulate how much and when the propellant is delivered. A series of values is designed to create different zones propellant can and cannot access during flight such that each thruster receives the required propellant, but propellant is unable to leak from the spacecraft. Figure 46 presents an overview of MAPLE SIRUP's fuel system.

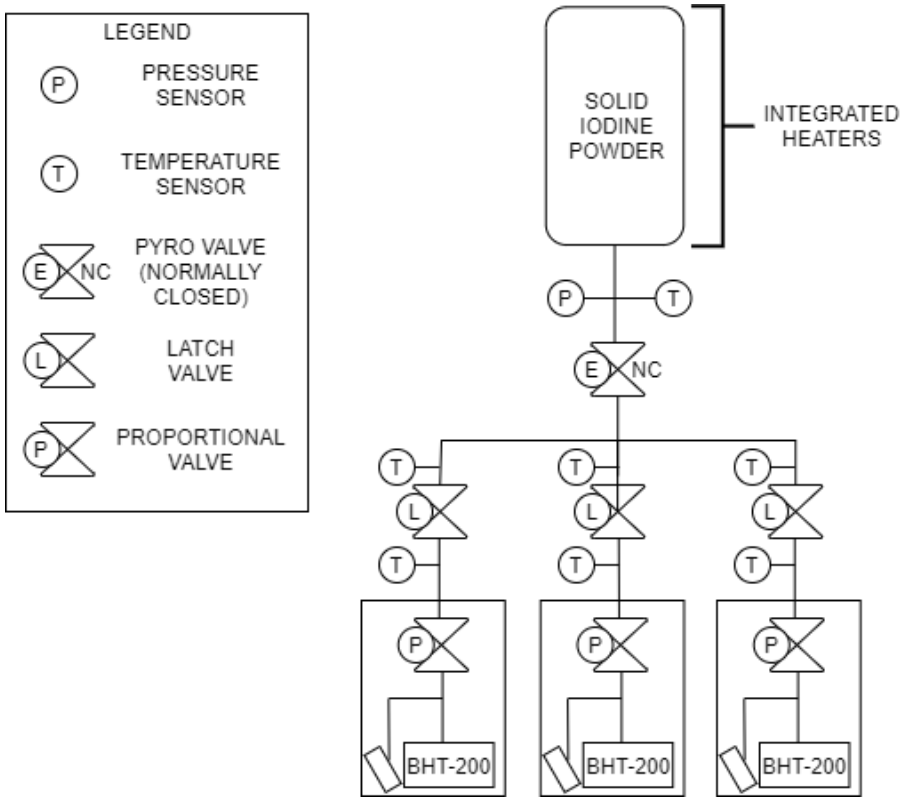

Figure 46. Propulsion Block Diagram

The first valve from the top is a single-use sealed, normally closed valve, intended to contain the fuel during launch and on-orbit checkout before the Earth Departure Burn starts. This valve is more resistant to leakage while closed than the latch or proportional lower down in the flow path to prevent any premature leakage of fuel, however, it cannot be reseated. A preliminary selection for this type of valve is the ArianeGroup Shape Memory Alloy Valve [44]. This particular valve serves as a reference for the size, mass, and flow characteristics expected for this section of the

flow system. Additionally, it offers a non-hazardous method of operation, trading, and explosive charge that may require extra safety testing for a shape memory alloy that can be easily operated with heat that is already required for the propellant and will be discussed later on in this section.

Figure 47. ArianeGroup SMA Valve [44]

The next type of valve in the feed system is a set of three latch valves, one for each thruster. These valves offer simple bang-bang control of which thruster will receive fuel at any given time, enabling the spacecraft to disable a thruster while not in use to prevent fuel leakage. Preliminary data was gathered on the MOOG-051-271 .75N Thrust Monopropellant Thruster Valve [45] for the same purposes as the Arianne SMA Valve.

Figure 48. MOOG-051-271 Latch Valve [45]

The final type of valve included in the feed system are Proportional Flow Control Valves (PFCVs), designed to provide continuous variability in the flow rate of propellant delivered to the thrusters. These valves, in tandem with the power system, determine the output of the thrusters at any given time. Additionally, they provide a layer of redundancy to the latch valves in protecting the fed system from leakage. In the same fashion as the previous two types of valves, the MOOG Electric Propulsion 51E339 PFCV [46] was investigated as a baseline.

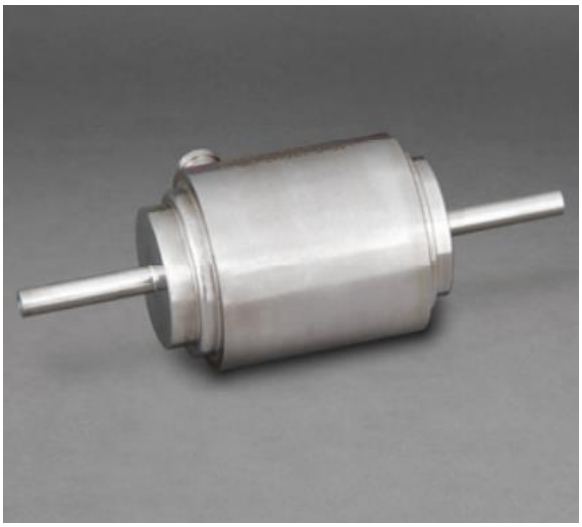

Figure 49. MOOG Electric Propulsion 51E339 [46]

Iodine must be sublimated to travel through the feed lines, so a series of heaters must be incorporated to proper sublimation and prevent crystal deposition. The energy required can be determined by calculating the max flow rate, specific heat, and heat of vaporization, seen in the equations below.

$$\dot{m} = \frac{T}{gI_{sp}} \tag{4.6}$$

$$\dot{Q} = \dot{m}(C\Delta T + L) \tag{4.7}$$

In these equations, $\dot{m}$ is the total mass flow rate for all active thrusters, *T* is the total thrust, *Isp* is the specific impulse, g is Earth's gravitational acceleration, $\dot{Q}$ is the required heat flux, C is the heat capacity of solid iodine, ΔT the required change in temperature, *L* is the heat of

vaporization. Using thruster performance and chemical data [36, 41], the max flow rate is 2.99 mg/s/thruster for a total of 8.97 mg/s. Using this value to find the heating power required and assuming 0 ℃ storage and feed pressure of 10 kPa [36, 47], yields 1.68 W required to vaporize the max throughput of iodine. The aforementioned SMA Valve has two integrated heaters to operate it, each operating at 12 W, so if selected it would have more than enough heating capacity to ensure propellant vaporization.

Solid storage also necessitates a system to force the propellant into said feed lines since there is no pressure in the tank and the acceleration of the spacecraft is minute and not available at the start of burns. Current small-scale tests indicate a spring-loaded canister is capable of containing and delivering iodine powder [48], but more research is needed to determine a method to reliably deliver propellant to the feed lines.

4.3 System Considerations

Once the individual components of the propulsion system have been selected and evaluated individually, their performance once integrated into the overall spacecraft must be considered.

4.3.1 Number of Thrusters

Because of excess power available during the Near-Earth phase of the mission, it is possible to utilize multiple thrusters for certain segments of flight. This strategy does partially conflict with the reasoning to exclude the RIT 10X for its higher power requirements; however, the previously discussed volume advantages of using iodine propellant were deemed more important than the mass savings the higher I_{sp} of the RIT. Table 4 compares the mass and volume required for 13.6 km/s of ΔV with the BHT-200-I and RIT 10X. Additionally, the RIT 10 X requires its propellant to be stored in a pressure vessel, negating some of the mass savings from a higher I_{sp}.

Thruster	Isp	Mass	Volume
BHT-200-I	2091 s	73 kg	14.8 L
RIT 10 X	3000 s	55.6 kg	25.2 L

Table 4. Fuel Mass Comparison Between BHT-200-I and RIT 10X

The exact amount of power available at the beginning and end of the mission, as seen in Section 5.2, allows for two additional thrusters to be used for the first stages of flight for a total of three. The three thrusters will be in a line aligned with the horizontal plane of the spacecraft. Each thruster will be set to draw 368 W, for a total of 1104 W at BOL not including control and loss. As the available power decreases, the middle thruster will be deactivated. As available power decreases even further near Iris, the middle thruster will be reactivated and the outer two will be deactivated.

4.3.2 Thruster Lifetime

Hall Effect thrusters, such as the BHT-200, are limited in their total impulse life by the erosion of the channel from ion sputtering, exposing magnetic components [49]. Because of the long “on times” inherent to EP, thruster lifetime is an important consideration. Recently, a similar thruster, the BHT-600, was experimentally validated for 7198 hrs (300 days) on xenon by Busek and NASA Glenn RC before the test was voluntarily terminated [50]. This is not the exact same thruster or fuel as selected for this spacecraft, however, the BHT-200 and 600 are similar and significant data was not found on the BHT-200 or iodine propellant. As discussed in Section 4.4, the total burn time of the spacecraft is nearly 500 days (12000 hrs). This is split among the three thrusters included on the spacecraft. The central thruster is designated to have the longest run time of approximately 344 days (8253 hrs), while the outer thrusters are expected to burn for 249 days (5977 hrs). Only the central thruster exceeds the current best-estimate for the mission lifetime, however, it is expected the combination of iodine and increased operating power will

accelerate degradation. Expecting to exceed this estimate may indicate wear issues, but with a theoretical launch approximately 5 years in the future, further testing and advancements can be anticipated to resolve potential concerns.

4.3.3 Simplifications

Because of time, research, and expertise limitations, some elements of the propulsion subsystem were not included in the systems analysis, namely the Power Processing Unit (PPU) and thruster mounting/gimbals. The PPU is important to the actual operation of the propulsion system but does not have a major impact on analyzing and designing the top-level system. Therefore, it is assumed to be a black box capable of supplying the required power to the thrusters. A generic PPU was based on the Aerojet Rocketdyne XR-5 4.5 kW Hall Thruster PPU [51]. This particular example can deliver more power than is required, so it was scaled down from 4500 W to 1200 W, resulting in a mass of ~3.5 kg. This figure is similar to that of Apollo PPU from Apollo Fusion [52], so is not unreasonable for a first-pass assumption. Many electric propulsion systems are mounted on some type of gimbal to enable more precise pointing than the bus can provide and to isolate the thruster [53]. This is however a complex mechanical problem to solve and was not deemed a useful application of resources for this level of analysis. Neither of these simplifications are expected to have a negligible impact on the final system conclusion, and both provide opportunities for future work to expand upon this project.

4.4 Trajectory

Section 4.1.1 briefly introduces estimates of the required ΔV for rendezvous, but knowing an approximate total is not sufficient to get a spacecraft to its target. Delivered impulse is tied directly to flight time, so determining the parameters of each burn is crucial. Iris's orbital information is detailed in Table 5, and a visual representation of its orbit is shown in Figure 50.

Semi-major Axis (a)	2.387375 AU
Eccentricity (e)	.230145
Inclination (i)	5.522 deg
Ascending Node (Ω)	259.563 deg
Argument of Periapsis (ω)	145.202 deg
Mean Anomaly (M)	247.426 deg
Periapsis Time (t_p)	26 Jul 2021 07:46:01

Table 5. 7 Iris Orbital Elements [54]

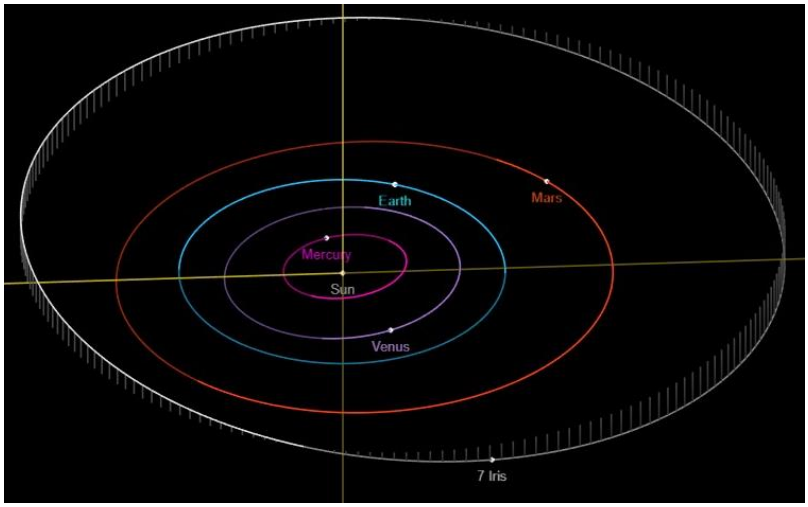

Figure 50. 7 Iris Location near Rendezvous [54]

Trajectory analysis was carried using a combination of Copernicus and STK. Trajectories were composed of several segments corresponding to the phases of flight described in Table 1. Table 6 provides a more detailed overview of these orbit segments and Figure 51 and Figure 53 are orbit track plots of the mission. Significant trial-and-error iterations were required in addition to numerical solvers as the acceleration of MAPLE SIRUP is very low, on the order of 0.4 mm/s^2, making multi-month burns a necessity. Because of the long periods of deep-space travel and the low gravitational pull of Iris, orbital perturbations were also considered. The barycenter gravity of all planets in the solar system was added to the gravity of the central body. The solar radiation pressure on the large solar panels was also added. ACS thruster fuel use was however not considered as it was not finalized during this analysis. As seen in Figure 52, the mass

remaining at Iris is 76.965 kg, meaning the required propellant is 73.035 kg. 75.26 kg is loaded onto MAPLE SIRUP, meaning there is a 3% fuel margin available.

Mission Phase	Segment Name	Duration (days)	Thrust (mN)	I_{sp} (s)	ΔV (km/s)
Near-Earth Operations	Earth Departure Burn	97.352	60	2045.6	3.7676
	Earth Departure Coast	190.784	--	--	
Deep-Space Operations	Inclination Burn	151.686	43.5	2274	5.1340
	Mars-Crossing Coast	237.285	--	--	
	Apogee Raise Burn	137.483	20	1996	2.5659
	Belt Coast	179.000	--	--	
	Iris Catch-Up Burn	107.800	20	1996	2.2781
Near-Iris Operations	Positioning Coast	87.187	--	--	
	Relative Velocity Burn	0.352	20	1996	0.00790
	Close Approach Coast	74.063	--	--	
	Iris Circularization Burn	1.206	20	1996	0.02705
Summary	Weighted Average	1264.198 (3.461 yr)	35.04	2090.78	13.7805

Table 6. Mission Segment Overview

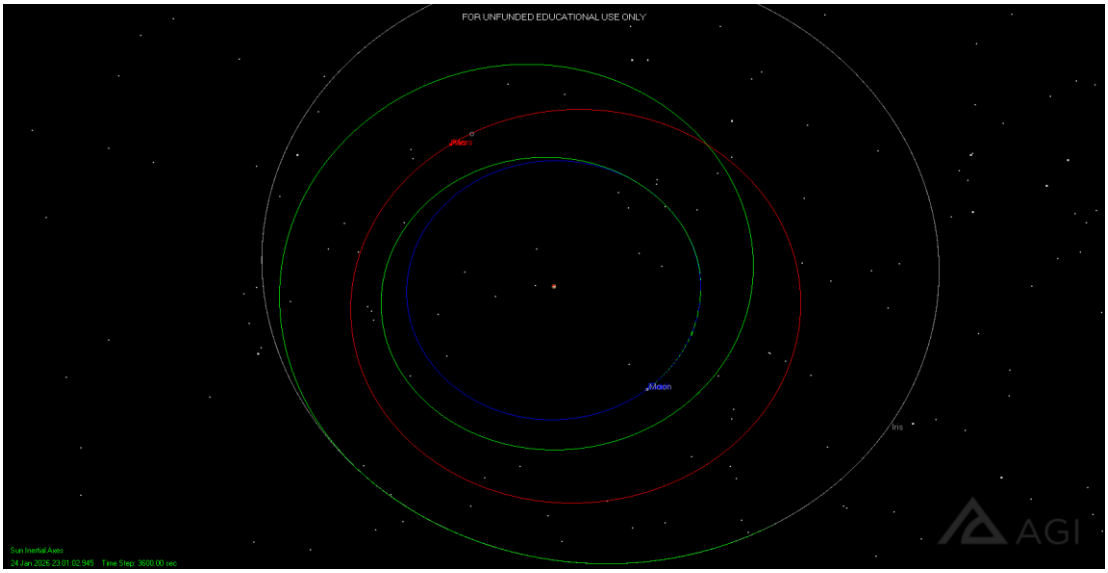

Figure 51. MAPLE SIRUP Orbit Track Top View

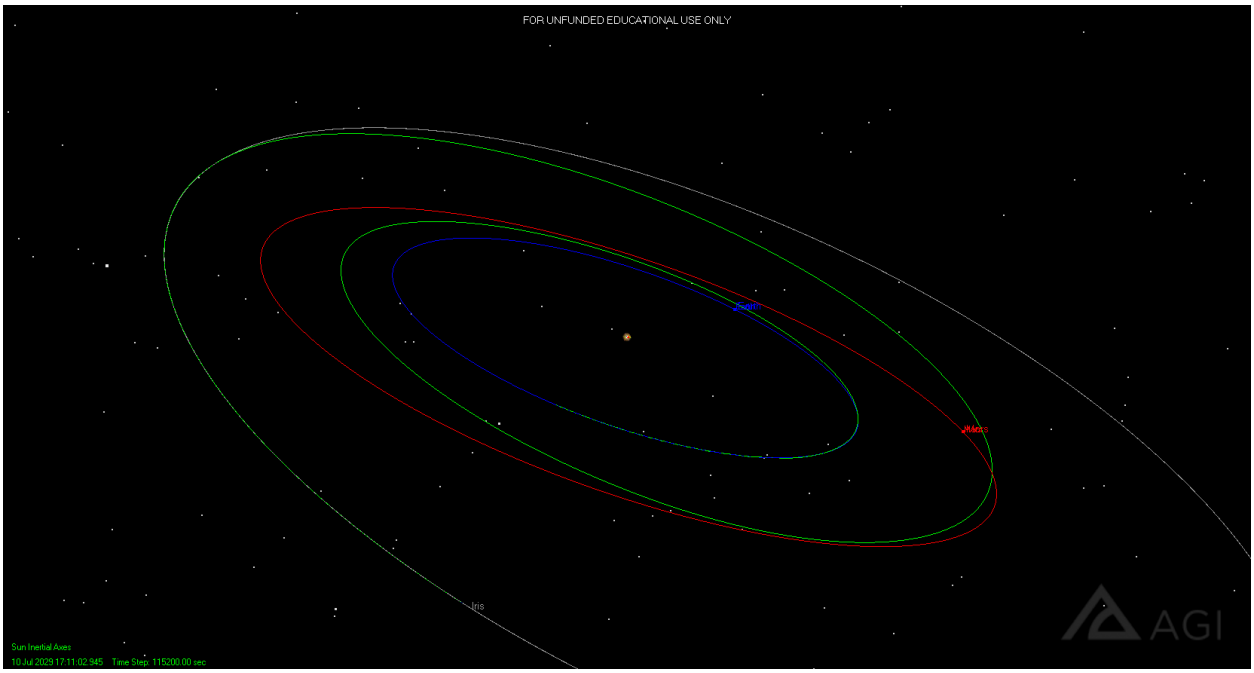

Figure 53. MAPLE SIRUP Orbit Track Side View

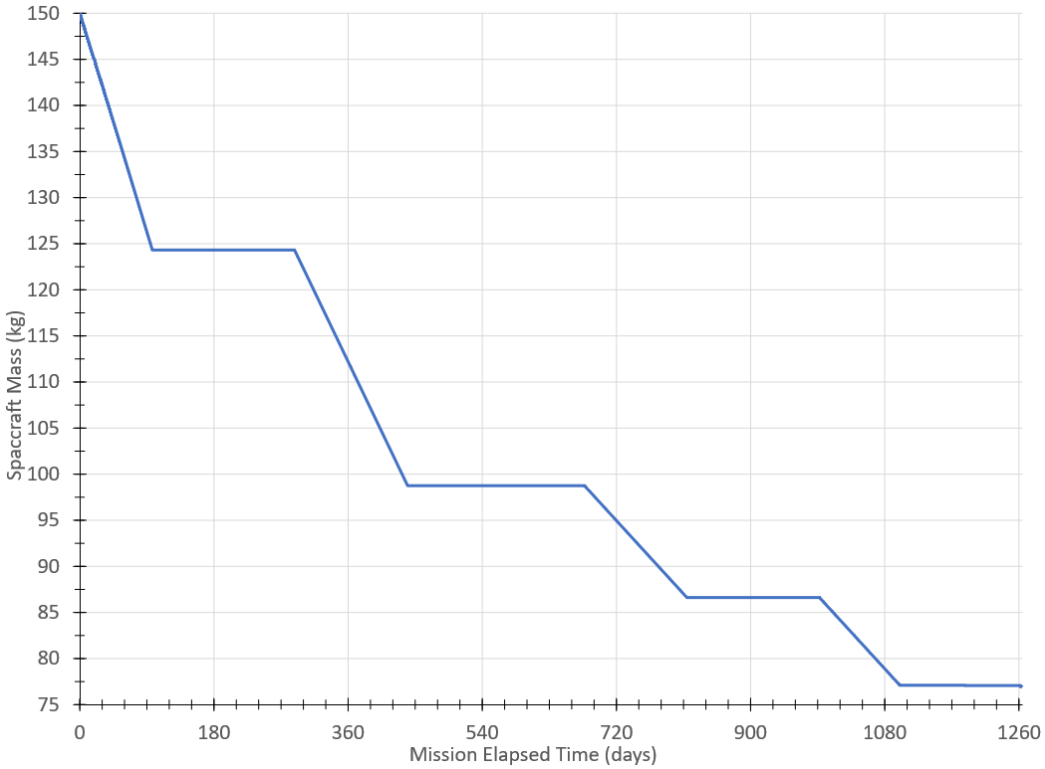

Figure 52. Spacecraft Mass over Time

4.4.1 Earth Departure

The initial geocentric phase of this mission is critical as we do not have access to a dedicated launch vehicle due to the size of the spacecraft. Therefore, a rideshare option that maximizes initial orbital energy is desired to reduce the penalty of not being able to be delivered directly to an Earth escape trajectory. MAXAR Space Infrastructure (MSI), formally Space Systems Loral (SSL), offers the ability to deliver up 90 kg, or even 150 kg, to geostationary orbit [55] with a relatively consistent frequency. The SSL 1300 host spacecraft can be launched on SpaceX Falcon 9s, as detailed in Section 3 [28] . Beginning the mission from near geostationary, at an altitude of 35,976 km, reduces the time and fuel needed to escape to a heliocentric Iris transfer orbit thereby freeing up mass for other subsystems. MAPLE SIRUP's launch date and true anomaly are sensitive to disturbances, so it will likely be launched several months before its mission begins to begin thrusting on time. The mission is set to begin on January 24th, 2026 just before 10:20 pm UTC, after which all three thrusters will burn along the velocity vector for just under 97.5 days, ending at approximately 3.6 million km from Earth or four times Earth's Sphere of Influence, depicted on Figure 54. This is the only time during flight all three thrusters can be active simultaneously. After this burn is a 191-day coast period, taking MAPLE SIRUP halfway to the orbit of Mars in preparation for its deep-space operations.

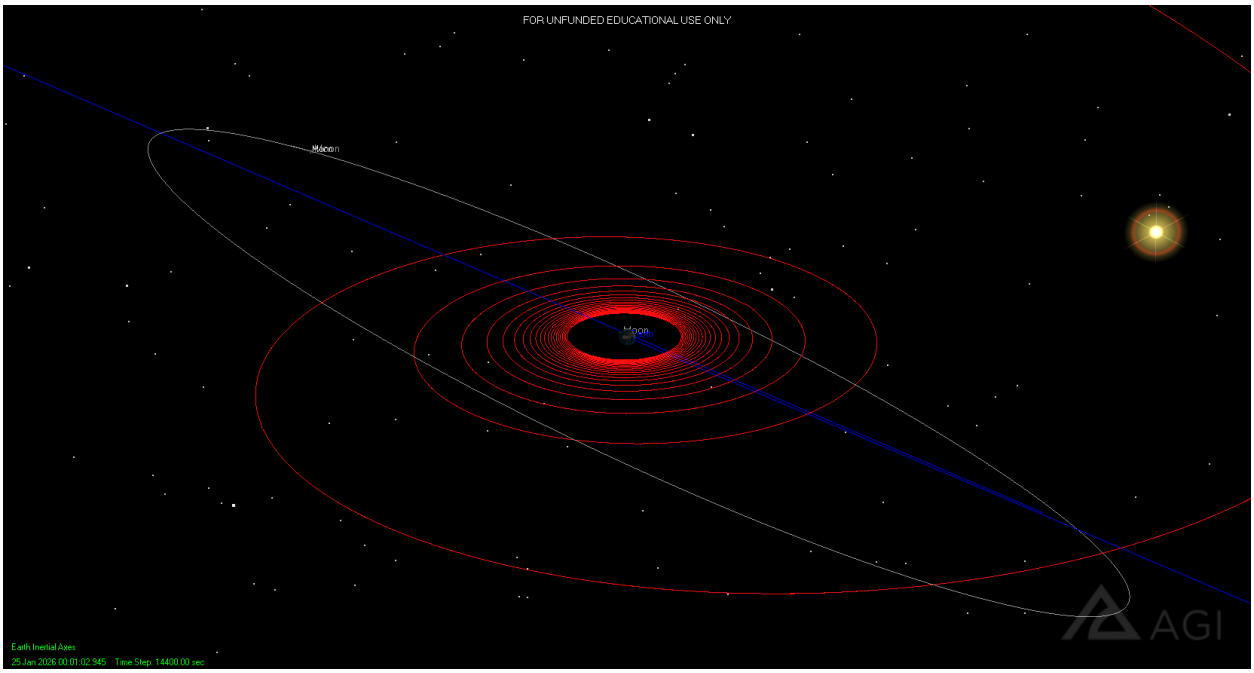

Figure 54. Earth Departure Spiral Out

4.4.2 Deep Space Operations

The deep-space operations of MAPLE SIRUP consist of two burns and two coast periods. Even though MAPLE SIRUP's thrust is very low, thrusting is not required for the entire mission, requiring coast periods. The first midcourse burn segment is positioned near the aphelion of the Earth Departure Coast and lasts for 151.5 days using the outer pair of thrusters. The initial thruster vector is -37.7° out of the plane with an increase of -0.01°/day, ending at -39.2°, now to orient MAPLE SIRUP towards Iris, which is at a 5.5° inclination. It would be slightly more efficient to increase the inclination farther out in the trajectory as the velocity would be lower, however, the maneuver must be performed here to match planes. The angular magnitude increases over time as the spacecraft moves slightly farther away from the sun over the course of the burn. Following this burn is a 237-day coast where the spacecraft travels half an orbit ending past the orbit of Mars and setting up the second burn near an apsis point for efficiency. This second apogee raise burn lasts for 137.5 days with a significantly reduced inclination change of

-0.6° out of the plane and uses only the central thruster. This burn positions MAPLE SIRUP to rendezvous with Iris near its perihelion to maximize the available solar power and optimize the capture burn. After this burn, there is a final 179-day coast catching up to Iris.

4.4.3 Near Iris Operations

The objective of the 7 Iris orbit is to have a periapsis altitude below 500 km to support the selected payload. Determination of this limit was reached in collaboration with the payload team to balance required fuel and sensor capability.

Following the aforementioned coast period is a 108 day burn away from 7 Iris using the central thruster to slow down. 7 Iris' low gravity of .08 m/s^2 [56] requires the spacecraft to expend significant amounts of propellant to catch up as minimum attractive force is exerted on the spacecraft. This catch-up burn almost syncs MAPLE SIRUP up with the orbit of 7 Iris, but final correction burns must be performed after a coast of 87 days. The capture burn is a series of two burns, one of which cancels relative velocity and sets MAPLE SIRUP on a near-impact free-fall trajectory and the second finalizes the capture into an 82 km x 332.1 km orbit normal to its sun vector with a period of 18.86 hrs, well inside the envelope determined by the payload sensors.

These three segments last approximately 0.35 days, 74 days, and 1.2 days respectively. MAPLE SIRUP arrives in its final orbit just before 18:30 UTC on July $9^{th,}$ 2029, and is anticipated to stay there for at least 180 days however no life-limiting systems have been identified thus far. Iris's aphelion is almost 3 AU, so power, thermal, and communications issues may arise near that point, but capture occurs near 7 Iris' perihelion for fuel savings so these issues are unlikely to manifest rapidly.

5 Power

The role of the power subsystem is to make sure sufficient power is available for the spacecraft to carry out its intended functions. Due to the length of this mission, Solar Array degradation and end-of-life power are significant and will be considered when selecting the components for this subsystem. This section discusses the design and analysis for the power subsystem of MAPLE SIRUP. Which includes hardware selection and power generation, storage, and consumption analysis.

5.1 Power Overview

On a spacecraft, power is one of the most important subsystems and is tasked with generating, storing, distributing, and conditioning power. To effectively accomplish these tasks, the proper hardware must be selected. This hardware can be divided into multiple categories: solar arrays and solar cells, electrical power systems, and batteries. Solar arrays and solar cells are responsible for generating power on the spacecraft by converting solar flux into usable power. The electrical power system is responsible for the distribution and conditioning of power. Batteries are responsible for storing the power generated by the solar arrays and supplying power to the spacecraft during an eclipse or provide supplemental power when demand exceeds supply.

Figure 55 below shows the components of the Colony-1 bus and examples of hardware that can be used for the power subsystem of a spacecraft are shown. Such as Triple-Junction solar cells, Lithium-Ion Polymer batteries, and a 3U electrical power system. The reason for this figure is because the Colony-1 is a small satellite, therefore there will be similarities between the hardware on the Colony-1 and the hardware on MAPLE SIRUP due to its size limitations.

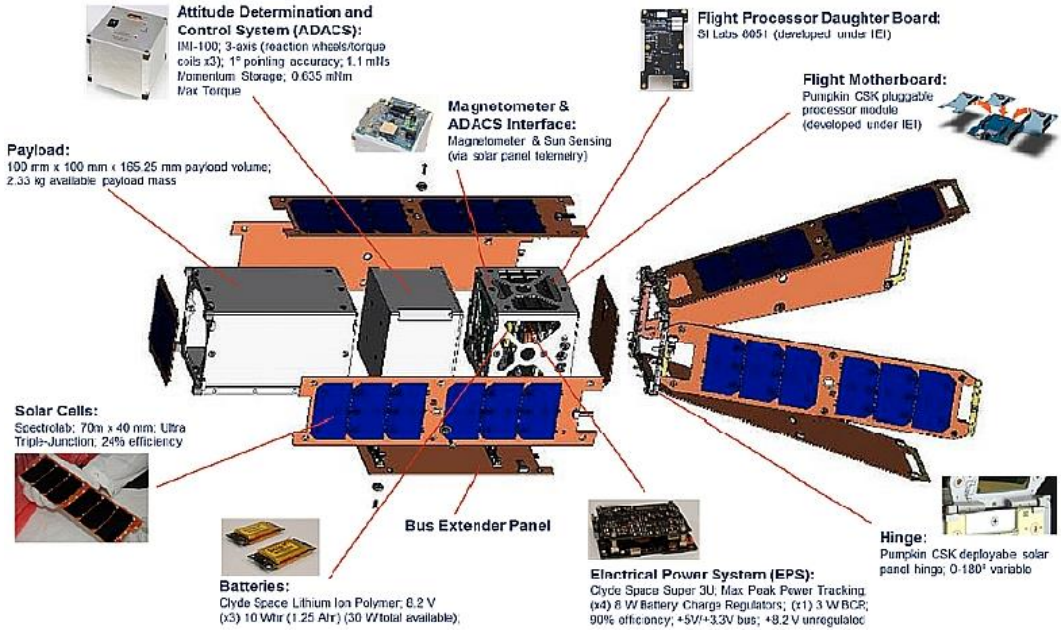

Figure 55. Components of the Colony-1 b=Bus [107]

5.2 Power Budget

A power budget is a list of all the power requirements for each component of a spacecraft and is an important tool for the power subsystem because it allows for the subsystem to properly accommodate and keep track of the power needs of each component in the spacecraft. This is especially true for SmallSats, because of their smaller size a SmallSat cannot produce and store as much power as other spacecraft. With a power budget, it can be determined whether certain components are feasible for the spacecraft given its limitations. Below in Table 7, the power budget for MAPLE SIRUP is shown. This table gives detail on the power needs for each component such as power required, operating voltage, and current required.

Subteam	Component	Manufacturer	Power (W)	Operating Voltage (V)	Current (A)
Propulsion	BHT-200	BUSEK	370	8-13.0	-
	BHC-1500	BUSEK	7.5	-	-
	Feed Lines	-	8	-	-
	Allite AE81	Allite Inc.	18	-	-
	PPU	-	15	-	-
Instrumentation	TriScape100 Imager	Simera Sense	5.5	5	-
	Argus 1000 Infrared Spectrometer	Thoth Technology	1.47	5	-
	FiberTek 2U CubeSat Lidar	Fibertek	14.3	3	-
	Flat Plasma Spectrometer	-	3	2.5	-
ADCS	Sputnix SXC-FW4-02	Sputnix	2	4-15.0	-
	Marotta MicroThrusters	Marotta	28	2.5	-
	Sagitta Star Tracker	arcsec	2	5	0.16
	NewSpace Fine Sun Sensor	NewSpace	0.05	5	0.01
	Space Micro Coarse Sun Sensor	Space Micro	0	-	0.0035
	Analog Devices Digital Gyroscope	Analog Devices	0.042	5	0.008
TCDH	IRIS DST	NASA	35	9-28.0	-
	Custom Patch Antenna	-	0	-	-
	KRYTEN-M3	Clyde Space	1	3.3	-
Power	ISIS Modular EPS	CubeSatShop	0.2	8-16.0	3
	ISIS Power Battery Pack	CubeSatShop	-	8-16.0	-
	rHawk Solar Array	MMADesign	-	-	-

Table 7. Power Budget of the Spacecraft

5.3 Hardware Selection

Selecting the proper hardware is a critical step in ensuring the power subsystem fulfills all of the needs of the spacecraft. To find the best hardware, there are many important factors to consider which will be discussed below.

5.3.1 Solar Arrays

Solar Arrays are responsible for generating power, this is accomplished through the use of solar cells which can convert sunlight into usable power. These solar cells collect flux given off from the sun and based on the efficiency of the cell more or less power is generated using the available flux. There is some variety in the solar cells used in a solar array based on the task that the array needs to accomplish. For arrays used in spaceflight, typical photovoltaic cells used are Triple Junction Gallium Arsenide cells. The reason these cells are so effective for spaceflight is because of their strong low light performance, their UV and radiation resistance, their high efficiency, and their relatively low mass. There are other types of cells such as silicon single junction, however, these cells are not as well suited for spaceflight because of their efficiency. Compared to multi-junction cells the efficiency of single-junction cells is lower. This is a problem because in spaceflight to generate as much power as a multi-junction cell a single-junction cell would need to have a greater area, which usually results in a greater mass making them less ideal for spaceflight.

When using solar cells there are many important factors to consider for the best power generation such as the distance from the Sun. The distance from the Sun changes the amount of flux available for the cells to absorb. To determine how much flux will be available at the spacecraft the following equation can be used:

$$q_{sol} = \frac{1367}{Dist\ to\ Sun^2} \tag{5.1}$$

In the Figure below, the graph shows that the solar flux at the spacecraft decreases exponentially as the distance from the Sun increases. Therefore, efficient solar cells are valuable because they can generate more power than other less efficient panels with the same amount of flux.

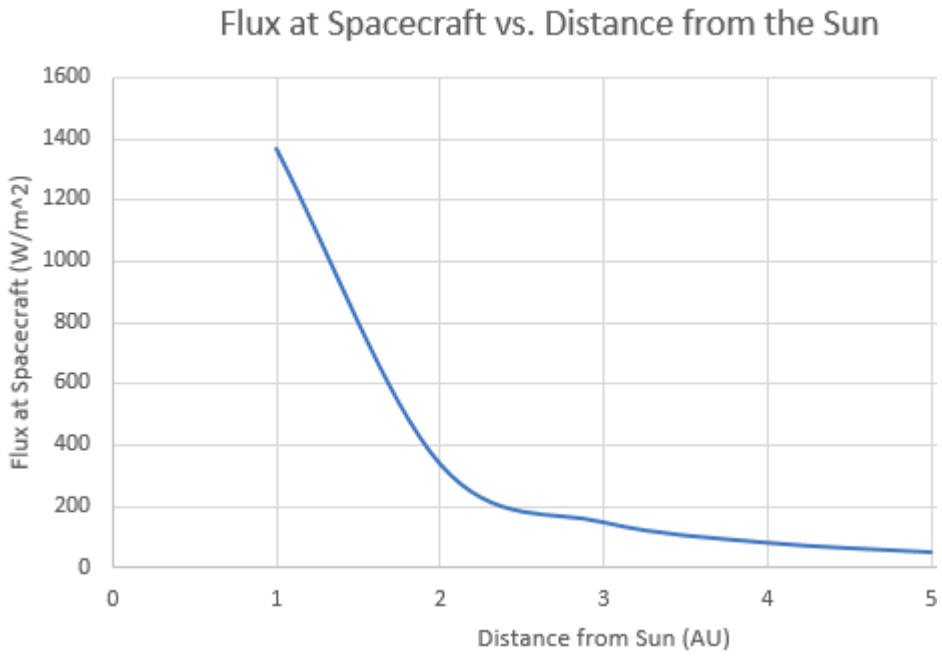

Figure 56. Graph of flux at Spacecraft vs. Distance from the Sun

Other important factors to consider for optimum power generation are the Solar Array size and the temperature. Solar Array size is important because the greater the area of the Solar Array the more power that can be generated. To determine the optimum solar array size the power required, and the array power output needs to be considered. The ideal array size can be determined using the following equations

$$P_0 = q_{sol} * n \tag{5.2}$$

$$P_{BOL} = P_0 * Id * \cos(\theta) \tag{5.3}$$

$$Ld = (1 - Yd)^{t_m} \tag{5.4}$$

$$P_{EOL} = P_{BOL} * Ld \tag{5.5}$$

$$A_{sa} = \frac{P_{sa}}{P_{EOL}} \tag{5.6}$$

Po: Ideal power output

qsol: Solar flux

n: Cell production efficiency

PBOL: Beginning of life power production capability per unit area

Id: Inherent degradation

Ld: Lifetime degradation

Yd: Annual environmental degradation rate

tm: Mission lifetime

PEOL: End of life power production capability per unit area

Asa: Area of solar array

Using the ideal power output, you can determine the power that your solar panel needs to generate at the end of the mission which can then be used to determine the area the solar array needs to be to supply enough power for the entire mission. This also relates to the distance from the sun, because the greater the distance from the Sun the lower the ideal power output will become, making a larger solar array required.

Temperature is important to consider when trying to optimize power generated with a solar array because the temperature can affect the efficiency of the solar array. For instance, solar cells are more efficient at lower temperatures making proper thermal control a necessity. Another

factor that needs to be considered is the peak power point of the solar array. The peak power point is the point at which the array current and voltage are optimized for maximum power generation.

Throughout the mission, the distance to the sun and the temperature will vary, meaning that throughout the mission the power generated by the solar array will vary as well. Another factor that will affect the amount of power generated by the solar array is the degradation of the array. Over time the solar array will lose effectiveness due to degradation causing the power generated to decrease over time, resulting in the end of life (EOL) power generation to be lower than the ideal power generation. There will also be times when the spacecraft is in eclipse, meaning that power generation with solar arrays is not possible. Therefore, when selecting a solar array, one must account for these fluctuations to ensure that the spacecraft continues to get the necessary power.

5.3.2 Electrical Power Systems

An electrical power system board monitors and controls the entirety of the power subsystem and contains power distribution and conditioning modules. A power distribution module allows the electrical power system to take power from a single source, in this case, the Solar Array, and distribute the power to multiple components. A power conditioning module allows the electrical power system to ensure that the power being supplied to each part of the spacecraft has the proper current and voltage for that component. The electrical power system also monitors and maintains all the hardware connected to the power system to ensure the best performance of each component.

Looking at the figure below, the way in which an EPS functions can be seen. First, power is taken in from the solar array and conditioned using the power conditioning module. Then the power goes to the battery unit, where excess power is stored, and then distributed via the power distribution unit and sent to the components.

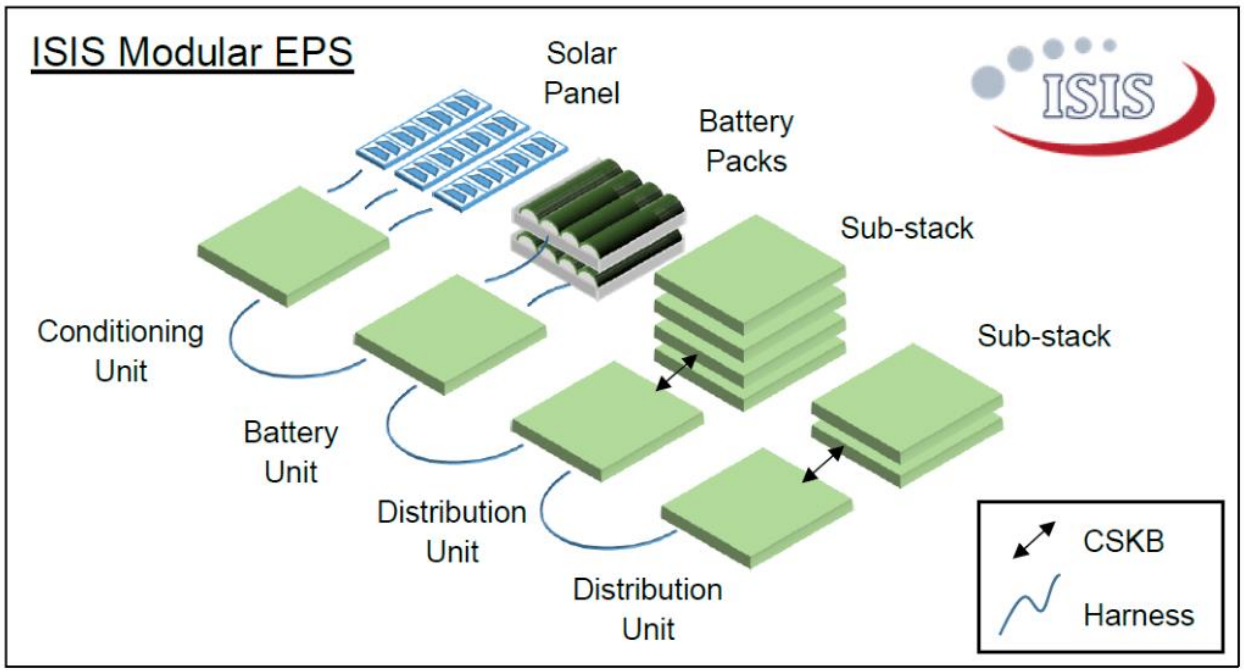

Figure 57. Configuration of the ISIS Modular EPS [58]

5.3.3 Batteries

Power storage is essential for keeping a spacecraft operational when it is not able to generate power, or the power being generated is not enough to meet the spacecraft's needs. Power storage is performed using batteries such as Lithium-Ion batteries. Lithium-Ion batteries are typically used for CubeSats because they have a large energy capacity for their size due to the high energy density of these batteries. An important factor to be aware of when it comes to batteries is their temperature. Many batteries will experience a drop in efficiency or instability when the temperature becomes too extreme. To avoid this thermal controls will need to be put in place to monitor the batteries on the spacecraft.

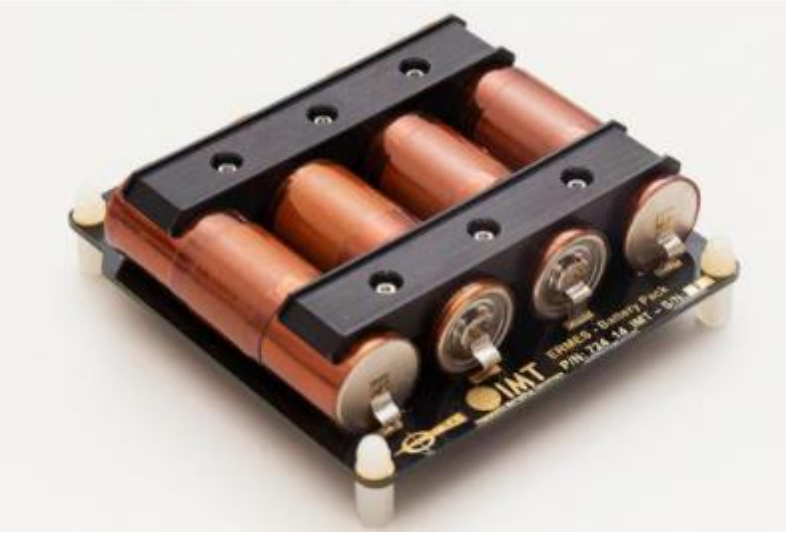

Figure 58. Example of Lithium-Ion Battery Pack [108]

When selecting batteries for a spacecraft there are many important factors to consider. These factors include the power required during an eclipse, battery efficiency, battery capacity, and battery mass.

The power required during an eclipse is one of the most essential factors to consider when selecting which type of battery to use. This is because when the spacecraft is not in an eclipse, power will constantly be generated by the solar array so the batteries will not be needed. Also, the battery capacity needed is directly tied to the power required during an eclipse as seen in the equation below:

$$Cr = \frac{P_E t_E}{DOD * Nn} \tag{5.7}$$

This equation uses the time in eclipse (t_E), the number of batteries (n), the depth of discharge (DOD), and the efficiency of the batteries (N).

Once you know the battery capacity needed it is important to calculate the mass of the batteries needed to store that much power. The greater the mass of the batteries the greater the final mass of the spacecraft which will put more stress on the propulsion subsystem. Using the

specific energy density of the batteries and the capacity, the mass of batteries required can be determined using the following formula

$$m_b = \frac{Cr}{E} \tag{5.8}$$

Where Cr is the battery capacity and E is the specific energy density. Once the battery mass required is determined the number of batteries needed to reach that mass can be determined simply by dividing the required mass by the mass of each battery.

5.4 Power Subsystem Analysis

To begin evaluating the power subsystem the most important part is to determine the power required by every component on the spacecraft. To accomplish this each sub-team listed their components with their power requirements, these were then grouped by sub-team and made into a master power list, shown in Figure 59. Using this list, it is possible to determine the power

needs of each sub-team. It also gives the team the ability to evaluate whether their components are feasible based on their components' power requirements.

Subsystem	Basic Power		PGA		Predicted Power	
Electronics	36	W	35	%	48.6	W
Structure		W	25	%	0	W
Thermal Control		W	50	%	0	W
Propulsion	231	W	81.2	%	418.5	W
Batteries		W	25	%	0	W
Wire Harnesses		W	100	%	0	W
Solar Array		W	35	%	0	W
Hardware		W	35	%	0	W
Mechanisms		W	25	%	0	W
Instrumentation	24.77	W	75	%	43.3475	W
ADCS	32.092	W	0	%	32.092	W
Total	323.862	W			542.5395	W

Figure 59. Master Power List

The next step that needs to be taken to evaluate the power subsystem is determining the amount of power that is generated using the solar arrays on the spacecraft at the end of life. This is completed using the following equation:

$$P_{EOL} = n * q_{sol} * Id * \cos(\theta) * Ld \tag{5.9}$$

In this equation the power production capabilities of the solar arrays at the end of the mission life are determined. This is done using the cell production efficiency (n), the solar flux (q_{sol}), the cosine loss angle (θ), the inherent degradation (Id), and the lifetime degradation (Ld). By determining the end-of-life power production capabilities of the solar array we can determine if the spacecraft is generating enough power to meet the spacecraft's requirements when out at

IRIS. If it is not generating enough then we can use the result from this equation to determine what size the solar array needs to be based on the power needs of the other subsystems.

5.4.1 Final Hardware Configuration

The hardware that composed that SmallSats power subsystem was continuously iterated upon throughout the design process. Final components were selected only after a thorough analysis of the capabilities and performance of the available hardware based on the needs of the mission.

The Solar Array selected for this mission was the rHawk Solar Array developed by MMA Design [57]. This Solar Array features triple junction (ZJT) InGaP/InGaAs/Ge Solar Cells with an efficiency of 29.5% at 29C. The main reasons this Array was selected were the stowed envelope, its scalability, and its ability to articulate. The Array has a stowed envelope of the Array is 19'' x 14'' x 9'' for each wing. An envelope of this size allowed for the spacecraft to fit comfortably within the launch vehicle, which had 1m x 0.5m x 0.5m available space, resulting in a margin of 0.05m on the closest dimension. The scalability of the solar array was important because it allowed for the Array to be sized precisely for the spacecraft's power needs. The Solar Array having the ability to articulate was necessary as it allowed for the panels to always be properly oriented towards the sun for the greatest efficiency and put less pressure on the ADCS system for sun pointing.

To store excess power generated by the Solar Array the ISIS Power Battery Pack was selected [58]. This battery pack is Lithium-Ion and consists of 4 cells in series with a storage capacity of 45Wh per pack. The reason this pack was selected was due to its high storage capacity per unit mass, giving 45Whr at only 252.0g, as well as the fact that it was designed to be used with the EPS selected for this mission and is easily scalable.

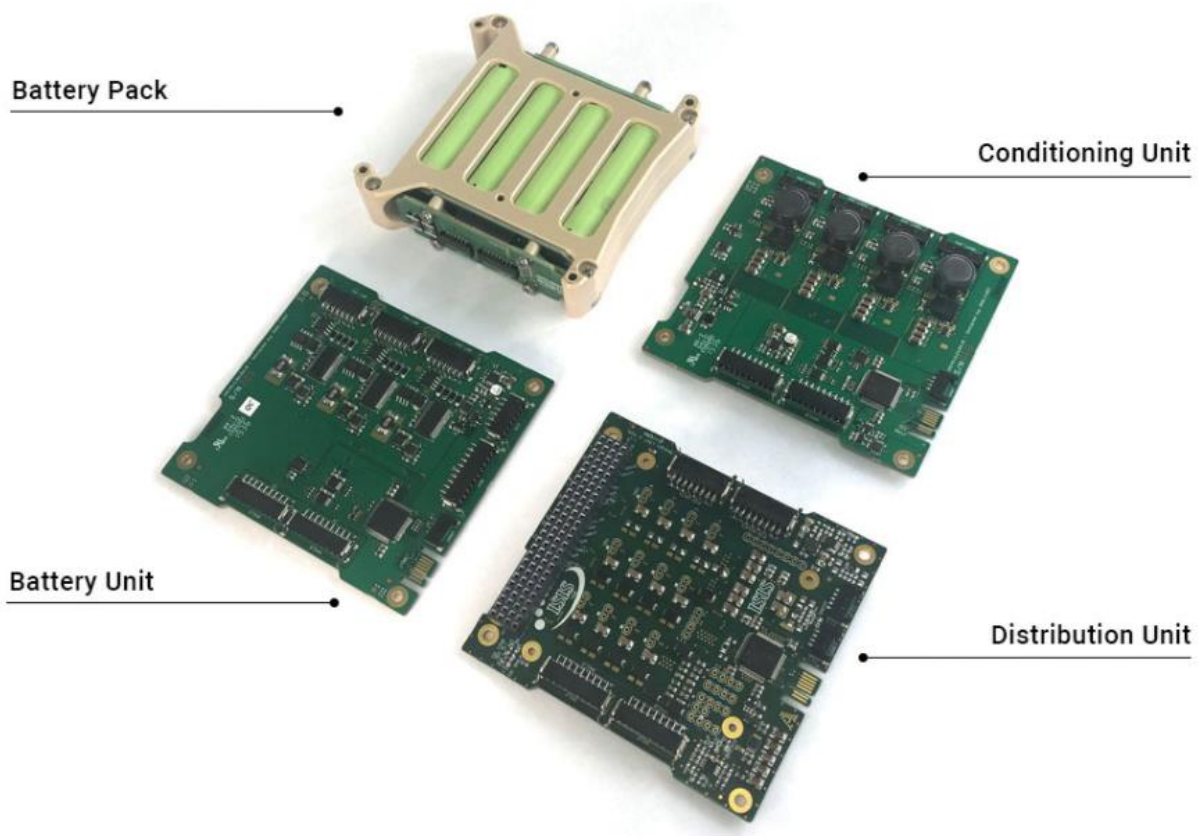

Figure 60. ISIS Modular Electrical Power System [58]

The EPS that was chosen for this mission was the ISIS Modular Electrical Power System [58]. This EPS has over-current protection and contains power conditioning, distribution, and battery units. Giving the EPS the ability to control power conditioning and distribution. With the ability to perform hardware-based maximum power point tracking. The power conditioning unit of this electrical power system has four MPPT channels and a maximum input current of 3A for each of these channels. The conditioning unit also has a maximum power input of 39W in each channel with an output voltage of 16V. The power distribution unit has 8 switchable voltage lines, 3 switchable and 1 permanent battery voltage lines, and features a maximum current in each of the lines of 3A. The Battery unit is capable of heating and balancing the battery and has a max input power of 25.6W with a max output power of 64W both at 16V. Connected to the

battery unit will be the battery packs which feature Lithium-Ion at an operating voltage of 8V-16V with a capacity of 45Wh [58].

5.5 Power Subsystem Results

STK simulations and a dynamic power model in Excel workbooks were used to ensure that the selected hardware would be able to perform as hand calculations had predicted. The STK simulations were used to analyze the distance of the spacecraft from the sun and its orbital trajectory. While the Excel workbooks were used to model the solar intensity, the power generated by the solar panels, the power consumed by each subsystem, and the stored power.

5.5.1 STK Simulations

A model of the spacecraft and its orbital trajectory was created using STK, shown in Figure 51. Using this, key data was able to be simulated: the distance between the sun and spacecraft

throughout the mission, Figure 61. This data was generated using the report and graph manager and then was exported into excel.

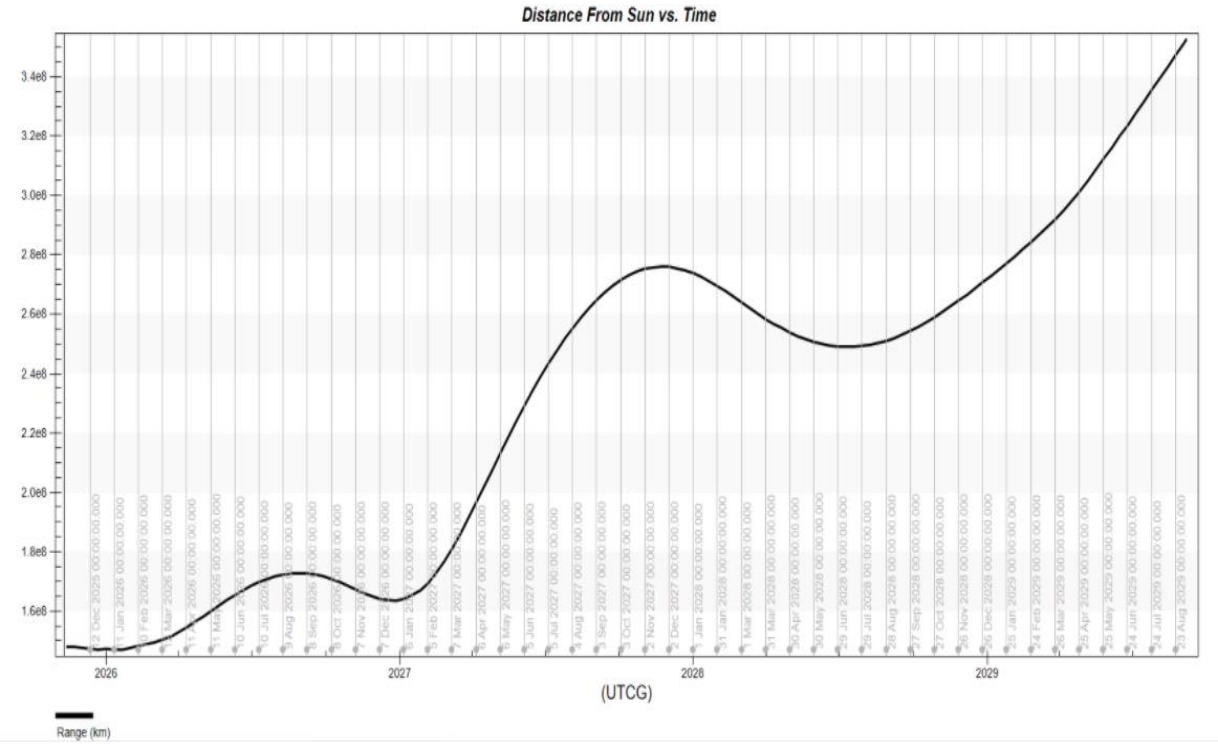

Figure 61. Distance from Sun vs. Time Graph

5.5.2 Excel Data

Using an Excel workbook models of the solar intensity, the power generated by the solar array, the battery charge, and the power consumed by each subsystem over time were created. The solar intensity and power generation models were created using the distance from sun data that was imported from STK by modifying the data using the equations seen in 5.3.1. The other

models were created by inputting the power consumed/stored next to the day in which that data occurred for the entire mission lifetime.

5.5.2.1 Solar Array Power Generation

This graph in Figure 64. Power Output vs. Time Graph shows the solar power generated throughout the entire mission. This graph is based on the rHawk Solar Array with an area of 6.4m and an efficiency of 29.5%. The goal of the Solar Array was to be able to provide approximately 380W when the spacecraft is near Iris and, based on the STK simulation, this goal was reached with the spacecraft capable of generating 375W at the end of the mission. This result is corroborated when examining the solar intensity graph in Figure 63. As you can see solar intensity follows a similar curve when compared to power generation, that is because both solar intensity and the power generated by the Solar Array are directly related. When looking at the graph it shows that at Iris the solar intensity is around 285 W/m^2. With that amount of intensity, a Solar Array with an area of 6.4m can be expected to generate roughly 380W of power further corroborating the results from Figure 64. An important factor that needed to be considered when modeling the solar array was the degradation over time. The mission lasts close to 3.5 years and over that time the cells lost a significant amount of their power-generating capabilities, 9.3%. This degradation can be seen when comparing the ideal power generation

graph in Figure 62 with the power generation graph in Figure 64. As you can see the end of life power in Figure 64 is around 9% less than that of the EOL power in Figure 62.

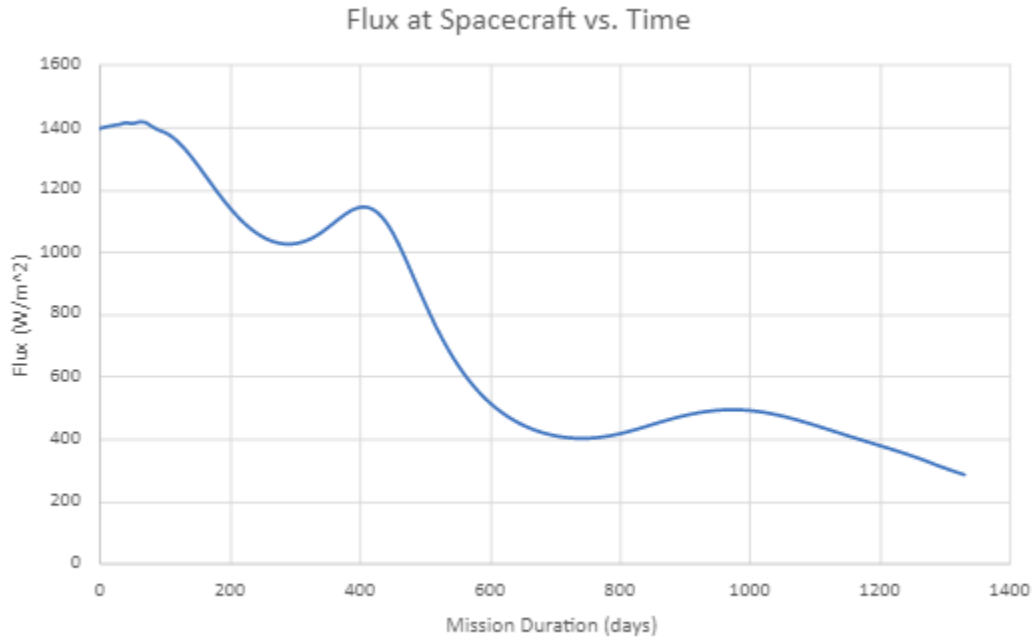

Figure 63. Flux at Spacecraft vs. Time Graph

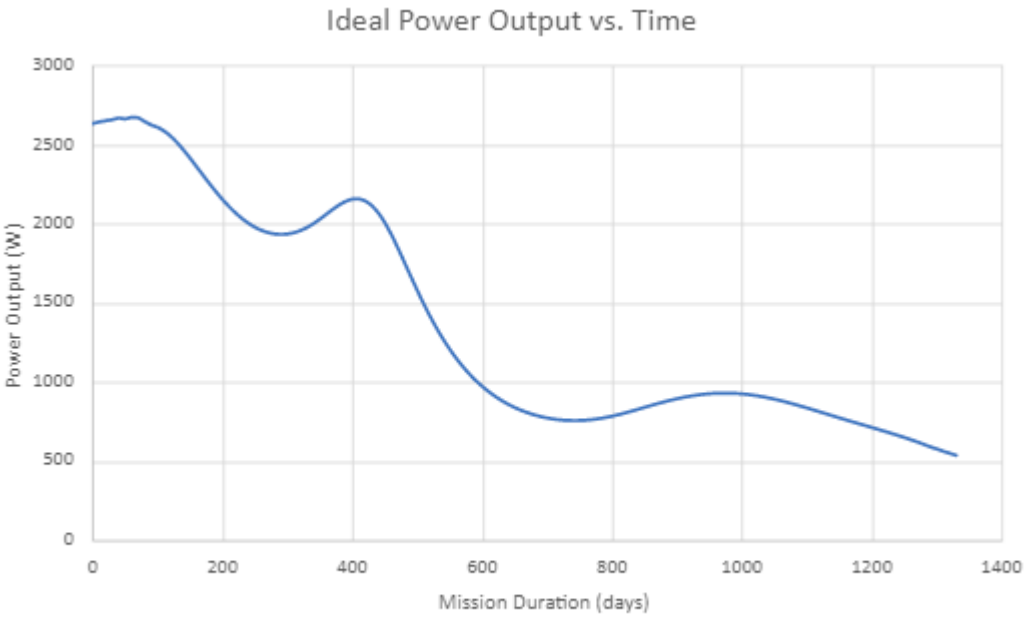

Figure 62. Ideal Power Output vs. Time Graph

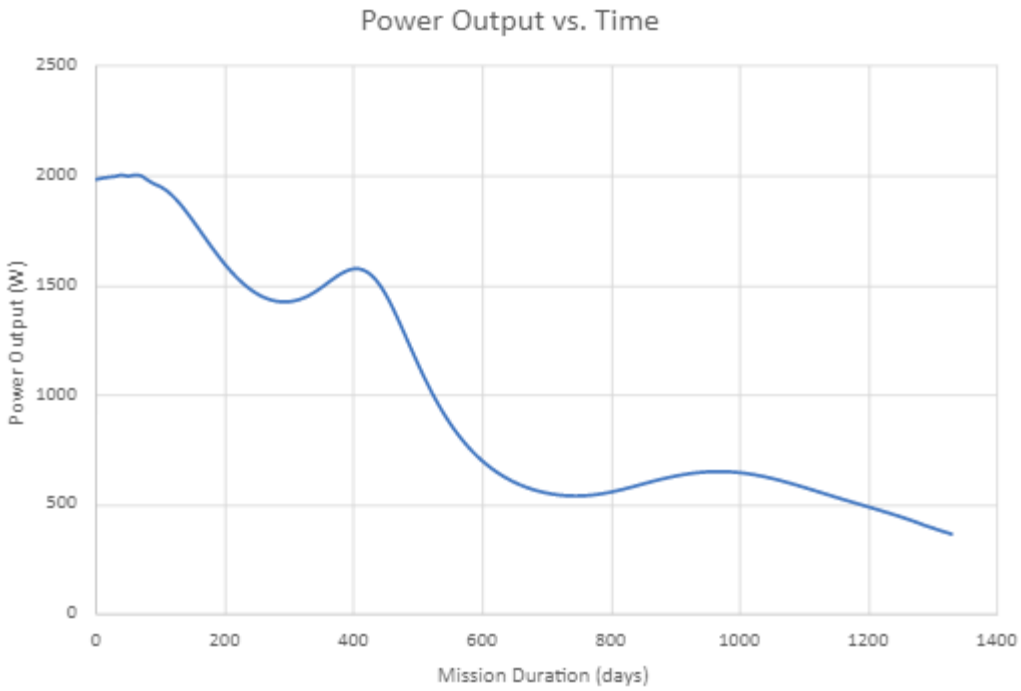

Figure 64. Power Output vs. Time Graph

5.5.2.2 Battery Charge

Looking at the graph in Figure 65 it is shown that after the initial launch there is no significant use of battery power throughout the mission. This is because the batteries were necessary to supply power to the spacecraft during the initial detumble before the Solar Array was deployed. However, after that, the Solar Arrays can handle the majority of the spacecraft's power needs. This is because there is no significant period of eclipse that the spacecraft goes through and therefore once the array is deployed there will constantly be power being generated.

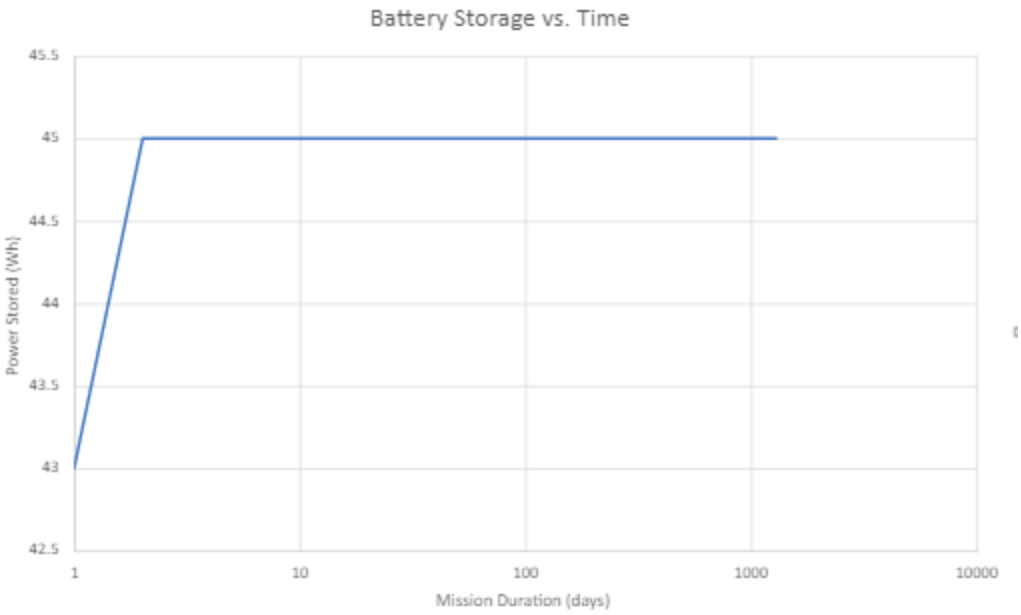

Figure 65. Battery Storage vs. Time Graph

5.5.2.3 Power Consumption

When examining the graphs of the power consumed by each subsystem in Figure 67 it is clear that the majority of the power is being consumed by the propulsion subsystem. This was expected especially since electric propulsion is being used on the spacecraft. Combining the data shown in the total power consumed graph in Figure 66 with the power generated by the Solar Array graph in Figure 64 it is clear that throughout the mission the Solar Array will generate adequate power to keep all of the subsystems running during the mission. The key moment to look at is when the spacecraft is near Iris at the end of the mission, this is when the spacecraft will be the furthest from the sun and therefore will generate the least power. The power needed at this time is roughly 370W which is why the Array was sized to provide 375W at that distance. This power generation along with the power stored in the batteries will be able to meet all the spacecraft's power consumption needs.

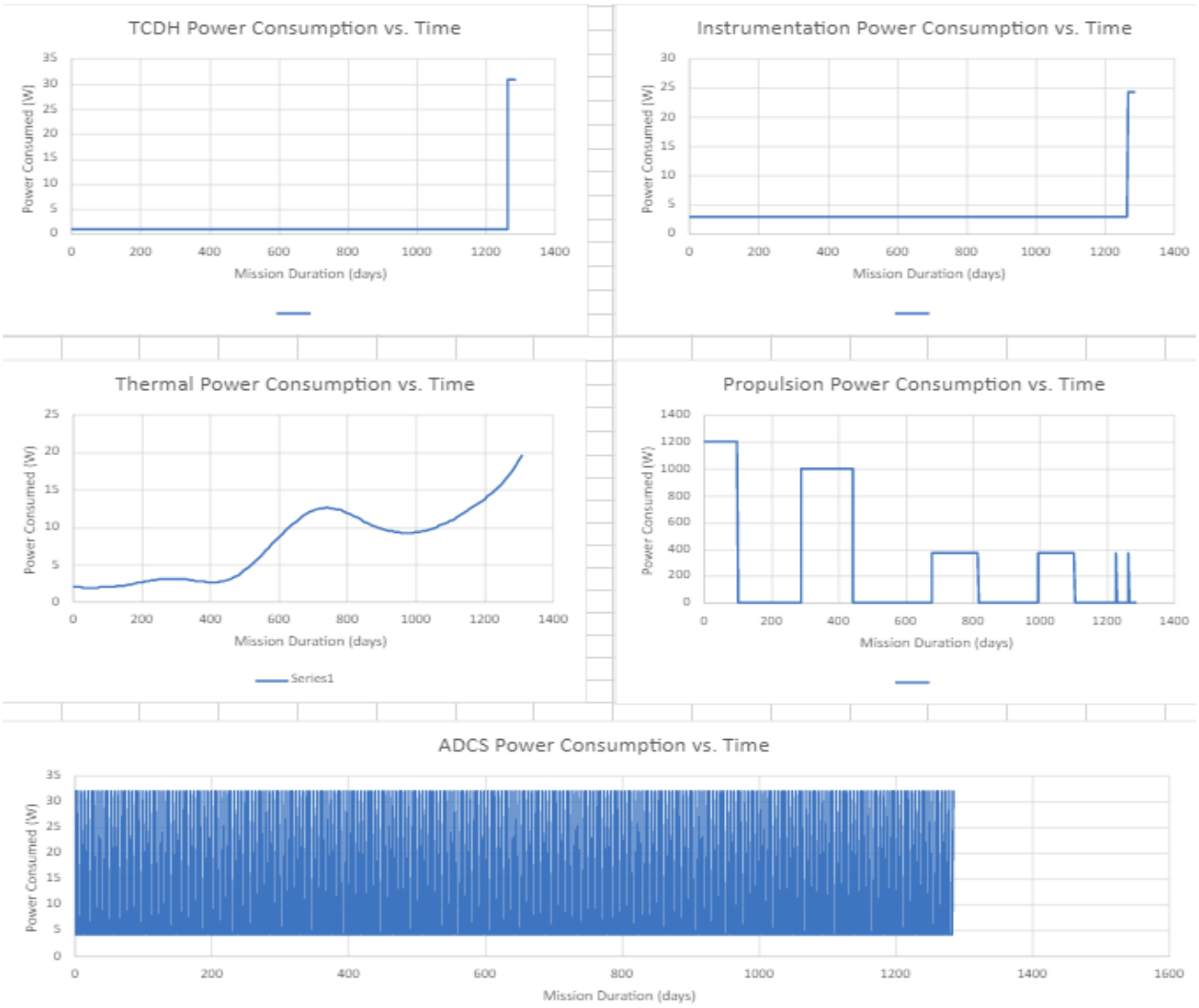

Figure 67.Power Consumed by Each Subsystem vs. Time Graphs

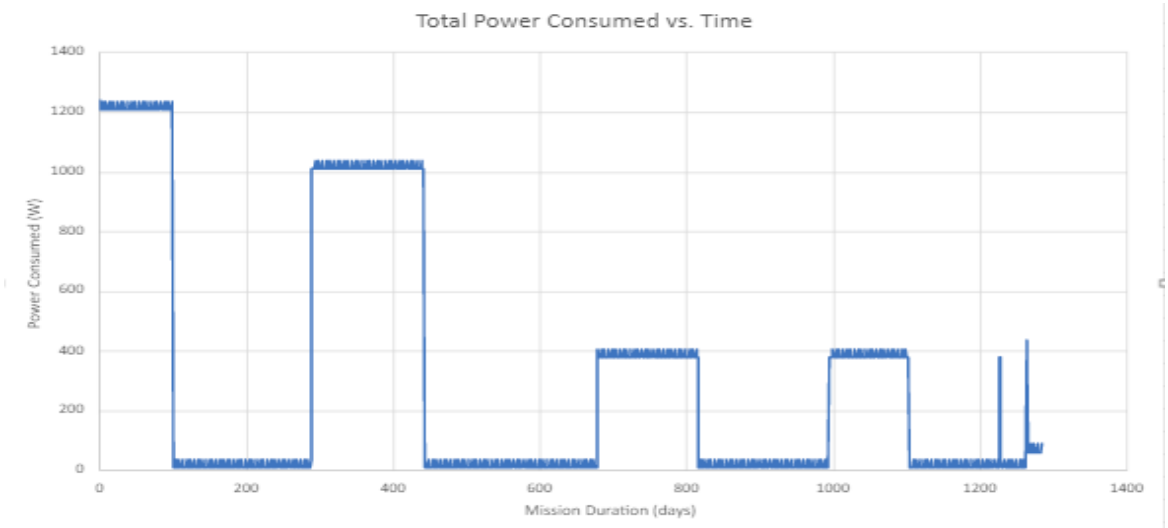

Figure 66. Total Power Consumed vs. Time Graph

6 Command and Data Handling

The command and data handling (CDH) subsystem deals with all communications to and from a ground station on Earth. It consists of an on-board computer with flight software, a radio transceiver, and an antenna. Ground stations must be considered when designing a CDH subsystem, as they must be compatible with the radio frequency and utilize an antenna large enough to receive the spacecraft's signals. This section describes the components chosen for the CDH subsystem on MAPLE SIRUP and presents preliminary calculations and simulations of the spacecraft's connection to ground stations.

6.1 On-Board Computer

The on-board computer (OBC) can be thought of as the brain of the spacecraft [59]. Any information passed between systems or to and from the ground stations will be processed by the OBC. Flight software must be installed on the OBC for it to function. Some examples of flight software include FreeRTOS, core Flight System, and KubOS. A previous CubeSat design MQP at WPI used the Kryten-M3 OBC from Clyde Space and the FreeRTOS flight software [60].

For MAPLE SIRUP, the same Kryten-M3 OBC was chosen. It is one of the lightest and most power-efficient OBCs. In addition, its wide temperature range is ideal for tolerating deep space. Figure 68 and Figure 69 show an image of the computer and its specifications. It has various interfaces for connecting to the payload and other data-producing devices, including 17 general-purpose input-output (GPIO) pins. These are standard 3.3-volt pins that are used for communicating data between most electronics. It weighs less than a tenth of a kilogram and never draws more than one watt [61].

Figure 68. Image of the Kryten-M3 OBC [61]

General	
Design Life	5 years in LEO
Processor	Smart Fusion 2 SoC including an ARM Cortex-M3 processor delivering 62.5 DMIPS
Processor Clock	50 MHz
SCET	Real time counter (w/40mins. Backup Power)
MRAM	8 MB
Operating Temperature Range	-40°C to +80°C
Boot Image Storage	256 kB eNVM + 8MB MRAM
Radiation (TiD)	20 kRAD
Typical Energy Usage	6.4 mJ/DM
GPS (PLUS model only)	<10m RMS position accuracy <1m/s RMS velocity accuracy

Interfaces		
I2C		2
SPI	7 Chip Select Lines	1
UART	3.3 V Logic	8
RS422 1	(can be used as 2xRS485)	1
CAN		1
DTMF		1
	JTAG w/ETM Support + 1 Serial	
Debugging	Debug	1
LVDS	20x Lines, Expansion	1
QSPI	(2x LVDS, 1x 3V3 Logic)	3
GPIO	3.3 V Logic	17

* Not all interfaces available simultaneously

Size, Weight & Power	
Nominal Power Consumption	400 mW (typ), 1 W max
Mass	61.9 g
Length	95.89 mm
Width	90.17 mm
Height*	5.51 mm

* Height from top PCB to lowest component

Figure 69. Specifications of the Kryten-M3 [61]

6.2 Radio

The radio is what allows the spacecraft to communicate with the ground stations. It is a multi-part component consisting of an antenna, a transmitter, and a receiver (often, the last two are combined into a transceiver) [62]. Communication happens using radio waves, typically at

and above the ultra-high frequency (UHF) range. Figure 70 shows the UHF and the higher frequency bands that satellites use for communication. S-band communication would result in low bandwidth and a low data rate. At relatively small distances like LEO or GEO, this does not cause an issue. However, most interplanetary missions utilize X-band and even K-band communication for the higher bandwidth. This offsets the large distances that the signal travels, at the cost of more power and more complex radios and antennas. Communication in the K band is possible, but still in the early phases for SmallSats and, as such, was not considered for this mission [63]. A previous CubeSat design MQP chose a transceiver and antenna from Innovative Solutions in Space (ISIS) in the S-band [5].

Figure 70. IEEE Designation of Radio Bands [63]

SmallSat and CubeSat radios and antennas are typically S-band, as these types of spacecraft rarely leave Earth orbit. This made choosing these components for MAPLE SIRUP a unique challenge. Luckily, the Jet Propulsion Laboratory in California developed a radio for SmallSats that is capable of X-band communication. Not to be confused with the mission target asteroid, the Iris Deep Space Small Satellite Radio was chosen for this mission. It weighs just above one kilogram and occupies a volume of only 500 cm^3 [64]. Figure 71 shows an image of the radio.

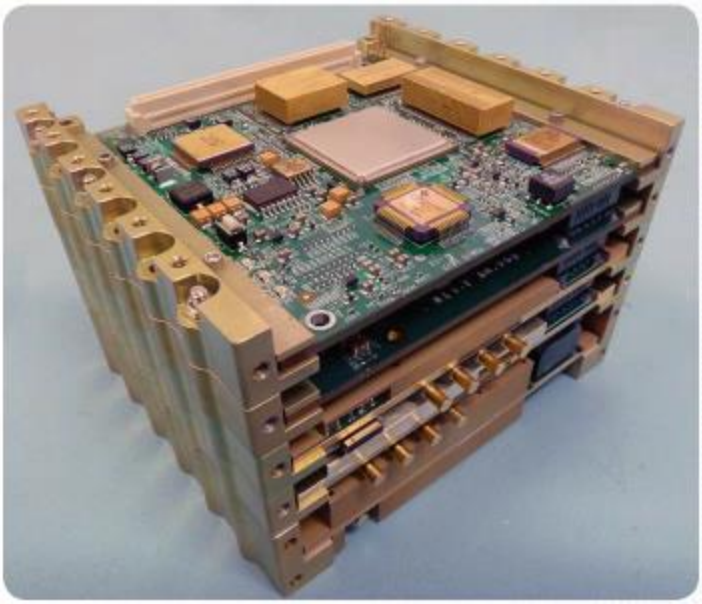

Figure 71. Image of the Iris Deep Space Small Satellite Radio [64]

When considering an antenna, standard CubeSat patch antennas offered small apertures and low gains which are not suitable for anything beyond LEO. The pioneering interplanetary CubeSats MARCO used a complex, unfolding "reflectarray" due to their low single-side surface area [65]. MAPLE SIRUP is significantly larger than the 6U MARCO CubeSat and has a maximum single-side surface area of 2,000 cm^2. A patch antenna was sized for the top-facing side of MAPLE SIRUP, allowing space at the corners for the attitude control thrusters discussed in the Attitude Determination and Control section. It is a 400 mm by 500 mm rectangle with 82 mm squares cut from each corner. It is 4.7 mm thick and weighs 1.49 kg. The aperture of this patch antenna is 0.17315 m^2. With an estimated antenna efficiency value of 0.41, the effective aperture can be calculated using Equation 6.1.

$$\mu * A = A_e \tag{6.1}$$

where μ is the efficiency and A is the actual antenna aperture. This, in turn, is used to calculate the antenna gain.

$$\frac{4\pi * A_e}{\lambda^2} = G \quad (6.2)$$

$$10 * \log_{10}(G) = G_{dBi} \quad (6.3)$$

In these equations, λ is the equivalent wavelength to the communication frequency, and G is the antenna gain. In Equation 6.2, the gain is unitless, whereas in Equation 6.3, the gain is a factor of an isometric antenna expressed on a logarithmic scale. The gain of the custom patch antenna for MAPLE SIRUP is 28.4 dBi, or 700.4.

6.3 Data and Storage

Typical spacecraft cannot be in constant communication with a ground station because of the Earth's rotation and the satellite's orbit. Even in GEO, it is difficult for spacecraft to maintain constant communication with ground stations due to several factors including position, velocity, and atmospheric inference. Because of this, spacecraft must store their data before it can be transmitted to a ground station. The amount of storage space required depends on the rate at which the spacecraft's payload or other sensors produce data, as well as the total amount of data that will be produced. The Kryten-M3 computer has 4 gigabytes of flash storage for data built-in [61]. Some payload instruments also have built-in data storage, as discussed in Section 2. Of the payload instruments on MAPLE SIRUP, the most data-producing ones are the TriScape Imager and the Lidar. The 4-gigabyte storage can hold almost 4,000 full-resolution images from the TriScape Imager, or 11 days' worth of constant Lidar readings. Also, the TriScape Imager has 128 gigabytes of built-in storage. This allows it to store about 128,000 more full-resolution images in addition to the 4-gigabyte storage in the OBC. Even with the other payload devices and health data from the other subsystems, the 4-gigabyte storage will be enough for this mission.

6.4 Ground Stations

Communications with missions into deep space are supported by NASA's Deep Space Network (DSN), as typical ground stations cannot reliably receive signals from beyond geocentric orbits. The DSN utilizes radar dishes with 70-meter diameters to track spacecraft up to 10 billion kilometers from Earth [66]. All missions that have traveled beyond lunar orbit have utilized the DSN or another similar ground station network.

As mentioned earlier, a spacecraft cannot maintain constant communication with a ground station. Typically, a satellite will budget its data production while considering the amount of time a downlink to a ground station will be available. The DSN eliminates this concern by using three ground stations, evenly spaced 120 degrees apart around the Earth, to give full coverage of the sky. To simulate this, the 70-meter antennas at Goldstone, California; Madrid, Spain; and Canberra, Australia were imported into *Systems Toolkit*. Figure 72 shows how MAPLE SIRUP always has access to at least one of the three ground stations. As the spacecraft loses sight of one station, it enters the view of another. Therefore, as long as the relevant antenna is not in use by another mission, MAPLE SIRUP can downlink whenever necessary.

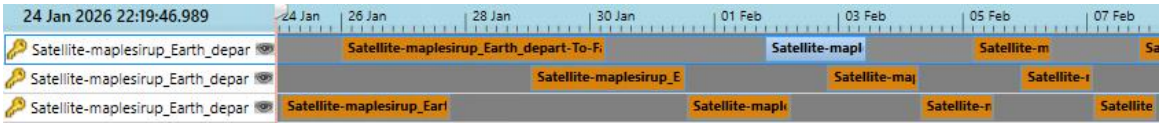

Figure 72. Access Times to Each 70-meter Antenna

Another important consideration is the duration of a single access period once MAPLE SIRUP is at Iris. This would set a maximum limit on the data size for a single transfer window. This can also be modeled using *Systems Toolkit*, revealing the average duration of access between MAPLE SIRUP and the Goldstone antenna to be 46,000 seconds. This will be important in the Data Rate section.

The performance capabilities of the Deep Space Network's 70-meter antennas are organized in Table 8 below. These are average estimates based on data released by the JPL.

	Receiving Gain	Transmitting Gain	Transmitting Power
DSN 70-meter Antenna	74 dBi	73 dBi	20,000 W

Table 8. 70-meter Antenna Capabilities [67, 68]

6.5 Data Rate Equations

The data rate for any telemetry link is calculated using the Shannon-Hartley Capacity theorem:

$$B * \log_2(1 + \frac{S}{N}) = C \tag{6.4}$$

Here, *B* is the bandwidth of the telemetry link and *S* divided by *N* is the signal-to-noise ratio. The signal *S* is equivalent to the received power at the antenna's effective aperture, which is in turn calculated from the signal power density,

$$\frac{P_t * G}{4\pi * R^2} = \rho \tag{6.5}$$

where P_t is the transmitted power from the Iris radio, *R* is the distance to asteroid 7 Iris, and *G* is the unitless gain of the spacecraft antenna. Using this, the received power is

$$\rho * \mu * A_r = P_r \tag{6.6}$$

where A_r is the receiving antenna aperture and μ is the receiving antenna efficiency. For MAPLE SIRUP and most interplanetary missions, these values are calculated from the 70-meter antenna values in Table 8.

The noise value in the Shannon-Hartley theorem is only introduced through an amplifier, which increases the signal strength after it is received at the DSN. The amplifier is kept cold to minimize the amount of noise added to the signal. The total noise in the signal is calculated with:

$$k * T * B = N \quad (6.7)$$

In Equation 6.7, k is the Boltzmann constant and T is the temperature of the system. Lower temperature systems add less noise to a signal. B is the bandwidth of the signal.

The signal-to-noise ratio can now be calculated, using P_r as S in Equation 6.4. Space losses are already accounted for, but other losses must be considered in the signal-to-noise ratio. The next section shows the results of these calculations.

6.6 Data Rate

Using the equations and constants established in Data Rate Equations, the downlink and uplink data rates can be calculated. Table 9 below summarizes the values used and calculated to find the final data rates.

	Downlink (S/C to Earth)	Uplink (Earth to S/C)
Transmitting Power (W)	3.8	20,000
Aperture (m^2)	0.17315	3800
Antenna Efficiency	0.41	0.67
Effective Aperture (m^2)	0.071	2546
Distance (m)	$4.077 \cdot 10^{11}$	$4.077 \cdot 10^{11}$
Power Density (W/m^2)	$1.275 \cdot 10^{-21}$	$1.762 \cdot 10^{-13}$
Receiving Aperture (m^2)	3800	0.17315

Receiving Antenna Efficiency	0.67	0.41
Eff. Receiving Aperture (m^2)	2546	0.071
Received Power (W)	$3.245 \cdot 10^{-18}$	$1.251 \cdot 10^{-14}$
Amplifier Temperature (K)	28.5	273
Noise Spectral Density (W/Hz)	$3.935 \cdot 10^{-22}$	$3.493 \cdot 10^{-21}$
Bandwidth (GHz)	0.05	0.045
Noise (W)	$1.967 \cdot 10^{-14}$	$1.572 \cdot 10^{-13}$
Losses	0.7	0.7
Signal-to-Noise Ratio	0.0001155	0.04647
Data Rate Capacity (bps)	**8331.58**	**3,268,540**

Table 9. Summary of Values for Downlink and Uplink Data Rates

Using the downlink data rate given in Table 9, the time required to send back payload data can be calculated. For the Lidar instrument, the total data size will depend on how long the instrument needs to run. For this reason, a ratio of times is given for the Lidar's last column in Table 10.

Payload Sensor	Data Produced	Data Size	Time to Completely Transfer
TriScape Imager	Image	14.71 MB/image	14,125 seconds (~4 hours)
Argus Spectrometer	Image	513 B/image	0.049 seconds
Plasma Spectrometer	Image/Reading	8.203 kB/image	7.877 seconds
Lidar	Surface Scan	4 kB/s	3.84 seconds / second of Lidar

Table 10. Time to Transfer Payload Data

In addition, the total amount of data transferable in a single access window can be determined. This amount is simply the data rate multiplied by the duration of the transmission. Using the average access duration of 46,000 seconds from the Ground Stations section, the average amount of data transferable in a single access window from Iris is about 48 megabytes. This is enough to transfer multiple TriScape Imager images, despite their large individual file size.

7 Attitude Determination and Control

The ADC system uses sensors to determine the satellite's orientation at any time and compare it to the desired attitude. Then, it calculates the required adjustments using control algorithms and makes those changes through actuators. This section details the sensors, actuators, and control algorithms that will be used for MAPLE SIRUP's ADC system. It provides a rationale for each component that was selected and describes how they will be used together to perform detumble, initial attitude determination, and constant attitude maintenance.

7.1 Rotations

Determining the spacecraft's attitude is equivalent to calculating the rotation between the body and inertial frames. This rotation is most commonly described in three different forms: Euler Angles, Direction Cosine Matrix, or Quaternions. Euler Angles are the easiest to comprehend – three angles describing the rotation about each axis. A direction cosine matrix, or rotation matrix, is a 3x3 dot product representation such that any 3-dimensional vector in the body frame v^b multiplied by the matrix from the body frame to inertial frame R_b^i will result in that same vector represented in the inertial frame v^i [69]:

$$\begin{bmatrix} v_1^b \\ v_2^b \\ v_3^b \end{bmatrix} R_b^i = \begin{bmatrix} v_1^i \\ v_2^i \\ v_3^i \end{bmatrix} \tag{7.1}$$

The rotation matrix from the inertial frame to the body frame is simply the inverse of that from body to inertial:

$$R_i^b = {R_b^i}^{-1} \tag{7.2}$$

A quaternion consists of a 3-component vector and a single scalar value. It is usually represented as a 4x1 column vector with its vector component $\boldsymbol{q}_{1:3}$ followed by its scalar component q_4 [70].

$$\boldsymbol{q} = \begin{bmatrix} \boldsymbol{q}_{1:3} \\ q_4 \end{bmatrix}, \text{ where } \quad \boldsymbol{q}_{1:3} = \begin{bmatrix} q_1 \\ q_2 \\ q_3 \end{bmatrix} \tag{7.3}$$

This is the preferred method of storing rotation data because running computations with 3x3 matrices are very demanding compared to a simple four-value vector. Quaternions also avoid the issue of singularities, when two axes happen to align with each other, and information is lost for one of the three dimensions. However, they are not the most useful when rotating vectors between frames. To do this, quaternions can be converted directly to a rotation matrix using this relationship [71, 72]:

$$R = \begin{bmatrix} 1 - 2q_2^2 - 2q_3^2 & 2q_1q_2 - 2q_3q_4 & 2q_1q_3 + 2q_2q_4 \\ 2q_1q_2 + 2q_3q_4 & 1 - 2q_1^2 - 2q_3^2 & 2q_2q_3 - 2q_1q_4 \\ 2q_1q_3 - 2q_2q_4 & 2q_2q_3 + 2q_1q_4 & 1 - 2q_1^2 - 2q_2^2 \end{bmatrix} \tag{7.4}$$

7.2 Attitude Dynamics

The rotational motion of a rigid body can be completely modeled in relation to its orientation, angular velocity, and angular momentum. The detailed derivations of these equations are provided in [70]. This section presents the final dynamic equations that represent how these three properties change over time. As discussed in Section 7.1, the orientation will be given in the form of a quaternion. The rate of change of a quaternion is given as

$$\dot{\boldsymbol{q}} = \frac{1}{2}\, \Omega\, \boldsymbol{q} \tag{7.5}$$

Where $\boldsymbol{\Omega}$ is the 4x4 cross-product matrix of the spacecraft angular velocity $\boldsymbol{\omega}$:

$$\Omega = \begin{bmatrix} 0 & \omega_z & -\omega_y & \omega_x \\ -\omega_z & 0 & \omega_x & \omega_y \\ \omega_y & -\omega_x & 0 & \omega_z \\ -\omega_x & -\omega_y & -\omega_z & 0 \end{bmatrix} \tag{7.6}$$

Next, the rate of change of the spacecraft angular velocity in the body frame is

$$\dot{\boldsymbol{\omega}} = J^{-1}[-\boldsymbol{\omega} \times (J\boldsymbol{\omega}) + \boldsymbol{T}] \tag{7.7}$$

where J is the 3x3 inertia matrix of the spacecraft and **T** is the total torque being exerted on the spacecraft. Finally, the spacecraft angular momentum in the body frame is modeled as

$$\dot{\boldsymbol{H}} = \boldsymbol{T} - \boldsymbol{\omega} \times \boldsymbol{H} \tag{7.8}$$

Together, Equations *(*7.5), *(*7.7), and *(*7.8) were used to fully describe the dynamic rotational motion of the spacecraft.

7.3 Sun Vector Model

The sun vector represents the vector that points from the spacecraft to the center of the sun. This is a very useful observation model because the sun's extremely bright light makes it easy to find using photosensors. It is important to know the sun vector so that the ADC system can point the solar arrays for maximum power generation. This vector can also be modeled mathematically as a function of time using the Astronomical Almanac's algorithm for the approximate solar position [4, 73]. It begins by calculating the mean longitude of the sun, L, the mean anomaly of the Earth in its orbit, g, and the obliquity of the ecliptic.

$$L = 280.460° + 0.9856474° * (JD - 2451545) \tag{7.9}$$

$$g = 357.528° + 0.9856003° * (JD - 2451545) \tag{7.10}$$

$$\varepsilon = 23.439° + 0.0000004° * (JD - 2451545) \tag{7.11}$$

where JD is the Julian Day of the desired time. We then calculate the value R and the ecliptic longitude, λ. The ecliptic latitude is assumed to be 0 due to the small inclination of Earth's orbit.

$$R = 1.00014 - 0.01671\cos(g) - 0.00014\cos(2g) \tag{7.12}$$

$$\lambda = L + 1.915°\sin(g) + 0.020°\sin(2g) \tag{7.13}$$

Finally, the vector coordinates of the sun's position relative to the inertial reference frame are given by:

$$x = Rcos(\lambda) \tag{7.14}$$

$$y = Rcos(\varepsilon)\sin(\lambda) \tag{7.15}$$

$$z = Rcos(\varepsilon)\sin(\lambda) \tag{7.16}$$

The sun vector can also be obtained using the STK model developed for the mission but was not fully available due to software difficulties.

7.4 Sensor Selection

A variety of sensors and actuators are required to measure the spacecraft's attitude, then orient it correctly. Some of the most common sensors used for this include sun sensors, star sensors, earth sensors, magnetometers, GPS, and gyroscopes [9]. For this mission, magnetometers will not be used because MAPLE SIRUP will be too far from Earth to reliably use its magnetic field to determine the attitude, and there is no other planned science on this mission that involves a magnetometer. Similarly, GPS and earth sensors will not be useful once the satellite leaves GEO. It will, however, make use of multiple sun sensors, three gyroscopes, and two star trackers. These sensors were carefully selected to maximize performance while minimizing size and weight.

7.4.1 Sun Sensors

Sun sensors are common on spacecraft and usually use a photocell or diode to relate current flow with the incidence angle of light, which determines the location of the sun with respect to the spacecraft [74]. One of the main tasks for the ADC system is to keep the solar panels pointed at the sun for maximum solar power availability. To accomplish this, the system will need at least one fine sun sensor. These work by producing voltages, which change based on the incident angle of sunlight to the photosensor. With horizontal and vertical sensors, they can produce 4 analog voltages that are read by a built-in microcontroller that then calculates the estimated sun vector [74]. This sensor will be mounted on one side of the satellite so that it points in the same direction as the solar arrays. As long as the sun is in its field of view, it can provide reliable information to stay pointed towards the sun.

But, if at any point in the mission the sun is not in the sensor's field of view, there is no way to determine where it is or how to find it. Therefore, we must mount sun sensors on the other five faces of the spacecraft to achieve full-sky coverage. However, these additional sensors do not need to be as accurate or reliable as the main sensor. They will just indicate which faces of the satellite can see the sun, and minor attitude adjustments can be made until the sun enters the main sensor's field of view. Then, normal operation will continue with the fine sun sensor.

The NCSS-SA05 analog sun sensor (see Figure 73), made by NewSpace Systems, was selected by the 2017 MQP Team [4]. It offers an accuracy of ± 0.5° with a mass of less than 5g, while also consuming very little power, which is often limited in SmallSat missions [74]. No other options with a comparable mass performed with this level of accuracy, therefore we will continue to use this sensor.

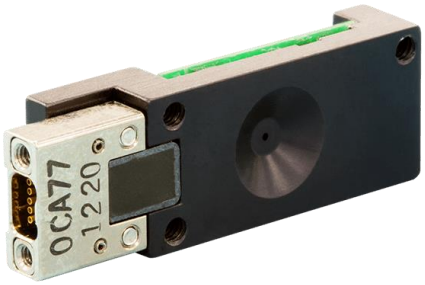

Figure 73. NewSpace Systems NCSS-SA05 Analog Sun Sensor [74]

Mass	< 5 g
Dimensions	33mm x 11mm x 6mm
Power	< 50mW
Voltage Supply	5V
Field of View	114°
Accuracy	< 0.5°
Operating Temperature	-25 to 50 ℃

Table 11. NCSS-SA05 CubeSat Sun Sensor Specifications

The other five faces will have less accurate, coarse sun sensors. The 2017 ADC Team determined that the CSS-01,02 Coarse Sun Sensor, made by Space Micro, was a great fit for this purpose [4]. With over 20 years of flight heritage, this sensor offers a simple, reliable design to provide coarse sun vector information with an accuracy of ± 5° while drawing no power at all from the satellite [75]. The sensor is shown in Figure 74.

Figure 74. Space Micro CSS-01,02 Coarse Sun Sensor [75]

7.4.2 Star Tracker

The sun sensor configuration will provide location data about the sun to keep the solar arrays pointed for maximum power production. To gain access to information about 3-dimensional spacecraft attitude, MAPLE SIRUP will also include two star trackers. These are cameras that take pictures of the sky and compare them to an onboard catalog to identify stars with known positions, which allows them to compute the position of the spacecraft [76].

When selecting a star tracker, the most important thing for this mission was accuracy. Figure 75 shows the star tracker options that were considered. The 'Score' column is a weighted sum of the four parameters, where accuracy is weighted 60%, volume 20%, mass 10%, and power 10%. The goal is to minimize all of these, therefore the lowest score wins.

Component	Mass		Volume		Power		Accuracy		Score
Sagitta ST	0.25	kg	2.14E-04	m^3	1	W	2	"	1.33
KU Leuven Mini ST	0.1	kg	0.000016	m^3	1	W	20	"	12.11
STAR-T3	0.35	kg	3.60E-04	m^3	1	W	2	"	1.34
OCE Tech ST	0.085	kg	1.03E-04	m^3	0.5	W	5	"	3.06

Figure 75. Star Tracker Decision Matrix

Based on these scores, the Arcsec Sagitta Star Tracker, shown in Figure 76, is the best option. It provides 2 arcsec attitude accuracy, with slightly less mass and volume than the STAR-T3. It is also advertised for its robust, custom algorithms and easy interfacing [77]. The OCE Tech ST Series was also considered for its low mass and volume. But, as mentioned, accuracy was the most important figure when selecting a system.

Figure 76. Arcsec Sagitta Star Tracker [77]

There are two of these star trackers looking out the bottom of the spacecraft to avoid direct sunlight as much as possible. They will also be mounted in opposite directions about 40° from the vertical to maximize the amount of sky they cover. These two systems will be sufficient to accurately measure the satellite's attitude throughout the mission.

7.4.3 Gyroscope

The last sensor for the MAPLE SIRUP ADC system is a gyroscope. This is a spinning wheel that measures the rotation rate of the satellite and uses the conservation of angular momentum to determine its orientation. MEMS (microelectromechanical system) gyros are digital sensors that can perform the same measurements but are becoming more popular due to their small size and simplicity [78]. To get full information about the spacecraft's rotation, a gyroscope sensor must be mounted on each of the three axes of rotation [9]. By measuring the angular velocity of the spacecraft, control algorithms can determine the counter torques needed for detumbling, initial attitude determination, and attitude maintenance throughout the entire mission.

The 2017 ADC Team determined a digital gyroscope to use for these exact purposes, so we will continue to use their choice [4]. The ADXRS453, made by Analog Devices, is a high-performance, single-axis gyroscope optimized for platform stabilization. This device comes in

two different packages: the SOIC_CAV package for z-axis response, and the LCC_V vertical mount package for x, y, or z-axis response [79]. The two configurations are shown in Figure 77. This mission will require one SOIC and two vertically mounted gyroscopes to measure angular velocity in all three axes.

Figure 77. ADXRS453 Gyroscope Vertical (left) and SOIC (right) packages [79]

Analog Devices recommends the EVAL-ADXRS453Z breakout board (seen in Figure 77, attached to the gyroscope chips) to implement the digital outputs of the ADXRS453 into an existing system [79].

7.5 Actuator Selection

Actuators are the devices that perform the changes in spacecraft orientation. Normally, they are divided into two different categories: active and passive [9]. Active actuators involve a control feedback loop to apply torque to the spacecraft until it reaches its desired orientation, then constantly make small adjustments to stay within attitude tolerance. This torque comes from an internal source of power or fuel, such as thrusters or reaction wheels. Passive actuators involve the careful use of environmental disturbances to keep the spacecraft in a stable

state. This includes magnetic torquers, as well as the use of gravity gradient torque and solar radiation pressure [80].

7.5.1 Disturbance Torques

One main reason that satellites require an attitude control system is that over time, environmental effects can cause the spacecraft to spin. These effects are called disturbance torques. For this mission, the only disturbance torques that are significant at geostationary orbit and beyond are gravity and solar radiation, as shown in Figure 78. Although, due to the size of MAPLE SIRUP, these torques will be even less than the magnitudes shown – mostly on the order of 10^{-7} Nm at GEO.

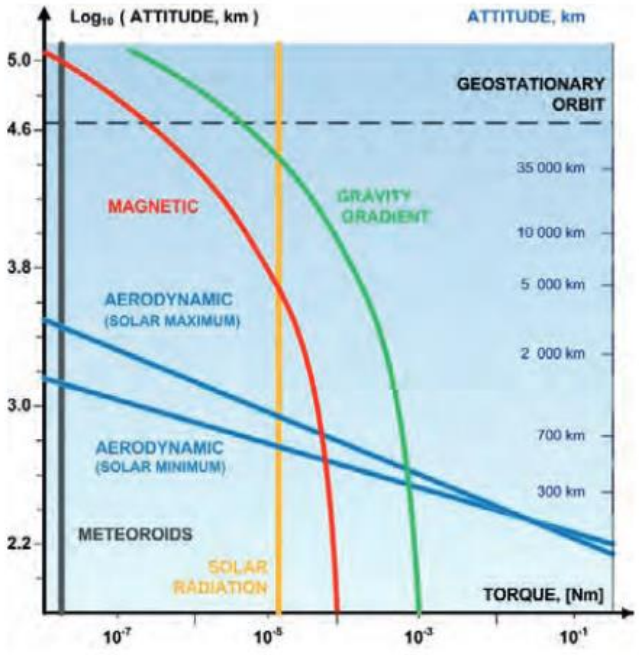

Figure 78. Magnitude of Disturbance Torques Relative to Orbit Altitude [81]

To calculate the magnitude of these disturbance torques, we need to know the moment of inertia of the spacecraft. The estimated 3D moment of inertia matrix *J* was computed using

SolidWorks for two main mission configurations: the folded launch configuration and the deployed flight configuration.

$$J_{folded} = \begin{bmatrix} 3.40 & 0.01 & 0.01 \\ 0.01 & 5.10 & 0.07 \\ 0.01 & 0.07 & 4.21 \end{bmatrix} kgm^2 \quad (7.17)$$

$$J_{deployed} = \begin{bmatrix} 5.25 & 0.01 & 0.19 \\ 0.01 & 123.63 & 0.26 \\ 0.19 & 0.26 & 119.78 \end{bmatrix} kgm^2 \quad (7.18)$$

The torque produced by gravity is modeled by this equation:

$$T_g = \frac{3\mu}{2R^3} |J_z - J_y| \sin(2\theta) \quad (7.19)$$

Where μ is the gravitational parameter for Earth (398600 km^3/s^2) and R is the orbital radius (42164km for GEO). J_y and J_z are the second and third diagonal elements of matrix J. θ is the maximum angle that the local vertical makes with the z-axis (assume 45° for worst-case torque) [81]. Proceeding with the calculation, the maximum gravitational torque on the SmallSat is estimated to be 4.1 x 10^{-7} Nm.

The torque produced by solar radiation is given by this equation:

$$T_{sp} = \left[\frac{J_s}{c} A_s \cos(I) (1 + q)\right] (c_{sp} - c_g) \quad (7.20)$$

Where J_s is the solar constant (1367 W/m^2 at Earth), c is the speed of light (3x10^8 m/s), and A_s is the surface area of the CubeSat (the largest face is estimated to be 1.9 m^2). I is the incidence angle of solar radiation, which is assumed 0 for maximum torque. q is the reflectance factor, which we assume constant at 0.6 [81]. c_{sp} - c_g is the distance between the center of solar pressure and the center of gravity of the CubeSat (we will assume a maximum displacement of 1 cm). This results in an estimated solar radiation torque of 6.9 x 10^{-7} Nm. This is the greater of the two disturbance torques and will be used to determine the required torque of the reaction wheels.

7.5.2 Reaction Wheels

Because this spacecraft is relatively small, the ongoing disturbance torques it experiences will be small enough to be managed by just a reaction wheel system. For control in all three axes, only three wheels are necessary, but there will be a 4-wheel system to help increase torque capabilities and provide a back-up wheel [82]. When the spacecraft needs to rotate to a desired attitude or stabilize its current orientation, the system spins the reaction wheels at a certain rate to change their angular momentum. The conservation of angular momentum states that the total system (satellite and reaction wheels) must keep a constant angular momentum. So, if the angular momentum of the reaction wheel is increased by some amount, then the angular momentum of the satellite must decrease by that exact amount [9]. These angular momentums are represented by:

$$H_{Total} = H_{SC} + H_{RW} \tag{7.21}$$

If H_{RW} changes by an amount ΔH_{RW}, then

$$\Delta H_{SC} = -\Delta H_{RW} \tag{7.22}$$

So that angular momentum is conserved.

$$H_{Total} = H_{SC} + H_{RW} + \Delta H_{RW} - \Delta H_{RW} \tag{7.23}$$

$$H_{Total} = H_{SC} + H_{RW} \tag{7.24}$$

Although reaction wheels offer on-demand spinning without requiring a propulsion system with fuel, one main downside is that, over time, they build up momentum that exceeds the maximum speed of the wheel. This is called saturation and can be dealt with by spinning the wheels in the opposite direction. To keep the spacecraft stable, a separate torque must be applied

that opposes the reaction wheels [83]. The maximum momentum storage that will build up in one-quarter of an orbit can be estimated with this equation:

$$h = T_{max}\frac{P}{4}(0.707) \tag{7.25}$$

where P is the period of the satellite's orbit (assumed to be 86160 seconds at GEO), and T_{max} is the maximum torque that the wheel must produce [83]. To make up for the previous moment of inertia assumptions, we will assume a maximum torque of 8.3 x 10^{-7} Nm, which is the maximum disturbance torque (in this case, the torque due to solar radiation pressure) multiplied by a margin factor of 1.2. The maximum required momentum storage is estimated to be 1.05 x 10^{-2} Nms.

The selected reaction wheels must meet the following requirements: A maximum torque capability of 8.3 x 10^{-7} Nm and maximum momentum storage of 1.05 x 10^{-2} Nms. A simple decision matrix was used to identify a reaction wheel that surpassed these requirements but also had the lowest mass, volume, and power consumption. As shown in Figure 79, the Sputnix SXC-FW4-02 was considered the best option. The CubeWheel options did not meet the angular momentum storage requirement, the Sputnix SX-RW-50-2.0 was too large and used too much power, and the MAI-400 produces less maximum torque, while also consuming more power.

Requirements:	--		---		---		---		1.05E-02	N.m.s	8.30E-07	N.m
Component	Mass		Volume		Power		Max. Power		Ang. Mom. Storage		Max Torque	
CubeWheel Small	0.06	kg	2.05E-05	m^3	0.15	W	0.65	W	1.77E-03	N.m.s	2.30E-04	N.m
CubeWheel Small Plus	0.09	kg	4.84E-05	m^3	0.19	W	2.3	W	3.60E-03	N.m.s	2.30E-03	N.m
Sputnix SX-RW-50-2.0	2.5	kg	1.76E-03	m^3		W	40	W	2.00E+00	N.m.s	5.00E-02	N.m
Sputnix SXC-FW4-02	0.13	kg	1.88E-04	m^3	0.5	W	2	W	2.50E-02	N.m.s	1.20E-03	N.m
MAI-400	0.11	kg	4.18E-05	m^3	0.85	W	2.2	W	1.11E-02	N.m.s	6.35E-04	N.m

Figure 79. Reaction Wheel Decision Matrix

Figure 80 shows the Sputnix SXC-FW4-02, which is a system of 4 reaction wheels mounted in a pyramidal configuration [84]. This allows for full, three-axis control of the spacecraft's attitude and includes a fourth wheel to increase the torque capability and provide a backup if one

breaks. This will be placed under the main fuel tank in the spacecraft body, as close as possible to the center of mass, to simplify control.

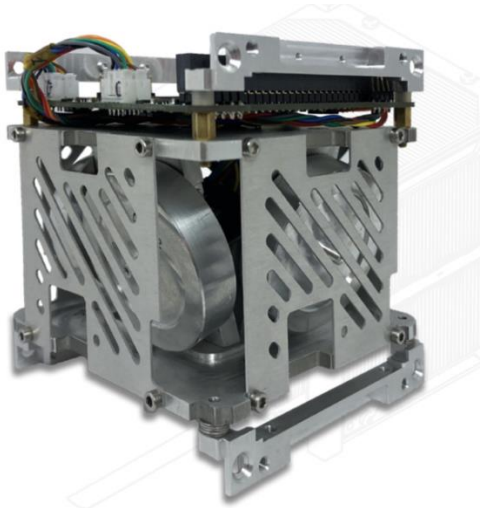

Figure 80. Sputnix SXC-FW4-02 Reaction Wheel System [84]

7.5.3 ACS Thrusters

As mentioned before, reaction wheels cannot be the only attitude control system because of their momentum build-up that must be routinely "dumped." This process is known as desaturating the wheels [85]. This mission will use a set of small cold gas thrusters as a secondary ACS. The maximum force required by the thrusters to desaturate the reaction wheels is given by

$$F = \frac{h}{Lt} \tag{7.26}$$

Where h is the stored momentum, L is the moment arm of the thrusters (distance to cg of CubeSat), and t is the burn time of the thruster, which can be assumed to be 1 s [83]. This results in a maximum required thrust of 1.3×10^{-2} N for the thrusters to desaturate the reaction wheels.

Figure 81 shows the thruster options that were considered for MAPLE SIRUP. The only one that meets the torque requirement for desaturating the reaction wheels is the Marotta cold gas microthruster. It also happens to have the best properties by far of the options compared.

Requirements:							1.32E-02	N
Component	**Mass**		**Volume**		**Power**		**Thrust**	
ThrustMe I2T5	0.9	kg	5.00E-04	m^3	10	W	2.00E-04	N
VACCO PUC	0.434	kg	3.58E-04	m^3	15	W	5.40E-03	N
IFM Nano Thruster	0.67	kg	8.25E-04	m^3	40	W	4.00E-04	N
Marotta Microthruster	0.06	kg	6.00E-05	m^3	7	W	1.05E-01	N

Figure 81. RCS Thruster Decision Matrix

The Marotta Microthruster (see Figure 82) is a cold gas thruster that requires a supply of pressurized gaseous nitrogen (GN2) [86]. For simple control of all three axes, there will be 16 thrusters on the spacecraft – two mounted in each corner – shown in Figure 83. Each thruster is labeled one through sixteen and Table 12 shows which four thrusters must be fired to rotate the satellite in each direction.

Figure 82. Marotta Cold Gas Microthruster [86]

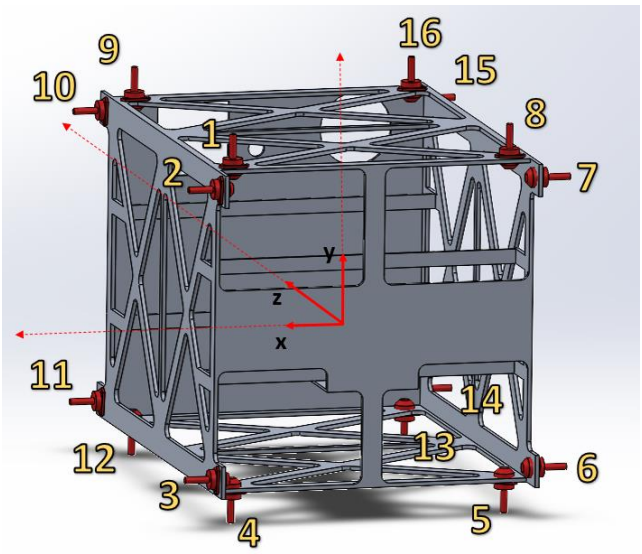

Figure 83. ACS thruster configuration diagram

Axis Rotation	Thruster #'s
+ x axis	4, 5, 9, 16
- x axis	1, 8, 12, 13
+ y axis	2, 3, 14, 15
- y axis	6, 7, 10, 11
+ z axis	2, 6, 10, 14
- z axis	3, 7, 11, 15

Table 12. ACS thruster firing configurations

There are two custom-sized fuel tanks mounted inside the spacecraft that supply enough GN2 for the ACS thrusters to provide torque for the spacecraft when necessary. The fuel mass required for any given thrust can be calculated using the total impulse delivered by the thruster I_{tot} and the specific impulse I_{sp}.

$$M_{fuel} = \frac{I_{tot}}{I_{sp} g} \tag{7.27}$$

The specific impulse for this thruster is 65 s and g is the acceleration due to gravity, 9.8 m/s^2. The total impulse is calculated using the simple relationship

$$I_{tot} = Ft \tag{7.28}$$

where F is the total force, or thrust, applied during the impulse and t is the pulse time of the thrusters. The ACS thrusters are mainly used for desaturating the reaction wheels but can also help the wheels turn the spacecraft for large maneuvers when needed. The total fuel mass required to routinely desaturate the reaction wheels throughout the entire mission is 0.1220 kg, which is further explained in Section 7.6.3. To make up for all assumptions, a 1.5 factor of safety is added to this, totaling 0.1464 kg of fuel mass required for all ACS needs.

The fuel tanks were designed to hold this much GN2 at 2000psi, requiring an internal volume of 359 cm^3 per tank. For cylindrical tanks with spherical end caps and a wall thickness of 0.9 mm, their radius is calculated to be 27.7 mm. The total mass of each fuel tank, including the fuel inside, is 0.201 kg.

7.6 ADC Algorithms

So far, the satellite can measure its current state using data from onboard sensors, and then orient itself using the chosen actuator system. But there must be an onboard computing system, which uses various algorithms to analyze the sensor data and output the required torques to reach the desired attitude. This section presents the results of numerous control systems designed in MATLAB to perform some of the major requirements of the ADCS. All simulations use the attitude dynamics discussed in Section 7.2 along with a proportional-derivative controller. It was discovered that the integral term of the PID controller had very little effect on the system because the sum of error was always limited by the maximum torque output of the actuators.

The commanded torques will depend heavily on the spacecraft moment of inertia, which was obtained using the 3D model in SolidWorks. MAPLE SIRUP has two main configurations that were considered: the stowed launch configuration and the deployed flight configuration. The only difference between these is that in the launch configuration, the solar arrays are folded towards the main body, whereas in the flight configuration, they are fully extended so they can generate power. As discussed earlier, Eq (*7.17*) and (*7.18*) show the calculated inertia matrices for these two configurations.

7.6.1 Detumbling

The detumble phase is the simplest and is done entirely in GEO once MAPLE SIRUP is released from the launch vehicle. The onboard gyroscopes measure the angular velocity of the satellite in all three axes, and the corresponding reaction wheels spin to produce a counter torque that eventually brings the spacecraft to a stable state. The chosen Sputnix reaction wheels include an internal algorithm that determines how fast to spin each wheel to produce the desired output torque [84]. The system uses a feedback loop to continuously compute the error between the desired and current angular velocity and adjust its output torque as it gets closer to the desired value [87]. In the case of the detumble phase, the desired value for angular velocity is zero. The simulations are analyzed by their settling time, or how long it takes the system to reach 95% stability, which is represented by a red dot in all of the analysis graphs. The total settling time for any maneuver will always be the time it takes the y-axis to settle because it has the largest moment of inertia.

First, the simulation analysis shows the difference between detumbling in launch configuration (Figure 84) vs. flight configuration (Figure 85). It assumes an initial angular

velocity of 0.5 °/s (0.009 rad/s) on each axis, which is the maximum spin guaranteed by the launch vehicle upon release into GEO [28].

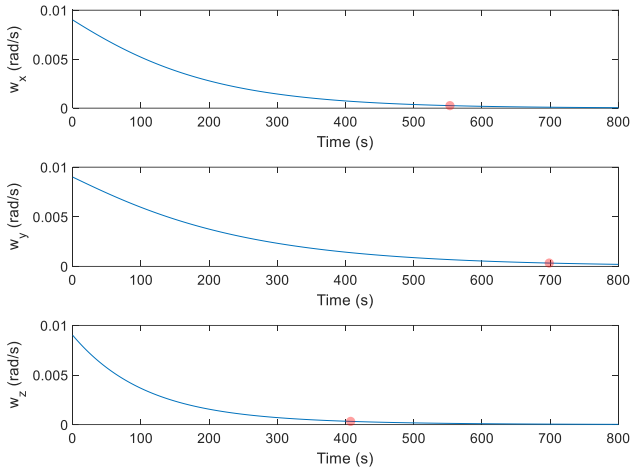

Figure 84. Detumble simulation in launch configuration

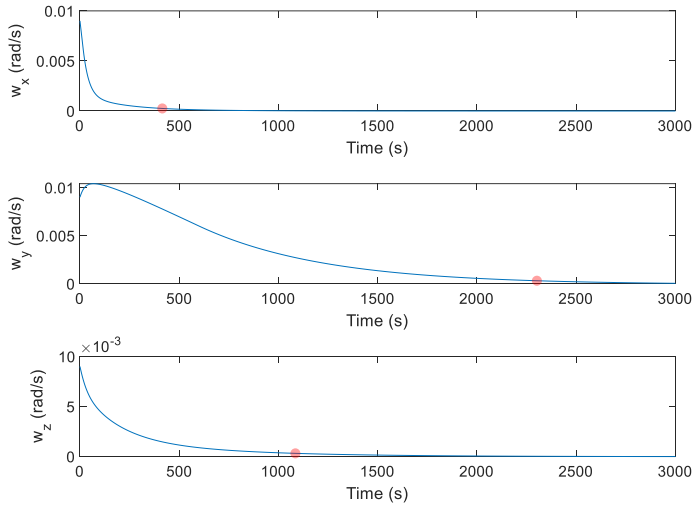

Figure 85. Detumble simulation in flight configuration

Performing the detumble in launch configuration reduces the maximum settling time from over 2300 s to about 700 s. This is a major decrease in the total phase time, so the detumble phase will happen while MAPLE SIRUP is in launch configuration. However, because the solar

arrays will still be folded, the reaction wheels and on-board computer will have to receive power from the spacecraft batteries.

The main concern with the detumble phase is the angular momentum buildup of the reaction wheels. The spacecraft begins with an arbitrary, non-zero angular velocity imposed by release from the launch vehicle. The reaction wheels apply the toque required to bring that angular velocity to zero. This leaves the wheels spinning with that change in angular momentum. Because the wheels cannot exceed their maximum spin rate or angular momentum, the detumble simulation was modified to take longer, but keep the wheels within their limits. After this phase, they will need to be desaturated, which is described in Section 7.6.3.

Figure 86 shows the angular velocity of the spacecraft in all three axes for the duration of detumble. This phase can be completed in about 480 s, which is acceptable because MAPLE SIRUP will have one orbital period in GEO (about 24 hours) to complete its initial detumble and attitude determination phases.

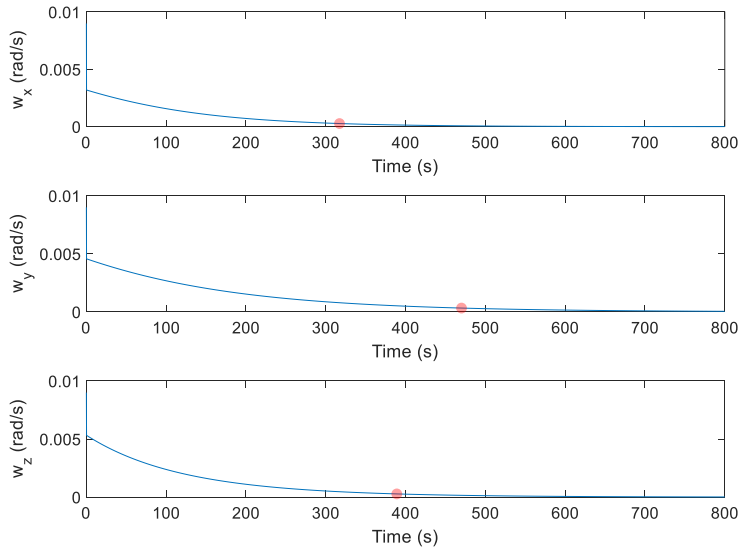

Figure 86. Angular velocity during detumble

Figure 87 shows the angular momentum of the reaction wheels in all three axes throughout the detumble maneuver. The maximum angular momentum for these reaction wheels in each axis is 0.025 Nms, which is represented by the dashed lines in the figure. The controller gains were manually selected to get as close as possible to this limit to minimize settling time. This analysis demonstrates that the reaction wheels can complete the detumble phase in launch configuration.

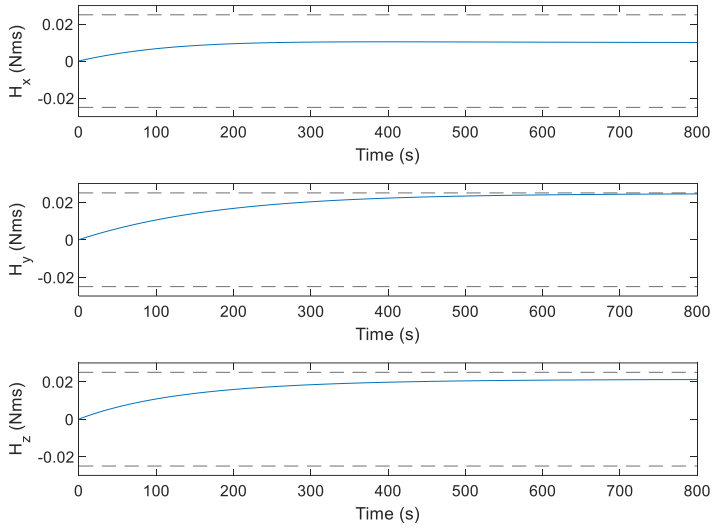

Figure 87. Reaction wheel angular momentum during detumble

7.6.2 Initial Attitude Determination and Alignment

After the detumble phase, the solar arrays will deploy into the flight configuration and MAPLE SIRUP will need to determine its initial attitude using the star trackers. They each provide the spacecraft attitude in quaternion form by comparing visible stars with their onboard catalogs. The system will then compute the error between the current and desired orientation.

For this phase, the desired orientation is constrained by the velocity vector and the sun vector. Before the spacecraft can begin its departure from GEO, the + z axis needs to be oriented along the velocity vector, which is determined using the STK orbit trajectory. It is also important that the + y axis is pointing towards the sun vector. The solar panels have their own motors that

allow them to rotate on one axis. This is useful because the velocity vector and the sun vector are not always perpendicular to each other, and therefore the spacecraft z any y axes could not both be aligned at the same time. As long as the + y axis is aligned so that the sun vector is within ±90° of it, then the solar panels can control the pitch angle (around the x axis) to ensure they are normal to the sun for maximum power generation.

The initial alignment maneuver was analyzed two separate times: once using the reaction wheels, and once using the thrusters. This was to determine if the reaction wheels would be strong enough to perform the maneuver alone, which would save on fuel mass required for the thrusters. Figure 88 shows the time it takes for the error quaternion to converge to the identity quaternion [0 0 0 1], which represents that the spacecraft attitude has reached the desired orientation. Using only the reaction wheels, the spacecraft can fully align in about 1800 s, which can still be done within the initial GEO coast period.

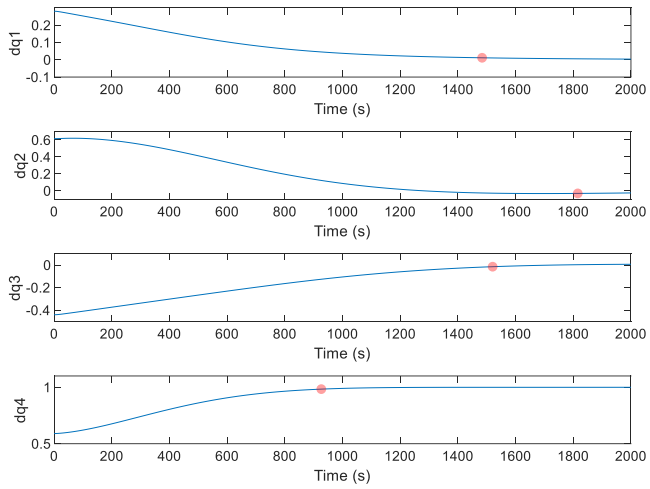

Figure 88. Error quaternion for initial alignment using reaction wheels

Once again, this must be performed within the reaction wheel angular momentum limit. Figure 89 shows that the y-axis angular momentum is as close to the limit as possible to minimize settling time.

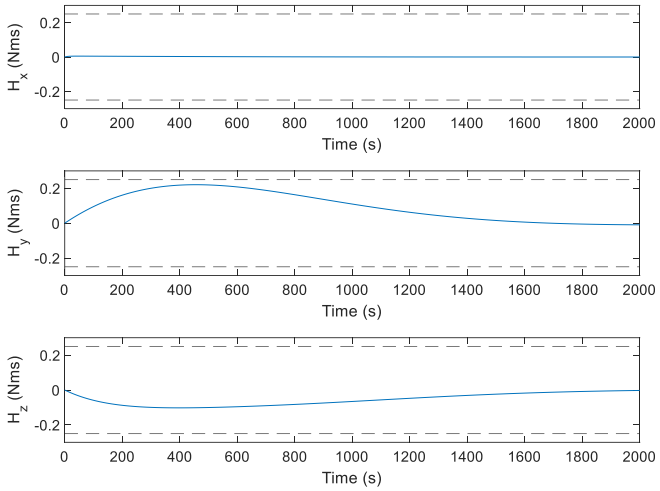

Figure 89. Reaction wheel angular momentum during initial alignment

Unlike the detumble maneuver, the initial alignment starts and ends with zero angular velocity. This means that the wheels spin up in one direction, then as the spacecraft approaches the desired attitude, they spin back the other way to slow down the angular rate to zero. Because of this, the reaction wheels return to a low speed and do not have to be desaturated after the maneuver. Also, as expected, the x-axis is not altered because this rotation will be controlled by the solar panels.

Table 13 shows the maximum torque available for each axis based on the maximum thrust for a set of four thrusters and the moment arm distance of those thrusters from the center of the spacecraft. Because more torque is available compared to the reaction wheels, using the thrusters to align the spacecraft should take much less time.

Axis	Max Thrust	Moment Arm	Max Torque
X	1.68 N	0.2283 m	0.3835 Nm
Y	1.68 N	0.2706 m	0.4546 Nm
Z	1.68 N	0.1799 m	0.3022 Nm

Table 13. Maximum thruster torque available in each axis

As expected, Figure 90 shows that the initial alignment maneuver can be completed in about 120 s using the thrusters. The fuel mass required for alignment was calculated using the total impulse expended for the maneuver and the specific impulse of the thruster. The total fuel mass to align all axes is 0.1131 kg, which is very large compared to the estimated total amount of fuel load, discussed in Section 7.5.3. Because time is not a concern in this maneuver, it is better to use the reaction wheels, which also do not have to be desaturated afterward.

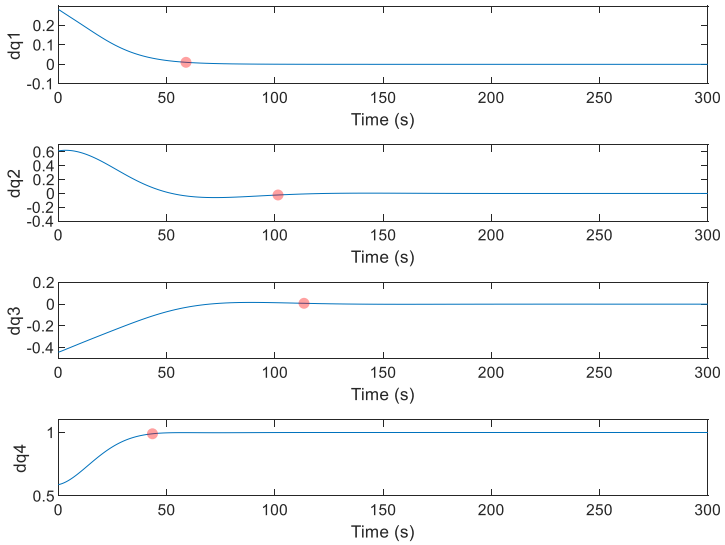

Figure 90. Error quaternion for initial alignment using thrusters

7.6.3 Attitude Maintenance

Once the spacecraft is finished initial alignment and begins its journey away from Earth, the majority of the mission is ensuring the propulsion system remains parallel to the velocity vector and the solar panels can see the sun. This is done using a simple orbit propagator to constantly estimate the spacecraft's position and velocity vector in the inertial frame. The reaction wheels are used to counter any disturbances, such as gravity or solar pressure, that may steer the spacecraft away from the desired orientation. These disturbances are very small, as discussed in Section 7.5.1, but eventually, the wheels may reach their angular momentum limit and require desaturation.

As mentioned in Section 7.6.1, the first time the wheels will need to be desaturated is after the detumble phase. The spacecraft stops rotating and changes to the deployed flight configuration, then the thrusters will be available for desaturation. Based on the angular momentum of the wheels, the ACS thrusters' pulse for their minimum impulse bit (~0.1 s) with a specific amount of thrust. Then, the wheels decrease their speed to counter the thruster torque, which is designed to stabilize them near zero angular momentum.

The analysis was done for the worst case, where each axis has built up the maximum allowable angular momentum, 0.025 Nms. Figure 91 shows the spacecraft's angular velocity during desaturation. In this case, the thrusters were fired for 0.1 s, which causes the sudden change in angular velocity. Then, the reaction wheels begin to decrease their speed to bring the spacecraft to rest. For maximum buildup, this process takes about 300 s.

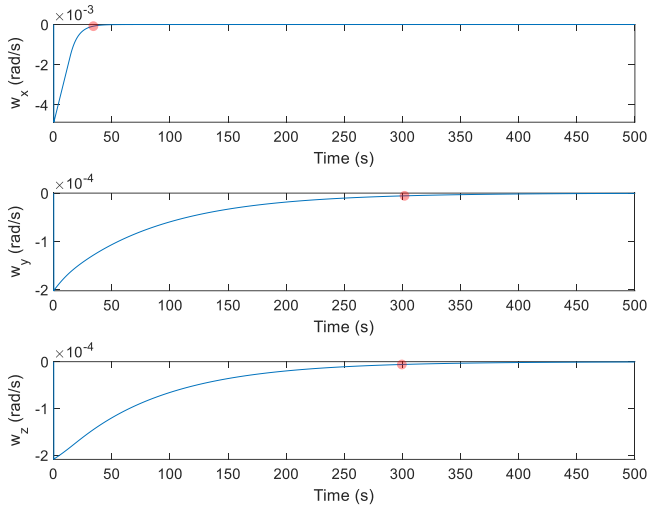

Figure 91. Spacecraft angular velocity during desaturation

Figure 92 shows the wheel angular momentum over this same period. As expected, the graph converges to the dashed line, which represents zero angular momentum, in all axes.

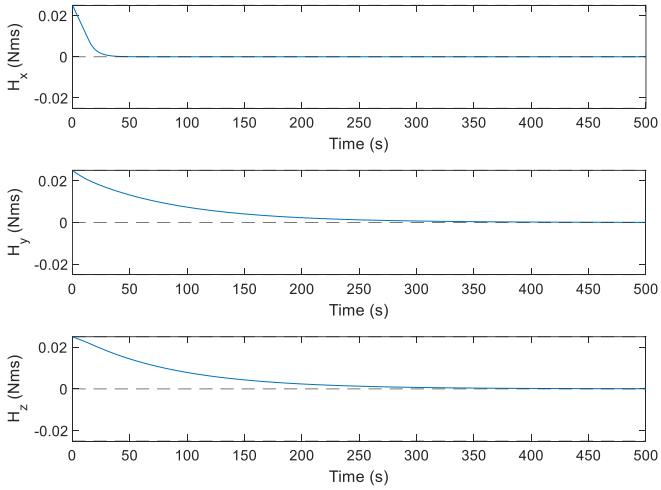

Figure 92. Reaction wheel angular momentum during desaturation

After the initial alignment phase, the reaction wheels ensure the stability of the spacecraft throughout all burn and coast phases. The only disturbances that are considered to act on the spacecraft during this time are gravity and solar pressure. Section 7.5.1 estimates both torques to

have a maximum value on the order of 10^{-7} Nm. Once MAPLE SIRUP enters the earth departure phase, these effects will decrease as it gets farther away from the Earth and the Sun.

More than half the mission will be spent in deep space operations. The main concern during this phase is solar radiation pressure, estimated at 10^{-7}–10^{-8} Nm between Earth and Iris because the gravity disturbance is on the order of 10^{-10} – 10^{-14} Nm. To estimate how many times the reaction wheels must be desaturated throughout the mission, a constant disturbance torque of $5*10^{-8}$ Nm is assumed throughout the 1264-day mission. Figure 93 shows that the reaction wheels need to be routinely desaturated about every 480,000 s, or 5.5 days. This means that the desaturation process needs to occur about 228 times throughout the entire mission. To consider the assumptions made in this estimate, a margin factor of 1.2 is added, making it a total of 273 times.

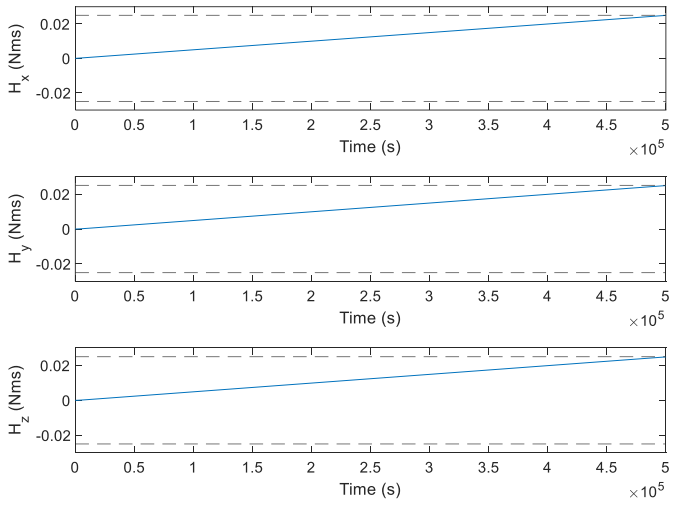

Figure 93. Reaction wheel angular momentum under constant disturbance torques

All the analysis above considers most of MAPLE SIRUP's operations and ADCS requirements from Earth launch to Iris arrival. Once the spacecraft arrives at Iris, it must orient itself so that the payload is aligned with the asteroid for taking measurements and images and the

solar panels can still see the sun for power generation. This part of the mission was not fully analyzed when designing this ADC system due to time constraints and the complexity of near-Iris operations. The existing control systems can be used with different pointing requirements to simulate these mission phases. It is recommended that future projects consider these requirements and provide an in-depth analysis for the science portion of the mission.

8 Environment

Mission longevity and orbital parameters are limited by the physical properties and limits of the spacecraft. Each component has a survivability rating that provides guidelines for temperature, vibration, radiation, and other categories. If the components experience conditions beyond these guidelines, then they might fail, leading to the end of an important mission. It is the environmental subsystem’s goal to protect the spacecraft from these hazards.

8.1 Environmental Effects

As discussed in Environment, the satellite will encounter charged particles, thermal loading, space debris, and strong magnetic interference with its components. Any of these issues can be fatal to the mission’s success.

8.1.1 Vacuum

The vacuum of space causes outgassing, which is the release of volatiles from materials. These particles can then deposit on surfaces of the spacecraft, especially cold surfaces. Since the payload will be facing away from the Sun during the satellite's trajectory, it is most likely the coolest external surface of the spacecraft. These particle deposits can affect the optical properties of the payload surfaces and could jeopardize the mission. To combat this issue, the team has researched the properties of the spacecraft materials and chose materials that are less likely to outgas or have been flight-proven without outgassing issues. In addition, the payload was placed opposite from the propulsion thrusters to reduce iodine condensation on sensitive equipment.

8.1.2 Thermal Extremes

Thermal shock is not a large concern because the satellite is on an interplanetary trajectory for the majority of the mission. Satellites that orbit Earth are subject to frequent periods of sun and eclipse, the transition between the two conditions will produce a significant fluctuation in

heat flux on the spacecraft. These fluctuations lead to material degradation. Although MAPLE SIRUP begins its mission in GEO it quickly begins the interplanetary leg of the mission, where there will not be periods of eclipse; therefore, thermal cycling will not be a significant concern for the spacecraft. However, the satellite will experience longer durations of sun exposure which may warm some surfaces of the spacecraft. On the other hand, surfaces that do not face the sun will be exposed to the cold of deep space which will draw heat away from components. It is important to regulate the internal temperatures of the spacecraft since the heat can radiate from the outer surfaces towards the inner surfaces. In-depth thermal analysis can be found throughout Section 9.1. Each electronic component has an operations temperature, at which the device functions properly, and a survivability temperature, where the properties of the material and circuitry are reaching their physical limits before failing prematurely. Also, each fluctuation in heat degrades the material properties causing hardness or brittleness of the satellite [88]. Every material in the spacecraft has a unique coefficient of thermal expansion (CTE), meaning each part of the spacecraft will expand or shrink at different rates. By choosing metals such as 6061-T6 or 7075 aluminum that have low CTE, it will ensure the spacecraft structure is stable throughout the mission. Also, when modeling the chassis of the satellite, it is imperative to account for this extra expansion and contraction.

8.1.3 Space Debris

As satellites collide, implode, or retire, they leave behind large amounts of material that hinders new satellite launches. These over 500,000 pieces of “space junk” create a hazard for spacecraft since it is difficult to locate and avoid every single piece of junk [89]. Satellites and space junk are traveling at 18,000 miles per hour in LEO so if a collision occurs it can destroy valuable equipment. The MQP team has chosen to use the MSI PODS rideshare program which

would carry MAPLE SIRUP to ~300 km above GEO. By doing so it would allow the spacecraft to save weight and avoid collisions with larger space junk.

Micrometeorites can travel at over 60 km/s. If one were to strike the spacecraft it could lead to craters on the spacecraft, spalling of coatings, or damage solar cells. Since the micrometeorites follow an orbit, they would likely collide with surfaces adjacent to the spacecraft's ram direction. One way to reduce damage from Micrometeorites is to ensure the solar array is directional and faces tangent to the velocity vector for the majority of the mission. In addition, all mission-critical components should be placed within the frame of the spacecraft, preferably within its separate protective containment.

8.1.4 Magnetic Fields

The magnetic field of Earth and other bodies may interfere with crucial electronic components. Sensitive electronics like the attitude control system, the onboard computer, and the payload would normally need to be shielded from magnetic interference so that the spacecraft can accurately deliver and receive information [90]. This will not affect MAPLE SIRUP since it is not orbiting Earth for the majority of the mission. However, this will affect the ADCS system since it can no longer determine its position through Earth’s magnetic field. The inclusion of star trackers is necessary to compensate for this lost functionality and is discussed in more detail in Star Tracker.

8.1.5 Space Plasmas

Atomic Oxygen, or AO, is produced when ultraviolet (UV) radiation reacts with molecular oxygen in the upper atmosphere. Since UV radiation is plentiful in space it is important to understand how AO oxidizes many metals and materials containing carbon, nitrogen sulfur, and hydrogen bonds. AO can be described as a bleaching process. Since MAPLE SIRUP is made of

different materials, the components need to be protected with coatings such as silicon dioxide or glass. These materials have already been oxidized, making them immune to further degradation. The team used MLI film that can be wrapped around components to protect it from the harsh space environment.

Plasma is a high-energy particulate and is composed of positively charged oxygen ions and free electrons. Electrons can impact any surface of the spacecraft whereas ions can only impact leading edges which can cause ion sputtering, arcing, and parasitic currents in solar arrays. Plasma activity is still relatively unknown but affects large amounts of communication networks. To prepare for plasma and particulate radiation, the solar arrays have been sized in anticipation of material degradation. If the solar arrays were to be degraded too much, then it may be impossible to run all payloads and computers at the same time when orbiting 7 Iris.

8.1.6 Radiation

Similar to AO, UV radiation is plentiful in space but leads to the darkening of surfaces. The particles can damage polymers by cross-linking and hardening the material or chain scission which weakens the materials. Particle radiation occurs from galactic cosmic rays, solar proton events, and radiation belts. AO and UV radiation often trump the side effects of ionizing radiation, but ionizing radiation can influence avionics by causing bit errors. The total non-ionizing dose is the damage to solar cells or materials due to ionosphere particles colliding with the satellite and dislodging atoms out of their lattice. [10] This can be mitigated by choosing electronics that are radiational tolerant (RAD-hard) or by shielding them from radiation. This could also disrupt traditional ADCS systems by causing an excess of error.

8.2 Environmental Analysis

Systems Toolkit (STK) is a powerful software tool that can be used to simulate the environments of a satellite's orbit. With varying density models, it allows a team to accurately model and graph drag, temperature, magnetic flux, and power generation from solar panels. STK is limited in its ability to model most environmental effects beyond 120,000km from Earth. Since our mission is far from Earth and not every area of space is known, it is crucial to account for the unknown and protect the spacecraft adequately for the longevity of the mission.

Previous MQPs have completed a drag analysis and its effects on fuel consumption, but no team has completed an in-depth analysis of the effects of radiation on the spacecraft. Also, our team is the first MQP satellite team to attempt an interplanetary mission. Since our trajectory is so long, we will encounter large variations in the space environment especially as we arrive at our target asteroid 7 Iris.

8.2.1 Models

Figure 94 shows the geomagnetic indices that MAPLE SIRUP will experience on its mission to 7 Iris. The data was collected from STK's Space Environment Effects Tool (SEET). Two variables can be used to measure geomagnetic activity, the Ap and Kp indices. The Ap index is the measure of the general level of geomagnetic activity over the globe for a given day. The Kp index is the global geomagnetic activity index based on 3-hour measurements from ground-based magnetometers around the world. The range of the Kp index is from 0 to 9, 0 being quiet activity and 9 being a very major storm. MAPLE SIRUP will experience a maximum of ~4 meaning active magnetic activities on the satellite. As the spacecraft's trajectory goes away from the Earth and Sun, the magnetic indices decrease. The range of Ap index is 0 to 400, 0 being quiet and 400 being a very major storm. The analysis shows a maximum Ap index of ~26

and the value decreases as the spacecraft distances itself from the Earth and Sun. It needs to be noted that STK is not capable of correctly calculating the magnetic effects on MAPLE SIRUP beyond the 120,000km limit. Therefore, these calculations can only be of reference for near-earth operations. In general, the further away from Earth we are the less Geomagnetic interference there will be, so it is not a topic of concern.

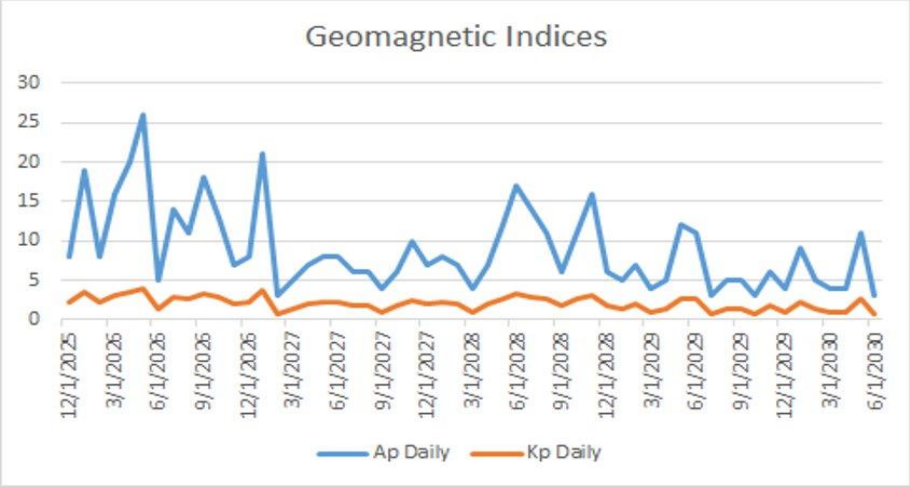

Figure 94. Geomagnetic Indices along MAPLE SIRUP's Trajectory

The below chart supports Figure 103 which shows the surface equilibrium temperature of several metal finishes over the lifetime of the mission. Figure 95 below shows the change in temperature of MAPLE SIRUP's chassis along with the mission lifespan. The simulation used a 0.25m^2 area 6061-T6 aluminum plate with an absorptivity of 0.031 and emissivity of 0.039. The graph shows that the maximum temperature of the plate was 101.421 degrees Celsius and at the end of the mission it had a low of -22.935 degrees Celsius. This confirms the necessity to have active and passive thermal control as described in Section 9. Thermal Control.

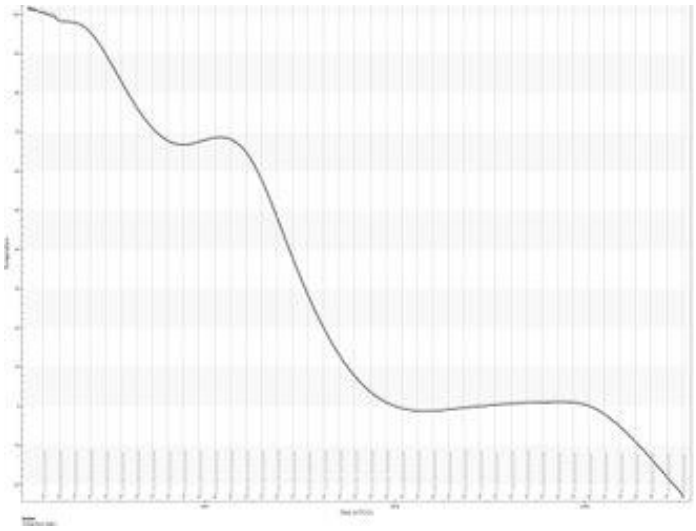

Figure 95: Temperature Simulation of Chassis in STK

The following two figures demonstrate radiation's effect on a spacecraft. To limit material fatigue, key components will be wrapped in an MLI blanket allowing for thermal control and environmental protection. STK has limited ability to perform radiation analysis so both of the following graphs utilize an aluminum detector since most MLI blankets have an aluminum external sheet. Figure 96 shows radiation dosage relative to shielding thickness. With a shielding thickness of 82.5 mills, aluminum takes on 190.061 rad per day. With a thickness of 232.5 mills it takes on 1.42254 rad per day and with 457.5 mills it takes on 0.574509 rads per day. The graph shows that radiation dosage drops exponentially as the shieling thickness increases.

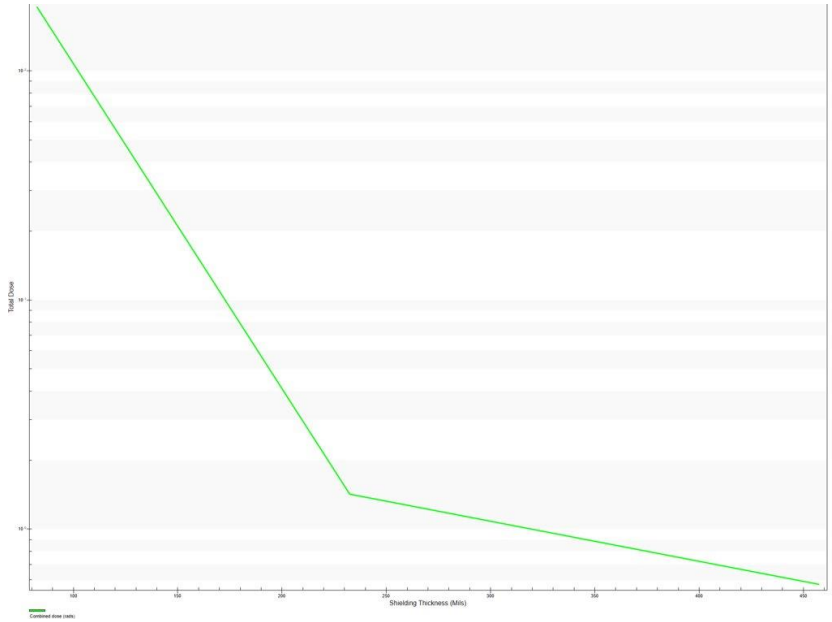

Figure 96: Radiation Dosage Relative to Shielding Thickness (Aluminum)

Figure 97 shows the total ionizing dosage over the lifetime of the mission. There are three lines on the graph representing different shielding thicknesses. Since STK is only able to use preselected materials, it is not possible to test MLI, but aluminum serves as an adequate substitute. The line of interest is the top green line which represents a 5mm thick sheet of aluminum (196.85 mills). The last known radiation dosage at STK's 120,000 km limit was 3.33017 rad per day. When extrapolating this measurement over the life of the mission, MAPLE SIRUP will have a total ionizing dosage of 3.916 Krad. This dosage is not a concern for the payload nor the spacecraft's internal electronics since the outer MLI blanket will absorb the radiation. In addition, the payload components remain operational at total ionizing dosages that far exceeding 3.916 Krad.

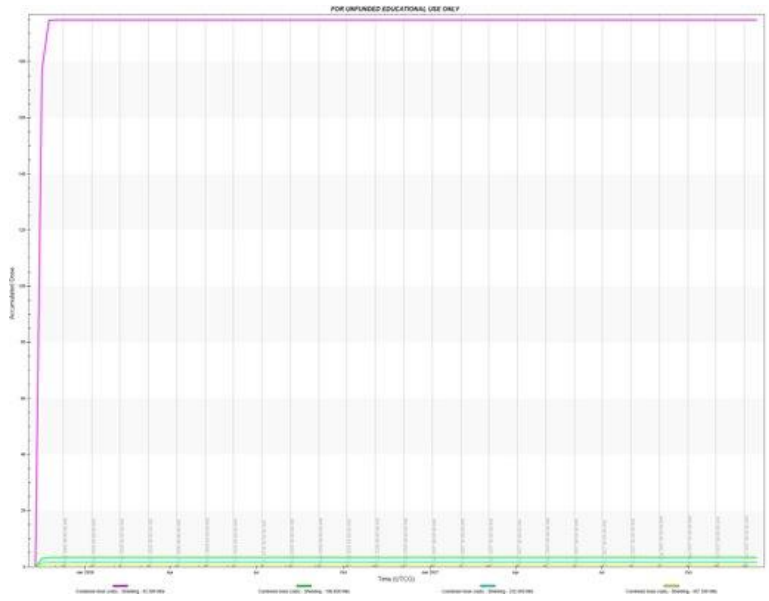

Figure 97: STK Radiation Total Ionizing Dosage Over Mission Lifetime

9 Thermal Control

The deep space and near-7 Iris thermal environments are significantly different from those encountered near Earth, presenting unique challenges for managing the temperature of spacecraft [12]. This section covers the thermal control subsystem in detail, including background information, simple and simulated analysis, and component selection.

9.1 Thermal Control Background

To understand thermal control systems, the mechanisms of heat transfer must be understood. While each of these mechanisms do not play an equal role in the design of a spacecraft, a full understanding of simple thermal mechanics allows for more rigorous analysis and design of components and system integration.

9.1.1 Conduction and Convection

There is no significant atmosphere in space, meaning that spacecraft are unable to shed heat into the local environment through conduction and convection [13]. Convection is the process of hotter fluid rising and colder fluid sinking to a heat source, where the cold fluid is subsequently heated, and the process continues. It is described by the equation

$$q = hA\Delta T \tag{9.1}$$

where q is heat dissipated, A is the surface area, h is the heat transfer coefficient, and ΔT is the temperature change [91]. Conduction is the transfer from more energetic to less energetic particles in contact with each other, as described by

$$q = \frac{kA}{\Delta x}(T_1 - T_2) \tag{9.2}$$

for a symmetric rectangular body, where k is thermal conductivity [91]. Both processes require fluid or particle contact with a body, transferring energy to the surrounding environment. Instead, spacecraft can only exchange heat through radiation, the emission and absorption of energy from its surfaces at a much lower rate than either convection or conduction [12]. Radiators are devices that radiate heat from their large surface area into space as infrared radiation, as described by

$$q = \varepsilon \sigma A T^4 \tag{9.3}$$

where q is heat dissipated, ε is the emissivity of the panel, σ is the Stefan-Boltzmann constant, A is the surface area of the panel, and T is the absolute temperature of the panel [91]. This makes spacecraft in direct sunlight prone to overheating since it cannot easily reject heat. Conversely, spacecraft tend to rapidly lose heat when out of sunlight, transitioning quickly from extreme heat to extreme cold. A spacecraft without sufficient thermal control systems can reach temperatures as low as -150 ℃ and as high as 150 ℃ in Earth orbit [5]. When a spacecraft rapidly shifts between these extremes it is called “thermal shock” and is one of the most intense mechanical loads that a spacecraft can experience regularly [12]. During its four-year mission, as the spacecraft travels from a geostationary orbit to the asteroid belt, it will be subject to a gradually changing thermal environment. In a geostationary orbit, the sun is not the only source of thermal radiation – both the Earth and moon reflect sunlight and can result in distributed heating across a spacecraft [92]. Because MAPLE SIRUP will be deploying from GEO, the flux received from the Earth and moon is minimal. However, periods where the Earth and moon move between the spacecraft and the sun result in shadowing and thermal shock. The spacecraft is suddenly only exposed to the cold ambient temperature of deep space and not incoming solar radiation. Once outside of the Earth’s sphere of influence, the spacecraft’s primary source of thermal flux will be

the sun [12]. The amount of exposure will decrease over time as the spacecraft flies farther from the sun.

9.1.2 Thermal Equilibrium

The primary method of heat transfer in the space environment is through radiation emitted from all bodies due to the movement of energetic particles within them. A body is in thermal equilibrium when it is outputting the same amount of thermal radiation as it is receiving. When a body is emitting and absorbing radiation with complete efficiency in this state, with wavelength determined by emittance, it can be described as blackbody radiation [12]. All radiation obeys the inverse-square law of intensity. As radiation travels outwards from its source it decreases in intensity quadratically as described by

$$\phi = \frac{P_{out}}{4\pi r^2} \tag{9.4}$$

where ϕ is the flux in power per unit area, P_{out} is the power output of the radiating body at its surface, and *r* is the distance from the body to the surface through which the flux is received [91]. The effective incoming flux on a surface is also modified by the view factor, a quantity that accounts for a difference in angle between incoming radiation and the body's surfaces. For a flat body, such as the side of a spacecraft, the view factor can be defined as

$$F = \left(\frac{R}{r}\right)^2 \cos(\beta) \tag{9.5}$$

where F is the view factor, R is the radius of the emitting body, and β is the angle from an axis perpendicular to the plane of the spacecraft's surface to the direction of the emitting body [12].

For a body in thermal equilibrium, this can be expanded to describe both the absorption and radiation processes as

$$A_{inc}\phi\alpha = A\varepsilon\sigma T^4 \quad (9.6)$$

where A_{inc} is the area receiving direct sunlight modified by the view factor *F*, α is the absorptance of that surface, and ϕ is the solar flux at the spacecraft's current distance from the sun [93]. Therefore, when the spacecraft is in an equilibrium state, it has a uniform surface temperature dependent on the distance from the sun, surface area facing the sun, total surface area, emittance, and absorptance as described by

$$T = \left(\frac{A_{incident}\phi\alpha}{A\varepsilon\sigma}\right)^{\frac{1}{4}} \quad (9.7)$$

[93]. This model does not account for internal heat sources such as active electronics, differences in absorptivity based on varying surface materials and finishes, or imperfect heat transfer through the interior of the body. However, it remains useful for understanding the basic processes behind passive thermal control of a spacecraft.

Small spacecraft generally do not have room for complex thermal control systems. This necessitates novel approaches to maintaining internal spacecraft temperature [94]. By applying emissive coatings to spacecraft body panels, existing structural components of a spacecraft can act as their own radiators instead of requiring additional hardware [95]. This includes body paneling, structural members, and deployable solar panels, all of which provide additional surface area to be used for radiating heat.

9.1.3 Surface Finishes

Passive and active thermal control mechanisms are utilized by spacecraft to maintain thermal stability. Passive systems function without needing power or commands from the flight computer [92]. The simplest of these are surface finishes. Many different finishes exist to fulfill a variety of purposes and are generally divided into paints, which are applied as a liquid, and coatings,

which are applied as a solid [96]. The application method does not change the performance of the finish, only the manufacturing techniques required. Finishes modify a surface's emittance ε and absorptance α, fractions governing how quickly a surface radiates and absorbs heat. Specialized finishes, such as nonspecular white paint, have a solar absorptance value between 0.05 and 0.2, decreasing the rate at which the surface heats up when exposed to direct sunlight [96]. These finishes can also increase the emittance of surfaces, with values of up to 0.92, increasing the efficiency of the radiation process described above. Black surface finishes likewise have emittance on the order of 0.91, but also increase absorptivity at nearly 0.98, making them useful for when components will require passive heating. Grey finishes lower both absorptivity and emittance to values on the order of 0.25, but are less commonly applied than white and black [96]. The behavior of certain coatings can be seen in Figure 98.

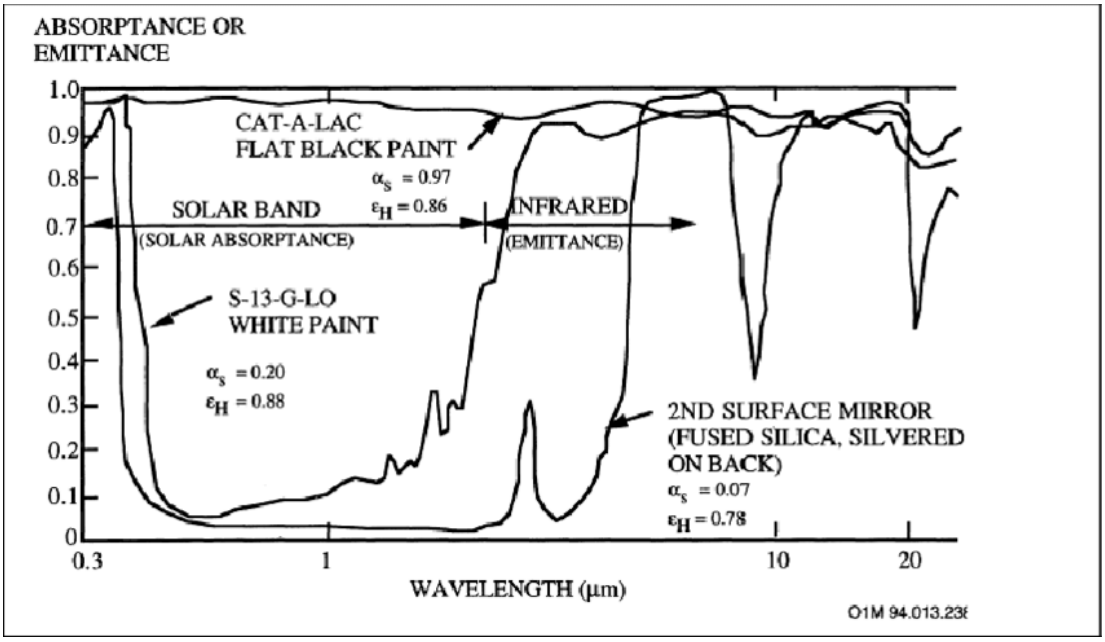

Figure 98. Absorptance and Emittance by Wavelength [12]

In situations where a traditional paint or coating-based finish is not practical, other materials can be applied to achieve similar results. Thermal tapes made from aluminized or silvered

Kapton are common in smaller spacecraft. These are easily applied to irregular surfaces and do not require as many specialized tools as traditional finishes [13]. Treating the bare metal can also provide a finish, although these tend to have very low emittance values compared to their alternatives [93]. The properties of a variety of common surface finishes can be seen in Figure 99, plotted by possible absorptance versus emittance values.

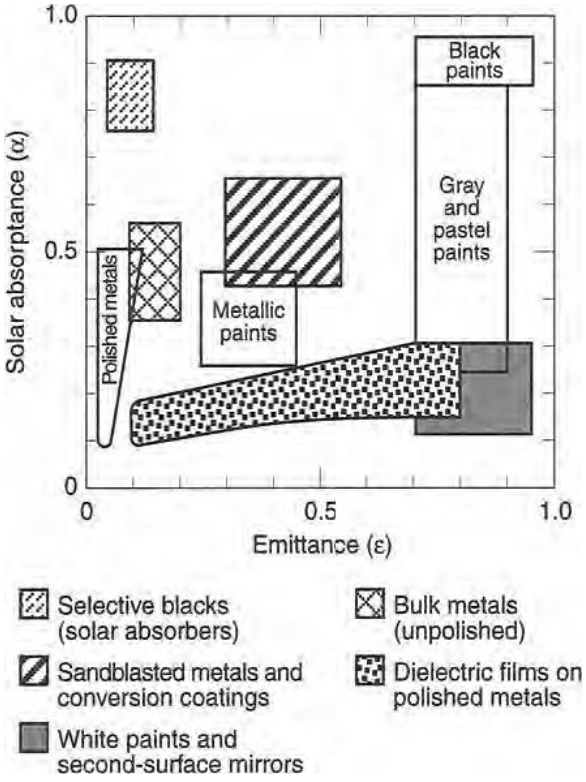

Figure 99. Surface Finish Properties by Type [104]

9.1.4 Heat Exchangers

Thermal transport or exchanger systems are used to manage where heat is transported inside of a spacecraft and come in both passive and active varieties. Heat pipes are often paired with active heat exchangers, using liquid flow with an evaporator and condenser to manage heat across components [92]. Thermal straps, as seen in Figure 100, are passive thermal exchangers made of many layers of thin conductive material stacked closely together and used to connect a heat source to the location that the heat must be transported between. Due to their lightweight

and lack of power requirements, thermal straps are preferable for small satellite missions that use high-power electronic devices [94]. In most small spacecraft, thermal straps will be used to share the heat with the exterior of the spacecraft to be radiated into space.

Figure 100. Flexible Thermal Strap [94]

9.1.5 Insulation

Insulation is also important for maintaining spacecraft temperatures. Multi-Layer Insulation (MLI) serves to insulate components and allow them to maintain temperatures without gaining or losing excess heat [13]. MLI is composed of repeating thin layers of plastic films, with reflective aluminized mylar on the exterior surfaces. While commonly used on large spacecraft, the efficiency of MLI decreases with size due to the decrease in surface area contact between the layers, making it less ideal for small spacecraft [13]. While this loss in efficiency can be compensated for by compressing the MLI blankets, some spacecraft opt for simpler and cheaper solutions [97]. Instead, low emissivity metallic tapes and coatings provide lightweight and efficient insulation for the interior of small spacecraft [13].

Some spacecraft, including small CubeSats, have been designed to use novel insulators like Aerogel. Insulating blankets made from this low-mass material are functional for temperatures between -200 ℃ and 200 ℃ [98]. Aerogel has significantly lower thermal conductivity than other insulating materials with its thermal conductivity of 0.014 W/m*K, being over 5 times less conductive than Polyimide, which is present in Kapton tapes [98]. As Aerogel technology matures, it is being integrated into MLI blankets for improved insulation alongside providing spacecraft with extra micrometeoroid protection [99].

Insulation can significantly lower the power requirements of the thermal control system by minimizing the need for powered heater units. Powered electronics generate heat and must be at a specific temperature range to function, as detailed in Section 9.1.2 By balancing the amount of insulation present around electronic components with the efficiency of the spacecraft's radiators, the system can reach a state where the heat generated by active electronics is enough to keep them in their designated temperature range [97]. In this case, power going to the onboard electronics can be controlled to maintain necessary temperatures, instead of budgeting extra power to electric heater units.

9.1.6 Active Thermal Control

Active thermal controls heat or cool the spacecraft's components through more complex mechanisms, often requiring power and management by the flight computer. The simplest active thermal control systems are patch heaters [92]. These are resistors placed inside of overlapping insulated sheets or tape. By running current through the patch heater and causing it to warm, the local temperature can be regulated. The area affected by a patch heater is small, so they are primarily used for pre-warming electronics and other temperature-sensitive components to their operating temperature.

Radiators are necessary for removing excess heat but operate at a steady rate based on their surface area and temperature as described in Eq 9.5. To allow for more precise control of the radiating area, a spacecraft can make use of louvers. These devices are a series of pivoting shutters installed over a radiator surface. They are controlled with bimetal springs, with each metals' thermal expansion coefficient resulting in specific movement at corresponding temperatures [100]. The spacecraft's temperature can be passively controlled using this system. The springs open and close the louvers at certain boundary temperatures, increasing and decreasing the radiator area at the upper and lower bounds, respectively [100]. The construction of an array of louvers using bimetal actuator springs can be seen in Figure 101.

For missions where sunlight availability is low, meaning both colder temperature and lower available power, radioactive elements are used as heaters [13]. Radioisotope Heater Units, or

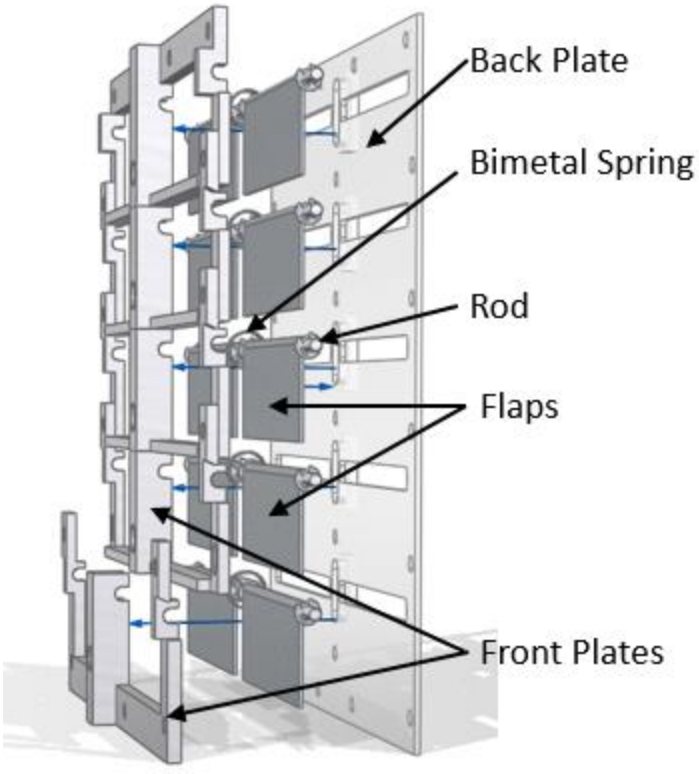

Figure 101. Thermal Louvers for a 1U CubeSat [100]

RHUs, are capsules weighing in at less than a gram containing a small piece of radioactive plutonium. They produce a steady output of heat and do not require any control systems or power input and can last for decades [13]. However, access to the elements necessary for radioisotope heating is difficult to arrange, restricting RHUs to large flagship missions. Additionally, the risks involved with launching radioactive material into space pose restrictions on launch sites and trajectories.

9.1.7 Target Temperatures

The reason for thermal control on a spacecraft is the sensitivity of mechanical and electronic components to temperature. All components have a survival temperature range as to not sustain permanent damage [12]. They also have an operating temperature range and a "turn-off" temperature where the device can be powered on outside of design specifications. [12]. Finally, a thermal deformation upper bound is when a device's geometry will be physically altered, acting as an absolute limit on allowable temperature [12]. These temperature ranges vary on a component-by-component basis, but general trends and ranges for common components can be identified, as displayed in Table 14.

	Operating Temperature		Turn-Off Temperature		Survival Temperature	
Component	**Lower Limit**	**Upper Limit**	**Lower Limit**	**Upper Limit**	**Lower Limit**	**Upper Limit**
Digital Electronics	0 °C	50 °C	-10 °C	50 °C	-55 °C	125 °C
Analog Electronics	0 °C	45 °C	-10 °C	50 °C	-55 °C	125 °C
Batteries	0 °C	20 °C	-10 °C	30 °C	-10 °C	30 °C
Momentum Wheels	0 °C	40 °C	-5 °C	45 °C	-20 °C	50 °C
Antennas	-90 °C	100 °C	-90 °C	100 °C	-90 °C	150 °C
Solar Panels	-100 °C	120 °C	-100 °C	125 °C	-100 °C	125 °C

Table 14. Weighted Predicted Component Survival Temperatures [12, 91]

As mechanical structural components are much less sensitive to temperature changes than electronics and instrumentation, the majority of any given thermal control system is dedicated to electronics [91]. Generally, the most temperature-sensitive components of a spacecraft are the batteries and scientific instrumentation [12]. Modern high-density batteries, such as lithium-ion polymer batteries commonly used in CubeSats, have a smaller survival range than most of the electronics they power and therefore act as the limits of the electronics bay temperatures.

9.1.8 Analysis Tools

Complex thermal analysis is not possible to do by hand, instead of requiring numerical differential equation solvers. *COMSOL Multiphysics* is two software systems that utilize finite element analysis to create these types of physics simulations, for fluid, thermal, electrical, and dynamic structural systems. The heat transfer module of *COMSOL Multiphysics* was used by the thermal control sub-team due to ease of integration with existing CAD models and data, and a precedent set by previous MQP teams in using the software for their spacecraft's thermal analysis [92].

9.2 Preliminary Analysis

Before beginning a full thermal analysis of the spacecraft, the nature of space thermal environment must be determined. Additionally, a simple analysis of thermal control techniques may show which materials and systems will be effective and necessary. After determining the thermal environment and the thermal control systems to be implemented, analysis can be continued on a simulated physics model in *COMSOL*.

9.2.1 Incoming Solar Radiation

Solar radiation is the primary external heat source of a spacecraft in deep space. As the power output of the sun is known, based on the solar constant *s* and the Earth's distance from the sun *r*, the flux at any point in the solar system can be estimated.

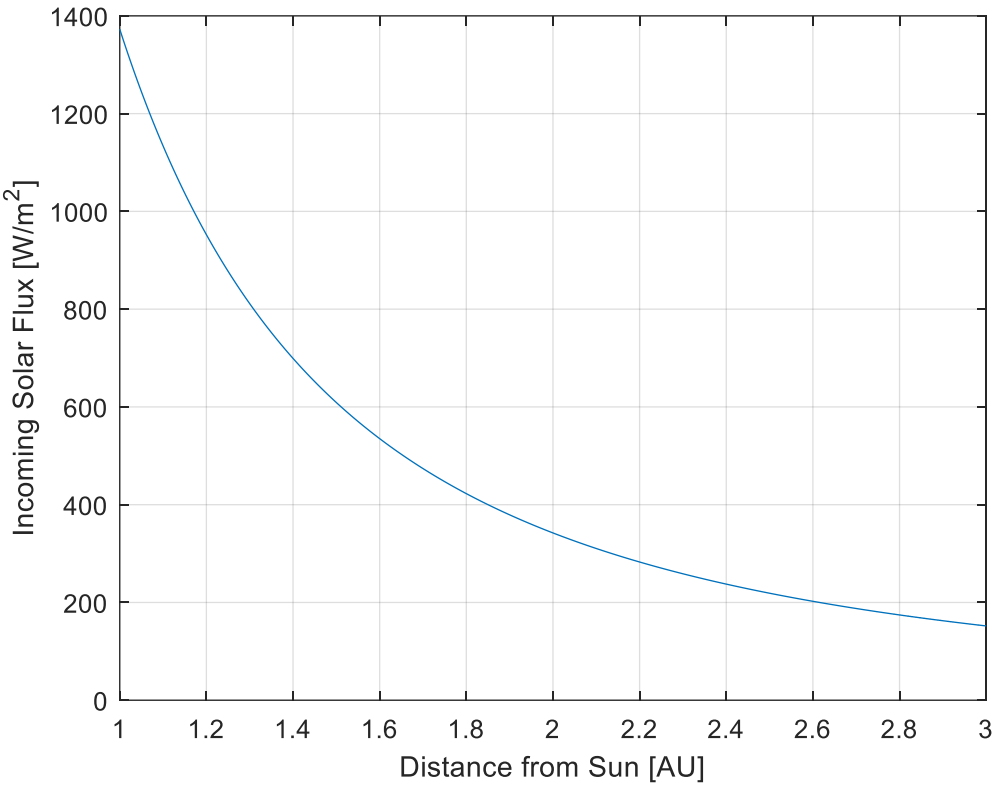

Figure 102. Incoming Solar Radiation

As seen in Figure 102, the incoming solar thermal flux decreases nonlinearly as the distance between the spacecraft and the sun increases, obeying the inverse square law. The spacecraft will therefore need to be designed to survive with a maximum incoming solar thermal flux of 1367 W/m^2 when at Earth, and a minimum solar thermal flux of 317 W/m^2 when at Iris.

9.2.2 Idealized Blackbody Analysis

To understand the effects of different surface finishes on the blackbody radiation behavior of a spacecraft in thermal equilibrium, a model was created of a simplified perfectly rectangular

spacecraft with dimensions of 1 m by 0.5 m by 0.5 m, with a deep space thermal background of 2.9 K. The spacecraft is assumed to be isothermal and have no internal heat sources. Using equations 9.4 and 9.7, a simple model can be constructed.

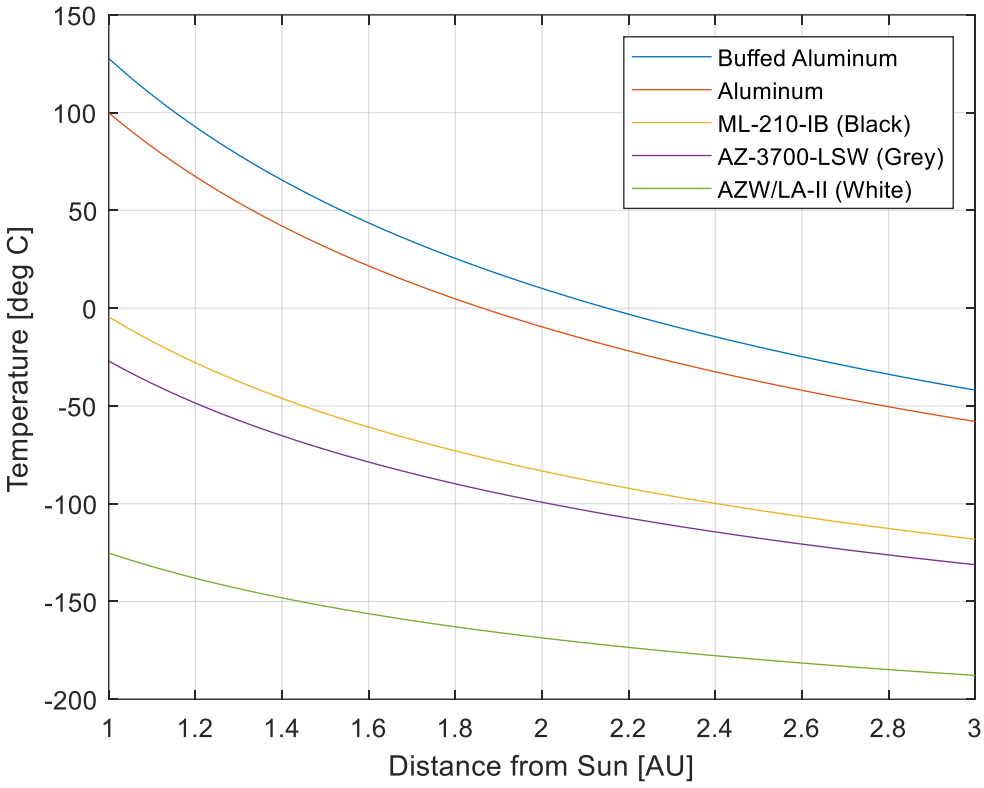

Figure 103. Thermal Equilibrium Temperature During Spacecraft Flight

While this data is not representative of the actual spacecraft, it demonstrates the general effect that surface finishes have on spacecraft thermal control. As expected, based on the results shown in Figure 103, the equilibrium temperature decreases as the spacecraft travels further from the sun. Because this model was constructed assuming a uniform finish, it is also not representative of a spacecraft where different surfaces are covered in different materials. By varying coverage, the equilibrium temperature can be adjusted to fit mission specifications.

9.3 COMSOL Analysis

The physics simulation software environment *COMSOL Multiphysics* was used for thermal simulation of both 2D and 3D models of the spacecraft. This software allows for models created in CAD programs such as *SolidWorks* to be imported. Meshes can be generated from these models, which *COMSOL* can analyze using a variety of built-in toolkits. For the problem of thermal analysis of a spacecraft traveling through interplanetary space, the *Heat Transfer in Solids* and *Surface-to-Surface Radiation* modules were used. These simulate the physics of heat transfer between contacting surfaces and between spaced surfaces via radiation, respectively. Space is treated as a vacuum for these simulations, and therefore convection is not considered.

9.3.1 Configuration

To maintain consistency across multiple simulations, the *Heat Transfer in Solids* and *Surface-to-Surface Radiation* modules were configured consistently. As the spacecraft is in an interplanetary trajectory and not a close planetary orbit for the majority of its flight time, the solar constant, planetary IR flux, planetary albedo, and view factor vary depending on the specific phase of the flight being simulated. Assuming the spacecraft is oriented at a 90-degree angle with incoming solar radiation in deep space, the values and equations in Table 15 were used to define the basic space environment, where *r* is the radius of the spacecraft from the Sun in units of meters.

Parameter	**Variable**	**Value**
Solar Flux	S	$\frac{3.846*10^{26}}{4\pi r^2}$ [W/m^2]
Deep Space Temp	T_{space}	2.7 [K]
Waste Heat Generation	E_{waste}	0.2

Table 15. Global Parameters

Due to the multi-year trajectory of the spacecraft, COMSOL simulation was not possible for the entire mission flight time. Instead, an analysis was conducted at specific radii from the Sun to gain an understanding of how the spacecraft's temperature changes as it moves outwards from Earth towards Iris. The distances from the Sun that analysis was conducted at are detailed in Table 16.

Analysis Point	**Radius [AU]**	**Time of Flight [days]**
Deployment in GEO	1	0
Arrival at Iris	2.1	1300

Table 16. Thermal Analysis Points

The material properties of the spacecraft components must be defined for *COMSOL* to simulate thermal conductivity and transfer inside the model. To maintain consistency across simulations, materials were selected from *COMSOL*'s material catalog and assigned to specific components as described in Table 17. For simplicity of simulation, all components were assumed to be of homogenous composition and density.

Component	**Material**
Spacecraft Frame	6061-T6 Aluminum
Bolts and Fasteners	6061-T6 Aluminum
Printed Circuit Boards (PCB)	FR-4
Solar Panels	InGaP/InGaAs/Ge
Sensors and Science Instruments	HDPE
Iodine Propellant Tank	AE81 Allite Super Magnesium
Nitrogen Propellant Tanks	6061-T6 Aluminum

Table 17. COMSOL Component Materials

9.3.2 Heat Transfer in Solids

After defining the properties of the spacecraft for the point on the trajectory being simulated, the *Heat Transfer in Solids* module was configured. The default settings for the module, *Solid*, *Initial Values*, and *Thermal Insulation* were set up first. The entire spacecraft assembly is considered to be heat-transfer solids, so no changes are made to the *Solid* setting. The temperature in the *Initial Values* setting specifies the starting temperature on every component at the beginning of the transient simulation time. This value is determined experimentally by finding the steady-state temperature of the spacecraft at a given radius from the Sun and is only relevant for transient (time-dependent) simulations. The *Thermal Insulation* setting was not changed, although some domains were overwritten by the Surface-to-Surface Radiation module.

Besides the default settings, the *Heat Flux* setting was initially added to the simulations. This setting allows for the specification of general inward heat flux on a boundary, which can be either a static value or a function. For cases where the spacecraft is oriented perpendicular to incoming solar radiation, this value was set to the solar flux S defined in Table 16. For cases where the spacecraft is not oriented perpendicular to incoming solar radiation, Equation 9.4 was used to calculate the effective incoming solar radiation on each sun-facing boundary for a given angle. This simulated the effects of the spacecraft receiving incoming solar radiation across multiple surfaces. To increase the accuracy of the studies, later simulations instead used the *External Radiation Source* module. This module instead created an incoming solar radiation flux from a specified direction, meaning it would apply to all boundaries with visibility to the source as opposed to just those boundaries specified by the *Heat Flux* module. Side-by-side tests of both modules confirmed consistency in the results when acting on the same boundaries.

To simulate the heat emitted by electronics inside the spacecraft, the Heat Source setting was used. This allows for domains within the assembly to function as a heat source, given a Q_0 value in W/m^3. All electronic components were treated as solids of constant density for these calculations. As the volume and power use of each component was known, the value could be found through algebra. While not a true description of the heat propagation within components, this approximation allowed for the overall power usage and the general effect of waste heat of components to be accounted for in the simulation. This was important to consider as the waste heat generated by components can be used to keep the electronics within their survival temperature ranges, reducing the load placed on dedicated heater systems and lowering thermal control system power requirements. For 2D simulations, these values were given in terms of watts per square meter instead.

9.3.3 Surface-to-Surface Radiation

Unlike with the *Heat Transfer in Solids* module, not all domains are selected in the *Surface-to-Surface Radiation* module. Initially, only the outwards-facing domains of the spacecraft were selected for initial *Surface-to-Surface Radiation* analysis. While all components emit and receive radiation, internal radiation has negligible influence on the temperature of components compared to contact heat transfer. By neglecting this effect, simulation time is shortened significantly, as radiation simulation is computationally intense. Later high-detail simulations incorporated the module across all boundaries after the initial simulations were validated. The *Diffuse Surface* and *Initial Values* settings were used in the Surface-to-Surface Radiation module.

The *Diffuse Surface* setting governs the behavior of boundaries as reflective radiation-emitting surfaces. This automatically calculates the view factor to other surfaces and performs the radiative analysis. The ambient temperature, T_{amb}, was set equal to the background

temperature of deep space T_{space} specified in Table 15. This was universally defined for all boundaries. Diffuse emissivity was separately defined for each emissive surface. Surface finishes are a significant influence on the spacecraft's thermal control system, and different coatings have different surface emissivity values. The values of emissivity of various surface finishes are found in Table 18. The *Initial Values* setting functions much like the setting of the same name for the Heat Transfer in the Solids module. For consistency between modules, the initial temperature set here was equal to that in the previous module.

9.3.4 Iterative Thermal Control Subsystem Design

The goal of the thermal control subsystem was to keep all components within necessary survival and operation temperature ranges while minimizing the required power and mass. An idealized configuration is sketched in Figure 104. The sizing of the thermal control subsystem, composed of surface finishes, MLI, radiators, and patch heaters, was therefore dependent on the steady-state temperatures of sensitive components during flight. An iterative process was made to size the thermal control subsystem appropriately in which the temperatures of relevant components were found, thermal control elements such as radiator surface area and heater power were changed to compensate for temperatures being too high or too low, and the simulation was run again, and the entire process repeated.

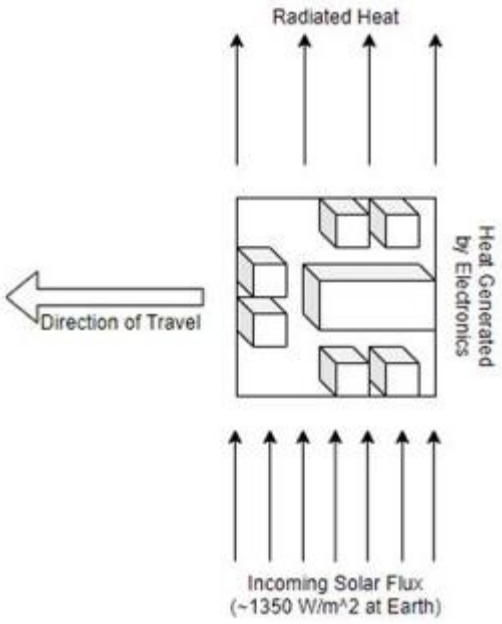

Figure 104. Thermal Control Subsystem Theoretical Design

Simple 2D analysis, while not representative of the actual spacecraft, was a useful tool for understanding the problem and quickly testing techniques and configurations. COMSOL supports analysis of 2D objects with all modules and settings that do not require 3D domains, including both the Heat Transfer in Solids and Surface-to-Surface Radiation modules. As the times required to run simulations in 2D are significantly shorter than those in 3D, simple simulations like those seen in Figure 105 were used extensively to validate concepts before integrating them into the actual model.

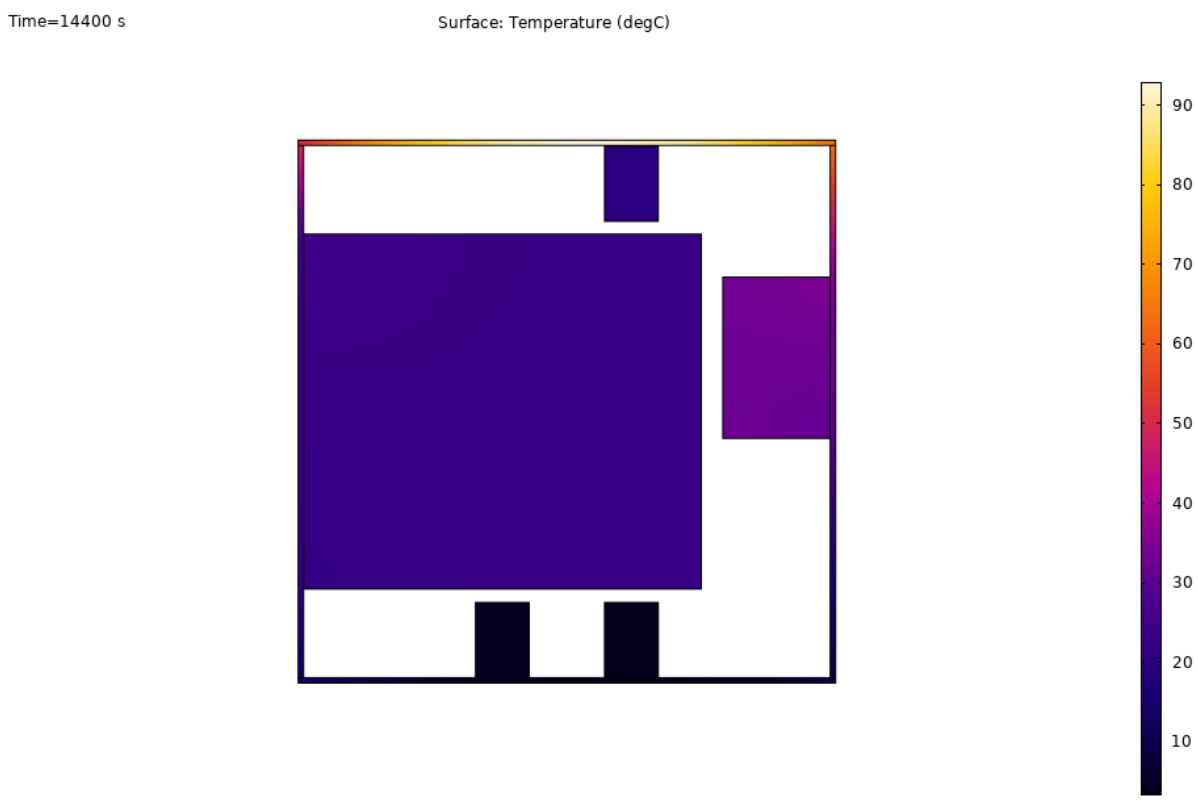

Figure 105. 2D Simplified Thermal Model

9.3.5 Spacecraft Thermal Analysis Setup

Simplifications to the spacecraft's 3D model were made to assist in simulation speed. All components of the spacecraft were replaced with simple geometries of equivalent exterior dimensions and volume. Fasteners were removed, and the surfaces they were connecting were merged into single parts if made of the same material. Attitude control thrusters, sun sensors, and other components external to the spacecraft's body were removed. Deployable solar arrays were removed from the models after determining that their effect on the temperature of internal electronics was negligible, due to their ability to act as their own radiator surface and limited thermal connection to the rest of the spacecraft. The spacecraft frame itself was the least simplified component as it acts as the primary thermal conductor in the system. Mounting holes for fasteners were removed, but cutouts and internal struts were not.

The mesh size in the spacecraft model was not uniform across the entire body, as seen in Figure 106. Sections of the frame with no connection to other components were assigned a coarse mesh. The mesh increases in fidelity closer to points where components contact the frame. This means that the temperature analysis near interfaces between components and the frame is done with a higher degree of detail without applying that same detail to potions of the model where uniform, simple temperature distribution is expected. The mesh includes some thin surfaces relative to the mesh size, increasing the risk of errors induced by mathematical singularities. This was considered when analyzing the results of all simulations. Due to their

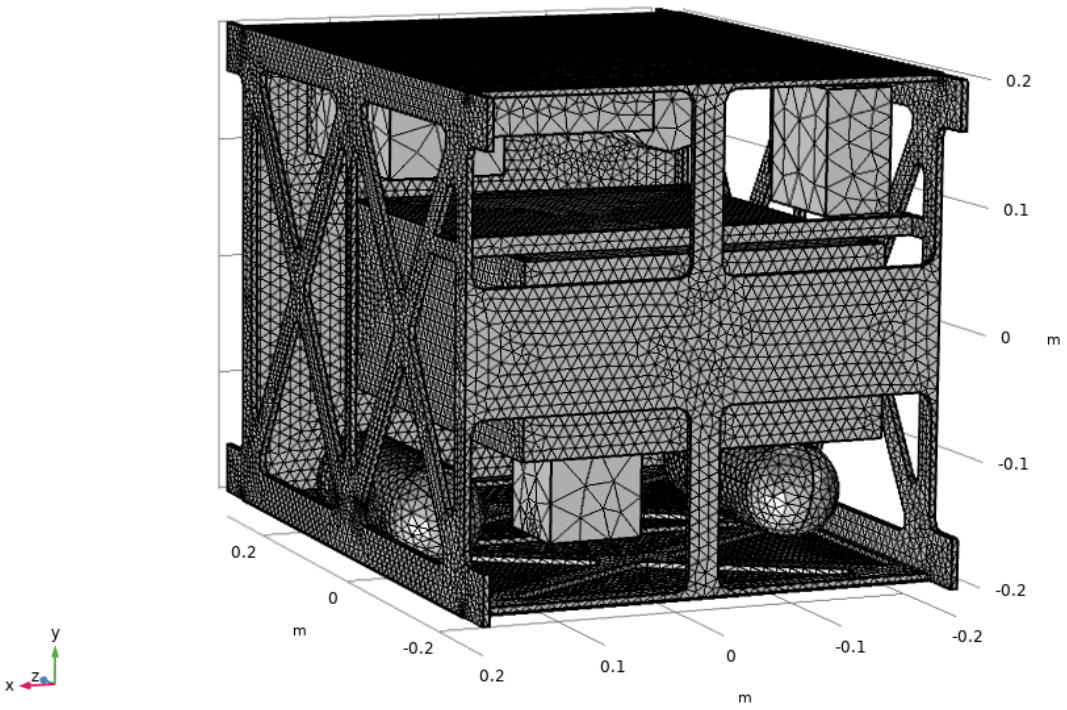

Figure 106. Spacecraft Thermal Mesh

minimal effect on the steady-state temperature of internal components and the significant increase in simulation time required for analysis, the solar arrays were excluded from the iterative simulations.

Both incoming solar radiation and the waste heat of internal electronics were considered in the 3D simulations. The power usage per component was taken from Figure 39, modified by the waste heat generation percentage in Table 15. Surface-to-surface radiation was enabled between internal faces through the *Diffuse Surface* module as seen in Figure 107. The emissivity values of the internal boundaries were controlled to approximate the effects of MLI wrapped around temperature-sensitive components. Surfaces that had a minimal effect on total heat gain and loss were neglected to aid in ease of simulation.

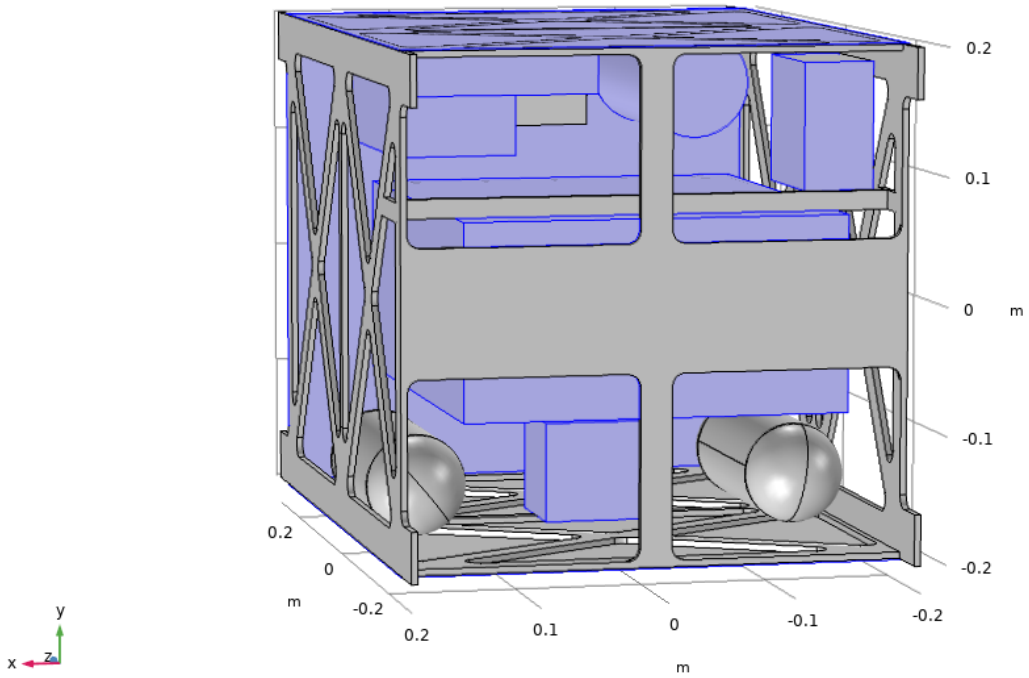

Figure 107. Spacecraft Diffuse Surfaces

9.4 COMSOL Simulation Results

After performing iterative simulation and modification of the thermal properties of the spacecraft, the thermal profile of MAPLE SIRIP for operation both around Earth and 7 Iris was found. The waste heat produced by electronic components was found to be the dominant effect

on component temperatures as opposed to incoming solar radiation. This is due to the relative thermal isolation of these components from the frame and low thermal conductivity. Given these observations, the thermal control system was designed around retaining waste heat from the electronic components to maintain steady-state temperatures in their survival and operational ranges.

To better retain heat, the *Diffuse Surface* boundaries of the electronic components were set to low emissivity values, as shown in Table 18. This was to simulate the effects of low-emissivity coatings and MLI covering the devices, allowing for significantly improved heat retention. By taking this approach to thermal control, the power requirements placed on electric heaters were significantly lowered. The effect of a closed radiator face, obstructed by passive thermal louvers, was simulated as detailed in Section 9.1.6. Higher emissivity coatings were applied to components that tended to overheat due to their small size and proportionally higher power usage per unit volume.

Component	**Effective Emissivity**
Open Radiator	0.91
Closed Radiator	0.1
Electronics Box	0.05
LIDAR	0.05
Color Imager	0.05
PPU	0.05
Reaction Wheels	0.05
IRIS DST	0.05

KRYTEN	0.05
Propellant Tank	0.05

Table 18. Effective Emissivity for Internal Radiation

A drop in steady-state temperatures of both the spaceframe and all internal components was observed as the distance from the sun increased. Two primary configurations of the spacecraft were simulated: a model where the sun-facing surfaces were coated in an extremely low absorptivity white coating and the radiators have a low emissivity, as seen in Figure 108 and

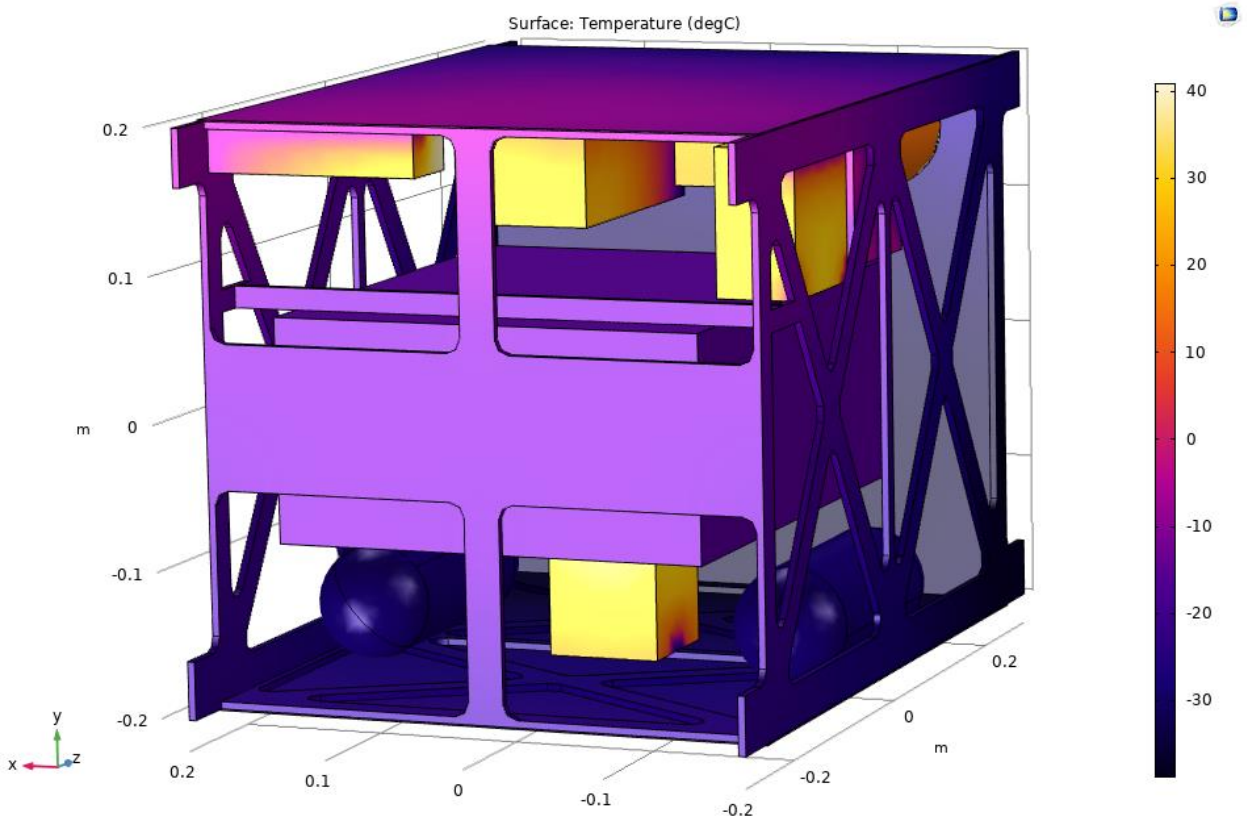

Figure 108. Steady-State Spacecraft Temperature at Earth (α = 0.25±0.05)

Figure 109, and a model where the sun-facing surfaces have moderately absorptive white-grey coatings and thermal louvers were used to lower the emissivity of radiators as the distance from the sun increased, as seen in Figure 110 and Figure 111.

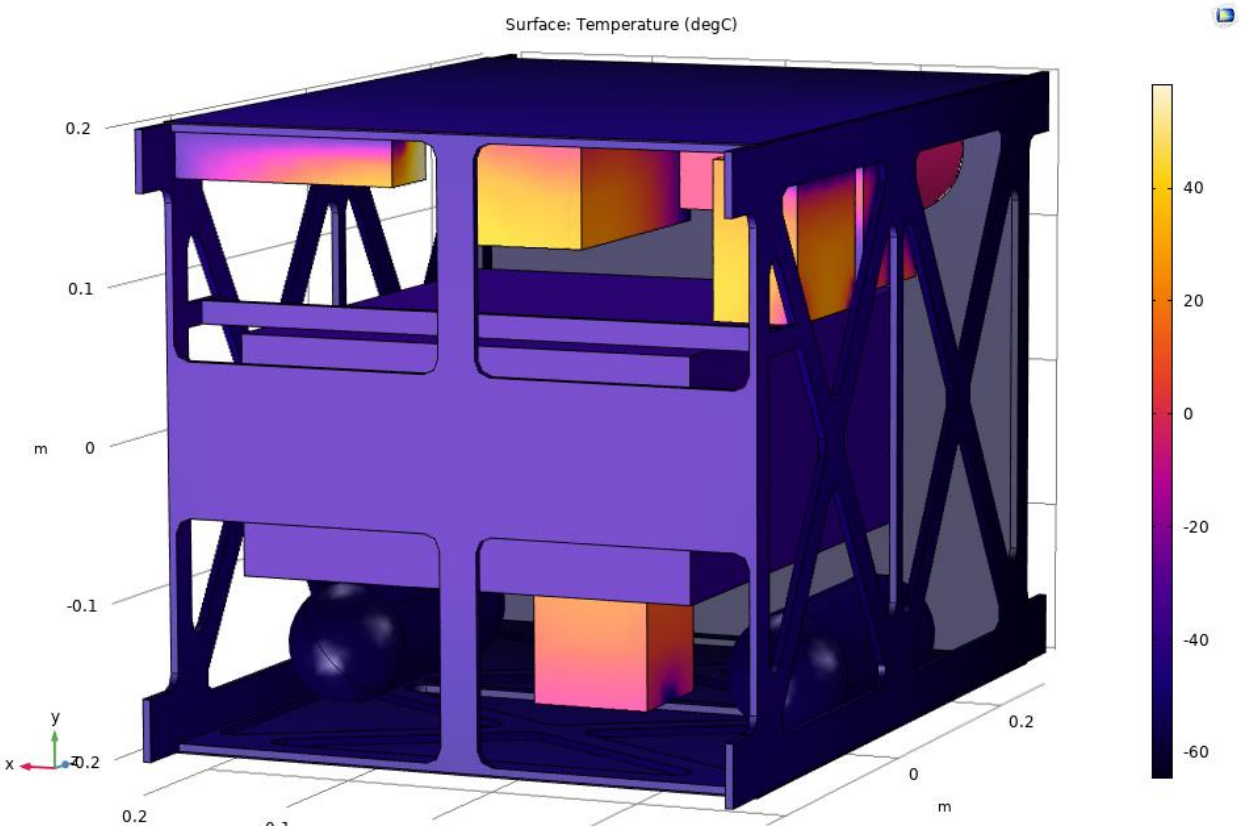

Figure 109. Steady-State Spacecraft Temperature at 7 Iris (α = 0.25±0.05)

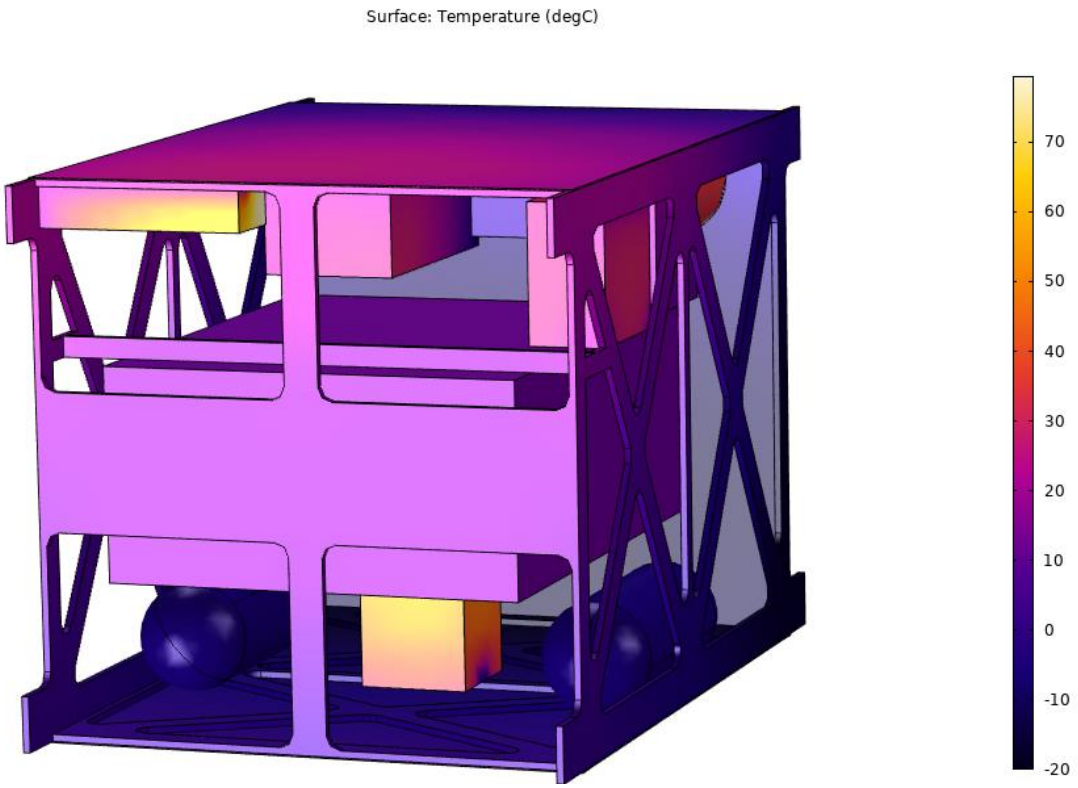

Figure 110. Steady-State Spacecraft Temperature at Earth (α = 0.50±0.05)

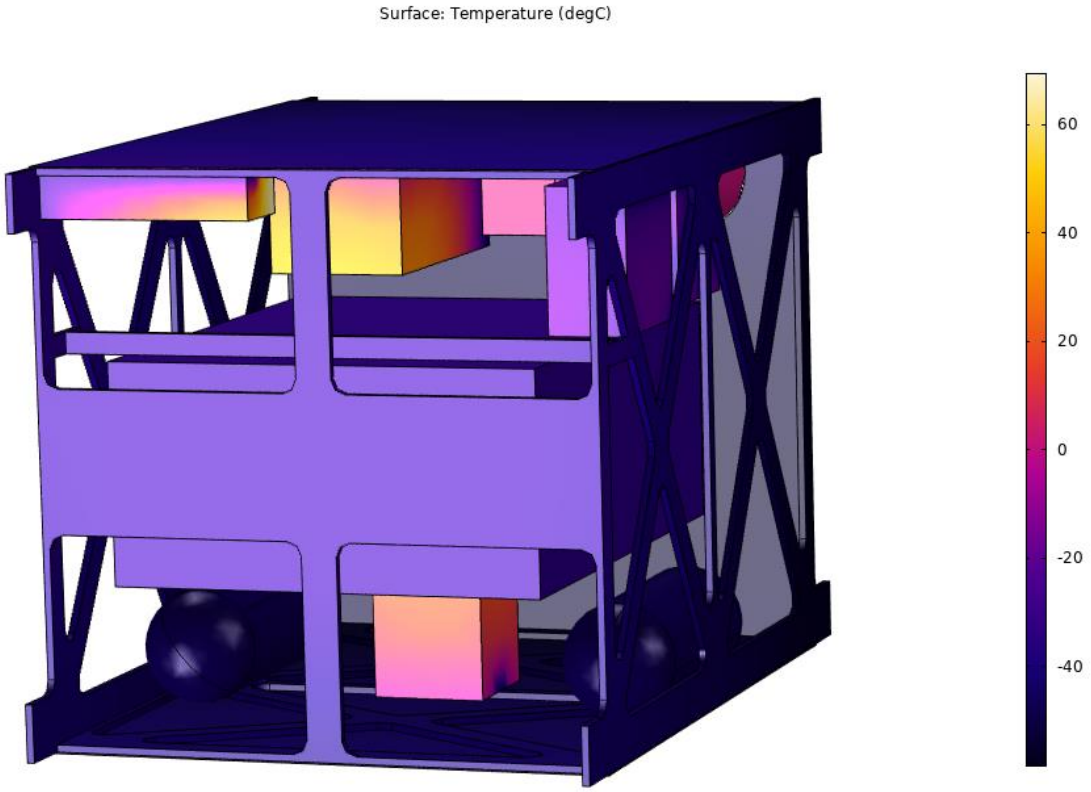

Figure 111. Steady-State Spacecraft Temperature at 7 Iris (α = 0.50±0.05)

The simulations were conducted for a steady-state case with constant solar exposure at each test distance, as MAPLE SIRUP spends most of its flight time with no obstruction between it and the sun. The necessity of sizing the thermal control system for operation with the extremely low effective external heating while at Iris, on the order of fewer than 100 W/m^2, means that the thermal control system is also effective when in eclipse.

Passive heating and heat-retention mechanisms alone were found to not keep components in their survival range for the duration of the mission. Additional heat provided by low-mass patch heaters, as detailed in Section 9.1.5, was necessary. The required additional heater power for each component was determined iteratively at the incoming solar radiation condition of Iris, the coldest part of the mission, as seen in Table 19 and Table 20. The heater powers required represent peak values, which occur when the components are in their lowest power-consumption modes.

Component	**Heating at BOM [W]**	**Heating at EOM [W]**
Electronics Box	0	3
LIDAR	2.5	6
Color Imager	0	0.5
PPU	0	3
Reaction Wheels	2	2
IRIS DST	1	2
KRYSTEN	0	4.5
Spectrometer	0	2.5

Table 19. Thermal Control Heater Power ($\alpha = 0.25 \pm 0.05$)

Component	Heating at BOM [W]	Heating at EOM [W]
Electronics Box	0	3
LIDAR	0	6
Color Imager	0	0.1
PPU	0	2
Reaction Wheels	2	2
IRIS DST	1	2
KRYSTEN	0	2
Spectrometer	0	2.5

Table 20. Thermal Control Heater Power ($\alpha = 0.50 \pm 0.05$)

The simulations revealed the temperatures that different spacecraft components reached during different phases of flight, using different thermal control schemes. The temperatures were compared with the temperature range details in Table 14 by plotting the total range of temperatures observed per component throughout the flight as seen in Figure 113 and Figure 114.

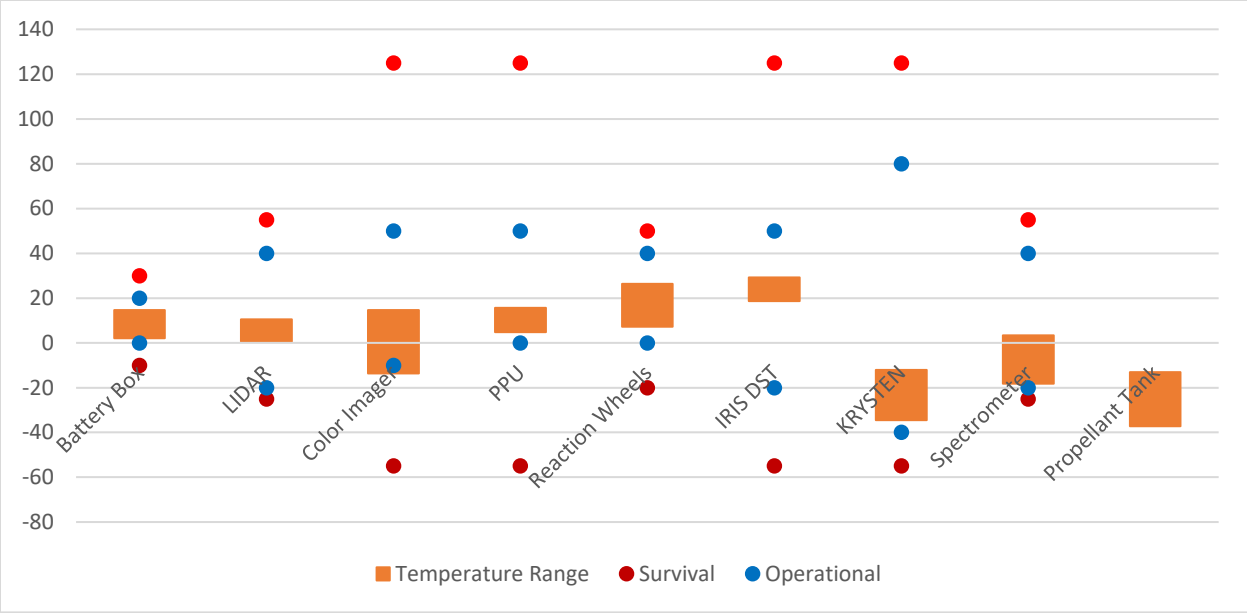

Figure 112. Component Temperature Ranges (α = 0.25±0.05)

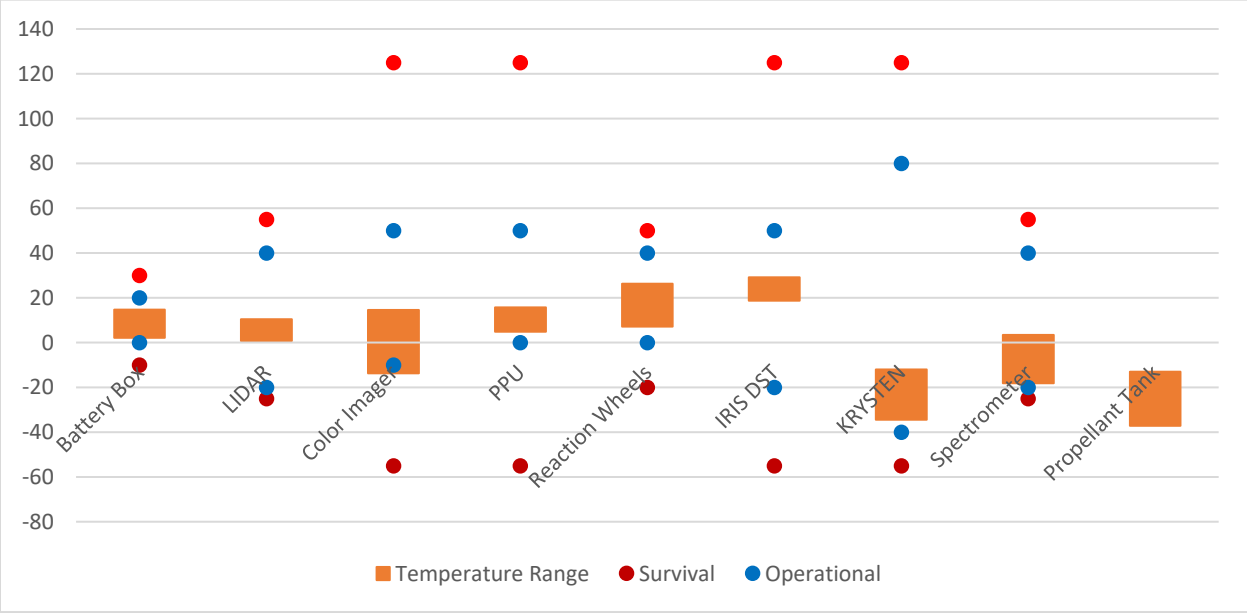

Figure 113. Component Temperature Ranges (α = 0.25±0.05)

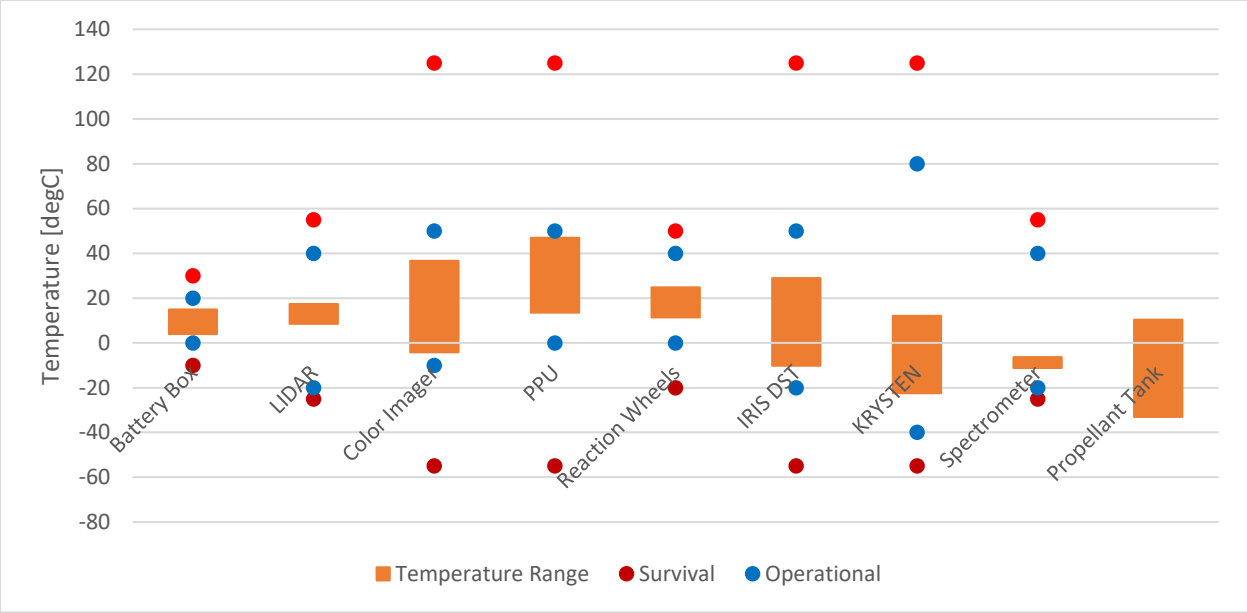

Figure 114. Component Temperature Ranges ($\alpha = 0.50 \pm 0.05$)

9.5 Conclusions

Based on the results from the *COMSOL* simulations of both cases, the ideal case is utilizing the moderately absorptive sun-facing coating of 0.5. While at Earth this results in higher peak component temperatures, including some surface areas exceeding their temperature ranges, the average volumetric temperatures remain within acceptable bounds. The additional absorptivity significantly benefits the spacecraft while further away from the sun as it raises the overall steady-state temperature of the spacecraft frame and components. This means that less power is necessary to keep components within their operational range.

However, the more absorptive coating may necessitate the use of thermal louvers to increase radiator efficiency while at Earth and decrease efficiency while at 7 Iris. While thermal louvers were not necessary in the cases investigated in Section 9.4, this may not hold true after testing and formation of more detailed simulations, as peak temperatures nearly reached their operational upper limit. The case with a very low absorptivity on the sun-facing sides of the spacecraft does not require thermal louvers, as the radiating surfaces do not need to be as

efficient as those in the previous case. This lowers the hardware mass of the thermal control system, as no moving parts are necessary, but also raises the heating power requirement, as the spacecraft reaches a lower steady-state frame temperature in all phases of flight.

Assuming a stock MLI mass of 1.2 kg/m^2, the required mass of MLI to enclose all electronics was 1.36 kg. To enclose the remaining open body panels required another 0.96 kg. As the mass of patch heaters and thermal coatings is negligible compared to the mass of MLI, the total thermal control subsystem mass is approximately 2.37 kg. Thermal louvers would likely increase this mass significantly but were not considered in the final system iterations as discussed above.

Some assumptions made during the thermal analysis process may not be accurate to actual spaceflight hardware. To create a more accurate model of the spacecraft for an in-depth analysis, models of the components that are not approximated as homogenous volumes should be developed. The heating of the components should also be discretized to the locations of electronics and patch heaters, as opposed to the current model which assumes uniform volumetric heating across the entire component.

The development of a more accurate model of incoming solar radiation should also be considered. The current steady-state models assume that incoming radiation is only along the y-axis direction. This assumption is valid for most phases of flight, as the spacecraft will be orbiting the sun and maintaining constant orientation along its velocity vector while under thrust. However, this assumption does not entirely hold during the deployment and initial exit from Earth's sphere of influence. While the spacecraft must reorient itself to face the sun as it orbits Earth during this phase of the mission, it experiences a period where the viewing angle to incoming radiation is altered. The effect this has on the spacecraft is likely minimal based on

testing of steady-state temperatures at different angles, but the time-dependent case should be considered for a more complete model.

10 Thermal Vacuum Chamber

Thermal vacuum chambers are necessary for testing spacecraft hardware. They allow for the simulation of thermal loads a spacecraft will experience, including prolonged exposure to heat and cold in a vacuum, and thermal shock when transitioning from eclipse to daylight. By creating a TVAC from a system of a liquid nitrogen-cooled shroud and heat lamps, pre-existing vacuum chambers can be given the capability to conduct these tests.

10.1 Design

The TVAC is designed to accomplish several objectives:

1. Fit within existing WPI Aerospace Department vacuum chamber, T2
2. Fit at minimum a 6U CubeSat
3. Not exceed MQP budget of $1750
4. Be constructible by MQP team and outside contractors within MQP timeframe
5. Achieve desired temperature control range of -170 °C – 125 °C
6. Measure test article temperatures

The overall design of the TVAC is a thin, aluminum shroud riding on T-slot extrusions in the vacuum chamber. This shroud has integrated tubing to circulate liquid nitrogen from an external system for cooling. Additionally, there is a T-slot post in front of the shroud to hold the heating lamps. A SOLIDWORKS model of the thermal shroud assembled inside the vacuum chamber with four heat lamps and a sample holder plate is shown in Figure 115.

Figure 115. Model of Shroud with Lamps in Vacuum Chamber

10.1.1 Physical Dimensions

The shroud is a 32-inch inner diameter aluminum cylinder that is 0.125 inches thick and has 35 ft of 0.5-inch D-tubing wrapped around it as a cooling coil. This shroud is supported by three 2-inch x 2-inch L-brackets with corresponding arcs cut out to rest the shroud in. These brackets are supported by plastic sliders riding in the vacuum chamber's 1.5-inch T-slot rails. The heating lamps are supported by a T-slot cross brace between the integrated rails and a 19.375-inch vertical T-slot post. The lamp sockets are affixed to a horizontal T-slot attached to this post. The sample is held on an 18-inch x 18-inch x 1/8-inch steel plate that is perforated to maximize radiation and minimize conduction. This plate is secured in each corner to a 6 inch, 5/16-18 threaded rod ending in a custom shoe to rest on the inside of the shroud.

10.1.2 Material Selection

The TVAC cell must be able to reach both high and low temperatures without damaging itself due to thermal shock. Therefore, the materials selected for construction must be able to withstand repeated heating and cooling cycles while still being affordable and machinable. To determine ideal materials, datasheets for common materials were analyzed and compared, as seen in Table 21.

Requirements			Material/Component
Minimum Temp	-170	°C	Liquid Nitrogen
Maximum Temp	125	°C	Heat Lamps
Thermal Expansion Coefficient	24	με/°C	Aluminum (age hardened)
	10	με/°C	Steel
Thermal Conductivity	120	W/m°C	Aluminum (age hardened)
	60	W/m°C	Steel

Table 21. Aluminum and Steel Thermal Properties

The material must be an effective thermal conductor, able to reach the low temperatures required and effectively transfer heat to the coolant. Deformation due to heat when the lamps are active must be limited or warping of the test cell may result in long-term damage to itself, the electronics, and the liquid nitrogen feed system. Due to its good thermal conductivity, relatively low thermal expansion coefficient, price, and ease of manufacturing, aluminum was selected as the primary material both for the cell walls and the liquid nitrogen tubing.

10.1.3 Cooling

While not directly illuminated in space, spacecraft are subjected to temperatures below 4 K, but reliably cooling something on Earth to such a temperature is exceedingly difficult. However, in most cases the difference between very cold and extremely cold is negligible, so temperatures

of around 100 K are used [14]. This is achievable with liquid nitrogen (LN2), which is readily available in lab settings.

Our system is designed to utilize an expendable supply of LN2 from the lab hosting the vacuum chamber for simplicity and convenience. The LN2 is piped around the outer shell of the thermal device in flattened, D-shaped tubes. The shape of these tubes yields a greater contact area with the device shell, allowing for improved heat transfer and ease of construction.

10.1.4 Heating

The thermal system must be capable of simulating direct sunlight scenarios, where the spacecraft would be subjected to an incoming flux of up to 1.4 kW/m^2 in Earth orbit. Heat lamps are arrayed on one side of the device and directed towards the center to achieve desired heating. Heat lamps do not instantly reach their maximum output radiation, although this is unlikely to cause a significant issue with test results. Additionally, the heat lamps may require a few minutes to reach their operating temperature, but this will not cause any issues when collecting test results. A possible solution to the lamps heating up would be to install a shading mechanism to block the heat lamps while they reached desired output temperatures. This concept would still radiate heat to parts in the vacuum chamber and add unnecessary complications to the project design. For these reasons, the team opted not to use shading mechanisms.

Heat transfer occurring in an idealized model between the walls of the TVAC cell and the object being tested can be described mathematically, using the equations detailed in Section 9.1.2. For an example where all surfaces are treated as diffuse blackbodies,

$$q_{net} = \sigma F_{i-j}\left(T_i^4 - T_j^4\right)\left(A_i - A_j\right) \quad 10.1$$

where σ is the Stefan-Boltzmann constant and F_{i-j} is the view factor from surface *i* to surface *j* [12]. The view factor of two nested spherical bodies must be modified to account for the fact that radiation strikes both the internal and external bodies. This leads to a view factor of

$$F_{j-i} = \frac{r_i^2}{r_j^2} \tag{10.2}$$

where r_i and r_j are the radii of the inner and outer bodies, respectively [12]. Considering this alongside previously examined equations, the heat flux from the outer body to the inner body can be calculated as

$$q_{j-i} = q_j \frac{r_i^2}{r_j^2} \tag{10.3}$$

for the spherical example [12]. This is not entirely reflective of the radiation interaction between the cylindrical walls of the actual TVAC and the irregularly shaped test body. However, the relationships can be used for simple preliminary analysis and understanding of the principles behind thermal radiation in an enclosed environment. Further analysis was carried out using the thermal analysis component of *COMSOL Multiphysics*.

The thermal vacuum chamber will be heated by four "250R40/10/120V 250-Watt Red Safety Coated Heat Lamps" [101]. Each lamp emits 250 watts of power which, when combined, will emit a total of 1000 watts of power. The Sun's flux energy in LEO is estimated to be 1400 watts of power so by combining four bulbs it will provide a similar environment to space while consuming a reasonable amount of energy. These bulbs also have a safety coating making them durable and likely to survive vacuum pressures. These bulbs were chosen instead of an infrared quartz heating element due to their convenience in power delivery and price.

As seen in Figure 115, the lamps are mounted to T-slot beams utilizing a T-nut, bolt, washers, and conduit hangers to grasp the bulb's socket. This set-up will hold the bulb firmly in place ensuring the test chamber is safe. These bulbs are wired outside of the chamber to a controllable four outlet power relay module. This module controls when the lights are powered on and the inclusion of a voltage regulator could allow the vacuum chamber to perform testing at different power levels.

Analysis of both the cooling and heating cycles was done with the same thermal analysis software as the spacecraft, *COMSOL Multiphysics*. The primary focus of the thermal testing was to identify the cooldown time required for a test mass to reach expected on-orbit temperature in the range of -150 to -100 degrees Celsius. The computer analysis also assisted in identifying the impact of different materials on the TVAC's performance, such as thin steel threaded rods and Teflon insulation.

10.1.5 Electronics

The TVAC system must collect and log temperature measurements for the shroud, lamps, and sample under test. The data acquisition system for the TVAC (TVAQ), is based on the system developed for WPI's 2021 FSAE Electric Major Qualifying Project [102], consisting primarily of a Teensy microcontroller and a Raspberry Pi. The TVAQ measures temperature with K-Type thermocouples connected to AD8495 thermocouple analog amplifiers, which are in turn connected to the digital to analog converter of the Teensy. The Teensy collects the data, converts it to a usable format, and streams it to the Pi for logging and display. The flow of this process can be seen in Figure 116 with 4 heat lamps (L) and 5 thermocouples (T). The Teensy communicates with the Pi using custom C++ code created by the EFSAE MQP, and the Pi logs the data with Python code written by this MQP team. The full code can be found in the Appendix

at the end of this report. This Python code generates a CSV file, console output, a live temperature plot, seen in Figure 117, and controls the heating system through the relayed power outlet. Figure 118 is a flow diagram of the entire process for running a test with the TVAC.

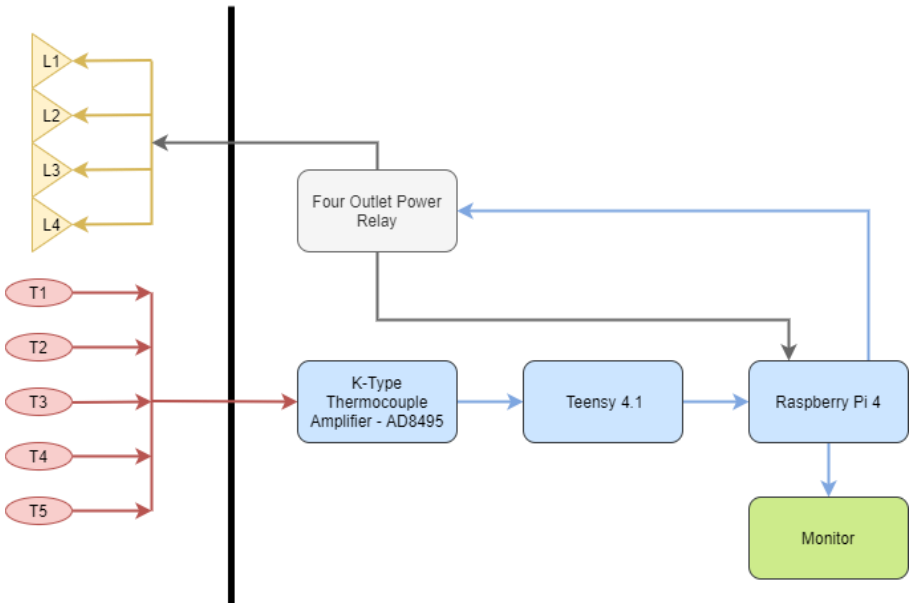

Figure 116. TVAC Connection Diagram

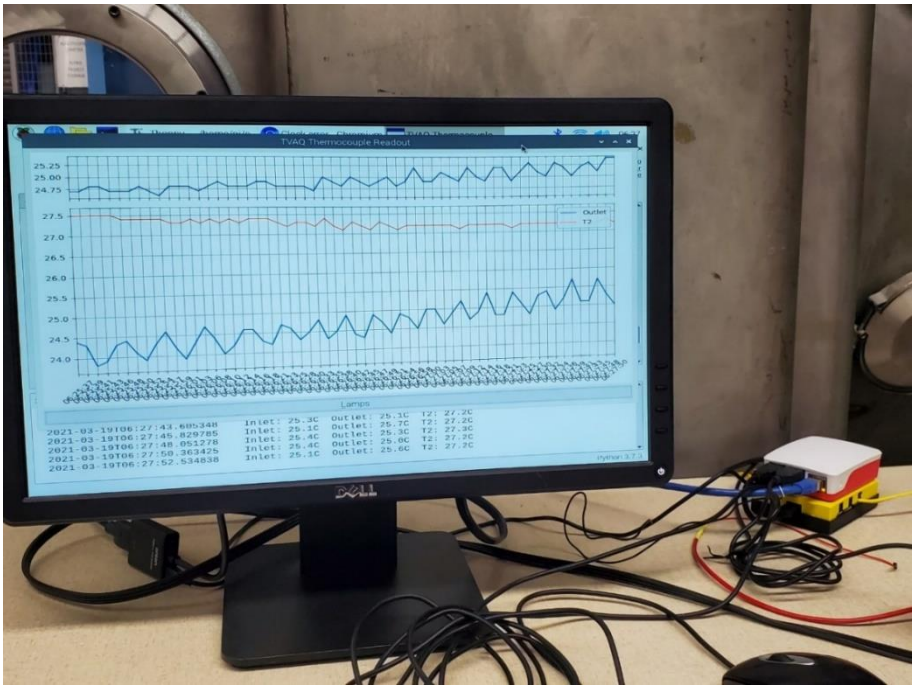

Figure 117. Example Output of the TVAQ

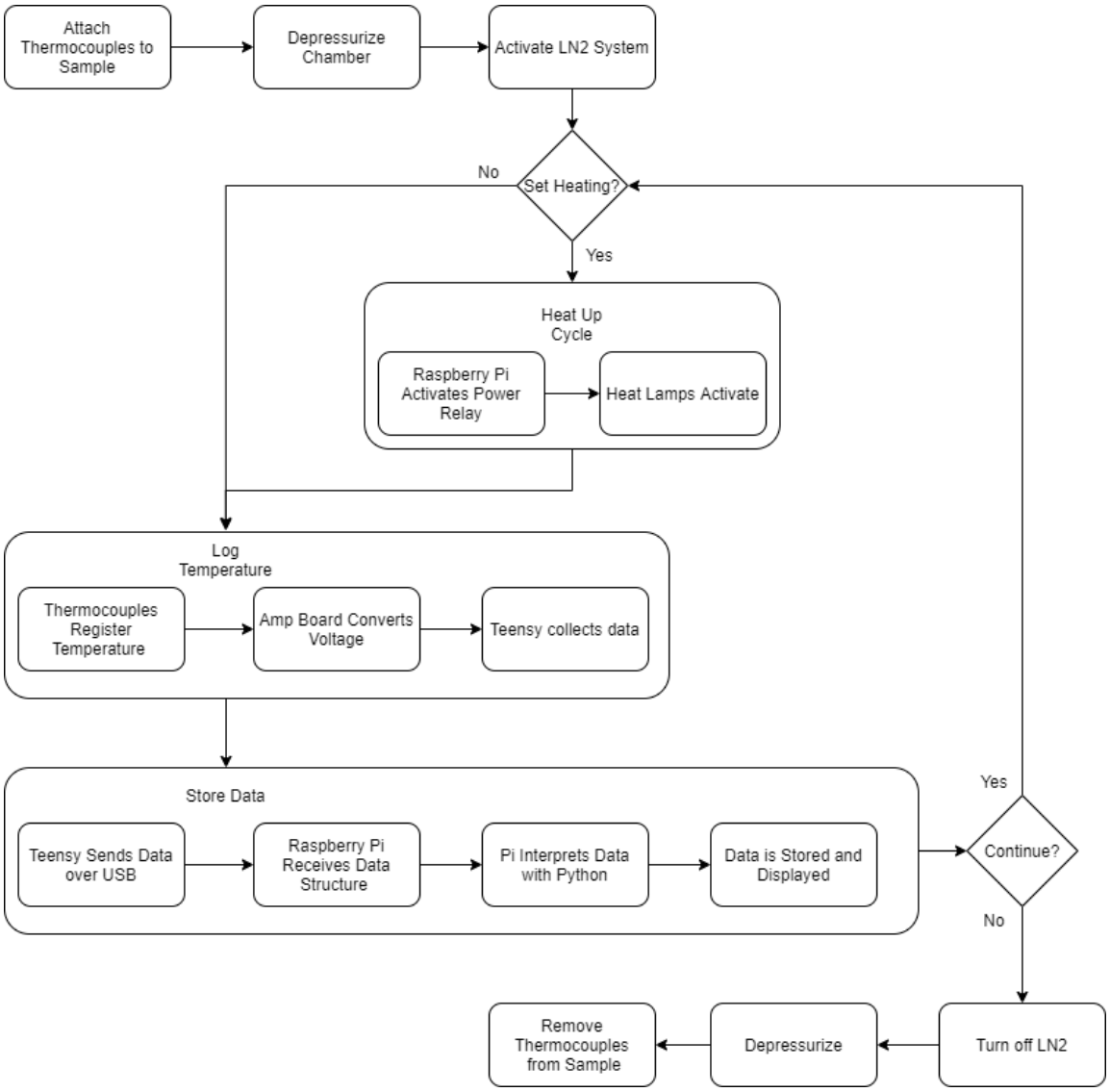

Figure 118. TVAQ Process Flow Diagram

10.2 Construction

The aluminum thermal shroud was generously manufactured and donated by Dynavac, a company located in Hingham, MA that specializes in space simulation systems [103]. The main components requiring construction by the MQP team were the sample holder, the lamp supports, and the TVAQ.

10.2.1 Physical Components

The first subassembly for the TVAC was a sample holder. This platform was designed to hold samples in the center of the thermal shroud while simultaneously minimizing the effects of conduction between the shroud and the sample. Low-carbon steel was chosen as the construction material for the sample plate and supports due to its high resistance to deflection and low thermal conductivity compared to aluminum. The steel sample plate was supported by four threaded rods attached to the steel feet, allowing the height of a sample to be adjusted.

The feet for the sample plate were cut roughly to size on a horizontal bandsaw and then machined in an enclosed CNC milling machine to ensure that they fit properly to the curvature of the shroud. The holes in the feet were also drilled and tapped with the machine. Holes were drilled into the steel sample plate with a hand drill, as the plate was too large to fit in any of the CNC mills available for use.

The second subassembly constructed by this MQP was the lamp support. As mentioned in Section 10.1.1, it is composed of several sections of T-slot aluminum extrusion. The original design was to have the same sliders as support the shroud attached directedly to the bottom horizontal piece of extrusion, however, the central holes were not large enough to tap for the included screws. Instead, L-brackets with sliders were used to secure the lamp holder to the vacuum chamber’s mounting rails. The T-slot aluminum was cut to size using a horizontal bandsaw, with no further machining required.

10.2.2 Electrical Components

Before the final assembly of the TVAQ, the system was mocked up on a breadboard, pictured in Figure 119, to confirm the functionality of the software described in Section 0. Once the system was validated, the connections were soldered to a prototype board for compactness and robustness and placed in a custom housing, as seen in Figure 120 and Figure 121, respectively.

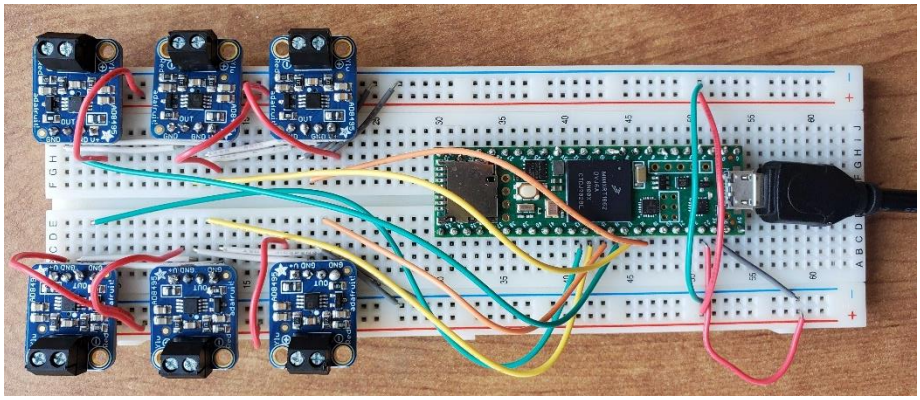

Figure 119. Breadboarded TVAQ

Figure 120. Soldered TVAQ

Figure 121. Assembled TVAQ

The system was able to accurately log temperature data to the display and file, as discussed in Section 0, however, the connection between the Pi and the outlet relay was unable to be established possibly due to the Pi not supplying enough activation current. Thus, the lamps were manually plugged in to begin the heating cycle and unplugged to begin the cooling cycle. But using this concept, the lamps can be controlled by the Raspberry Pi in future tests.

10.3 Testing

The vacuum chamber the TVAC was designed for uses a three-stage system of pumps to lower tank pressure. First, a standard mechanical pump lowers the pressure until a second, lower-pressure diaphragm pump is activated to bring the pressure down to a rough vacuum. This means that the pressure is on the order of 10^{-2} Torr. Finally, a cryopump is used to bring the pressure down to a fine vacuum with pressures on the order of 10^{-7} Torr.

The TVAC system was tested under vacuum with a pressure on the order of 0.1 Torr, considered rough vacuum. The pressure could not be lowered further due to problems with the cryopump. The LN2 cooling system proved to be too complex and expensive for this project,

therefore this test only includes a heat-up cycle using the lamps and a natural cool-down cycle from heat dissipation. While these pressure and cooling approximations are not representative of the actual space environment or the intended operation of the TVAC system, it provides preliminary data for proof of concept.

The thermal shroud and heat lamps were assembled, as seen in Figure 122, to best replicate the model in Figure 115. The sample holder plate was not included in this test due to time constraints and delivery delays. Instead, a spare piece of aluminum was placed on a raised bar to act as the test sample. The thermocouples were mounted in three locations of interest: one at the tubing inlet of the shroud (closest to the front of the tank), one at the outlet (closest to the back of the tank), and one on the sample.

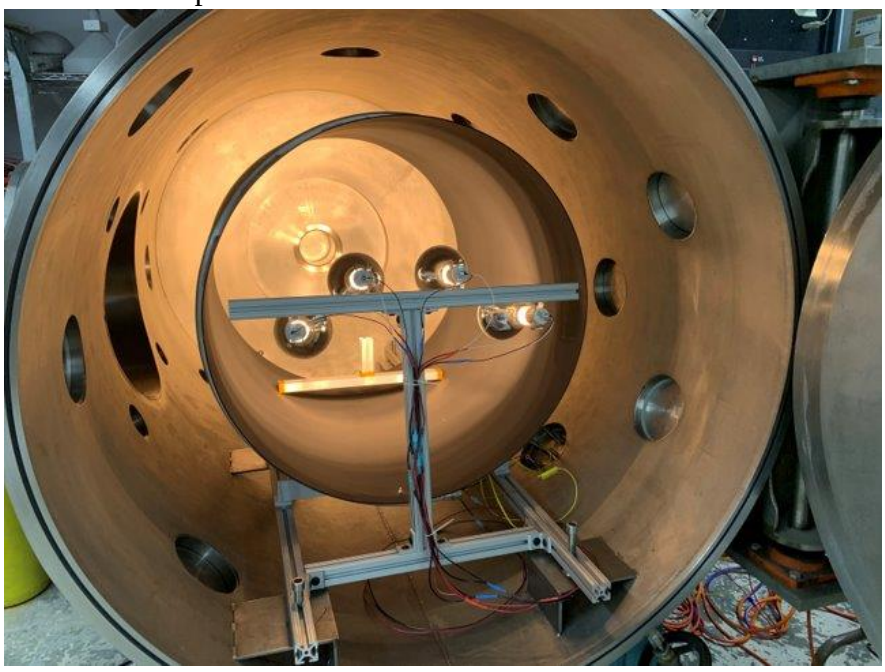

Figure 122. Full TVAC Test Assembly

The vacuum chamber was then sealed and pumped down to about 10 mTorr using the mechanical pump followed by the blower. As mentioned before, the cryopump was not functional at this time, so the tank pressure slowly rose until reaching a steady state at around 100 mTorr.

The team spent about 5 minutes ensuring that the system and data collection were fully functional before beginning the test. Next, the four lamps were plugged in and left on for approximately 35 minutes. Then, they were unplugged, and the system was left for about 7 hours to cool down while remaining at rough vacuum. A graph of this temperature data for all three thermocouples throughout the entire test is shown in Figure 123.

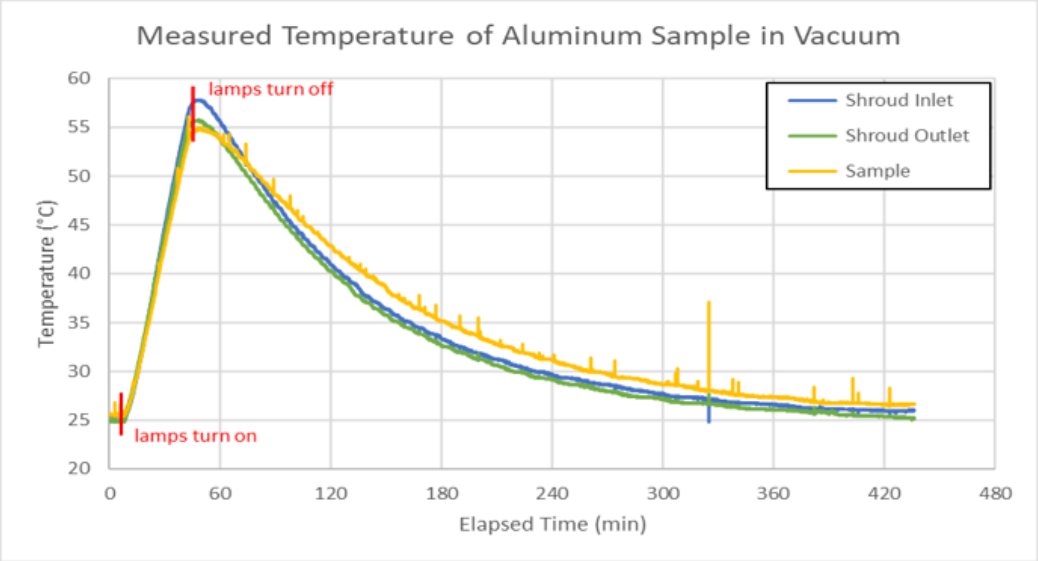

Figure 123. Graph of Temperature Data for TVAC Test Run

The data from this test was then compared to simulated cases of the TVAC generated in COMSOL along the same time intervals, as shown in Figure 124. The test data yielded higher sample temperatures than the simulation did by approximately 10 to 20 degrees Celsius, depending on the area being examined. This may be due to the simulation's use of a point heat source instead of independent lamps that project heat in a specific direction. This results in the sample in the test receiving more incoming radiation than that in the simulation, where more is lost to the walls and the open area outside the shroud. Also, because the cryopump was not available for this test, the chamber pressure was higher than what is typically used to simulate a space environment, and the simulations assumed a perfect vacuum. Any air in the chamber

becomes a source of heat convection, and therefore would result in higher temperatures from the heat lamps than just pure radiation. Simulations of the cool-down cycle were also created as seen in Figure 125, but these could not be validated as the liquid nitrogen system was not assembled.

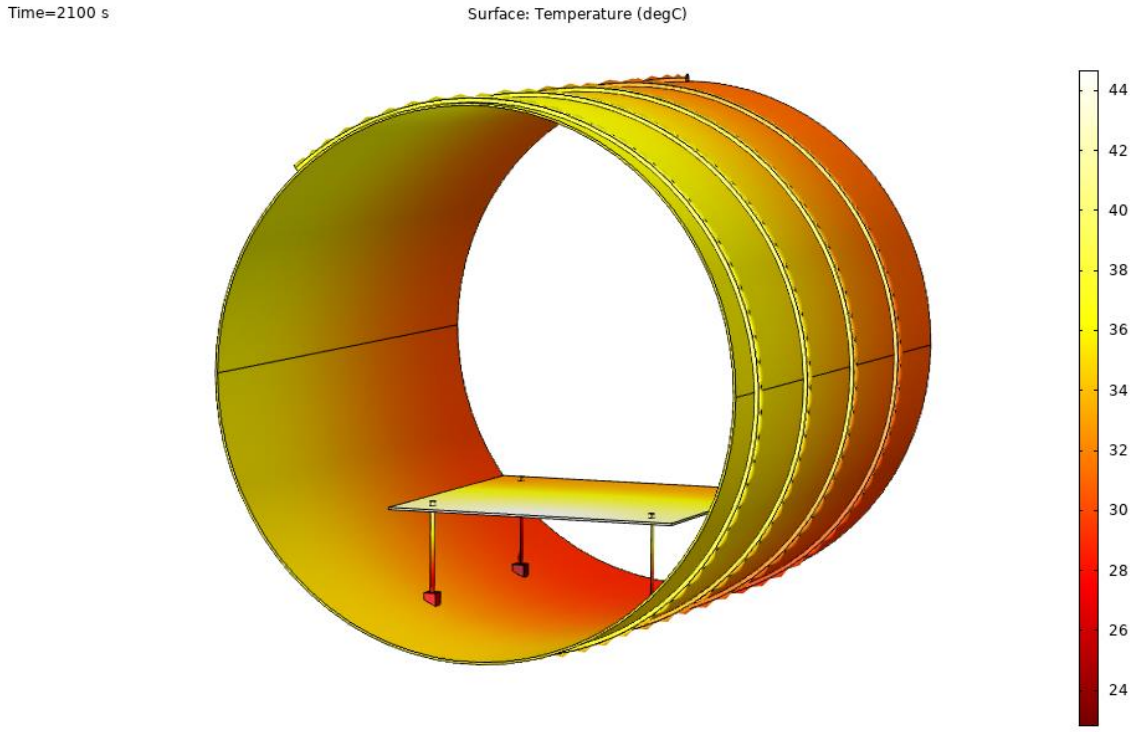

Figure 124. COMSOL Simulation of TVAC Heat-up Cycle

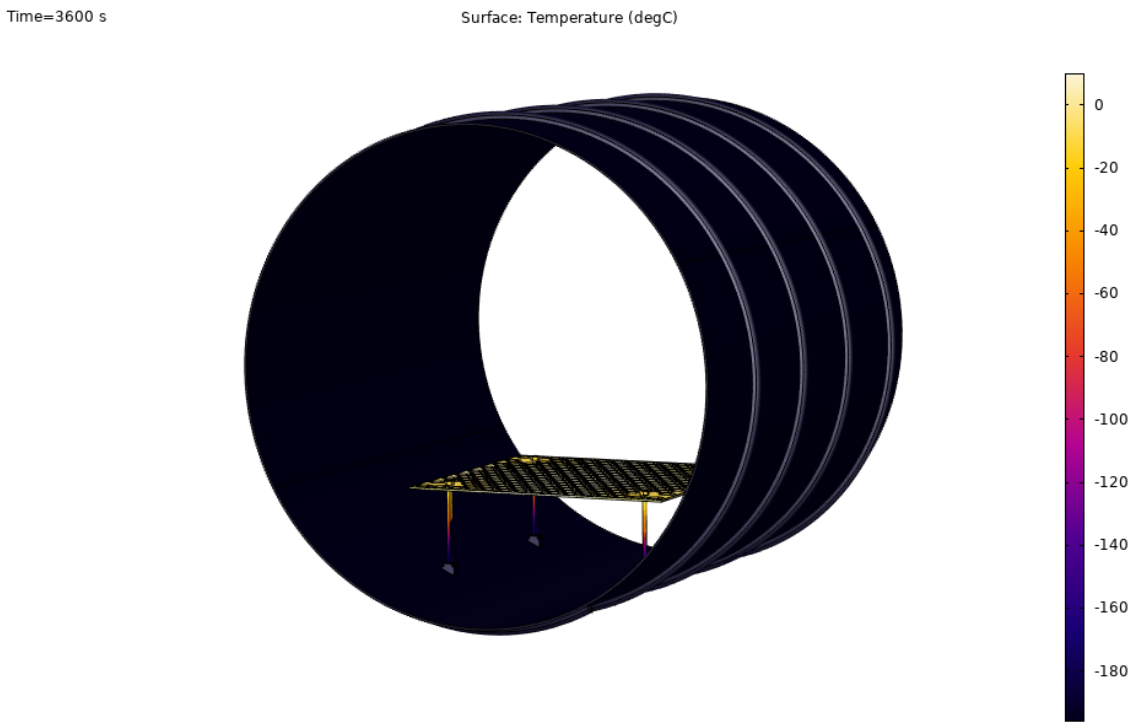

Figure 125. COMSOL Simulation of TVAC Cooldown Cycle

11 Conclusion and Future Work

MAPLE SIRUP's final mass allocation is broken down in Table 22. As expected, the design grew in mass and overall dimensions as it matured. The current iteration of the spacecraft is near the chosen rideshare system's mass limit of 150 kg. As expected, the fuel and solar panels are the most massive components and have little opportunity to shrink.

Subsystem	Component	Mass (kg)
Payload	TriScape100 Color Imager	1.1
	Argus 2000 Infrared Spectrometer	0.280
	Fibertek 2U Concept Lidar	2

	Concept Plasma Spectrometer	0.5
	Summary	**3.88**
Structures	Skeleton Frame	6.15
	Rideshare Adapter	.5
	Summary	**6.55**
Propulsion	**Fuel**	**75.26**
	PPU	3.50
	BHT-200-I (x3)	3.30
	Tank	1.81
	PFCV (x3)	0.36
	SMA Valve	0.18
	Latch Valves (x3)	0.09
	Feed Lines	0.04
	Summary	**9.27**
Power	ISIS Modular Electric Power System	0.4167
	rHawk Solar Array (x2)	25.6
	Summary	**26.0167**
Command and Data Handling	Iris Deep Space Transponder	1.1
	Kryten-M3	0.0619
	Custom-Sized Patch Antenna	1.49
	Summary	**2.6519**
Attitude Determination and Control	NCSS-SA05 Fine Sun Sensor	0.005
	CSS-01,02 Coarse Sun Sensors (x5)	0.1
	Arcsec Sagitta Star Trackers with Mounts (x2)	0.62
	ADXRS453 Gyroscopes (x3)	0.03
	Sputnix Reaction Wheels	0.13
	Marotta Microthrusters (x16)	0.96
	Full GN2 Fuel Tanks (x2)	0.402
	Plumbing/Piping	0.84

	Summary	**3.09**
Thermal Control	Internal Component MLI	1.36
	Body MLI	0.96
	Patch Heaters	0.05
	Summary	**2.37**
Total	**Subtotal**	**129.0886**
	Connectors and ancillary components (fasteners, wiring, etc. assumed 15%)	19.4
	Summary	**148.4886**

Table 22. Mass Breakdown

The design of MAPLE SIRUP establishes the feasibility of an interplanetary SmallSat mission. Each subsystem on the spacecraft has been analyzed for its functionality, efficiency, and applicability to the chosen mission profile of a geostationary rideshare launch targeting the main-belt asteroid 7 Iris. These subsystems have been integrated into a cohesive spacecraft and adapted to work in tandem with each other to complete the mission objectives.

Given the time and resource constraints inherent to student groups, alongside additional challenges from working remotely during the COVID-19 pandemic, some areas could be expanded on for spacecraft analysis. Future teams investigating the mission to 7 Iris or similar asteroids should consider the studied areas that could use expansion. Proceeding with the design and construction of MAPLE SIRUP or similar missions would require additional analysis and physical testing to validate the existing design and future technologies that must be implemented for it to be successful.

11.1 Payload

The primary objective of the payload subsystem was to identify payloads that would provide needed information about 7 Iris. After numerous trade studies, MAPLE SIRUP has been

equipped with a TriScape100 Color Imager, Argus 2000 Infrared Spectrometer, Fibertek 2U Lidar, and Concept Plasma Spectrometer. The plasma spectrometer provided a secondary mission objective which was to collect data about plasma activity during the trajectory to 7 Iris. The secondary objective is relevant due to the lack of data on plasma activity in the solar systems and the need to further understand its behaviors to limit interruptions in earth communication systems. The payload subsystem successfully provided power, data, and mass budgets to other sub-systems which guided their component decisions. Lastly, the payload subsystem created vibration, radiation, and thermal limits that guided other subsystem's component decisions and analysis.

There are many areas regarding the spacecraft's payload that could be further explored. Firstly, analysis can be completed to estimate exactly how long it will take to image the target by incorporating its rotations, the spacecraft's orbit, and both items' axis of rotations. Also, further research could be done on secondary mission objectives. The addition of several small sensors could be used to further map proton and energy activity in other areas of the solar system. Also, due to the large file sizes of some payloads, the research could be completed on how to better compress data for communication back to Earth. Lastly, MAPLE SIRUP's mission included the use of two prototype pieces of equipment; future reports on the equipment's TRL after further testing can help confirm the feasibility of the mission.

11.2 Structures

The objective of MAPLE SIRUP's structural system is to carry and support the craft and its components throughout its mission. This must occur while obeying mass, volume, and environmental constraints. Mass and volume constraints of the craft are achieved with the selection of 6061-T6 Al and dimensions of the design. The excitation environment of the launch

vehicle is examined in relation to the spacecraft's natural frequencies. Additionally, using random vibration analysis, the resultant equivalent stresses are modeled. Neither resonance nor failure of the structure occurs.

There are several avenues that could support further research. Analysis of the structural soundness of mounting hardware and interactions with the internal components could be done. If any internal components fail, the resulting collisions and spacecraft functionality could be analyzed. Additionally, the effects of acoustics and shock could take place. Material testing could occur with access to testing equipment and without restrictions to in-person interaction. The effects of thermal shock, random vibration excitation, acoustic excitation, and mechanical loads could be examined through simulation and testing, allowing comparison and further prediction to the behavior of the spacecraft in a vacuum experiencing loads and excitations.

11.3 Propulsion

The objective of MAPLE SIRUP's propulsion system is to deliver the payload to the mission target of 7 Iris, a required ΔV of 13.6 km/s. This performance must be achieved whilst conforming to the mass and volume constraints of the chosen SmallSat form factor. Minimization of mass and volume comes from maximizing the propellant's specific impulse density (ρI_{sp}). MAPLE SIRUP's propulsion system is fueled by iodine, with a ρI_{sp} at least 25% higher than traditional xenon options. A set of three BHT-200-I thrusters was selected to propel MAPLE SIRUP on its roughly 3.5-year journey to 7 Iris for their compatibility with iodine, high I_{sp} and thrust, and moderate power usage. This system requires just over 75 kg of fuel, resulting in a propellant mass fraction of approximately 50%, leaving enough mass budget open for MAPLE SIRUP's other systems.

There are several avenues to expand upon the propulsion system described in this paper: the primary three being system integration, trajectory optimization, and iodine propellant validation. Complete and robust mounting hardware was not investigated for the components of the propulsion system, only preliminary fixtures to mate in the CAD assembly and determine a mass estimate. Updating these features with input from the structural team would improve the cohesiveness and reliability of the spacecraft. Although a significant effort was invested in reducing the fuel mass required for rendezvous, further reduction is expected to be possible. The use of gravity assists was not thoroughly investigated, which would decrease fuel required at the expense of possibly restricting the already tight launch window. Additionally, error analysis was not performed for the trajectory to quantify how sensitive it is to thrust, pointing, and other disturbance errors. Finally, more research is required on the storage and use of iodine propellant for electric thrusters. The preliminary data available indicates satisfactory performance, however, more testing is necessary to evaluate how iodine is delivered from a propellant tank as well as the lifetime of thrusters using iodine.

11.4 Power

The design goal of the power subsystem was to supply the spacecraft with enough power to get to Iris and to perform the tasks needed when at Iris. This goal was accomplished with the power subsystem generating 375 W at Iris with 90 Whr of power storage. Accomplishing this goal also required that the power subsystem fit within the volume requirements of the launch vehicle and stayed within the mass budget of the spacecraft. This was successfully done, with each solar array having a stowed envelope of 48 x 36 x 23 cm and mass below 30 kg.

This power system could be expanded upon in the future by considering different power storage options. Since there was no significant eclipse period, and the spacecraft mass was

limited few power storage options were analyzed. With future investment into this system missions with greater scope and range could be accomplished.

11.5 Command and Data Handling

The CDH is designed to allow MAPLE SIRUP to send and receive commands, health, and payload data. The chosen components include the Iris Deep Space Transponder, the KRYTEN-M3 on-board computer, and a custom-sized patch antenna. Downlinking at 8.45 GHz, the mission can send 8,332 bits per second.

Although this rate is enough for mission functionality, improving it will greatly increase the amount of transferable data and, by extension, the analysis that can be done and the scientific knowledge that can be gained. The rate depends on both the received signal power and the channel bandwidth. Increasing the channel bandwidth requires more advanced radios and antennas, few of which are available for CubeSat missions. It is more feasible to increase the signal power with a more powerful radio or a larger and more efficient antenna.

11.6 Attitude Determination and Control

The ADC system described in this report was designed to meet the objectives of this project. The NewSpace Systems analog sun sensor, 5 Space Micro coarse sun sensors, 2 Arcsec Sagitta star trackers, and 3 Analog Devices gyroscopes are used to determine the spacecraft attitude adequately. The Sputnix reaction wheel system can perform all the analyzed maneuvers, while the 16 Marotta Microthrusters provide a second source of actuation for desaturation. All these selected devices maximize performance while only contributing a total mass of 3.09 kg to the spacecraft.

There are many ways to improve the attitude control system that was not considered in this project due to time constraints and available resources. Future projects should look to fully define the attitude requirements throughout the entire mission. For MAPLE SIRUP, this would include attitude maneuvers for inclination changes and operations once the spacecraft arrives at Iris. The science portion of the mission should be analyzed so that requirements such as payload and communications pointing are better considered. Another large area of attitude control is sensor noise. There will always be some amount of error in the equipment being used, so taking sensor readings to be the truth is a very large and unrealistic assumption. This can be considered by adding random noise to the star trackers, gyroscopes, and sun sensors, then filtering out this noise by comparing these measurements to predictive attitude models using a Kalman Filter.

11.7 Environment

The environmental subsystem was tasked with researching and identifying hazards that will affect the performance and longevity of the spacecraft. MAPLE SIRUP is embarking on an interplanetary mission, over which space conditions change considerably. Unlike LEO satellites, MAPLE SIRUP does not need to account for lengthy disturbances from magnetic fields, oxidation, or thermal shock. Instead, it needs to be more concerned with radiation, thermal control, photons, and plasma activity. The subsystem successfully estimated a total ionizing dosage that is reasonable when compared to the data collect from other interplanetary missions. Lastly, recommendations were given to thermal, ADCS, power, and communications sub-teams that helped determine components that would perform well during the mission.

There are several avenues for expanding on the environment subsystem in this report. Firstly, a more accurate radiation simulation can be completed once more data becomes available. STK has a limited ability to calculate interplanetary radiation and magnetic fields.

New software can be pursued to model these conditions more accurately. Also, further research can be done on modeling the effect of the radiation on each subsystem. For example, the effects of radiation on each subsystem could be graphed to identify which components are at the greatest risk. This extensive modeling may require assumptions to be made or inquiring with component suppliers to collect information on how they test their equipment.

11.8 Thermal Control

Improving the thermal control subsystem would require increasing the accuracy of the thermal model's assumptions and increasing the fidelity of the model. Finding more accurate information on the rate of waste heat generation of electronic components, creating transient models to simulate spacecraft rotation, and accounting for more spacecraft systems like the attitude control thrusters would lower the number of assumptions and increase overall simulation accuracy. The current model is limited in three primary ways – it assumes that electronics are homogenous volumes of a single material, that power is applied equally through an entire volume, and that conduction between adjacent components is perfect. By utilizing an assembly-based geometry in *COMSOL* with less simplified CAD models a more accurate picture of spacecraft component temperature could be found. However, this approach requires significant computational resources and runs the risk of encountering mathematical singularities during simulation due to complex mesh geometry with many overlapping thin surfaces. Testing spacecraft components in the TVAC will allow for validation of simulations and the thermal control subsystem, identifying areas that must be altered before final assembly.

11.9 Thermal Vacuum Chamber

The thermal shroud was initially out of the budget for this project but was successfully designed and manufactured as intended thanks to Dynavac's generous donation. The entire

TVAC setup was machined, assembled, and validated by a preliminary test run. The temperature data that was gathered proves the concept that this device can be used to simulate thermal environments, but many improvements can be made for future implementations. The most important consideration for subsequent tests is to make sure the chamber can be brought closer to vacuum. This was not possible in this project due to complications with the cryopump.

When comparing the heating results with COMSOL simulations, it was found that temperatures measured in the TVAC were higher than in the simulations. This was thought to be caused by the non-perfect vacuum in the chamber, as well as how the heat lamps were represented in the simulation. Future simulations could have multiple directional radiation sources instead of a point source. This would make a more accurate but more computationally intensive representation of the system.

The final improvement of the TVAC assembly that should be pursued is the addition of a controlled cooling system. The thermal shroud was designed to carry coolant through the tubing around its outer surface, but due to time and budget constraints, no source of cooling was implemented into the test for this project. The temperature data shows that it took about 7 hours after the lamps were turned off for the chamber to naturally cool down to its initial state. This is very unrepresentative of the space environment, where components can be exposed to near-instant thermal shock upon exposure to the sun. Integrating a cooling system, such as LN2, into the TVAC would allow for rapid heating and cooling cycles, which could better simulate this thermal shock when testing components.

11.10 Social Impacts

CubeSats and small satellites play a vital role in the space industry. Because of their small size, they are generally cheaper to build and launch than more traditional full-sized satellites.

This increases access to space, allowing more users to perform scientific and commercial missions, and enabling missions that may have previously been too expensive or experimental to attempt. Reducing the barrier to entry of the space industry also helps to remove the monopoly that is held by a select few governments, large corporations, and research institutions over deep space exploration and future exploitation.

This project has three primary impacts: the science it will conduct, the mission design it will validate, and the technology it will demonstrate. Asteroids are an area of interest for many scientists and engineers. Resource extraction from asteroids is currently being investigated by numerous companies and space agencies, to reduce our dependence on environmentally destructive and worker-exploiting terrestrial mining. As 7 Iris is an S-type asteroid, which means that it shows a difference in the diffuse reflection of solar radiation and therefore possibly contains magnesium, nickel, iron, and iron silicates. These materials can be used in a wide variety of fields to benefit society. Magnesium is often used in high-performance alloys and nickel can be used in the manufacturing of reusable batteries for electric vehicles.

The mission design of MAPLE SIRUP functions as a proof of concept that significant interplanetary science can be done with secondary payload spacecraft. Most interplanetary science missions are large, unique spacecraft that require years of research and development and are a primary payload of a launch vehicle. By using modern highly efficient propulsion systems and lightweight science equipment MAPLE SIRUP does not require space as a primary payload and can instead rideshare with a larger, more expensive spacecraft. Similar vehicles may be able to have even lower masses and cheaper design and manufacturing costs depending on the mission they share a ride with, especially if they can detach from their mothership with a positive characteristic velocity.

MAPLE SIRUP also acts as a technology demonstrator, specifically of iodine as a viable deep space propellant. As discussed in Section 4.2, iodine is still in the experimental phase for use with hall effect thrusters and has only been tested on Earth in vacuum chambers. Assuming the technology matures enough to perform on-orbit tests, MAPLE SIRUP will provide a platform for demonstrating its use in intensive, long-duration science missions. Iodine's low cost and ease of handling compared to conventional electric propellants like xenon and chemical propellant like hydrazine will enable more widespread use of efficient electric propulsion, further enabling small and low-cost interplanetary missions.

Appendix

Below is the Python code that runs on the Raspberry Pi write temperature data.

```
# PyQt imports
from PyQt5.QtWidgets import QPushButton
from matplotlib.backends.qt_compat import QtWidgets
from matplotlib.backends.backend_qt5agg import FigureCanvas
# Matplotlib imports
import matplotlib.pyplot as plt
import matplotlib.figure as mpl_fig
import matplotlib.animation as anim
# Matplotlib global setings
plt.rcParams['axes.grid'] = True
plt.rcParams['axes.xmargin'] = 0
plt.rcParams['figure.constrained_layout.use'] = True
# Communication and misc imports
import sys
import datetime as dt
import ArduinoCANInterface as iface
import struct
import serial.tools.list_ports
import RPi.GPIO as gpio

# General variable setup
global pin, heating, labels, lenbles
pin = 21
heating = False
gpio.setwarnings(False)
gpio.setmode(gpio.BCM)
gpio.setup(pin,gpio.OUT)
x  = []   # timestamps
yt = []   # sample temps
ys = []   # shroud temps
labels = ["Inlet","Outlet","T2","T3","T4"]
lenbles = len(labels)  # Teensy code supports up to 10 thermocouples but is limit
ed by this length

# Instructions
print("This program records and plots thermocouple data from the TVAC system")
print("It also controls the heating lamps in the chamber using the spacebar, Alt+
L, or clicking")
print("Data is logged to a csv file labeled with the start date in ISO8601\n")

# CSV Setup
```

```
csv_file = open("TVAC_"+dt.datetime.now().isoformat(timespec='seconds')+".csv",'w
')
csv_file.write("Timestamp,Inlet,Outlet,T2,T3,T4\n")

# Initialize Communication
ports = serial.tools.list_ports.comports()
validPort = ""
for port, desc, hwid in sorted(ports):
    if ("SER=" in hwid):
        print(hwid, port)
        validPort = port
print("Opening port {}".format(validPort))
iface.open(validPort, 115200)


def sample():
    '''Takes sample from C++ adapter for Teensy'''
    measurements = iface.getAll()
    data = []
    for id, v in measurements.items():
        raw = v[1]
        datum = struct.unpack('<i', raw)[0]/10.0
        data.append(datum)
    return data


class ApplicationWindow(QtWidgets.QMainWindow):
    '''The PyQt5 main window'''
    def __init__(self):
        super().__init__()
        # Window settings
        self.setGeometry(300, 300, 800, 400)
        self.frm = QtWidgets.QFrame(self)
        self.lyt = QtWidgets.QVBoxLayout()
        self.frm.setLayout(self.lyt)
        self.setCentralWidget(self.frm)
        # Place matplotlib figure
        self.myFig = MyFigureCanvas()
        self.lyt.addWidget(self.myFig)
        self.setWindowTitle("TVAQ Thermocouple Readout")
        # Add button
        lampbut = QPushButton("&Lamps",self)
        lampbut.setToolTip("toggles heat lamps on/off with\nspacebar / click / Al
t+L\nH appears when lamps are on")
        self.lyt.addWidget(lampbut)
```

```
        lampbut.clicked.connect(self.on_click)
        # Shows
        self.show()
        return

    def on_click(self):
        '''Sets heat lamp status'''
        global pin, heating
        if heating==False:
            gpio.output(pin,gpio.HIGH)
            heating = True
        elif heating==True:
            gpio.output(pin,gpio.LOW)
            heating = False


class MyFigureCanvas(FigureCanvas, anim.FuncAnimation):
    '''FigureCanvas for live plot'''
    def __init__(self) -> None:
        FigureCanvas.__init__(self, mpl_fig.Figure())
        # Store a figure and ax
        self.shroudax,self.sampleax  = self.figure.subplots(2,1,sharex=True,grids
pec_kw={'height_ratios': [1,4]})
        self._tline_ = self.shroudax.plot([0],[0])
        self._sline_ = self.sampleax.plot([0],[0])
        # Call superclass constructors
        anim.FuncAnimation.__init__(self, self.figure, self._update_canvas_, farg
s=(x, yt, ys), interval=1000, blit=False)
        return

    def _update_canvas_(self, i, x, yt, ys) -> None:
        '''Called regularly by the timer'''
        global labels, lenbles
        # Collates data for printing and saving
        temp_c = sample()[:lenbles]
        printstr = ""
        csvstr = ""
        for n in range(lenbles):
            tstr = str(temp_c[n])
            printstr += labels[n]+": "+tstr+"C  "
            csvstr += ','+tstr
        if heating:
            printstr += '  H'
        time = dt.datetime.now().isoformat()
        print(time,"  ",printstr)
```

```
            csv_file.write(time+csvstr+'\n')
            # Store
            x.append(dt.datetime.now().strftime("%H:%M:%S"))
            yt.append(temp_c[0:2])   # sensor numbers for shroud
            ys.append(temp_c[2:])  # sensor numbers for sample
            # Limit plot to last 60 samples
            samp_lim = 30
            x  = x[-samp_lim:]
            yt = yt[-samp_lim:]
            ys = ys[-samp_lim:]
            # Shroud Plot
            self.shroudax.clear()
            self._tline_ = self.shroudax.plot(x, yt)
            self._sline_ = self.shroudax.legend(labels[0:2],loc=1)
            # Sample Plot
            self.sampleax.clear()
            self.sampleax.plot(x, ys)
            self.sampleax.tick_params(axis='x',labelrotation=45)
            self._sline_ = self.sampleax.legend(labels[2:],loc=1)

            return self._tline_,self._sline_,


    qapp = QtWidgets.QApplication(sys.argv)
    app = ApplicationWindow()
    qapp.exec_()
    csv_file.close()
    iface.close()


    # Data Logger Python Library
    #
    # Imports library functions from c++ cpython bindings
    # Is automatically installed by CMake/cpack in
    # /opt/datalogger/bin/Python so that python scripts can easily import

    import sys

    if (sys.version_info > (3, 0)):
        sys.path.insert(1, '/opt/datalogger/lib/')
        # pylint: disable=import-error
        from libArduinoCANInterface import *
    else:
        print("This module can only be used in python3")
        exit(-1)
```

Below is the C++ code that runs on the Teensy to collect the temperature data.

```
#include “LoggerConnection.h”
#include “MovingAverage.h”

constexpr unsigned int k_numSensors = 1;
constexpr unsigned int k_ADCBitDepth = 10;
constexpr unsigned int k_writePeriodMillis = 500;


MovingAverage<10> avgs(0.05);

double getCelsius(double analogVal) {
  constexpr double Vref = 3.3;
  double V = analogVal*(Vref/(pow(2.0,k_ADCBitDepth)-1.0));
  double T = (V - 1.25) / 0.005;
  Serial.print(T);
  Serial.print(“  \n”);
  return T;
}

void setup(void) {
  Serial.begin(115200);
  analogReadResolution(k_ADCBitDepth);
  for (unsigned int I = 0; I < k_numSensors; i++)
    pinMode(A0 + I, INPUT);
}

unsigned long long millisSinceWrite = 0;

void loop() {
  //logData(millis(), 100, “Yo!”, 3);
  for (unsigned int I = 0; I < k_numSensors; i++) {
    avgs[i] = analogRead(A0 + i) * 1.0;
  }

  //logData(millis(), 1, reinterpret_cast<byte*>(&val), sizeof(val));
  int v = 1;
  //logData(millis(), 100, reinterpret_cast<byte*>(&v), sizeof(int));

  if (millis() - millisSinceWrite > k_writePeriodMillis) {
    millisSinceWrite = millis();
    for (unsigned int I = 0; I < k_numSensors; i++) {
      v = static_cast<int>(getCelsius(avgs[i])*10); //decicelsius
      //logData(millis(), 100, reinterpret_cast<byte*>(&v), sizeof(int));
```

```
    }
  }
}

/*****************************************************************************
*****************
 * \file  MultiMovingAverage.h
 * \brief templated exponentially-weighted moving averaging
 *
 * \author Ryan Johnson
 * \date January 6, 2021
 *
 *****************************************************************************
*****************/
#ifndef MULTI_MOVING_AVG_H
#define MULTI_MOVING_AVG_H

//! \tparam size Number of moving averages to use
template <int size=1> class MovingAverage {
public:
    class IndexProxy {
    public:
        IndexProxy(MovingAverage<size>& m, int idx)
            : m(m)
            , idx(idx)
        {
        }
        operator double() const { return m.avgs[idx]; }
        double& operator=(double v)
        {
            m.avgs[idx] = m.avgs[idx] * (1.0 - m.alpha) + v * m.alpha;
            return m.avgs[idx];
        }
    private:
        MovingAverage<size>& m;
        int idx;
    };

    //! \param alpha weight given to new values
    MovingAverage(double alpha)
        : alpha(alpha)
    {
    }
    IndexProxy operator[](int n) { return IndexProxy(*this, n); }
    operator double() const = delete;
```

```
    double& operator=(double v) = delete;


private:
    double alpha;
    double avgs[size];
};

// Template specializations for single-valued moving averages

template<>
MovingAverage<1>::operator double() const {
  return operator[](0);
}

template<>
double& MovingAverage<1>::operator=(double v) {
  operator[](0)=v;
  return avgs[0];
}

#endif // MULTI_MOVING_AVG_H

#ifndef LoggerConnection_H
#define LoggerConnection_H
#include <util/crc16.h>
#include <Arduino.h>


const char magic[4] = {170,170,170,0};

typedef struct {
    uint32_t id;
    uint32_t ts;
    uint32_t length;
    uint32_t crc;
} MessageHeader;

uint16_t make_crc(byte* src, size_t sz);

void logData(unsigned long time, unsigned int id, byte* data, unsigned int length
);

#endif // LoggerConnection_H
```

Below is sample temperature data that was collected during the TVAC test run.

Timestamp	Inlet	Outlet	Sample
2021-04-26T11:53:03.427682	25.4	25	25.5
2021-04-26T11:53:04.543326	25.4	24.9	25.5
2021-04-26T11:53:05.493797	25.4	25.1	25.5
2021-04-26T11:53:06.450358	25.5	25	25.5
2021-04-26T11:53:07.450517	25.5	24.9	25.6
2021-04-26T11:53:08.450280	25.4	24.9	25.5
2021-04-26T11:53:09.450030	25.5	24.9	25.5
2021-04-26T11:53:10.450349	25.4	25	25.5
2021-04-26T11:53:11.449724	25.4	25	25.5
2021-04-26T11:53:12.450545	25.4	25	25.5
2021-04-26T11:53:13.449623	25.4	24.9	25.6
2021-04-26T11:53:14.450418	25.4	24.9	25.5
2021-04-26T11:53:15.449952	25.5	24.9	25.6
2021-04-26T11:53:16.450117	25.4	24.9	25.6
2021-04-26T11:53:17.449606	25.4	24.9	25.5
2021-04-26T11:53:18.450219	25.4	25	25.6
2021-04-26T11:53:19.449796	25.4	25	25.5
2021-04-26T11:53:20.449569	25.4	24.9	25.5
2021-04-26T11:53:21.450156	25.4	24.9	25.6
2021-04-26T11:53:22.450331	25.4	25	25.5
2021-04-26T11:53:23.450087	25.4	24.9	25.5
2021-04-26T11:53:24.450212	25.4	24.9	25.7
2021-04-26T11:53:25.449462	25.5	25	25.5
2021-04-26T11:53:26.449352	25.4	24.8	25.5
2021-04-26T11:53:27.821170	25.5	24.9	25.5
2021-04-26T11:53:28.610590	25.4	24.9	25.6
2021-04-26T11:53:29.449339	25.5	24.9	25.5
2021-04-26T11:53:30.449681	25.5	24.9	25.6
2021-04-26T11:53:31.500139	25.5	25	25.6
2021-04-26T11:53:32.565065	25.5	25	25.7
2021-04-26T11:53:33.540687	25.5	24.9	25.6
2021-04-26T11:53:34.449670	25.5	24.9	25.5
2021-04-26T11:53:35.449390	25.4	24.9	25.6
2021-04-26T11:53:36.449780	25.5	25	25.6
2021-04-26T11:53:37.450031	25.4	24.9	25.5
2021-04-26T11:53:38.449277	25.4	24.9	25.5
2021-04-26T11:53:39.450292	25.5	24.9	25.5
2021-04-26T11:53:40.449829	25.4	24.9	25.5
2021-04-26T11:53:41.449653	25.5	24.9	25.5
2021-04-26T11:53:42.450144	25.4	24.9	25.5
2021-04-26T11:53:43.450165	25.4	24.8	25.6
2021-04-26T11:53:44.449994	25.5	25	25.6
2021-04-26T11:53:45.449801	25.5	25	25.6

References

[1] E. Mabrouk, "What Are SmallSats and CubeSats?," NASA, 25 February 2015. [Online]. Available: https://www.nasa.gov/content/what-are-smallsats-and-cubesats. [Accessed 30 April 2021].

[2] E. Kulu, "Nanosats Database," 4 October 2020. [Online]. Available: nanosats.eu. [Accessed 15 December 2020].

[3] JPL, "Mars Cube One (MarCO)," NASA, February 2020. [Online]. Available: https://www.jpl.nasa.gov/cubesat/missions/marco.php. [Accessed 15 October 2020].

[4] A. M. Rathbun, J. A. Agolli and J. Gadoury, "Design and Analysis of the Sphinx-NG CubeSat," Worcester Polytechnic Institute, Worcester, MA, 2017.

[5] T. Andreani, S. Joy, E. J. Beerbower, B. Snyder, R. Clavijo, J. Valero and G. Lee, *Design and Analysis of a 6U CubeSat and Mission,* Worcester: Worcester Polytechnic Institute, 2020.

[6] J. Mou and I. Webster, "Space Reference: Compiled Data & Simulations for 962,651 Celestial Objects," 2019. [Online]. Available: https://www.spacereference.org/asteroid/7-iris. [Accessed 15 October 2020].

[7] I. A. Crawford, "The Scientific Case for Human Spaceflight," in *Astronomy and Geophysics*, 1998, pp. 14-17.

[8] S. J. Ostro, C. Magri, L. A. M. Benner, J. D. Giorgini, M. C. Nolan, A. A. Hine, M. W. Busch and J. L. Margot, "Astrophysics Data System: Radar Imaging of Asteroid 7 Iris," Smithsonian Astrophysical Observatory, May 2010. [Online]. Available: https://ui.adsabs.harvard.edu/abs/2010Icar..207..285O/abstract. [Accessed 15 October 2020].

[9] Federal Aviation Administration, "Space Vehicle Control Systems," 2018.

[10] M. M. Finckenor and K. K. de Groh, "Space Environmental Effects," National Aeronautics and Space Administration, 15 March 2015. [Online]. Available:

https://www.nasa.gov/sites/default/files/files/NP-2015-03-015-JSC_Space_Environment-ISS-Mini-Book-2015-508.pdf. [Accessed 15 October 2020].

[11] J. L. Barth, "Space and Atmospheric Environments: From Low Earth Orbits to Deep Space," *In: Proceedings of the 9th International Symposium of Materials in a Space Environment*, pp. 16-20, 2003.

[12] L. V. Pisacane, The Space Environment and Its Effects on Space Systems, 2nd Ed, AIAA, 2016.

[13] NASA, "Thermal Control," 3 May 2020. [Online]. Available: https://www.nasa.gov/smallsat-institute/sst-soa/thermal-control. [Accessed 15 September 2020].

[14] R. S. S. Chisabas, G. Loureiro, C. d. O. Lino, J. P. O. Zabala and D. F. C. Salamanca, "Development of a Thermal-Vacuum Chamber for testing in Small Satellites," in *International Conference on Environmental Systems* , Charleston, 2017.

[15] J. S. Torrico, J. Gonzalez-Llorente and S. Sanchez-Sanjuan, "Mission esign "Satellite Libertad 2"," International Astronautical Federation, Jerusalem, Israel, 2015.

[16] H. J. Kramer, "OTB-1 minisatellite mission of SST-US with DSAC hosted payload," eoPortal Directory, [Online]. Available: https://directory.eoportal.org/web/eoportal/satellite-missions/o/otb-1. [Accessed 16 October 2020].

[17] SCS Aerospace Group, "Gecko Imager," SCS & Space Adviory Company, [Online]. Available: https://www.cubesatshop.com/wp-content/uploads/2016/11/Gecko-Brochure-2019-04-30.pdf. [Accessed 6 October 2020].

[18] P. E. Clark, B. Malphrus, D. Reuter, R. MacDowall, D. Folta, T. Hurford, C. Brambora and W. Farrell, "ntrs.nasa.gov," NASA, 2017. [Online]. Available: https://ntrs.nasa.gov/api/citations/20170002429/downloads/20170002429.pdf. [Accessed 5 March 2021].

[19] Thoth, "Argus 1000 Infrared Spectrometer," CubeSat Shop, [Online]. Available: https://www.cubesatshop.com/product/argus-1000-infrared-spectrometer/. [Accessed 3 October 2020].

[20] Fibertek, "3D Imaging Cubesat Lidar for Asteroid and Planetary Sciences, Phase I," NASA, 28 January 2020. [Online]. Available: https://data.nasa.gov/dataset/3D-Imaging-Cubesat-Lidar-for-Asteroid-and-Planetar/pwv5-c6mf. [Accessed 1 October 2020].

[21] H. J. Kramer, "eoPortal Discovery: Chang'e-1 (Lunar-1 Mission of China)," [Online]. Available: https://directory.eoportal.org/web/eoportal/satellite-missions/content/-/article/change1. [Accessed 19 March 2021].

[22] M. Storm, H. Cao, D. Engin and M. Albert, "Cubesat Lidar Concepts for Ranging, Topology, Sample Capture, Surface, and Atmospheric Science," Fibertek, Inc., 2017. [Online]. Available: https://digitalcommons.usu.edu/cgi/viewcontent.cgi?article=3781&context=smallsat. [Accessed 3 October 2020].

[23] S. Chesnevskaya, C. da Via, B. Utting, H. Lee Hughes and S. J. Watts, "ResearchGate," 2019 IEEE Nuclear Science and Symposium (NSS) and Medical Imaging Conference (MIC), May 2019. [Online]. Available: https://www.researchgate.net/publication/336955771_Radiation_testing_of_robotic_systems_-_LiDAR_as_a_case_study_-_Abstract. [Accessed 19 March 2021].

[24] E. E. Scime, A. Barrie, M. Dugas, D. Elliott, S. Ellison, A. M. Keesee, C. J. Pollock, A. Rager and J. Tersteeg, "key elements of a low voltage, ultra compact plasma spectrometer," *Journal of Geophysical Research: Space Physics*, vol. 121, no. 2, pp. 1452-1465, 2016.

[25] E. E. Scime, A. Barrie, M. Dugas, D. Elliott, S. Ellison, A. M. Keesee, C. J. Pollock, A. Rager and J. Tersteeg, "Key Elements of a Low Voltage, Ultracompact, PLasma Spectrometer," AGU Publications, 3 February 2016. [Online]. Available: https://agupubs.onlinelibrary.wiley.com/doi/pdf/10.1002/2015JA022208%4010.1002/%28ISSN%292169-9402.MEASTECH. [Accessed 3 October 220].

[26] Y. Kovo, "Structures, Materials, and Mechanisms," National Aeronautics and Space Administration, 3 May 2020. [Online]. Available: https://www.nasa.gov/smallsat-institute/sst-soa/structures-materials-and-mechanisms. [Accessed 16 October 2020].

[27] J. M. Holt, Structural Alloys Handbook, West Lafayette: CINDAS/Purdue University, 1996.

[28] SSL, "PAYLOAD ORBITAL DELIVERY SYSTEM User's Guide," SSL, 2017.

[29] SpaceX, "Falcon User's Guide," Space Exploration Technologies, 2020.

[30] Paragon Systems, "What is Random Vibration Testing?," Paragon Systems, [Online]. Available: https://paragonsystems.net/understanding-random-vibration-testing-and-sine-testing/. [Accessed 17 March 2021].

[31] NASA GODDARD SPACE FLIGHT CENTER, "General Environmental Verification Standard for GSFC Flight Programs and Projects," NASA Goddard Space Flight Center, Greenbelt, Maryland, 2013.

[32] A. Harish, "What Is the Meaning of Von Mises Stress and the Yield Criterion?," 10 March 2020. [Online]. Available: https://www.simscale.com/blog/2017/04/von-mises-stress/. [Accessed 22 January 2020].

[33] Aerojet Rocketdyne, "Electric Propulsion Satellites Around the Globe," 2020. [Online]. Available: https://www.rocket.com/space/space-power-propulsion/solar-electric-propulsion. [Accessed 13 Dec 2020].

[34] spaceflight101.com, "Dawn Spacecraft & Mission Overview," 2020. [Online]. Available: https://spaceflight101.com/spacecraft/dawn-spacecraft-mission-overview/. [Accessed 8 Oct 2020].

[35] T. N. Edelbaum, "Propulsion Requirements for Controllable Satellites," *American Rocket Society*, vol. 31, no. 8, pp. 1079-89, 1961.

[36] J. Szabo, B. Pote, S. Paintal, M. Robin, A. Hillier, R. D. Branam and R. E. Huffman, "Performance Evaluation of an Iodine-Vapor Hall Thruster," *Journal of Propulsion and Power*, vol. 28, no. 4, pp. 848-57, 2012.

[37] NIST, "Isothermal Properties for Xenon," US Department of Comerce, 2018. [Online]. Available: https://webbook.nist.gov/chemistry/fluid/. [Accessed 8 Oct 2020].

[38] NIST, "Isothermal Properties of Krypton," US Department of Comerce, 2018. [Online]. Available: https://webbook.nist.gov/chemistry/fluid/. [Accessed 8 Oct 2020].

[39] National Center for Biotechnology Information, "PubChem Compound Summary for CID 6061, Methylhydrazine," 3 Oct 2020. [Online]. Available: https://pubchem.ncbi.nlm.nih.gov/compound/Methylhydrazine. [Accessed 8 Oct 2020].

[40] T. D. Smith, H. Kamhawi, T. Hickman, T. Haag, J. Dankanic, K. Polzin, L. Byrne and J. Szabo, "OVERVIEW OF NASA IODINE HALL THRUSTER," NASA Glenn Research Center, 2016.

[41] National Center for Biotechnology Information, "PubChem Compound Summary for CID 807, Iodine," 3 Oct 2020. [Online]. Available: https://pubchem.ncbi.nlm.nih.gov/compound/Iodine. [Accessed 8 Oct 2020].

[42] J. Szabo, M. Robin, 2. S. Paintal, B. Pote, V. Hruby and C. Freeman, "Iodine Propellant Space Propulsion," in *The 33rd International Electric Propulsion Conference*, The George Washington University, 2013.

[43] Allite Inc, "Allite Super Magnesium," 2020. [Online]. Available: https://alliteinc.com/super-magnesium/. [Accessed 5 Dec 2020].

[44] ArianeGroup GmbH, "Shape Memory Alloy Valve for Space Propulsion Systems," 2020. [Online]. Available: https://www.space-propulsion.com/spacecraft-propulsion/valves/shape-memory-alloy-valve.html. [Accessed 9 March 2021].

[45] MOOG Space and Defense Group, "Valves for Spacecraft Propulsion Systems," 2018. [Online]. Available:

https://www.moog.com/content/dam/moog/literature/Space_Defense/spaceliterature/propulsion/moog-monopropellant-thruster-valves-datasheet.pdf. [Accessed 9 March 2021].

[46] Moog Space and Defense Group, "Spacecraft Regulators," [Online]. Available: https://www.moog.com/content/dam/moog/literature/Space_Defense/spaceliterature/propulsion/moog-proportional-flow-control-valve-datasheet.pdf. [Accessed 9 March 2021].

[47] NIST, "Iodine NIST Chemistry WebBook, SRD 69," U.S. Secretary of Commerce, 2018. [Online]. Available: https://webbook.nist.gov/cgi/cbook.cgi?ID=C7553562&Mask=4&Type=ANTOINE&Plot=on. [Accessed 10 March 2021].

[48] K. A. Polzin, J. F. Seixal, S. Mauro, J. Waggoner and R. Coker, "Sublimable Propellant Source for Iodine-fed Ion Propulsion System". Unites States of America Patent 10,399,708, 3 September 2019.

[49] S. Y. Cheng and M. Martinez-Sanchez, "Modeling of Hall thruster lifetime and erosion," in *International Electric Propulsion Conference*, Florence, 2007.

[50] J. Szabo, L. Byrne, M. Strain, S. Paintal, S. Sawyer, T. Yu, G. Kolencik, V. Hruby, T. Grey, D. Petters, T. Haag, J. Mackey and Z. Taillefer, "One Million Newton-Second Duration Test of a 600 Watt Hall Effect Thruster Fueled By Xenon," in *AIAA Propulsion and Energy Forum*, Virtual, 2020.

[51] Aerojet Rocketdyne, "In-Space Data Sheets," 8 April 2020. [Online]. Available: https://www.rocket.com/sites/default/files/documents/In-Space%20Data%20Sheets%204.8.20.pdf. [Accessed 14 March 2021].

[52] Apollo Fusion, "Apollo Power Processing Unit (PPU)," 2020. [Online]. Available: https://apollofusion.com/ppu.html. [Accessed 15 March 2021].

[53] J. S. Snyder, D. M. Goebel, V. Chaplin, A. L. Ortega, I. G. Mikellides, F. Aghazadeh, I. Johnson, T. Kerl and G. Lenguito, "Electric Propulsion for the Psyche Mission," in *International Electric Propulsion Conference*, Vienna, Austria, 2019.

[54] Jet Propulsion Laboratory, "JPL Small-Body Database Browser 7 Iris (A847 PA)," 2020. [Online]. Available: https://ssd.jpl.nasa.gov/sbdb.cgi?sstr=7. [Accessed 13 Dec 2020].

[55] MAXAR Space Infrastructure, *PAYLOAD ORBITAL DELIVERY SYSTEM (PODS) User's Guide,* 2017.

[56] J. Hanuš, M. Marsset, P. Vernazza, M. Viikinkoski5, A. Drouard, M. Brož1, B. Carry, R. Fetick, F. Marchis, L. Jorda, T. Fusco, M. Birlan, T. Santana-Ros, E. Podlewska-Gaca, E. Jehin, M. Ferrais, J. Grice, P. Bartczak, J. Berthier, J. Castillo-Rogez, F. Cipriani, F. Colas, G. Dudziński, C. Dumas, J. Ďurech, M. Kaasalainen, K. Kryszczynska, P. Lamy, H. Le Coroller, A. Marciniak, T. Michalowski, P. Michel, M. Pajuelo, P. Tanga, F. Vachier, A. Vigen, O. Witasse and B. Yang, "The shape of (7) Iris as evidence of an ancient large impact?," *Astronomy and Astophysics,* vol. 624, 2019.

[57] M. Design, "rHaWK Solar Array," MMA Design, [Online]. Available: https://mmadesignllc.com/product/r-hawk-solar-array/. [Accessed September 2020].

[58] CubeSatShop, "ISIS Modular Electrical Power System," CubeSatShop, 2020. [Online]. Available: https://www.cubesatshop.com/product/isis-modular-electrical-power-system/. [Accessed 9 10 2020].

[59] "Flight Software," Arizona State University, [Online]. Available: http://phxcubesat.asu.edu/subsystems/flight-software. [Accessed 10 10 2020].

[60] R. Galliath, O. Hasson, A. Montero, C. Renfro and R. David, "Design and Analysis of a CubeSat," WPI, Worcester, 2019.

[61] AAC Clyde Space, "AAC_Datasheet_Kryten_original.pdf," AAC Clyde Space, 28 July 2020. [Online]. Available: https://www.aac-clyde.space/assets/000/000/179/AAC_DataSheet_Kryten_original.pdf?1600342763. [Accessed 13 Dec 2020].

[62] W. J. Larson and J. R. Wertz, Space Mission Analysis and Design, El Segundo: Microcosm Press, 2005.

[63] Y. Kovo, "Communications," NASA, 3 May 2020. [Online]. Available: https://www.nasa.gov/smallsat-institute/sst-soa/communications. [Accessed 10 10 2020].

[64] Space Dynamics Laboratory, "iris.pdf," Space Dynamics Laboratory, 2016. [Online]. Available: https://www.sdl.usu.edu/downloads/iris.pdf. [Accessed 13 December 2020].

[65] R. E. Hodges, N. Chahat, D. J. Hoppe and J. D. Vacchione, "A Deployable High-Gain Antenna Bound for Mars: Developing a new folded-panel reflectarray for the first CubeSat mission to Mars.," *IEEE Antennas and Propagation Magazine,* vol. 59, no. 2, pp. 39-49, 2017.

[66] I. Tzinis, "70-meter Antenna," NASA, 8 June 2020. [Online]. Available: https://www.nasa.gov/directorates/heo/scan/services/networks/deep_space_network/complexes/70-meter. [Accessed 14 October 2020].

[67] T. Cornish, "205 - 34-m and 70-m Command," Jet Propulsion Laboratory, 15 December 2014. [Online]. Available: https://deepspace.jpl.nasa.gov/dsndocs/810-005/205/205D.pdf. [Accessed 14 December 2020].

[68] S. D. Slobin, "101 - 70-m Subnet Telecommunications Interfaces," Jet Propulsion Laboratory, 18 September 2013. [Online]. Available: https://deepspace.jpl.nasa.gov/dsndocs/810-005/101/101E.pdf. [Accessed 14 December 2020].

[69] C. Hall, "Attitude Determination," 18 March 2003. [Online]. Available: http://www.dept.aoe.vt.edu/~cdhall/courses/aoe4140/attde.pdf. [Accessed 1 October 2020].

[70] F. L. Markley and J. L. Crassidis, Fundamentals of Spacecraft Attitude Determination and Control, New York: Springer Science+Business Media, 2014.

[71] B. Kenwright, "Quaternions in Practice," 2013.

[72] B. K. Horn, "Some notes on Unit Quaternions and Rotation," 2001.

[73] J. Michalsky, "The Astronomical Almanac's algorithm for approximate solar position (1950–2050)," *Solar Energy*, December 1988.

[74] NewSpace Systems, "NSS CubeSat Sun Sensor," CubeSat Shop, [Online]. Available: https://www.cubesatshop.com/product/nss-cubesat-sun-sensor/. [Accessed 1 October 2020].

[75] Space Micro Inc., "CSS-01,02 Coarse Sun Sensors," SatSearch, 26 June 2020. [Online]. Available: https://satsearch.co/products/space-micro-css-01-02-coarse-sun-sensors. [Accessed 1 October 2020].

[76] J. Enright, D. Sinclair, C. C. Grant, G. McVittie and T. Dzamba, "Towards Star Tracker Only Attitude Estimation," in *Proceedings of the AIAA/USU Conference on Small Satellites*, 2010.

[77] arcsec, "Sagitta Star Tracker," CubesatShop, [Online]. Available: https://www.cubesatshop.com/product/kul-star-tracker/. [Accessed 28 October 2020].

[78] M. #23999, "SparkFun Learn," SparkFun Electronics, 1 February 2013. [Online]. Available: https://learn.sparkfun.com/tutorials/gyroscope/all. [Accessed 13 December 2020].

[79] Analog Devices, "High Performance, Digital Output Gyroscope," Analog Devices, 2011. [Online]. Available: https://www.analog.com/en/products/adxrs453.html#product-overview. [Accessed 5 October 2020].

[80] J. R. Wertz, D. F. Everett and J. J. Puschell, Space Mission Engineering: The New SMAD, Microcosm Press, 2011.

[81] M. Witzmann, "How to (III): Calculate Satellite Disturbance Torques," Valispace, 29 July 2020. [Online]. Available: https://www.valispace.com/how-to-calculate-satellite-disturbance-torques/#:~:text=During%20the%20lifetime%20of%20an,pointed%20in%20the%20right%20direction.. [Accessed 29 September 2020].

[82] IIT Bombay Student Satellite Team, "Satellite 101 Wiki," Indian Institute of Technology Bombay, 26 September 2020. [Online]. Available:

https://www.aero.iitb.ac.in/satelliteWiki/index.php/Main_Page. [Accessed 28 September 2020].

[83] M. Witzmann, "How To (IV): Size an Attitude Control System," Valispace, 1 August 2020. [Online]. Available: https://www.valispace.com/how-to-size-an-attitude-control-system/. [Accessed 30 September 2020].

[84] Sputnix Private Space Company, "Sputnix," Sputnix Private Space Company, 2020. [Online]. Available: https://sputnix.ru/en/equipment/cubesat-devices/reaction-wheels-block. [Accessed 28 October 2020].

[85] National Aeronautics and Space Administration, "SmallSat Institute: Guidance, Navigation and Control," NASA, 3 May 2020. [Online]. Available: https://www.nasa.gov/smallsat-institute/sst-soa/guidance-navigation-and-control. [Accessed 4 October 2020].

[86] Marotta Controls, Inc., "Marotta," Marotta Controls, Inc., 2020. [Online]. Available: https://marotta.com/products/flow-controls/satellite-propulsion-controls/cold-gas-microthruster/. [Accessed 2 November 2020].

[87] V. Carrara and H. Kuga, "Torque and Speed Control Loops of a Reaction Wheel," International Conference on Vibration Problems, 2013.

[88] "The Space Environment," Federal Aviation Administration, [Online]. Available: https://www.faa.gov/about/office_org/headquarters_offices/avs/offices/aam/cami/library/online_libraries/aerospace_medicine/tutorial/media/III.4.1.2_The_Space_Environment.pdf. [Accessed 15 October 2020].

[89] M. Garcia, "NASA.gov," NASA, 7 August 2017. [Online]. Available: https://www.nasa.gov/mission_pages/station/news/orbital_debris.html. [Accessed 19 March 2021].

[90] NASA, "Magnetopsheres," NASA, [Online]. Available: https://science.nasa.gov/heliophysics/focus-areas/magnetosphere-ionosphere#:~:text=A%20magnetosphere%20is%20the%20region,by%20the%20planet's%2

0magnetic%20field.&text=The%20magnetosphere%20shields%20our%20home,particles%20streaming%20off%20the%20sun.. [Accessed 15 October 2020].

[91] C. J. E. Keesee, "Spacecraft Thermal Control Systems," [Online]. Available: https://ocw.mit.edu/courses/aeronautics-and-astronautics/16-851-satellite-engineering-fall-2003/lecture-notes/l23thermalcontro.pdf. [Accessed 27 September 2020].

[92] D. Hyun Ko, S. Laudage, M. Murphy, D. Pelgrift and S. Young, "Design and Analysis of the Sphinx-NG CubeSat," WPI, Worcester, 2017.

[93] J. H. Henninger, "Solar Absorptance and Thermal Emittance of Some Common Spacecraft Thermal Control Coatings," NASA Goddard Space Flight Center, Greenbelt, 1984.

[94] D. W. Hengeveld, M. R. Wilson, J. A. Moulton, B. S. Taft and A. M. Kwas, "Thermal design considerations for future high-power small satellites," in *48th International Conference on Environmental Systems*, Albuquerque, 2018.

[95] NASA, "Iodine Satellite," 28 January 2020. [Online]. Available: https://www.nasa.gov/sites/default/files/atoms/files/isat_fact_sheet_26oct2015.pdf. [Accessed 19 September 2020].

[96] AZ Techology, Inc., "Spacecraft Thermal Control and Conductive Paints/Coatings* and Services Catalog," 1 January 2008. [Online]. Available: http://www.aztechnology.com/pdfs/materials-catalog.pdf. [Accessed 2 October 2020].

[97] J. Claricoats and S. M. Dakka, "Design of Power, Propulsion, and Thermal Sub-Systems for a 3U CubeSat Measuring Earth's Radiation Imbalance," *Aerospace,* vol. 5, no. 63, pp. 1-68, 2018.

[98] P. Shinde, A. Quintero, I. Tansel and S. Tosunoglu, "CubeSat Thermal Analysis," in *30th Florida Conference on Recent Advances in Robotics*, Boca Raton, 2017.

[99] Goddard Space Flight Center, "Aerogel-Based Multilayer Insulation with Micrometeoroid Protection," 27 August 2013. [Online]. Available: https://ntrs.nasa.gov/citations/20130013559.

[100] A. Evans, "Design and Testing of the CubeSat Form Factor Thermal Control Louvers," in *33rd Annual AIAA/USU Conference on Small Satellites*, Logan, 2019.

[101] BulbTown, "bulbtown.com," Bulb Town, [Online]. Available: https://www.bulbtown.com/250R40_10_120V_250_WATT_RED_SAFETY_COATED_HEAT_p/03510.htm#:~:text=Continuous%20Use%20Maximum%20Temperature%20is,Degrees%20Fahrenheit%20(260%20Celsius). [Accessed 05 March 2021].

[102] N. Alescio, N. Bajakian, C. Besch, K. Boenisch, S. Boyd, S. Cacapit, J. Chase, J. Duffield, K. France, T. Giddings, R. Johnson, T. Ninelsing, N. Parker, J. Ruddat, I. Salhi, T. Schaeffer, A. Siamwala and B. Steeves, "Design and Optimization of an Electric FSAE Vehicle," WPI, 2021.

[103] "Dynavac HomePage," Dynavac, 2021. [Online]. Available: https://dynavac.com/. [Accessed 2 May 2021].

[104] D. G. Gilmore, Spacecraft Thermal Control Handbook Volume 1: Fundamental Technologies, El Segundo: The Aerospace Press, 2002.

[105] Northrop Grmman, "Pressurant Tanks," 2020. [Online]. Available: https://www.northropgrumman.com/space/pressurant-tanks/. [Accessed 11 10 2020].

[106] Busek Space Propulsion and Systems Co, "BHT-200 Busek Hall Effect Thruster," 2019. [Online]. Available: http://busek.com/index_htm_files/70000700A%20BHT-200.pdf. [Accessed 11 10 2020].

[107] H. J. Kramer, "Colony-1 CubeSats of NRO," Sharing Earth Observation Resources, 2020. [Online]. Available: https://directory.eoportal.org/web/eoportal/satellite-missions/c-missions/colony-1. [Accessed 9 10 2020].

[108] I. M. Tecnologia, "Cubesat Battery Pack," Ingegneria Marketing Tecnologia, 2016. [Online]. Available: http://www.imtsrl.it/battery-pack.html.

[109] ArianeGroup GmbH, "Electric Ion Space Propulsion Systems and Thrusters," 2020. [Online]. Available: https://www.space-propulsion.com/spacecraft-propulsion/propulsion-systems/electric-propulsion/index.html. [Accessed 15 Dec 2020].

[110] Busek Space Propulsion and Systems, "BHT-600 Busek Hall Effect Thruster," 2019. [Online]. Available: http://busek.com/index_htm_files/70000701B.pdf. [Accessed 15 Dec 2020].

[111] D. Lev, R. Eytan, A. W. Gal Alon, L. Appel, A. Kapulkin and M. Rubanovych, "The Development of CAM200 - Low Power Hall Thruster," *JSASS Aerospace Tech. Japan,* vol. 14, no. 30, pp. 217-23, 2016.

[112] Rafael Ltd, "Rafael Space Propulsion Catalogue," 2019. [Online]. Available: https://www.rafael.co.il/wp-content/uploads/2019/03/RAFAEL_SPACE_PROPULSION_2019-CATALOGUE.pdf. [Accessed 15 Dec 2020].

[113] Exoterra, "Halo Hall-Effect Thruster," 2020. [Online]. Available: https://exoterracorp.com/wp-content/uploads/2020/08/NEWBrochureHaloThruster_Web-1.pdf. [Accessed 15 Dec 2020].

[114] D. M. Goebel and I. Katz, Fundamentals of Electric Propulsion: Ion and Hall Thrusters, Pasadena: JPL Space Science and Technology Series, 2008.

[115] T. Technology, "Argus 2000 IR Spectrometer," Thoth Technology, [Online]. Available: http://thothx.com/getmedia/4c0d3242-b4fb-4e9d-abf7-85dbb5c6653f/20180815-Argus-2K-Owner-s-Manual,-Thoth-Technology,-rel-1-03.aspx. [Accessed 16 March 2021].

[116] G. Dreijer, "TriScape 100," Simera Sense, 10 October 2019. [Online]. Available: https://satcatalog.com/datasheet/Simera%20Sense%20-%20TriScape100.pdf. [Accessed 12 March 2021].

This page unintentionally left blank.